

From Sunlight to Green Hydrogen

-

Metal Oxides as Extremely Thin Absorbers for Photoelectrochemical Water Splitting

vorgelegt von

M. Sc.

Matthias Johannes Müller

von der Fakultät II - Mathematik und Naturwissenschaften

der Technischen Universität Berlin

zur Erlangung des akademischen Grades

Doktor der Naturwissenschaften

Dr.rer.nat.

genehmigte Dissertation

Promotionsausschuss:

Vorsitzender: Prof. Dr. Matthias Bickermann

Gutachter: Prof. Dr. Roel van de Krol

Gutachter: Prof. Dr. Julien Bachmann

Tag der wissenschaftlichen Aussprache: 31.05.2021

Berlin 2021

Abstract

The global greenhouse gas emissions have to be drastically reduced within the next years to limit the anthropogenic climate impact. The largest emissions in the sectors energy, industry, traffic and buildings are driven by the use of fossil fuels, which therefore have to be replaced by renewable sources. A promising route to achieve this is the utilization of solar energy in the concept of photoelectrochemical (PEC) water splitting, which generates solar fuels. For this a photoelectrode is immersed in an aqueous electrolyte which drives electrochemical water splitting at its surface by photogenerated charge carriers. A variety of material requirements for the photoelectrode arises, e.g. a suitable bandgap and chemical stability. The material class of complex metal oxides offers a wide variety of possible photoelectrode materials coupled with the intrinsic stability of oxides. A bottleneck of these oxides is their usually moderate optical absorption and weak charge carrier transport properties. It is either necessary to work with nanostructured samples or with high quality thin films to address this mismatch. Two thin film deposition techniques to individually tackle these challenges are atomic layer deposition (ALD) and pulsed laser deposition (PLD). These two are used in this thesis to deposit extremely thin photoabsorbers. The growth processes, the film properties and the suitability of materials and processes are studied and evaluated.

The first part investigates ALD of Bi_2O_3 from $[\text{Bi}(\text{tmhd})_3]$. Thermal and plasma-enhanced (PE) deposition process are established with growth rates of 0.24 and 0.35 Å/cycle, respectively. The PE process does not only show an increased growth rate but also results in less carbon contaminations, 4.3 at.% compared to 9.4 at.% for the thermal process. Both effects are explained by incomplete ligand removal in the thermal process but complete removal in the PE process, which is shown by real-time spectroscopic ellipsometry (RT-SE). An improvement of the SE-model by fitting two layers allows to simultaneously follow the surface $\text{Bi}(\text{tmhd})_x$ layer as well as the bulk Bi_2O_3 film in the PE process.

The second part investigates ALD of $\text{Mn}_2\text{V}_2\text{O}_7$ as a possible ternary absorber material. Individual binary processes of MnO and VO_x are optimized at 200°C with growth rates of 0.91 Å/cycle and 0.25 Å/cycle, respectively. Both are combined in a supercycle to deposit the ternary $\text{Mn}_2\text{V}_2\text{O}_7$. Post-deposition annealing in argon leads to crystallization into the desired β -phase with an indirect bandgap of 1.83 eV. While the material does show a photoresponse in a PEC cell, the photocurrents are very low and correspond to absorbed-photon-to-current efficiency (APCE) values below 1%.

The last part investigates PLD of CuBi_2O_4 , especially the influence of the deposition parameters laser fluence, substrate temperature and oxygen background pressure. All thin films exhibit excellent quality in terms of phase purity, composition, bandgap (1.85 eV), charge carrier transport and photocurrents. As final quality criteria unmatched APCE values of up to 76% demonstrate the suitability of PLD to deposit high quality absorber materials. Low laser fluences and high substrate temperatures slightly improve the material properties while an oxygen background pressure should be avoided.

Kurzfassung

Innerhalb der nächsten Jahre müssen die globalen Treibhausgasemissionen substantiell reduziert werden um drastische Klimaveränderungen zu verhindern. Die größten Emissionen in den Sektoren Energie, Industrie, Verkehr und Gebäude beruhen auf dem Einsatz fossiler Energieträger welche folglich durch erneuerbare Ressourcen ersetzt werden müssen. Ein vielversprechender Ansatz ist die Nutzung von Sonnenenergie zur photoelektrochemischen Wasserspaltung, welche solare Brennstoffe erzeugt. Dabei wird eine Photoelektrode in wässrige Lösung getaucht und an ihrer Oberfläche wird die elektrochemische Wasserspaltung durch photogenerierte Ladungsträger angetrieben. Dies führt zu vielfältigen Anforderungen an das Material der Photoelektrode, wie eine passende Bandlücke und chemischer Stabilität. Die Klasse der komplexen Metalloxide beinhaltet eine Vielfalt möglicher Photoelektrodenmaterialien mit der intrinsischen Stabilität von Oxiden. Herausforderungen bei diesen Oxiden sind eine oft geringe optische Absorption kombiniert mit schlechtem Ladungsträgertransport. Um diese Diskrepanz zu lösen können nanostrukturierte Proben oder Dünnschichten mit sehr hoher Qualität eingesetzt werden. Zwei Abscheidemethoden die diese Ansätze bedienen können sind Atomlagenabscheidung (ALD) und Gepulste Laserabscheidung (PLD), welche in der vorliegenden Arbeit genutzt werden um extrem dünne Photoabsorber herzustellen. Die Wachstumsprozesse, die Dünnschichteigenschaften sowie die Eignung der gewählten Materialien und Prozesse werden untersucht und bewertet.

Der erste Teil behandelt die ALD von Bi_2O_3 aus $[\text{Bi}(\text{tmhd})_3]$. Ein thermischer und ein plasmagestützter Abscheidprozess werden etabliert mit Wachstumsraten von je 0,24 und 0,35 Å/Zyklus. Neben der erhöhten Wachstumsrate erzeugt der plasmagestützte Prozess auch geringer Kohlenstoffverunreinigungen von 4,3 at.% im Vergleich zu 9,4 at.%. Beide Effekte werden durch eine unvollständige Entfernung der Liganden im thermischen, aber vollständige Entfernung im plasmagestützten Prozess erklärt. Dies wird durch spektroskopischer Echtzeitellipsometrie (RT-SE) gezeigt. Eine Erweiterung zu einem optischen Zwei-Schicht-Modell ermöglicht die gleichzeitige Beobachtung der $\text{Bi}(\text{tmhd})_x$ Oberflächenschicht zusätzlich zur Bi_2O_3 Festkörperschicht.

Der zweite Teil untersucht die ALD von $\text{Mn}_2\text{V}_2\text{O}_7$, einem möglichen ternären Absorbermaterial. Die individuellen binären Prozesse zur Abscheidung von MnO und VO_x wurden bei 200°C optimiert und zu einem Superzyklusprozess kombiniert, um $\text{Mn}_2\text{V}_2\text{O}_7$ abzuscheiden. Die binären Wachstumsraten betragen 0,91 und 0,25 Å/Zyklus. Eine thermische Nachbehandlung in Argon führt zu einer Kristallisation in die gewünschte β -Phase mit einer indirekten Bandlücke von 1,83 eV. Das Material zeigt eine Reaktion auf Licht, aber die Photoströme sind sehr gering mit internen Quanteneffizienzen kleiner 1%.

Der letzte Teil untersucht die PLD von CuBi_2O_4 , insbesondere den Einfluss der Abscheidparameter Laserfluenz, Substrattemperatur und Sauerstoffdruck. Alle Dünnschichten sind von hervorragender Qualität im Sinne von Phasenreinheit, Zusammensetzung, Bandlücke (1,85 eV), Ladungsträgertransport und Photoströmen. Als finales Kriterium zeigen bisher unerreichte interne Quanteneffizienzen von bis zu 76% die

Eignung von PLD zur Abscheidung von Absorbermaterialien. Geringe Laserfluenzen und hohe Substrattemperaturen führen zu einer leichten Verbesserung der Materialeigenschaften während die Präsenz von Sauerstoff vermieden werden sollte.

Table of contents

1	Introduction.....	8
1.1	<i>Energy demand and CO₂ emissions.....</i>	8
1.2	<i>Limits of solar energy</i>	9
1.3	<i>Solar hydrogen production</i>	11
1.4	<i>This thesis.....</i>	17
2	Methods and experimental section	19
2.1	<i>Thin film preparation</i>	19
2.1.1	Atomic layer deposition	19
2.1.2	Pulsed laser deposition	27
2.2	<i>Analytical techniques.....</i>	29
2.2.1	Spectroscopic ellipsometry.....	29
2.2.2	X-ray photoelectron spectroscopy	30
2.2.3	Time-resolved microwave conductivity	31
2.2.4	Photoelectrochemical measurements	34
2.2.5	Further techniques	35
2.3	<i>Setups & routines.....</i>	37
2.3.1	Sample preparation	37
2.3.2	Sample characterization.....	38
3	ALD of Bi₂O₃.....	42
3.1	<i>Thermal ALD of Bi₂O₃.....</i>	43
3.2	<i>Plasma-enhanced ALD of Bi₂O₃.....</i>	46
3.3	<i>Film properties</i>	47
3.3.1	Composition	47
3.3.2	Morphology.....	52
3.3.3	Crystallinity	56
3.3.4	Optical properties	56
3.4	<i>Real-time spectroscopic ellipsometry</i>	58
3.4.1	Single-layer optical model	58
3.4.2	Double-layer optical model	60
3.5	<i>Conclusion, remarks and further steps</i>	63

4	ALD of $\text{Mn}_2\text{V}_2\text{O}_7$	65
4.1	<i>Film growth</i>	66
4.1.1	Binary ALD of MnO_x and VO_x	66
4.1.2	Ternary ALD of $\text{Mn}_x\text{V}_y\text{O}_z$	69
4.2	<i>Sample characterization</i>	70
4.2.1	Crystallization into $\beta\text{-Mn}_2\text{V}_2\text{O}_7$	70
4.2.2	XPS evaluation of $\text{Mn}_2\text{V}_2\text{O}_7$	71
4.2.3	Further techniques	76
4.3	<i>MnO_x sacrificial layer</i>	78
4.4	<i>Photoelectrochemical film performance</i>	80
4.5	<i>Conclusion and outlook</i>	84
5	PLD of CuBi_2O_4	85
5.1	<i>Film growth & characterization</i>	86
5.1.1	Film thickness	86
5.1.2	Crystallinity and morphology	87
5.1.3	Composition	91
5.1.4	Optical properties	95
5.1.5	Charge carrier dynamics	99
5.2	<i>Photoelectrochemical film performance</i>	103
5.2.1	Linear sweep voltammetry	103
5.2.2	Incident photon-to-current and absorbed photon-to-current efficiency	105
5.3	<i>Conclusion and outlook</i>	108
6	Summary and outlook	109
7	Appendix	113
7.1	<i>Supporting data</i>	113
7.1.1	ALD of Bi_2O_3	113
7.1.2	ALD of $\text{Mn}_2\text{V}_2\text{O}_7$	115
7.1.3	PLD of CuBi_2O_4	120
7.2	<i>List of abbreviations and used constants</i>	132
7.3	<i>List of figures</i>	134
7.4	<i>List of tables</i>	138
7.5	<i>Acknowledgments</i>	139
7.6	<i>References</i>	140

1 Introduction

1.1 Energy demand and CO₂ emissions

The 2015 Paris agreement states that the global temperature increase should be kept well below 2°C while pursuing efforts to limit it to 1.5°C.¹ Universal consensus links this rise in temperature to the anthropogenic greenhouse effect with CO₂ as the primary greenhouse gas.^{2,3} As a consequence, the emissions of CO₂ have to decline drastically, by 7.6% per year between 2020 and 2030 for the 1.5°C goal.⁴ While this decline may be met in 2020 due to the Covid-19 pandemic, it will be a huge task for the coming years.⁵ Two values illustrate the challenge: over the last two decades the global CO₂ emissions increased by about 2% annually and the global energy demand will continue to grow by 1.3% annually during the next two decades.^{6,7}

To address this mismatch and to meet the Paris conditions today's major energy sources, oil, coal and natural gas, are not suited. Carbon-neutral energy has to be generated on large scale. Since nuclear power has many disadvantages, renewable energy sources are the obvious choice. These include solar energy, hydropower, biomass and wind, as well as some niche techniques like geothermal or tidal energy. The first four offer the largest potentials and are already playing a significant role in today's energy supply. Among these four one clearly stands out in renewable energy potential, which is solar energy.

Actual estimates of the energy potentials exist but show large variations depending on the underlying assumptions on technological and economic feasibility.^{8–12} What various reports have in common is the conclusion, that only solar and wind have enough potential to cover the global energy demand.

Putting it in numbers it looks like this: The global total energy demand in 2018 was about 600 EJ or 166 PWh.⁷ This energy corresponds to a constant and continuous power consumption of about 19 TW. Depending on the source, the potential of wind power is 4 – 600 TW, while estimates of solar potential range from 118 – 23000 TW.^{8–11} This clearly shows that solar energy is the most promising energy source. *Korfiati et al.* considered the solar potential on a more economic basis. They concluded that 613 PWh (= 3.7x the global energy demand) could be harvested annually with a competitive price tag of 3 – 20 ct/kWh.¹³ *IRENA* investigated the 2019 levelized cost of electricity which are 6.8 ct/kWh for solar energy, 11.5 ct/kWh for offshore wind and 5.3 ct/kWh for onshore wind.¹⁴ Furthermore auction and power purchase agreement (PPA) prices are given with 3.9 ct/kWh for solar energy and 8.2 and 4.3 ct/kWh for offshore and onshore wind, respectively. This shows the ongoing decline in renewable power generation prices. With the cheapest fossil-fuel competitor at an auction price around 4.9 ct/kWh solar energy is not only environmental friendly but also the cheapest available option.

1.2 Limits of solar energy

In principle, solar energy conversion using photovoltaic (PV) systems can fulfill the global energy demand. However, this is only the first step of a carbon neutral energy solution. Various additional challenges arise. Three main points are:

1) Transport distance: The optimal place to harvest solar energy may be far away from the big energy consumers. Around 70% of the global energy is consumed in cities but they cannot produce these amounts of energy themselves.¹⁵ For example Berlin has the potential to generate 5.9 TWh per year from photovoltaics.¹⁶ This covers only about 43% of the electricity demand of the city and even less of the total energy consumption. On the scale of Germany, about 742 TWh of electricity could be generated from PV on roofs and fronts of houses annually.¹⁷ This could in principle cover the German electricity consumption but only 30% of the total German energy consumption.¹⁸

To address this discrepancy remote areas have to be used to harvest solar energy. The electricity has then to be distributed by extensive grids. With increasing size, flexibility and resilience, building such grids become increasingly difficult. The maybe most famous attempt to realize such a system of remote solar energy production and extensive distribution, Desertec, failed in 2014.¹⁹

2) Temporal mismatch in supply and demand: The solar flux is inherently fluctuating not only due to e.g. clouds but also with the day-night cycle and the seasonal cycles, which are shown in Figure 1.

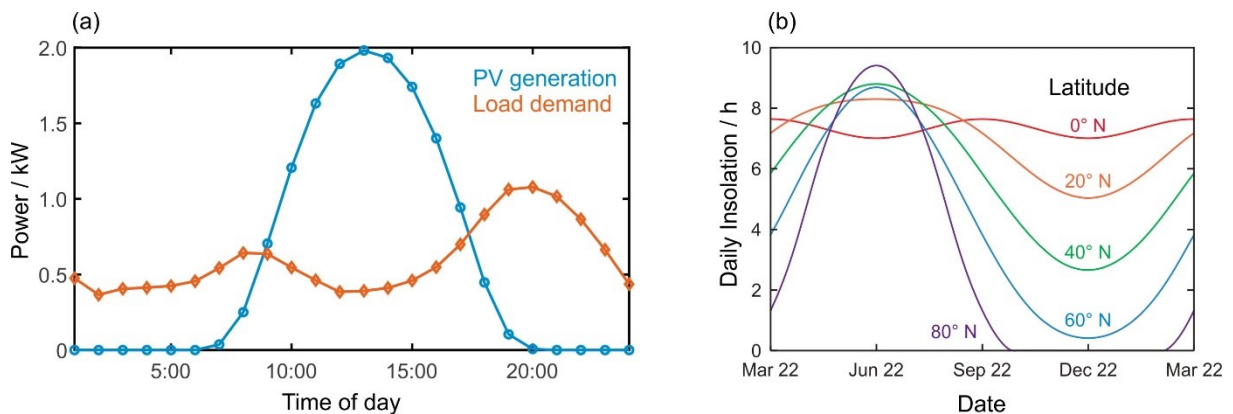


Figure 1: (a) Average daily PV generation and load profile of a typical south Australian household for 2015;²⁰
(b) Effect of latitude in the daily insolation throughout a year.²¹

Obviously the largest solar energy output is around noon when the sun reaches its maximum altitude (blue line) whereas the consumption maxima are in the morning the evening when PV generation is low (orange line). Similar mismatches occur throughout the year, especially outside the tropic latitudes. During summer the solar irradiation allows strong utilization of PV but its output decreases during winter.

With these fluctuations it is very challenging to operate an electrical grid around the year by PV only. A diversification of the energy sources can partly solve the situation but some fluctuations still remain. To make a renewable-based energy system operational and resilient energy has to be stored on varying time scales. Partially this is already done e.g. by pumped-storage hydroelectricity but these are mainly suited for shorter peak demands during daily cycles. Furthermore they heavily rely on the local topography. An upcoming technique is battery storage but in terms of cost, scarcity of materials and capacity they do not meet the requirements for large scale storage yet.²²

3) Electricity cannot replace everything: In many applications, like transport and heating, electricity can replace fossil fuels. However, some processes do not only rely on fossil fuels as energy source but as synthetic building block as well. Most prominently this includes ammonia synthesis in the Haber-Bosch process from grey hydrogen or chemical synthesis from oil products.²³ But also other applications are difficult to electrify due to practical considerations. Examples are the reduction of iron ore in the steel making process (technically difficult), aviation or heavy-duty transport (low energy density of electricity storage in batteries).²³ For these applications some kind of chemical fuel is needed or is at least most promising.

As a consequence, the use of solar generated electricity has to be accompanied by one or more technologies that address the issues of distribution, storage and chemical utilization. The probably most promising and internationally most promoted pathway is the adoption of hydrogen technologies in various applications.²³⁻²⁷ Benefits of hydrogen include the relatively easy and green production from water, the already existing industrial experience in handling and its versatile use in fuel cells, combustion and as a chemical feedstock.^{23,25} Together with CO₂ it is the key element in Power-to-X (PtX) and carbon capture and utilization (CCU) processes e.g. to produce renewable kerosene and other chemical compounds.²³ Long storage times are possible as well as large distance transport and it has the possibility to be adapted in heavy-duty transport and aviation.^{23,28}

However, various challenges remain to be solved. These mainly include the poor volumetric energy density and the currently high cost. For efficient transport and storage hydrogen has to be 'compressed' in some kind of way. This could include actual compression by high pressures, liquefaction at low temperatures or chemical binding e.g. in liquid organic hydrogen carriers (LOHCs) or ammonia. These additional conversion steps in the supply chain introduce energy losses. These are about 5 – 20% for compression, 20 – 45% for liquefaction and 45% for conversion into NH₃ or loading of LOHCs, all with respect to the initial gravimetric energy content of the hydrogen (J/kg).^{23,29} Even without these factors the current cost of green hydrogen is not yet competitive. It currently is in the range of 4 – 8 \$/kg. To be competitive with fossil sources the price has to drop to 1.2 – 2.5 \$/kg, which seems possible.^{23,28}

1.3 Solar hydrogen production

Innovations have to be adapted and huge upscaling processes have to be tackled to achieve the required cost reduction. As stated before sunlight is a desirable energy source, with various possible techniques to produce green hydrogen. The most promising techniques include combined PV-electrolysis systems, direct photoelectrochemical (PEC) water splitting and thermochemical water splitting.²⁴ In conservative practical estimations all three of these techniques can achieve solar-to-hydrogen (STH) efficiencies around 12%.³⁰ PEC water splitting e.g. offers the additional advantage of mild operating conditions at atmospheric pressure and ambient temperature.²⁴ Therefore the PEC water splitting process is introduced in more detail.

In photoelectrochemical water splitting a semiconductor (SC) is used as a photoelectrode, immersed in an electrolyte, and illuminated. The generated photovoltage drives the two reactions of water electrolysis, water oxidation (or oxygen evolution reaction OER) and water reduction (or hydrogen evolution reaction HER). To aid the understanding the basic principles of a semiconducting photoelectrode are described.

Semiconductors are bulk materials with a bandgap E_G of around 1 – 3 eV between the electron-filled valence band and the empty conduction band. A basic example of an intrinsic semiconductor is shown in Figure 2a. This could e.g. be undoped silicon. Important parameters defining the properties of the semiconductor are illustrated. The vacuum level E_{vac} is the energy where an electron is unaffected by the semiconductor (i.e. a free electron) and has no kinetic energy. The ionization energy IE is the minimum energy needed to remove an electron from the semiconductor, i.e. the difference of the valence band maximum E_{VBM} and E_{vac} . The electron affinity EA is the maximum energy gained when an electron is added to the system i.e. the difference between E_{vac} and the conduction band minimum E_{CBM} . The Fermi level E_F is defined as the energy with an occupation probability of 50%. In an intrinsic semiconductor (without illumination) this is exactly in the middle of the bandgap, as the number of electrons in the conduction band is the same as the number of holes in the valence band. The Fermi level can be seen as the average energy of an electron in the semiconductor and thereby as electrochemical potential of the electrons. The work function ϕ is the difference between E_{vac} and E_F . The bandgap E_G is the energy between the conduction band minimum and the valence band maximum and can also be calculated by $E_G = IE - EA$.

The amount of mobile charge carriers in the valence and conduction band can be changed by doping. Donor-dopants add free electrons to the conduction band, which is called n-type doping, visible in Figure 2b. Thereby the Fermi level is shifted towards the conduction band. Vice versa the addition of acceptor-dopants, adding free holes to the valence band, is called p-type doping, shown in Figure 2c. The Fermi level is shifted towards the valence band.

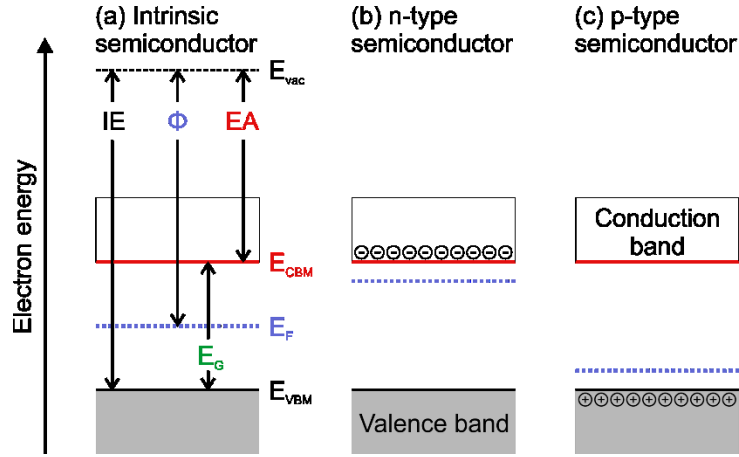


Figure 2: Energy diagrams of semiconductors; (a) intrinsic semiconductor including the definitions of the vacuum level E_{vac} , the energy of the conduction band minimum E_{CBM} , the Fermi level E_F the valence band maximum E_{VBM} , the ionization energy IE , the work function Φ , the bandgap E_G , and the electron affinity EA ; (b) an n-type semiconductor; (c) a p-type semiconductor.

For PEC applications the semiconductor is in direct contact with an electrolyte and illuminated. The corresponding situations are illustrated for an n-type semiconductor in Figure 3. Figure 3a shows the previously described semiconductor isolated next to an electrolyte. E_{redox} marks the redox potential of the reaction that should be driven, e.g. the OER.

In Figure 3b the semiconductor and the electrolyte are brought in contact, charge carriers can flow from one to the other. For the n-type semiconductor these are mainly electrons. This will happen until the electrons will have the same energy at both sides of the interface, i.e. if the Fermi level meets the redox potential. At this point a dynamic equilibrium of charge transport is reached. The initial energy difference between E_F and E_{redox} is counterweighted by a built up potential drop $\Delta\phi_{sc}$. This potential drop describes an upward band bending near the interface caused by the positive charges of non-mobile ionized donor species, which remain during depletion. This band bending is only occurring close to the interface in the so-called space charge region. The width of this space charge increases with increasing $\Delta\phi_{sc}$ and decreasing charge carrier concentrations and temperature. It is typically in the range of 5 – 500 nm.¹¹

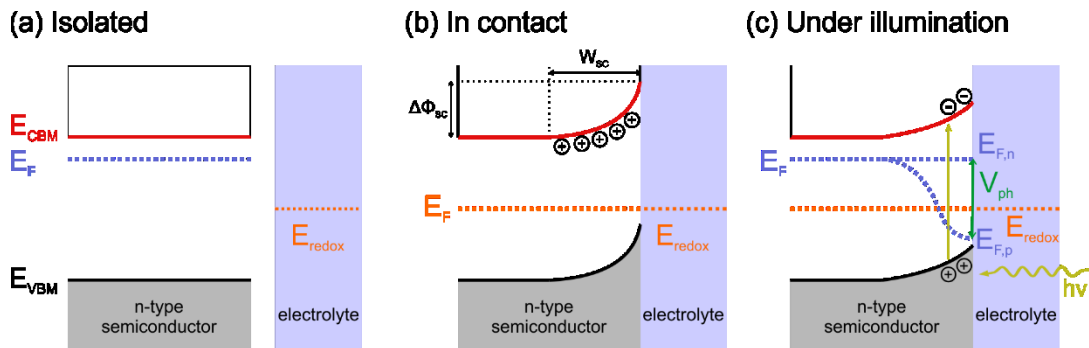


Figure 3: Energy diagrams of (a) an n-type semiconductor and an electrolyte; (b) an n-type semiconductor and an electrolyte in electrical contact with equilibrated Fermi level and redox potential, also indicated the width of the space charge region W_{sc} and the potential drop $\Delta\phi_{sc}$; (c) the semiconductor-electrolyte junction under illumination ($h\nu$) with Fermi level splitting into quasi Fermi levels of the electrons $E_{F,n}$ and the holes $E_{F,p}$, and the photovoltage V_{ph} .

Figure 3c shows the described junction under illumination. Light (shown as $h\nu$) excites electrons from the valence band into the conduction band and holes remain i.e. electron-hole pairs are generated. This external energy input disturbs the previously described equilibrium and the description with a single Fermi level is not suitable anymore. As an alternative the concept of quasi Fermi levels can be used to describe the situation. Separate quasi Fermi levels for electrons $E_{F,n}$ and holes $E_{F,p}$ represent their concentration at a certain point in the semiconductor. The additional electrons in the conduction band barely affect the overall electron concentration in an n-type semiconductor, therefore $E_{F,n}$ is practically at the same energy as E_F . The opposite is true for the holes, their initial concentration in the n-type semiconductor is very low. The photogenerated holes dominate, which causes the shown $E_{F,p}$ at a lower electron energy. The difference of the quasi Fermi levels, the quasi Fermi splitting, is interpreted as the thermodynamic driving force caused by the illumination, i.e. the photovoltage V_{ph} .

The generated charge carriers will not remain in their position after photoexcitation. The holes are consumed by the water oxidation (the OER) at the semiconductor/electrolyte interface. This interface therefore acts as a kind of ‘selective contact’ for holes. At the opposite side, the n-type semiconductor is in contact with an electrically conducting material with a lower work function. This material acts as a selective contact for electrons. These selective contacts form the driving force for charge separation. The electrons will move to the counter electrode, which is connected to the semiconductor, and drive the HER. More detailed introductions on semiconductors, junctions and their use in PEC applications are given in various textbooks.^{11,31,32}

The electrochemical splitting of water into H_2 and O_2 requires a thermodynamic voltage of 1.23 V. However, additional energy barriers must be overcome to drive the OER and the HER leading to required voltages of 1.6 – 1.8 V.^{33–37}

Generating such high voltages with photoelectrodes is far from trivial. In a single absorber this would require a very large bandgap, as e.g. TiO_2 with $E_g = 3.2$ eV exhibits. However, only a small fraction of the solar spectrum is converted into mobile charge carriers by such a wide bandgap absorber, limiting the theoretical solar-to-hydrogen (STH) efficiency to less than 2%.³³

A common way to circumvent such limitations is the utilization of two separate semiconductors in a tandem cell. Such a tandem consists of a large band gap top absorber and a small band gap bottom absorber. The top one absorbs high energy photons of the incoming light while low energy photons (i.e. $h\nu < E_{g,top}$) transmit onto the bottom absorber. Both absorbers generate a photovoltage. By a connection in series these voltages are summated to generate the desired 1.6 – 1.8 V.

The maximum theoretical STH efficiencies and the corresponding bandgaps were investigated in various studies with identified STH values of 21 – 31%.^{33,38,39} The bandgap of the top absorber is typically 1.65 – 1.8 eV, the bottom absorber has a bandgap of 0.95 – 1.34 eV, depending on the assumptions of the model. The widely used silicon with a bandgap

of 1.12 eV nicely fits the principal requirement for the bottom absorber. In combination with a 1.6 – 1.8 eV bandgap top absorber an STH efficiency of 25% is theoretically possible.³⁹

Numerous studies of such tandem PEC devices for solar water splitting were published, using silicon, perovskites, organic dyes, III/V semiconductors, and oxides as absorbers.^{40–45} STH efficiencies of up to 18.5% were reported.⁴⁶ However, each of the employed materials has its challenges, e.g. perovskites are struggling with stability, III/V-SC are expensive and not suitable for large scale fabrication and organic dyes only give low photocurrents. Each of these particular material classes was previously used to build photovoltaic devices and is now employed in PEC cells as well.³⁷

In this sense the case of oxides is special. This class of materials was not adopted from PV applications but specifically chosen to withstand the harsh photoelectrochemical conditions.³⁷ They are promising for PEC applications due to three important properties: (1) their inherent stability against oxidation (as they are already oxidized), (2) their easy fabrication and (3) their outstanding versatility with more than 8000 ternary oxides.^{35,47}

Early research focused on available and/or promising binary oxides like Fe_2O_3 , TiO_2 , Cu_2O or WO_3 .^{48–50} As these do not give the desired performances also ternary oxides were considered as possible absorber materials. Especially the yellow pigment BiVO_4 was investigated in detail due to the easy preparation and high defect tolerance.⁵¹ Other complex metal oxides that aroused interest of PEC researchers include CuBi_2O_4 , SnWO_4 , CuWO_4 , $\text{Mn}_2\text{V}_2\text{O}_7$, Fe_2TiO_5 , BiMn_2O_5 and $\text{Cu}_3\text{V}_2\text{O}_7$.^{47,52–59}

Moderate extinction coefficients and poor charge carrier dynamics are shared bottlenecks of these oxides.^{11,32,60,61} For example, a few μm of material may be needed for reasonable absorption and charge carriers generation, but simultaneously these charge carriers only have diffusion length of a few tens of nm before they recombine.^{50–52,60} This mismatch is illustrated in Figure 4.

Figure 4a shows the situation in an absorber on top of a flat substrate. The thickness is adjusted to the absorption within the material, which determined by its absorption coefficient through Lambert-Beer's law (Figure 4b). After excitation, the charge carriers can only travel distances much shorter than the film thickness due to the inherently short charge carrier diffusion length.³² Only electrons close to the substrate and holes close to the electrolyte are able to leave the absorber (indicated by the ruled areas at the interfaces) and thereby generate a photocurrent. The majority of charge carriers in the bulk of the film rather recombine in between without contributing to the current.^{51,62}

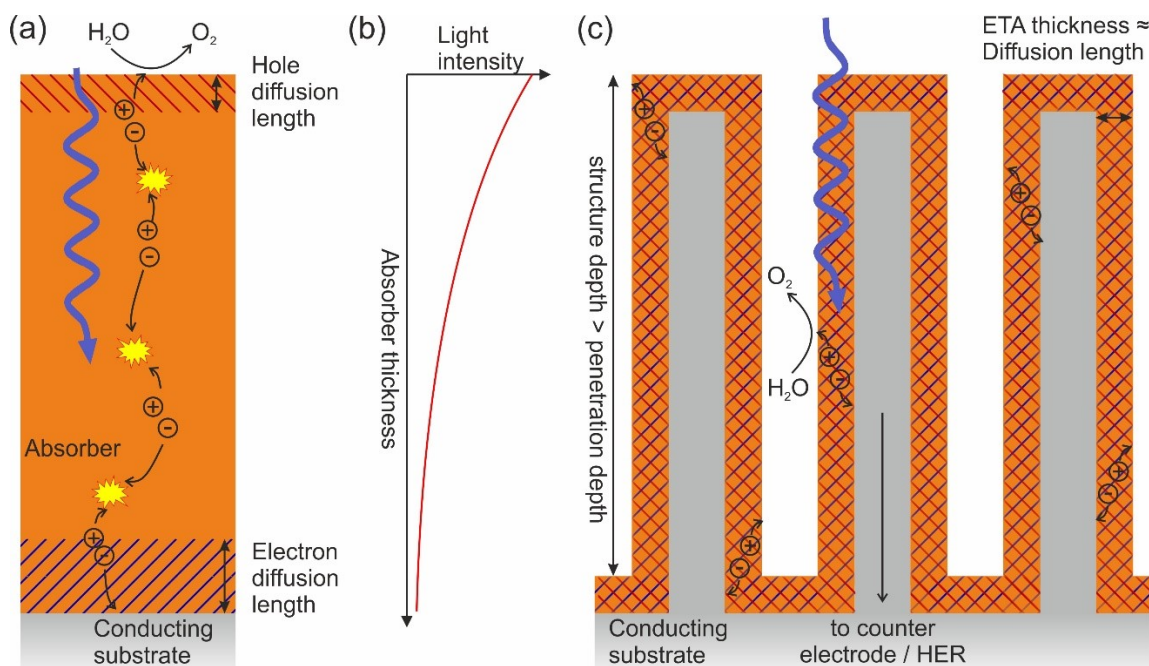


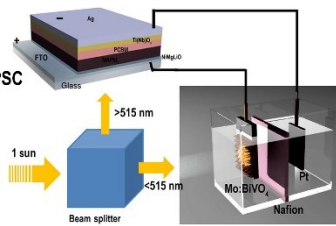
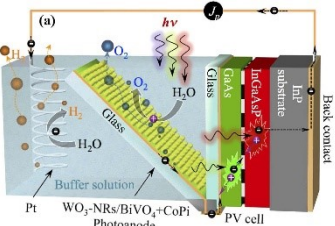
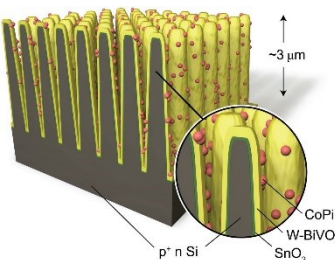
Figure 4: (a) Charge carrier transport in a flat metal oxide absorber anode; (b) Absorption according to Lambert-Beer Law with a moderate extinction coefficient; (c) Charge carrier transport in an ETA on a nanostructured scaffold.

This clear mismatch of charge carrier excitation and extraction has to be addressed.⁶³ A straightforward approach is the utilization of nanostructures to decouple light harvesting from charge carrier transport in a geometrical way, as shown in Figure 4c.⁶² A (conducting) high aspect ratio scaffold, e.g. nanocolumns or nanotrenches, is covered with an extremely thin absorber (ETA). Incident light from the top is absorbed vertically throughout the depth of the structure whereas the generated charge carriers only have to travel horizontally through the thickness of the ETA. Maximum photocurrents can then be achieved with a structure depth in the order of the absorption length and a film thickness in the order of the charge carrier diffusion length.^{62,64}

The use of metal oxide covered nanostructures in a tandem device was shown for various materials. BiVO₄ as oxide is among the most recent and successful examples as shown in publications of *Qiu et al.*, *Pihosh et al.* and *Chakthranont et al.*^{62,63,65} Their key parameters are summarized in Table 1.

The first two reports show impressive STH efficiencies proving the working principle of a tandem PEC device with an oxide top absorber. However, their bottom absorber and especially their complicated device architectures limit their use beyond the demonstration scope.

Table 1: Overview on published nanostructured tandem PEC devices employing BiVO₄.

Author	<i>Qiu et al.</i> ⁶⁵	<i>Pihosh et al.</i> ⁶²	<i>Chakthranont et al.</i> ⁶³
Used oxide	Mo:BiVO ₄	BiVO ₄	W:BiVO ₄
Oxide deposition	Spin coating	Electrodeposition	Spray pyrolysis
Scaffold material	SiO ₂	WO ₃	Si
Scaffold fabrication	Reactive ion etching	Glancing angle deposition	Deep reactive ion etching
Bottom absorber	Perovskite photovoltaic cell	III/V photovoltaic cell	Black Si (scaffold)
Device architecture	<p>Beam splitter</p> 	<p>PV cell perpendicular using scattered light</p> 	<p>Integrated stack</p> 
STH efficiency	6.2%	8.1%	0.45%

Chakthranont et al. report another way which is discussed in more detail. They employ a monolithic architecture, which essentially resembles Figure 4c. Furthermore the nanostructured scaffold (black silicon) acts as the bottom absorber. Unfortunately the resulting STH efficiency of 0.45% is very low. Two main reasons are identified: a low photocurrent from the BiVO₄ top absorber and an overall low photovoltage of the device. The maximum theoretical current density of the BiVO₄ absorber is mentioned to be 7.5 mA/cm². Contrary to that the actually measured current densities do not exceed 2.2 mA/cm², even if additional voltage is applied. Problems could be weak material properties or inaccurate estimations of structure depth and film thickness. In a two-electrode setup without an applied voltage (i.e. stand-alone spontaneous water splitting) the current density is even lower, around 0.3 mA/cm². This indicates that the photovoltage is very low and only facilitates minimal currents. The silicon shifts the onset potential by about 0.5 V while BiVO₄ can generate around 1 V, which leaves only minimal overheads to drive the OER and HER. A mentioned origin of losses are the BiVO₄-Si interface and the Si bulk due to defects created during nanostructuring. In summary *Chakthranont et al.* give an excellent proof of concept and starting point for further optimizations of nanostructured Si – metal oxide tandem PEC devices but not a suitable solution.

1.4 This thesis

The growth of thin films with excellent photoelectrochemical properties and onto nanostructures is far from trivial. Within this thesis two separate techniques are employed to grow extremely thin absorbers and to tackle both challenges from different angles.

In chapters 3 and 4 atomic layer deposition is used as a highly conformal thin film deposition technique. ALD is known for its excellent surface coverage over large areas and into complex geometries, as will be explained in section 2.1.1. But so far it has been rarely used for PEC absorbers due to impurity issues and the challenging process optimization.

In chapter 5 the opposite approach is applied. Pulsed laser deposition is utilized to grow high quality films with quick initial process setup but with difficulties when large areas or nanostructures should be coated.

Chapter 3 elucidates ALD of Bi_2O_3 , a binary oxide which is found in various promising ternary oxide absorbers. A thermal and a plasma-enhanced (PE) process for the deposition of Bi_2O_3 from $[\text{Bi}(\text{tmhd})_3]$ are optimized and the films are investigated in detail. It will be shown that the plasma-enhanced process offers benefits in growth rate and contamination level. Furthermore both processes are investigated by real-time spectroscopic ellipsometry giving additional insight into the growth. For the PE process a novel double-layer optical model is introduced allowing simultaneous screening of the periodic occurring $\text{Bi}(\text{tmhd})_x$ surface layer and the stepwise growing bulk Bi_2O_3 . However, difficulties in process control will be addressed leading to a dissuasion of the process.

Chapter 4 picks up on chapter 3 but with an alternative material, $\text{Mn}_2\text{V}_2\text{O}_7$. Thermal ALD processes of the binary oxides, MnO and V_2O_5 , are adapted and combined into a supercycle to deposit $\text{Mn}_2\text{V}_2\text{O}_7$. Crystallization into the desired β -phase is confirmed by XRD and an almost stoichiometric composition of $\text{Mn}_2\text{V}_{2.06}\text{O}_{7.12}$ is achieved. An additional MnO sacrificial layer is introduced to avoid photocorrosion and PEC activity is shown. However, the film performance is exceptionally low, which is most likely linked to intrinsically poor semiconductor properties of $\text{Mn}_2\text{V}_2\text{O}_7$.

Chapter 5 follows the second approach by PLD of CuBi_2O_4 from a single target. A case study follows the influence of the deposition parameters laser fluence, substrate temperature and background pressure on a range of film properties. It is shown, that low fluences and high substrate temperatures offer slight benefits, e.g. in terms of the often limiting charge carrier diffusion length. Moreover it is proven that PLD is an excellent technique to grow thin films in high quality, e.g. in terms of crystallinity and contamination levels. Especially the use of a single target allows quick access to reasonable results. This makes PLD especially suited for initial material studies to evaluate the overall suitability of the material for PEC.

In the final Chapter 6 the results are summarized and possible next steps are proposed. Furthermore some key findings of these thesis are discussed in a broader context. This includes the suitability of ALD and PLD to deposit extremely thin absorbers, their general

potentials in PEC research, the suitability of oxides as absorbers in PEC devices and the contribution of PEC water splitting on a global energy scale.

2 Methods and experimental section

2.1 Thin film preparation

A variety of thin film preparation methods are used in all sectors of thin film technology, in solar energy conversion this includes sputtering, evaporation or chemical vapor deposition (CVD).^{31,52,53} In this thesis two deposition techniques will be used which are known for their excellent growth control making extremely thin absorbers accessible, atomic layer deposition (ALD) and pulsed laser deposition (PLD).^{66,67}

2.1.1 Atomic layer deposition

Working principle

Atomic layer deposition is a CVD derived method relying on self-limiting chemisorption reactions. The films are grown in a layer-by-layer fashion by alternating exposure of the substrate to two (or more) gaseous precursors.^{68–70} Recently, this principle was even extended to solution based ALD.⁷¹ Mainly oxides are deposited in this manner by using a highly reactive and volatile metal organic precursor which will be oxidized by the co-reactant. This second precursor can e.g. be water, oxygen or ozone.^{67,72} The idealized reaction mechanism is illustrated in the top part of Figure 5.

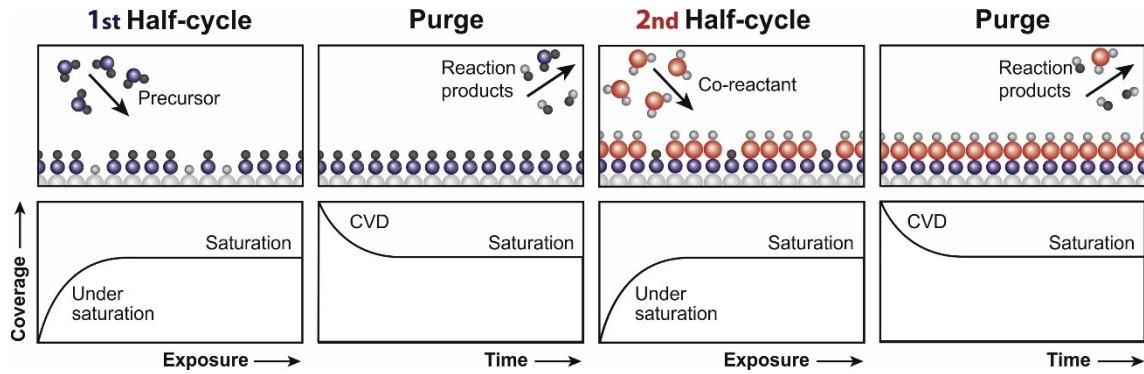


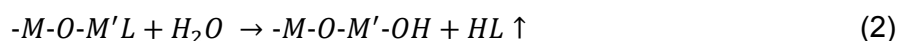
Figure 5: Surface reactions and saturation during an ALD cycle.⁶⁷

The first step in Figure 5 corresponds to the exposure with the metalorganic precursor $M'L_2$ leading to the chemisorption reaction:



The gaseous precursor undergoes a ligand exchange type reaction. The metal M' binds to the surface while the ligand L gets hydrated forming the (volatile) byproduct HL .⁷³ The byproduct is removed in a subsequent purge step. Both steps combined are referred to as the first half-cycle.

The third step is the exposure to the co-reactant. The remaining ligand is removed from the surface and a hydroxyl-terminated surface is generated:



Another purge step removes the byproducts, finishing the second half-cycle and completing the ALD cycle. In this way a hydroxyl-terminated surface is generated similar to the initial surface but with a single atomic layer of the desired metal oxide added. Hence the name atomic layer deposition. Other reaction mechanisms are possible, especially strong oxidizers (e.g. an O₂ plasma) can drive combustion-like mechanisms.^{66,73} Depending on the deposition parameters (primarily the used precursors) a characteristic growth rate is observed, referred to as growth per cycle (GPC). This is the most important descriptor of an ALD process. Thin layers with precise thickness control in the sub-nm range are grown by repeating the ALD cycle.

All surfaces used in this thesis are assumed to be hydroxyl-terminated, i.e. the deposited films itself (Bi₂O₃, Mn₂V₂O₇, and CuBi₂O₄) but also the surface of the used substrates (i.e. silicon (which has a native SiO₂ surface), FTO (dominantly SnO₂), and quartz (SiO₂)).^{68,74} Typically, oxide surfaces get hydroxylated when exposed to ambient air by the reaction of water with bridging oxygen at the surface:⁷⁵



The bridging oxygen species is less reactive than the hydroxyl termination, some precursors only react with the latter.⁷⁶ One further has to keep in mind that this is an equilibrium reaction which is usually shifted to the left with elevating temperatures on metal oxides.^{68,73,75,77} *Puurunen* for example assumes a steady decrease from 10 to 0 available surface sites per nm² between 0 – 1000°C.⁷³

The ALD mechanism relies on self-limiting chemisorption reactions, i.e. the precursors readily react with the initial surface groups as long as they are present and reachable. They do not react with newly formed surface groups, byproducts or the precursor itself. Since only a single monolayer is adsorbed, the reactions saturate and stop without the need for any external trigger. The purge steps remove any excess (i.e. unreacted) precursor molecules and byproducts. This self-saturating nature is the unique feature of ALD leading to the excellent thickness control, uniformity and conformality. These growth characteristics are described further in *Characteristics of ALD* below.

Each of the process steps (precursor adsorption, purge, co-reactant adsorption, and purge) can be described by a saturation curve where saturation is achieved after a certain time of exposure/purging, see the bottom part of Figure 5. Too short dosing times lead to incomplete surface reactions with a lower GPC. Too short purge times can lead to CVD-like gas phase reaction and an increased growth when precursors or byproducts are still present during reactant dosing.

In saturated conditions each ALD cycle adds a well-defined layer of the desired material. One would initially expect that one monolayer is deposited per cycle. Thereby the GPC would only be defined by the deposited material, i.e. given by the distance between two neighboring metal atoms in a crystal lattice, which is usually around 2 Å. However, practically the growth rates are often lower, sometimes only about 0.1 Å/cycle indicating sub-monolayer growth.^{70,78,79}

Two factors can lead to reduced growth rates by depositions of sub-monolayers: (1) A limited amount of available reactive surface sites and (2) steric hindrance of the adsorbed precursor molecules.⁷⁵

One reaction partner in the described mechanism is at the substrate surface, the reactive surface site. In general OH-groups are assumed to be such a reactive surface site.^{67,68,75} Depending on the precursor and the reaction mechanism other surface sites may not be reactive, as described oxygen bridges.^{75,76,78} Therefore very few reactive surface sites may be available, depending on the substrate material, the precursor and temperature. It is therefore possible that all reactive sites are occupied and still not a full monolayer is adsorbed.

The second factor is steric hindrance.^{67,70,78,79} In most cases the ligand of the metalorganic precursor is bulkier than the metal center. Therefore it may block access of the metal center to the reactive surface site.⁷³ For instance, thmd-containing precursors lead to adsorption densities below 1 adsorbate/nm² while up to 10 reactive surface sites/nm² are present.^{68,73,80} Therefore surface saturation is achieved while reactive surface sites are still present, i.e. with a sub-monolayer of the metal center. The size demand is one of the characteristics that has to be kept in mind for the appropriate precursor choice, especially when upscaling and cost reductions are planned.

More detailed insights into ALD growth are e.g. given by *Puurunen*.^{73,75}

Temperature windows

The described ALD mechanisms require a certain temperature. The temperature range in which ALD is operational with an (almost) constant GPC is called the “temperature window”. The range of the temperature window is dependent on the reactants and the reactor. The temperature window and its possible limits are schematically shown in Figure 6.

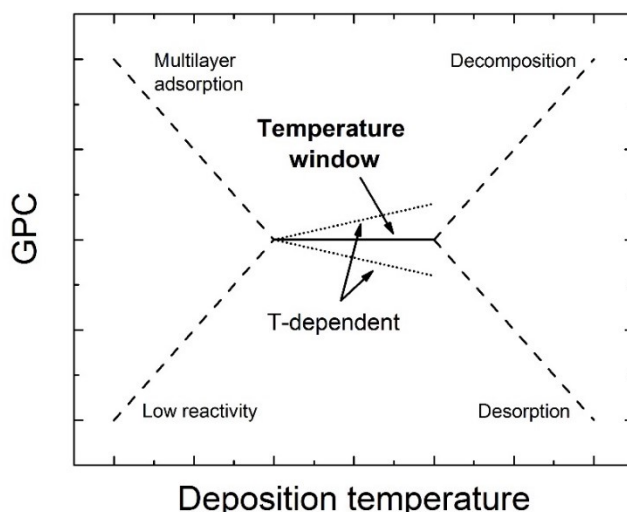


Figure 6: Temperature window of an ALD process.⁸¹

The chemical reactions during ALD have an activation energy. In ALD processes this energy has to be provided in both half cycles. In “classical” ALD processes this energy is provided by the temperature of the substrate. Processes relying only on thermal energy input

are therefore called thermal ALD (T-ALD). Contrary to that “energy-enhanced” ALD processes exists where additional energy supplied e.g. by a plasma in plasma-enhanced ALD (PE-ALD).

The limited reactivity of the precursors towards the surface sites gives in a lower limit of the usable substrate temperature. Below this temperature the GPC decreases as the chemisorption reaction cannot be driven.

The adsorption behavior of the precursors causes the second possible lower temperature threshold. If the pressure in the ALD chamber exceeds the vapor pressure of the precursor at the used temperature the precursor will condense and form multilayers. This leads to an increased growth rate. This temperature threshold therefore depends on the precursors (vapor pressure) and the reactor (base pressure).

At elevated temperatures the opposite effect can occur, even the more strongly bound chemisorbed monolayer may not be built and therefore the GPC decreases. Again, this “desorption” effect depends on the precursors and the pressure in the reactor.

The fourth possibility is decomposition of the precursor at high temperatures. At some point it is possible that a precursor thermally decomposes leading to CVD-like growth with increased deposition rates.

However, even within the temperature window the GPC is not necessarily constant. This is usually attributed to a varying amount of reactive surface sites with increasing temperature, but also changing reaction mechanisms are possible.⁷⁵ A temperature-dependent GPC within the temperature window has e.g. been reported for ALD of MnO_2 by *Mattelear et al.*, where the GPC increases with increasing temperature.⁸² To ensure ALD growth it is advised to establish saturation curves at both edges of the temperature window.

Characteristics of ALD

Three growth characteristics of ALD can be derived from the self-limiting nature of ALD, which are illustrated in Figure 7. The first is precise thickness control. The desired film thickness can be set precisely by the number of ALD cycles. With each cycle the film thickness increases by the GPC, which is in the Å range. Looking at PEC device preparation this control is very beneficial, e.g. ohmic resistances of protection layers can be minimized when the needed film thickness is set precisely.

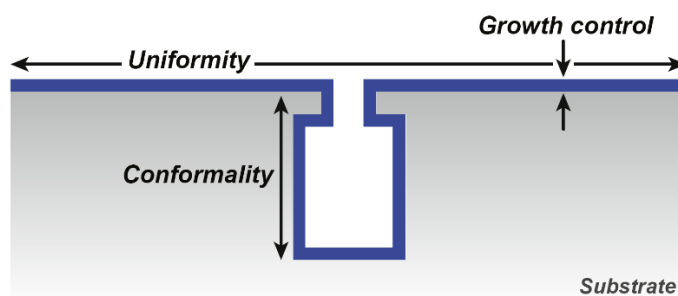


Figure 7: Thickness control, uniformity and conformality in ALD.⁶⁷

Excellent surface coverage is an implication of the self-limiting nature of ALD. Chemisorption occurs on the whole substrate, covering edges etc. and leaving no pinholes.^{81,83} In PEC applications this can avoid short circuits between an electrolyte and the back contact, making ALD attractive to deposit protective layers. The excellent surface coverage leads to the second and third characteristic of ALD: excellent uniformity and conformality. Uniformity refers to similar film thicknesses over large areas. Good uniformity offers great potentials for upscaling of ALD processes.

Conformality describes the coverage within complex geometries like high aspect ratio nanostructures, which is shown in Figure 8.^{80,84} Excellent uniformity makes ALD a powerful tool to grow metal oxides as extremely thin absorbers on nanostructured scaffolds, as described in chapter 1.3. A detailed look on conformality in ALD and ALD onto nanostructures is e.g. given by *Cremers et al.*⁸⁰

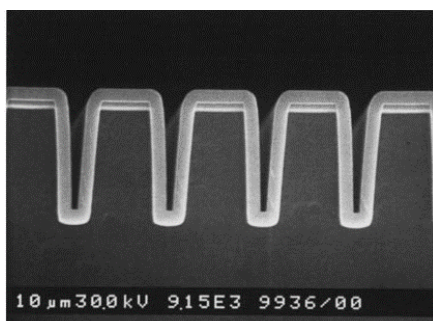


Figure 8: Perfectly conformal ALD-grown Al_2O_3 (light grey) on nanostructures (dark grey).⁸⁴

ALD precursors

As indicated above the precursor choice is essential when an ALD process is implemented. The precursors have to fulfil a variety of requirements which are:^{75,81}

1. Self-limiting adsorption mechanism
2. High vapor pressure
3. High reactivity towards the surface and the co-reactant
4. Thermal stability against decomposition
5. Availability
6. No etching processes of the surface or the growing film
7. Low toxicity, safe handling and easy byproduct treatment

As described above the first requirement is mandatory but factors 2 – 4 are crucial for efficient deposition processes as well. The vapor pressure of a precursor has to be at least in the range of the reactors base pressure at the deposition temperature to enable efficient dosing without condensation. The precursor should readily chemisorb at the substrate surface at the desired temperature. Some precursors require high temperatures to react, which is not compatible with sensitive substrates like organic compounds. The same is true for the co-reactant adsorption in the second half cycle. In addition, the precursor has to be stable to avoid

decomposition (in the bottle, in the gas phase, and on the surface) which can lead to CVD-like growth.

If these basic requirements are met some other beneficial aspects can be considered. Common precursors as trimethylaluminium (TMA) are easily commercially available. Less used precursors may be prepared upon order by specialized vendors. Otherwise precursors have to be synthesized by the respective research group. Precursor synthesis (and the preceding precursor design) is a whole research area itself with specialized research groups.

Etching processes can occur (see *ALD of multinary systems* below) where the by-products attack the substrate or the growing film itself, which is limiting the growth rate. Also components of the deposition tool can be vulnerable, e.g. chlorinated precursors may lead to HCl as byproduct which can cause corrosion problems in the pumps etc. Adequate off-gas treatment has to be ensured.

The second type of precursors are the co-reactants. The co-reactant usually introduces a second species into the growing film. In the work presented in this thesis this is oxygen for the desired metal oxides. The requirements are in principle similar to the metal organic precursors although they are usually more easily met. For example water, the most used co-reactant, is volatile, stable, available, non-toxic, and handled easily. As a consequence, the ability of water to remove ligands of the metal precursor is often the most critical aspect. If water is not effective in removing the ligands more potent oxidizers are required. These are for example H_2O_2 , O_3 , or an oxygen plasma. Less frequently used oxygen sources are alcohols or alkoxides^{72,81}.

Deposition of metals, nitrides, sulfides etc. require other co-reactants, e.g. hydrogen plasma, NH_3 , and H_2S . These processes are not considered in this work. An extensive database of all kinds of published ALD processes, the "Atomic limits" database, was recently established, which use is recommended. The overview periodic table of the database is shown in Figure 9, the database can be accessed via:

<https://www.atomiclimits.com/alddatabase>

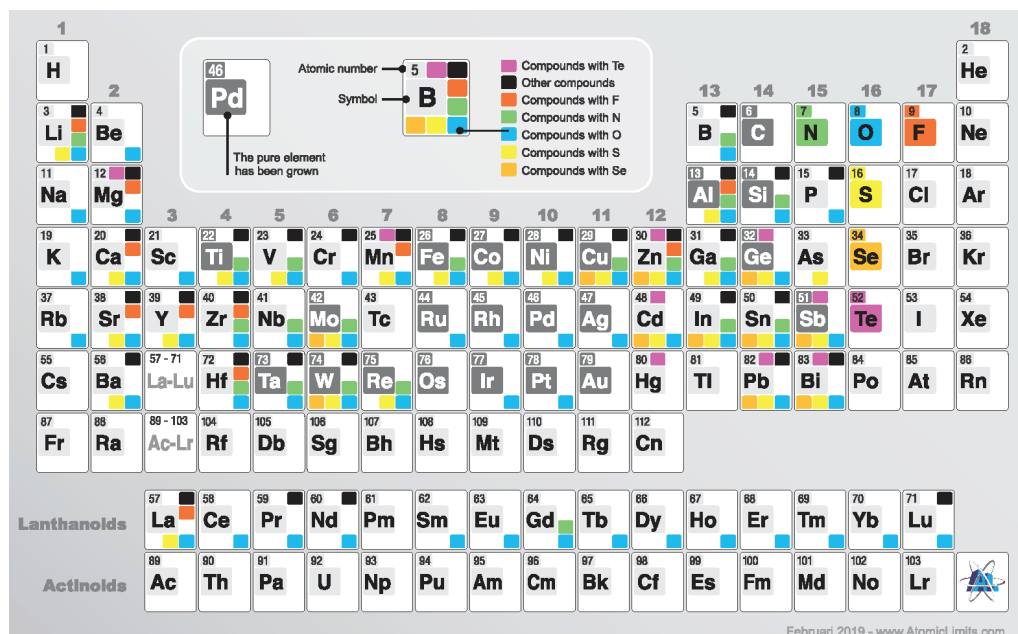


Figure 9: Periodic table figure of the "Atomic limits" ALD database.⁸⁵

ALD of multinary systems

The most extensively studied ALD processes (e.g. ALD of Al_2O_3 from TMA and water) deposit binary materials. Usually one element is introduced by the precursor (aluminium) and one from the co-reactant (oxygen). However, the most promising oxides for solar water splitting contain two or more metal species and making ALD of these materials more challenging.^{47,72}

Various approaches exist to deposit multinary systems by ALD. Very common is the supercycle approach. In this approach two binary ALD processes are executed in an alternating fashion, i.e. x cycles of material A and y cycles of material B form one supercycle, as illustrated in Figure 10. One defining factor of such a process is the cycle ratio CR defined as $CR_A = \frac{x}{x+y}$ and vice versa for material B, but expressions like $x:y$ are common as well. By altering the cycle ratio the stoichiometry of the desired multinary material can be tuned. Very small cycle ratios can be used to dope e.g. material B with material A.

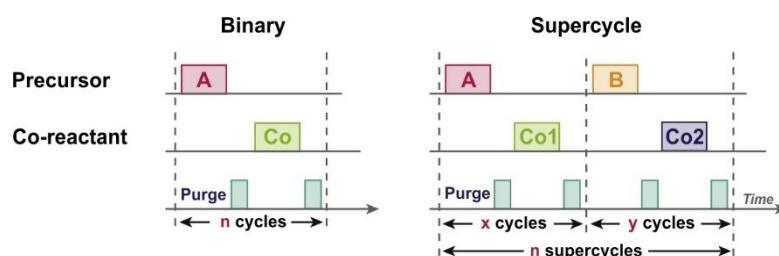


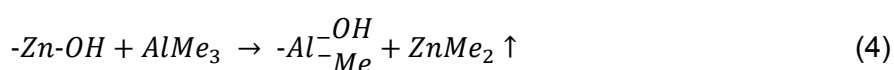
Figure 10: Schematic steps of a binary and a supercycle ALD process.⁶⁷

Furthermore, the bilayer period of a supercycle can be adjusted. Instead of 1 cycle A and 1 cycle B one could also perform 5 cycles of A and 5 cycles of B maintaining a CR of 0.5. The first case has a period of 2, i.e. the total amount of (binary) cycles in one supercycle. The second case has a period of 10. The period of a supercycle alters the distribution of the

materials A and B: a small period leads to a well distributed mixture while larger periods form nanolaminar stacks.

Finding compatible binary ALD processes is a main challenge in the supercycle approach. A key requirement is a matching deposition temperature, which is preferred to be kept constant throughout the deposition process (otherwise heating and cooling times would drastically increase deposition times). Therefore, the temperature windows of the individual ALD processes have to overlap.⁷² This may be tuned by the selection of precursors and co-reactants.⁶⁷ If the temperature criterion is met a multinary deposition should be possible.

Two more effects should to be taken into account to have precise process control. The first one are etching reactions. It is possible that ALD processes are not compatible because the precursors of process A etches the material deposited in process B e.g. by a ligand exchange reaction as discussed for Al₂O₃/ZnO ALD:⁸⁶



This loss in zinc has to be countered by increasing the cycle ratio of ZnO.

Second, nucleation plays an important role for all ALD processes but especially in supercycle ALD. As indicated above the substrate surface has an influence on the ALD growth. After nucleation of a (binary) ALD process the growth is steady, i.e. after each ALD cycle an identical surface is generated and the GPC is stable. At the beginning of a deposition this may be different. When material A is grown on a heterosurface, i.e. anything but A, the reactivity of the surface may differ, i.e. the number and type of surface sites. An increased reactivity leads to surface-enhanced growth with a larger GPC, a decreased surface reactivity to a nucleation delay, see Figure 11. Such a nucleation phase may not be present at all, but there have been reports of cases where it takes more than 100 cycles until the GPC stabilizes.^{54,87}

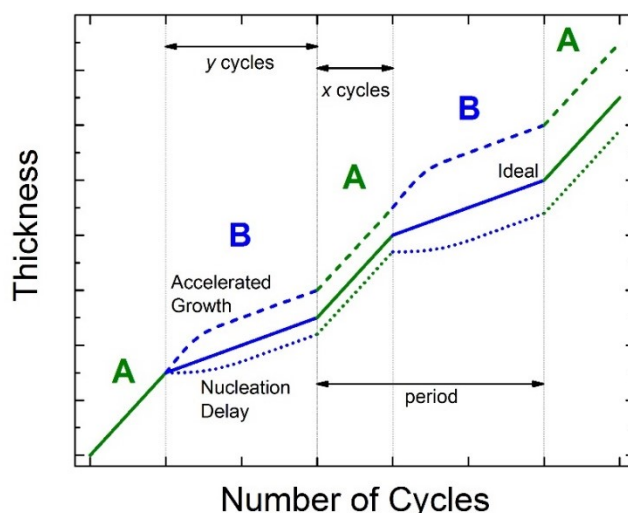


Figure 11: Thickness development during a supercycle ALD process; full line: ideal growth without nucleation effects, dashed line: with accelerated growth of B on A, dotted line: with nucleation delay of B on A.^{67,72}

The nucleation behavior plays a key role in supercycle depositions. For example, assuming a cycle ratio of 0.5 with a growth of a full monolayer and a period of two, each ALD cycle would be on a heterosurface. Therefore, the GPCs of binary processes may help to choose the initial

cycle ratio when developing the recipe, but the nucleation behavior should be studied in more detail for precise composition control. One way to reduce the influence of nucleation effects is an increased bilayer period of the supercycle.

A second approach is the deposition of stacks. Separate layers of the desired materials A and B are deposited on top of each other in individual processes. The resulting layered structure is then annealed to form a multinary phase. The benefit of this approach is its easy implementation: the depositions can be executed at different temperatures and the influence of nucleation processes are less pronounced. A drawback is the necessary annealing step, the sample must be heated to allow diffusion of the different elements throughout the whole film while all other components of the sample should not be affected. This is of course not always the case and gets more difficult when complex devices are built. One has to keep in mind that also a film deposited with the supercycle approach may requires annealing but the degree of reorganization within the film is minor compared to stack deposited films. Both techniques were utilized to deposit ternary metal oxide photoabsorbers, e.g. BiVO_4 by the supercycle approach and CuWO_4 by stack deposition-annealing.^{54,88,89}

Further possibilities to deposit multinary oxides are the utilization of single-source precursors with two (or more) different metals in one precursor molecule or co-dosing two (or more) precursors at the same time. A recent review by *Mackus et al.* gives a broad overview on ALD of multinary systems.⁷²

2.1.2 Pulsed laser deposition

Pulsed laser deposition (PLD) is a physical vapor deposition technique introduced by *Smith and Turner*. It caught interest as tool to deposit $\text{YBa}_2\text{Cu}_3\text{O}_{7-x}$, a high-temperature superconductor, from a stoichiometric target.^{90,91} Since then PLD has become an attractive technique to deposit a variety of thin film materials.^{92,93}

For PLD a high-powered pulsed laser (usually Nd:YAG or KrF-Excimer with pulse frequencies of 1 – 100 Hz) is focused on a target material. The laser pulses exhibit a high fluence (usually 1 – 5 J/cm^2) and rapidly heats up the target surface to up to more than 5000 K.⁹⁴ This temperature enables rapid evaporation of the target material at the irradiated spot. Thermal equilibration with the surrounding material is not possible in the timeframe of the short laser pulse (typically between 3 and 25 ns).^{92,95} The result is a stoichiometric ablation from the target.⁹⁵ The ablated material is partially ionized by the laser and forms a plasma plume, which rapidly expands away from the target surface and is collected by the substrate.⁹² This process is visible in Figure 12.

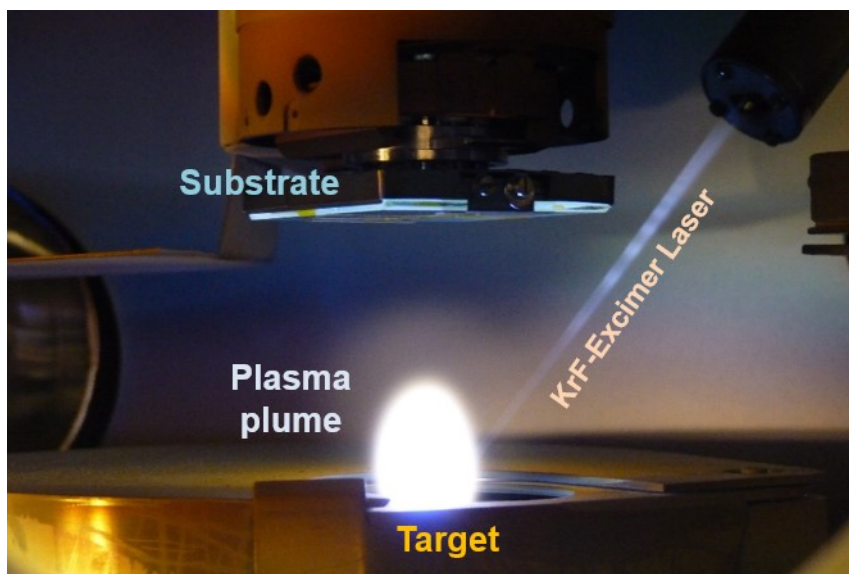


Figure 12: Photograph of the PLD setup during a deposition.⁹⁶

The ablated species typically have high kinetic energies in the range of several hundred eV and allow the formation of dense and compact films.⁹⁷ By the short pulse length a strong supersaturation of arriving species on the substrate is achieved, leading to a large number of nucleation sites compared to molecular beam epitaxy or sputtering, which allows smooth layer-by-layer growth.⁹²

An outstanding advantage of PLD is the availability of high-purity target materials and their direct deposition without the use of any additional compounds.⁹² Especially compared to wet chemical techniques like drop-casting this eliminates contamination sources like organic solvents, which could generate carbonaceous impurities. Furthermore, multiple targets can be utilized using a target carousel allowing complex stoichiometries by accurately tuning the number of shots on each target.⁹⁵ This has e.g. been shown for CuBi_2O_4 grown from Bi_2O_3 and CuO in this so called alternating target approach.⁹⁸

These features make PLD an excellent technique to deposit thin films with well-defined thicknesses and compositions while keeping simple morphologies.⁹⁷ Thereby it is especially suited to investigate fundamental material properties, generate new benchmarks thereof and to identify the performance limiting properties of photoelectrochemical materials.⁹⁷

The properties of the deposited films can be further tailored by the deposition parameters laser fluence, affecting the ablation behavior, background gas, affecting the target-substrate transfer, and substrate temperature, affecting the material accumulation and crystallization.^{99–}

2.2 Analytical techniques

2.2.1 Spectroscopic ellipsometry

Spectroscopic ellipsometry (SE) is an optical technique to determine the thickness and optical constants of thin films by the change in polarization upon reflection. A detailed description of the method, including instrumentation and application, is e.g. given by *Fujiwara* or *Tompkins and Irene*.^{103–105}

Considering reflection on a flat interface the polarization of incoming light can be divided into p- and s-polarization. For p-polarization the electric field E oscillates in the plane of incidence before and after reflection, while s-polarization is oriented perpendicular to p-polarization, as shown in Figure 13a.

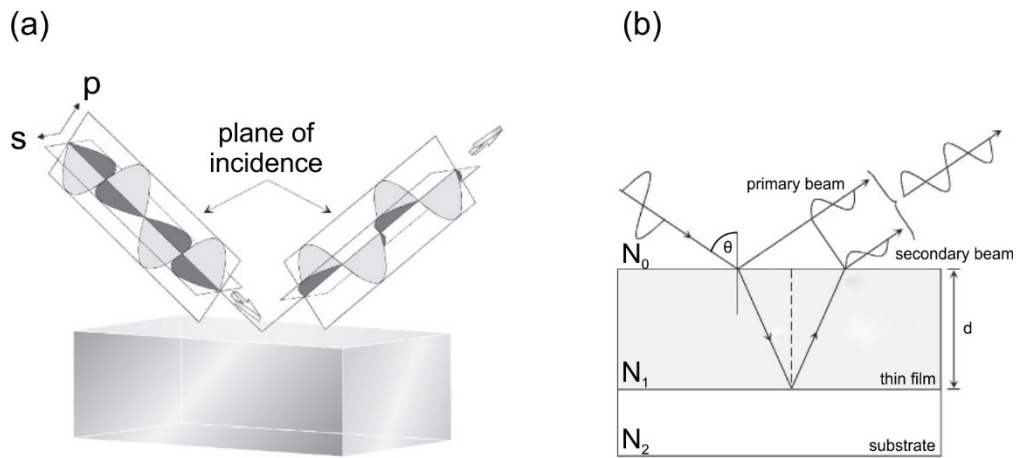


Figure 13: (a) Representation of the electric field part of p- and s-polarized light during reflection; (b) constructive interference at a thin film.¹⁰⁴

The boundary conditions dictate that the components parallel to the interface are continuous. These components are the electric field E of the s-polarized (visible in Figure 13a) and the magnetic field B of p-polarized light. Due to this requirement, s- and p-polarized light are affected differently and a change in polarization occurs. Applying the boundary conditions to the Fresnel equations describes the phenomenology that reflection and refraction induce a change in amplitude and phase of the p- and s-polarized light. The amount of change is determined by the thickness d and the complex refractive indices N of the materials. N is defined as the combination of the index of refraction n and the extinction coefficient k by $N = n + ik$. Furthermore absorption within the thin film and interference effects have to be considered as illustrated in Figure 13b.

This polarizing effect is utilized in SE. Two values are measured, the amplitude ratio Ψ and the phase difference Δ of the reflected p- and s-polarized light, as shown in Figure 14. Each for an instrument dependent set of wavelengths λ and, if possible, for a set of different incident angles θ . The calculation from Ψ and Δ to N and d is however not trivial and relies on a pre-defined optical model, which is optimized during evaluation. These optical models rely on known optical constants or specific oscillators to accurately resemble the desired materials.

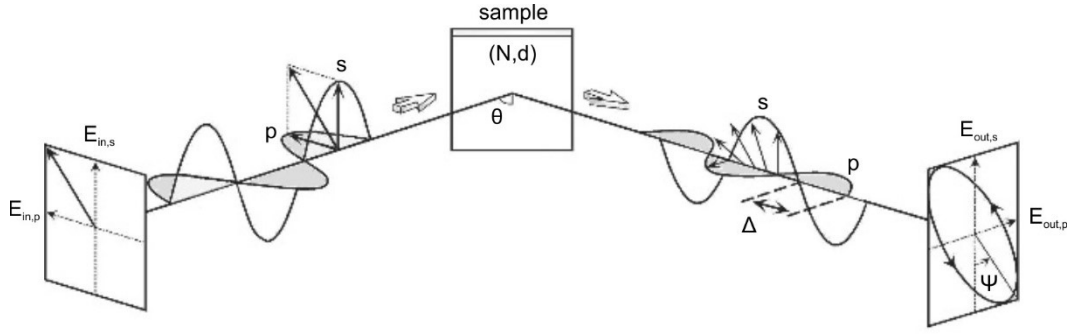


Figure 14: Scheme of an SE measurement: incident linear polarized light ($\Delta=0^\circ$, $\Psi = 45^\circ$) and reflected elliptical polarized light with altered Δ and Ψ values.

The two most interesting oscillators in the context of this thesis are the Cauchy and the Tauc-Lorentz oscillator. The Cauchy model is suited for transparent materials and to parameterize the major refractive indices.^{76,103} It is generally given by

$$n = n_0 + \frac{n_1}{\lambda^2} + \frac{n_2}{\lambda^4} \quad (5)$$

$$k = 0 \quad (6)$$

Where n_0 , n_1 and n_2 are the Cauchy parameters without a direct physical representation.

Tauc-Lorentz oscillators are especially suited for amorphous materials with a single bandgap, e.g. semiconductors or transparent conductive oxides.^{104,106} Crystalline fractions or higher-energy transitions can be taken into account by additional Lorentz oscillators.⁷⁶ Tauc-Lorentz oscillators are defined by

$$\varepsilon_{1,TL} = \varepsilon_\infty + \frac{2}{\pi} P \int_{E_0}^{\infty} \frac{\xi \varepsilon_{2,TL}(\rho)}{\xi^2 - E^2} d\xi \quad (7)$$

$$\varepsilon_{2,TL} = \begin{cases} \frac{A_{TL} E_0 (E - E_G)^2}{(E^2 - E_0^2) + C^2 E^2} \cdot \frac{1}{E} & \text{for } E > E_G \\ 0 & \text{for } E \leq E_G \end{cases} \quad (8)$$

Where ε_1 and ε_2 are the real and imaginary parts of the dielectric function defined by $\varepsilon_1 = n^2 - k^2$ and $\varepsilon_2 = 2nk$. Furthermore E is the photon energy, A_{TL} is the transition matrix element, E_G the bandgap, E_0 the peak transition energy, ε_∞ the high frequency dielectric constant, P the Cauchy principal part of the integral and C a broadening parameter.

2.2.2 X-ray photoelectron spectroscopy

X-ray photoelectron spectroscopy (XPS) is a common technique to investigate the composition of thin films or surfaces. Overviews are e.g. given by *Hüfner* or *Ratner and Castner*, a widely used handbook is written by *Moulder et al.*^{107–109}

XPS utilizes the photoelectric effect for both qualitative and quantitative elemental analysis. X-ray photons eject core electrons from the sample which are detected in dependence of their kinetic energy. To make these values comparable a suitable reference is required. Most

commonly this is the Fermi level of the spectrometer. By ensuring electrical contact between sample and spectrometer their Fermi levels adjust and the relation between the different values is:

$$h\nu = E_B + E_{kin} + \phi \quad (9)$$

Here, $h\nu$ is the known energy of the incoming photon, E_B is the binding energy of the electron in its initial state relative to the common Fermi level, E_{kin} is the kinetic energy of the photon measured by the spectrometer and ϕ is the work function of the spectrometer. ϕ is determined beforehand by calibrating the spectrometer. This is usually done with a piece of gold foil, since the binding energy of the Au 4f_{7/2} peaks is well known. The photon energy $h\nu$ is dependent on the X-ray source and usually in the range of 1 – 6 keV. Common X-ray sources are either metal anodes like aluminium or copper with fixed photon energies or adjustable synchrotron radiation.

The binding energy E_B is the desired value which is characteristic for each element and core level. Furthermore the local electron density induces small changes in the binding energy, the so-called ‘chemical shift’. This shift depends on the oxidation state, the binding modes and the surroundings of the investigated element and can be used to gather information on these. The characteristic binding energies are tabulated in databases to allow detailed assignment.^{109,110}

Apart from single signals at certain binding energies other effects may occur, which can give additional information on the sample. Most prominently these include multiplet splitting due to spin-orbit coupling in p, d or f states, satellite peaks due to shake-up or shake-off processes, or Auger lines.

Furthermore XPS is a quantitative technique. The specific signal intensity, i.e. its peak area, is directly dependent on the number of atoms in the sample. For normalization a sensitivity factor is used which accounts for different cross sections of the elements. The sensitivity factors are dependent on the measurement setup, e.g. the X-ray source and the incident angle. Sensitivity factors are usually reported in the respective manual of the XPS setup.¹¹¹ However, even then a calibration with samples of known stoichiometry can give different sensitivity factors.¹¹² The atomic fraction of each element can be calculated by:

$$Z_1 = \frac{\frac{A_1}{S_1}}{\sum_n \frac{A_n}{S_n}} \quad (10)$$

Here Z is the atomic fraction, A the peak area and S the sensitivity factor.

2.2.3 Time-resolved microwave conductivity

Time-resolved microwave conductivity (TRMC) is a contactless technique to evaluate the charge carrier transport properties in semiconductors. Among others *Savenije et al.* describe the technique in detail.¹¹³

The electric field of a microwave accelerates mobile charge carriers in a sample. Due to the high frequency of the microwaves (in the X-band 8 – 12 GHz) this induces a wiggling of the charge carriers rather than perturbing their diffusional motion. The ability to absorb the microwaves is directly dependent on the ability of the charge carriers to move i.e. their mobility and on their number i.e. the charge carrier concentration. Combined they give the photoconductivity. Therefore, from the absorption of microwave power, the photoconductivity of the material can be calculated. It is often possible to calculate the concentration of the photo-generated carriers from the incident light intensity and the absorption coefficient. With this information, it is then possible to calculate the mobility of the carriers. There is, however, one complication. The electric field affects all mobile charges, it is therefore not possible to distinguish the individual contributions from electrons and holes. Thus, only the weighted sum of their mobilities can be estimated.

These TRMC measurements can be conducted on all kinds of photoactive materials. However, low mobility samples as metal oxides may not give sufficient signal-to-noise ratios in simple transmission measurements. Therefore a specific cavity, with a size that corresponds to the microwave wavelength, is employed to generate a standing wave. The sample is positioned at the maximum amplitude, which increases the sensitivity of the setup by a factor of more than 10. Such a cavity is schematically shown in Figure 15.

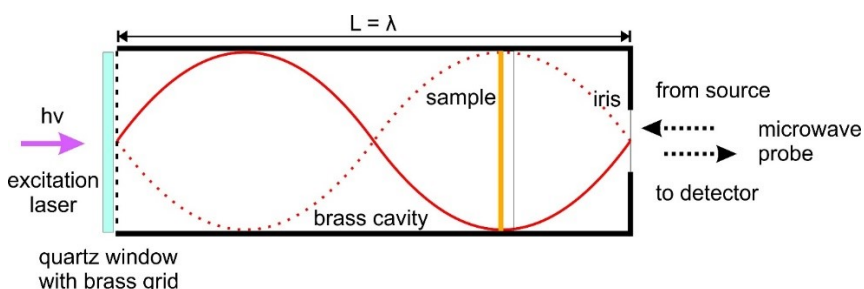


Figure 15: Schematic microwave resonant cavity, the red sinusoidal waves represent the standing wave conditions with the sample at a maximum, photoexcitation by a monochromatic laser from the left and microwave probing from the right.¹¹³

Microwaves are coupled in from the right through the iris. Within the cavity the majority of the microwaves are reflected by the brass grid on the left and the wall on the right, generating the standing wave. The brass grid offers a fair trade off between reflection of the microwaves and transmission of visible light. The laser excitation pulse is incoming through the quartz window and the brass grid, generating excited charge carriers in the sample. These absorb the microwaves, lowering the microwave power.

Throughout this process the reflected microwave power is constantly measured as a function of time with nanosecond resolution using a detector that is connected to an oscilloscope. The photoconductivity can be determined after laser excitation when the maximum of excited charge carriers is present. Subsequently the microwave absorption decreases which can either be attributed to a decrease in mobility, e.g. by trapping or by a decrease in amount of excited charge carriers. Both of these processes inhibit the charge

carrier transport and the decrease in absorption can be fitted as a decay function. The decay gives an effective lifetime of the excited charge carriers, also called TRMC decay time τ . Combining both values, photoconductivity and TRMC decay time, the diffusion length of the excited charge carriers is estimated.

The calculation of these values works as follows. Prior to the TRMC measurement itself the sensitivity factor K of the cavity is estimated from a measurement of the resonance curve. It is calculated by:

$$K = \frac{2Q_L(1 + \frac{1}{\sqrt{R_0}})}{\pi f_0 \epsilon_0 \epsilon_r L \beta} \quad (11)$$

With Q_L being the quality factor of the cavity, R_0 the depth of the resonance curve, f_0 the resonance frequency, ϵ_0 the dielectric permittivity of vacuum, ϵ_r the relative dielectric permittivity of the sample, L the length of the cavity and β the ratio of length to width of the cavity.

Following this the relative change in microwave power $\Delta P/P$ directly relates to the change in conductance ΔG :

$$\frac{\Delta P(t)}{P} = -K \Delta G \quad (12)$$

Where the conductance ΔG can be expressed as integrated conductivity at depth z $\Delta\sigma(z)$ over the film thickness d :

$$\Delta G = \beta \int_0^d \Delta\sigma(z) dz \quad (13)$$

In there the conductivity is the product of the number of charge carriers, their charge and their mobility

$$\Delta\sigma(z) = eN(z)\Sigma\mu \quad (14)$$

Here, e is the elemental charge, $N(z)$ the concentration of excited charge carriers at depth z and $\Sigma\mu$ the sum of electron and hole mobility $\mu_e + \mu_h$. This substitution gives:

$$\Delta G = \beta e \Sigma\mu \int_0^d N(z) dz \quad (15)$$

Assuming that no recombination occurs during the initial laser excitation the number of charge carriers (i.e. the integrated charge carrier concentration) equals the laser intensity I_0 times the sample absorptance at the laser wavelength, A , times the internal quantum yield in photoexcitation ϕ :

$$\Delta G = \beta e I_0 A \phi \Sigma\mu \quad (16)$$

And finally

$$\frac{\Delta P(t)}{P} = -K\beta e I_0 A \phi \Sigma \mu \quad (17)$$

to link the change in microwave power to the mobility sum $\Sigma \mu$. One has to keep in mind that the number of charge carriers can only be assumed to be $I_0 A \phi$ directly after photoexcitation. The number of charge carriers declines over time, as well as their mobilities, which is visible by the decay of the measured signal as mentioned above.

Nevertheless the representation of TRMC measurements shows $\phi \Sigma \mu$, denoted as photoconductivity, as “measured” value. Although this is not entirely correct this way of visualization is chosen to enable comparability with other studies. The optimal way to evaluate and present TRMC measurements is still part of discussions.

The TRMC decay time τ is extracted from fitted decay functions and the diffusion length L_D estimated by:

$$L_D = \sqrt{\frac{T k_B \tau \Sigma \mu}{e}} \quad (18)$$

Assuming that $\phi = 1$, with the temperature T and Boltzmann’s constant k_B .

2.2.4 Photoelectrochemical measurements

The photoelectrochemical (PEC) performance of the photoabsorber thin films are evaluated by photocurrent measurements. This includes linear-sweep voltammetry, chronoamperometry and incident photon-to-current efficiency. All of these measurements were performed in a home-built cell facilitating a three-electrode setup with frontside or backside illumination, as schematically shown in Figure 16. The three-electrode setup allows to ensure that there is a defined voltage between the reference and working electrode while the measured current is running between work and counter electrode. In this way it is possible to circumvent any influence of the reactions at the counter electrode and to focus exclusively on the working electrode with a well-defined potential.

In linear-sweep voltammetry the photocurrent is measured in dependence of the applied potential during a single sweep, usually from the open circuit potential to HER or OER conditions. When the measurement is continued by going back to the initial potential it is called cyclic voltammetry, which can consist of multiple cycles. The measurements can be conducted in the dark, under simulated sunlight (AM 1.5 illumination), or with chopped illumination to give information on the dark-, light-current and/or charge transfer kinetics.

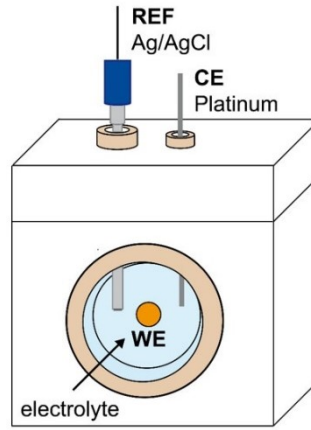


Figure 16: Schematic PEC cell with the sample as working electrode (WE), a platinum counter electrode (CE), a Ag/AgCl reference electrode (REF) and a quartz window for frontside illumination, illumination from the back is also possible through a hole (not visible) if the substrate is transparent.⁹⁶

In chronoamperometry the current is measured in dependence of the time while the applied potential is kept constant (therefore also called potentiostatic measurement). This is usually done to investigate the stability of a sample or to determine the photocurrent more accurately as kinetic effects leading to transients can be avoided.

Incident photon-to-current efficiency (IPCE) measurements rely on a different light source. Instead of AM 1.5 illumination a tunable monochromatic light source is used to investigate the wavelength dependence of the photocurrent while the potential is fixed. The IPCE is calculated by

$$IPCE(\lambda) = \frac{hc}{e} \frac{j(\lambda)}{\lambda I_0(\lambda)} \quad (19)$$

With λ being the wavelength of the incident light, h the Planck constant, c the speed of light, e the elemental charge, j the measured photocurrent density and I_0 the incident light intensity. By dividing the IPCE by the absorptance A the absorbed photon-to-current efficiency is calculated:

$$APCE(\lambda) = \frac{IPCE(\lambda)}{A(\lambda)} \quad (20)$$

2.2.5 Further techniques

X-ray diffraction

X-ray diffraction (XRD) is a common technique to investigate the crystal structure of materials. Scattering of X-rays at the atomic lattices is utilized to identify crystalline phases. Sharp signals are visible if constructive interference is occurring following Bragg's law:

$$n\lambda = 2d_{hkl} \sin\theta \quad (21)$$

Here, n is a positive integer, λ is the wavelength of the incident X-rays, d_{hkl} is the distance between crystal lattice planes, and θ is the half angle between the incoming and the outgoing

X-ray that enters the detector. The resulting diffractogram acts as fingerprint of the material and can be compared to diffractograms generated from reported crystal structures. Thin films only offer very little material to interact with the X-rays. In grazing incidence configuration the sample is illuminated at a very small angle (e.g. 0.5°), by this almost horizontal pathway a lot more material of the thin film can interact with the X-rays which increases the signal-to-noise ratio. In a first estimation the amount of illuminated material is proportional to the cotangens of the angle of illumination.

UVVis spectroscopy

UVVis spectroscopy is used to investigate the optical properties of the deposited films in terms of absorption coefficients α and bandgaps E_G . For this purpose the transmittance TR (i.e. the sum of transmission and reflectance) of the samples is measured using an integrating sphere. The absorption coefficient α is then calculated by

$$\alpha = \frac{-\ln(TR)}{d} \quad (22)$$

with d as film thickness.

The bandgaps are calculated from linear fits of the Tauc plots. There the parameter $(\alpha h\nu)^{\frac{1}{n}}$ is plotted vs. the photon energy with $n = 2$ for the indirect bandgap and $n = \frac{1}{2}$ for the direct bandgap. Tauc plots are a common way to determine the bandgap from the optical absorption of a material. By plotting $(\alpha h\nu)^{\frac{1}{n}}$ vs. $h\nu$, a quadratic ($n = 2$) or square root ($n = \frac{1}{2}$) type increase of the adsorption is visible in a linear way i.e. a straight line. When this linear part is extrapolated to $(\alpha h\nu)^{\frac{1}{n}} = 0$ the bandgap is determined with an easily adapted routine which enables comparability. A quadratic or square root type dependence are typical for an indirect or direct bandgap, respectively.

2.3 Setups & routines

2.3.1 Sample preparation

Substrate cleaning

Silicon substrates (Si-Mat, (100) orientation, n-type, $1 - 10 \text{ } \Omega/\text{cm}^2$) were rinsed with Millipore® water prior to depositions without additional cleaning. For Bi_2O_3 ALD an additional Al_2O_3 adhesion layer was deposited by 35 ALD cycles from trimethylaluminium (TMA, min. 98% Strem) and water (Millipore®) at the temperature of the subsequent Bi_2O_3 ALD process. The pulse/purge times were 0.1 s / 4 s / 0.1 s / 6 s. The Al_2O_3 thickness was measured by SE.

FTO (TEC 7, Pilkington) and quartz substrates (Spectrosil 2000, Baumbach & Co Ltd.) were cleaned in an ultrasonic bath of 1 vol.% Triton solution (Triton X-100, laboratory grade, Sigma Aldrich), deionized water, and ethanol ($\geq 99.99\%$, Sigma-Aldrich) for 15 min in each solution, followed by drying under a stream of compressed nitrogen.

Atomic layer deposition

All ALD experiments were performed on a Picosun® R-200 Advanced ALD reactor equipped with a remote plasma source (Picoplasma™). All samples were kept in the reaction chamber for 30 minutes before each deposition to reach a thermal equilibrium.

For Bi_2O_3 ALD tris(2,2,6,6-tetramethyl-3,5-heptanedionato)bismuth(III) ($[\text{Bi}(\text{tmhd})_3]$, min. 98%, Strem) was used as a bismuth precursor. Typical $[\text{Bi}(\text{tmhd})_3]$ exposure/purge times were 5 s/10 s and 3 s/5 s for the thermal (T-ALD) and the plasma-enhanced processes (PE-ALD), respectively. Water (Millipore®), kept at room temperature, or an oxygen plasma were used as the oxygen source for the thermal- and plasma-enhanced processes, respectively. Typical water exposure/purge times were 8 s/8 s. Typical exposure and purge times during the plasma step were 35 s and 15 s, respectively. Thermal ALD of Bi_2O_3 was usually performed at 270°C , whereas plasma-enhanced ALD was done at either 270 or 290°C . Typically, 100 ALD cycles were executed, resulting in 2–5 nm thick films.

For thermal ALD of Bi_2O_3 , real-time ellipsometry measurements, and plasma half-cycle optimization $[\text{Bi}(\text{tmhd})_3]$ was kept at 190°C in a Picohot™ 200 source system. The boosting functionality of the Picosun® R200 operation software was used for $[\text{Bi}(\text{tmhd})_3]$ injection. The boosting parameters were: 600 sccm “boost flow”, 0.5 s “pre-empty” (giving the effective $[\text{Bi}(\text{tmhd})_3]$ dosing time), 1.2 s “master fill”, and 0 s “post-empty”. For $[\text{Bi}(\text{tmhd})_3]$ exposures longer than 0.5 s the described exposure procedure was repeated with a purge time of 10 s following each dose. The maximum water exposure within one dose was 1 s followed by 8 s purging. For longer water exposures multiple consecutive water doses were executed, with a purge time of 8 s following each 1s water dose. Nitrogen gas (99.9999%) was used as carrier and purge gas; 50 sccm through the $[\text{Bi}(\text{tmhd})_3]$ and the water line, respectively. For all other plasma depositions $[\text{Bi}(\text{tmhd})_3]$ was kept at 190°C in a Picohot™ 300 source system. Again

nitrogen gas was used as a carrier and purge gas. An oxygen plasma was used as oxidant. An Ar/O₂ mixture (40/100 sccm) was ignited with a plasma power of 2800 W. The deposition temperature was varied between 200 and 330°C.

Precursors for V₂O₅ and MnO ALD were vanadium(V)tri-isopropoxy oxide (VTIP) and bis(ethylcyclopentadienyl)manganese(II) ([Mn(CpEt)₂]) kept in Picohot™ 200 sources, respectively. Depositions were usually carried out at 200°C with a thermal lid installed. VTIP was heated to 100°C and typical pulse / purge times were 0.1 s / 20 s / 2 s / 10 s. [Mn(CpEt)₂] was heated to 110°C and typical pulse / purge times were 0.5 s / 20 s / 0.5 s / 10 s.

Pulsed laser deposition

PLD experiments were performed using a custom-built pulsed laser deposition system from PREVAC. The target is hit by a KrF-excimer laser (LPXpro 210, Coherent) pulse ($\lambda = 248$ nm, 25 ns) with fluences of 1.5 – 2.5 J/cm². The substrate temperature was varied from room temperature (298 K) to 300°C. The background pressure in the chamber was 5x10⁻⁷ mbar (vacuum conditions) or a specific oxygen amount was introduced into the system. The target was prepared by mixing CuO (4.37 g) and Bi₂O₃ (25.63 g) in the stoichiometric ratio, grinding the mixture in a ball mill for 1 h, and pressing it into a pellet. Afterwards two sintering steps were performed. In the first, the pellet was annealed to 700°C with a heating rate of 150°C/h and kept at the final temperature for two hours. In the second one, it was annealed at 800°C and kept there for 10 h. The structure of the pellet was studied by XRD, which revealed a pure tetragonal CuBi₂O₄ phase.¹¹⁴ Typical densities of targets prepared in the described way are around 80% of the theoretical densities of monoclinic materials.

Annealing

If samples were annealed the following conditions were used: Bi₂O₃ was annealed in a muffle furnace at 450°C for 2 h in air with a heating rate of 10°C/min. If not explicitly stated otherwise Mn₂V₂O₇ was annealed in a tube furnace under argon flow at 500°C for 2 h with a heating rate of 10°C/min. CuBi₂O₄ was annealed in a muffle furnace at 550°C for 2 h in air with a heating rate of 10°C/min.

2.3.2 Sample characterization

Spectroscopic ellipsometry

Spectroscopic ellipsometry measurements were performed on a J.A. Woollam Co., M-2000X, 210 – 1000nm ellipsometer, both in-situ (i.e. mounted to the ALD reactor) and ex-situ. Ex-situ measurements were performed under three angles θ , 70°, 65° and 60°. In-situ measurements were performed under a fixed angle of 68°. Optical models rely on Tauc-Lorentz oscillators for Bi₂O₃, MnO_x and Mn₂V₂O₇ and Cauchy models for SiO₂, Al₂O₃, the Bi-thd surface layer and VO_x. The CompleteEASE software of Woollam was used to define and fit all optical models.

X-ray photoelectron spectroscopy

XPS measurements were executed using a SPECS PHOIBOS 100 hemispherical analyzer and a monochromatic X-ray source (SPECS FOCUS 500 monochromator, Al K α radiation, 1486.74 eV). XPS survey and fine spectra were collected at a normal angle from the surface. The pass energy was set to 30 and 10 eV for survey and fine spectra, with step sizes of 0.5 and 0.05 eV, respectively. The atomic sensitivity factors are 24.47, 15.23, 10.23, 3.1, and 1.0 for Bi 4f, Mn 2p, V 2p, O 1s, and C 1s, respectively.

All samples were exposed to air prior to analysis. The peak originating from adventitious carbon at the known binding energy of 284.8 eV was used to calibrate the energy scale of the spectra, if not explicitly stated otherwise. Shirley background subtraction was used to fit the photoemission lines in the fine spectra. The base pressure of the system was $\sim 10^{-9}$ mbar and the load lock was pumped until at least pressures below 3×10^{-7} mbar were achieved.

UVVis spectroscopy

UVVis measurements were conducted using a PerkinElmer Lambda 950 spectrophotometer with an integrating sphere. The samples were placed inside the integrating sphere with an offset of $\sim 7.5^\circ$ from the incident light, and the transmittance (TR, i.e., transmittance T + reflectance R) was measured.

X-ray diffraction

XRD measurements were conducted under grazing incident conditions (0.5°) on a Panalytical X'Pert Pro MPD using Cu K α radiation ($\lambda = 1.5406 \text{ \AA}$) with an acceleration voltage of 40 kV and an X-ray current of 40 mA. Scans were performed from $10 - 80^\circ$ (Bi₂O₃ and CuBi₂O₄) or $10 - 70^\circ$ (Mn₂V₂O₇) with a step width of 0.04° . Measurement times varied from 5 – 60 h, depending on the sample thickness.

Scanning electron microscopy and Energy-dispersive X-ray spectroscopy

Scanning electron microscopy (SEM) and Energy-dispersive X-ray spectroscopy (EDX) measurements were performed on a LEO GEMINI 1530 scanning electron microscope with an acceleration voltage of 10 kV. Samples deposited on FTO substrates with electronic contact to the instrument were used to minimize charging effects. One sample was investigated by RBS (see below) as an internal reference for the EDX measurements to determine stoichiometries.

Time-resolved microwave conductivity

TRMC measurements were performed using a wavelength-tunable laser (NT230-50-SH/SF, EKSPLA) at 410 nm as excitation source with a pulse length of 7 ns. The X-band (8400 – 8700 MHz) microwave probe was generated by a voltage-controlled oscillator (Sivers IMA VO3262X).

Photoelectrochemical measurements

Measurements were performed in three-electrode setup using a Ag/AgCl reference electrode ($E^0_{\text{Ag/AgCl}} = 0.199 \text{ V}$ vs normal hydrogen electrode, XR300 in $\text{KCl}_{\text{aq, sat}}$, Radiometer Analytical), a platinum wire as counter electrode and an EG&G PAR 273A potentiostat. The illuminated area was defined by a rubber sealing ring to 0.2376 cm^2 .

AM 1.5 illumination was generated by a solar simulator (WACOM, type WXS-50S-5H, class AAA). If not stated otherwise chopped light was used in frontside or backside illumination as mentioned in the respective chapters.

IPCE measurements used a Xe lamp (LSH302, LOT) with a monochromator (Acton Research Spectra Pro 2155). The incident light intensity was measured by a calibrated photodiode (PD300R-UV, Ophir) behind a PEC cell with a bare FTO coated glass substrate without electrolyte or quartz window to normalize for backside illumination through the substrate.

Measurements of $\text{Mn}_2\text{V}_2\text{O}_7$ used the following electrolytes: 1) $0.1 \text{ M K}_2\text{B}_2\text{O}_7$ solution adjusted to pH 9.2 with KOH and $0.5 \text{ M Na}_2\text{SO}_3$ as hole scavenger; 2) $0.1 \text{ M K}_2\text{B}_2\text{O}_7$ solution adjusted to pH 9.2 with KOH and $5 \times 10^{-2} \text{ M } [\text{Fe}(\text{CN})_6]^{3-/4-}$ as hole scavenger (from potassium salts); 3) 0.1 M KOH (pH 13) and $5 \times 10^{-2} \text{ M } [\text{Fe}(\text{CN})_6]^{3-/4-}$ as hole scavenger (from potassium salts).

Measurements of CuBi_2O_4 were executed in $0.1 \text{ M Na}_2\text{HPO}_4/\text{NaH}_2\text{PO}_4$ buffer (pH ~ 7 phosphate buffer) and $6\% \text{ H}_2\text{O}_2$ as electron scavenger (30%, stabilized).

Rutherford Backscattering Spectrometry

Rutherford backscattering spectrometry (RBS) was performed at the Ion Beam Facility (IBF) at DIFFER. The measurements used a $2.0 \text{ MeV } ^4\text{He}$ ion beam at a scatter angle of 163° . Data was analyzed using the simnra 7.01 and multisimnra software.

Mass spectrometry

Mass spectrometry (MS) analysis was performed using a Netzsch thermobalance STA409C coupled with a mass spectrometer to detect the decomposition of various components of the sample during annealing. The $\text{Mn}_2\text{V}_2\text{O}_7$ powder was placed in an Al_2O_3 crucible and heated with a heating rate of 10 K/min . The sample was kept under a constant argon flow of 80 mL/min to carry the vaporized sample to the mass spectrometer. Electron ionization with a tungsten filament was used to generate positive ions. Each mass/charge ratio was measured for 2 s .

Transmission electron microscopy

Cross-sectional transmission electron microscopy (TEM) images were recorded with a Philips CM12/STEM equipped with a LaB6 cathode, Super TWIN lens and a $2\text{k} \times 2\text{k}$ CCD camera from Gatan (Orius SC 830) operated at 120 kV . Bi_2O_3 films deposited on a $[100]$ n-type silicon substrate are cut into small pieces and glued face to face using epoxy resin. This

compound is sliced and polished till a sample thickness of 4 to 6 μm is reached. The sample is further thinned by argon bombardment (5kV, 2mA) till it becomes transparent for electrons.

Atomic force microscopy

Topographical measurements were conducted on an NTMDT NTEGRA Atomic force microscopy (AFM) in tapping mode at room temperature and ambient pressure.

Raman spectroscopy

Raman measurements were conducted on a Horiba HR800 spectrometer with a HeNe laser as a monochromatic light source. The HeNe laser is a 500:1 polarized 20 mW laser with a wavelength of 632.8 nm. The scattered light was detected with a cooled Si CCD camera with 1800 l/mm grid.

3 ALD of Bi₂O₃

Parts of this chapter are adapted from:

M. Müller, K. Komander, C. Höhn, R. van de Krol, A. C. Bronneberg, "Growth of Bi₂O₃ Films by Thermal- and Plasma-Enhanced Atomic Layer Deposition Monitored with Real-Time Spectroscopic Ellipsometry for Photocatalytic Water Splitting", *ACS Appl. Nano Mater.* **2019**, 2, 10, 6277 ¹¹⁵

Bismuth containing ternary oxides such as BiVO₄, CuBi₂O₄, BiMn₂O₅, Bi₂WO₆ or BiFeO₃ attracted much attention as photoabsorbers for PEC applications.^{55,116–118} Among these BiVO₄ and CuBi₂O₄ are the most thorough studied ones. However, ALD of such ternary oxides has been shown to be challenging. ALD of photoactive BiVO₄ is a successful example, as reported by *Stefik et al.*^{88,89} Even the previously described optimization from planar to nanostructured geometries has recently been reported by *Lamm et al.*¹¹⁹ The main challenge in these reports is the limited reactivity of the bismuth precursor [BiPh₃]. Only one monolayer of bismuth oxide can be grown on a heterosurface, i.e. on V₂O₅, in a thermal process.⁸⁸ The binary ALD process of Bi₂O₃ stops after a closed Bi₂O₃ film is deposited. Therefore the stoichiometry of a ternary film can only be tuned to some extent by adjustment of the cycle ratio. As a consequence only vanadium rich BiVO₄ films can be grown.⁸⁸ A phase pure BiVO₄ film can only be achieved if a selective subsequent V₂O₅ etching or an inhibition of the V₂O₅ ALD growth by alcohols is employed.^{88,89}

Therefore, these reports only provide useful information on one specific ALD process of BiVO₄. This process cannot be easily extended towards new ALD processes of other bismuth-based materials. A universal binary ALD process of Bi₂O₃ is therefore still a bottleneck limiting the deposition of bismuth based multinary oxides. This bottleneck will be addressed in this chapter.

A few studies on ALD of Bi₂O₃ exist, even a publication on various precursors is available.^{64,120–124} Unfortunately only two of these precursors are commercially available, which is an essential prerequisite for a universally usable ALD process. These are the above mentioned [BiPh₃] and [Bi(tmhd)₃]. As binary ALD of Bi₂O₃ from [BiPh₃] was not yet shown and the precursor is only available in the USA, [Bi(tmhd)₃] was chosen in this study and its structure is shown in Figure 17.

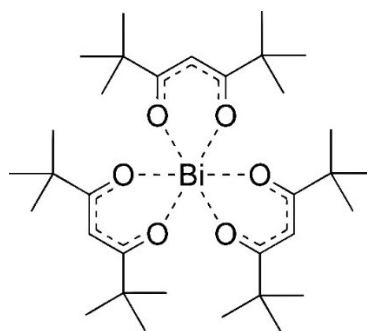


Figure 17: Chemical structure of [Bi(tmhd)₃] or tris(2,2,6,6-tetramethyl-3,5-heptanedionato)bismuth(III).

3.1 Thermal ALD of Bi₂O₃

The saturation curves of [Bi(tmhd)₃] and water were recorded to establish a thermal ALD process (T-ALD). The saturation curves are shown in Figure 18 a-c in red. Saturation is reached after 3.5 s [Bi(tmhd)₃] dosing, followed by a 3 s purge, 5 s water exposure and 8 s final purge, leading to a growth rate of 0.24 Å/cycle. The purge after the water exposure was not investigated in detail but previously optimized ALD processes at the setup (e.g. ZnO, Al₂O₃, TiO₂¹²⁵) showed that 6 – 8 s water purge sufficiently remove all excess water and reaction products. Deposition with these conditions onto a 4" wafer gives an excellent uniformity of 96%, proving the sufficient purge time and the exceptional surface coverage of ALD. The thickness distribution over the 4" wafer is shown in Figure 19a.

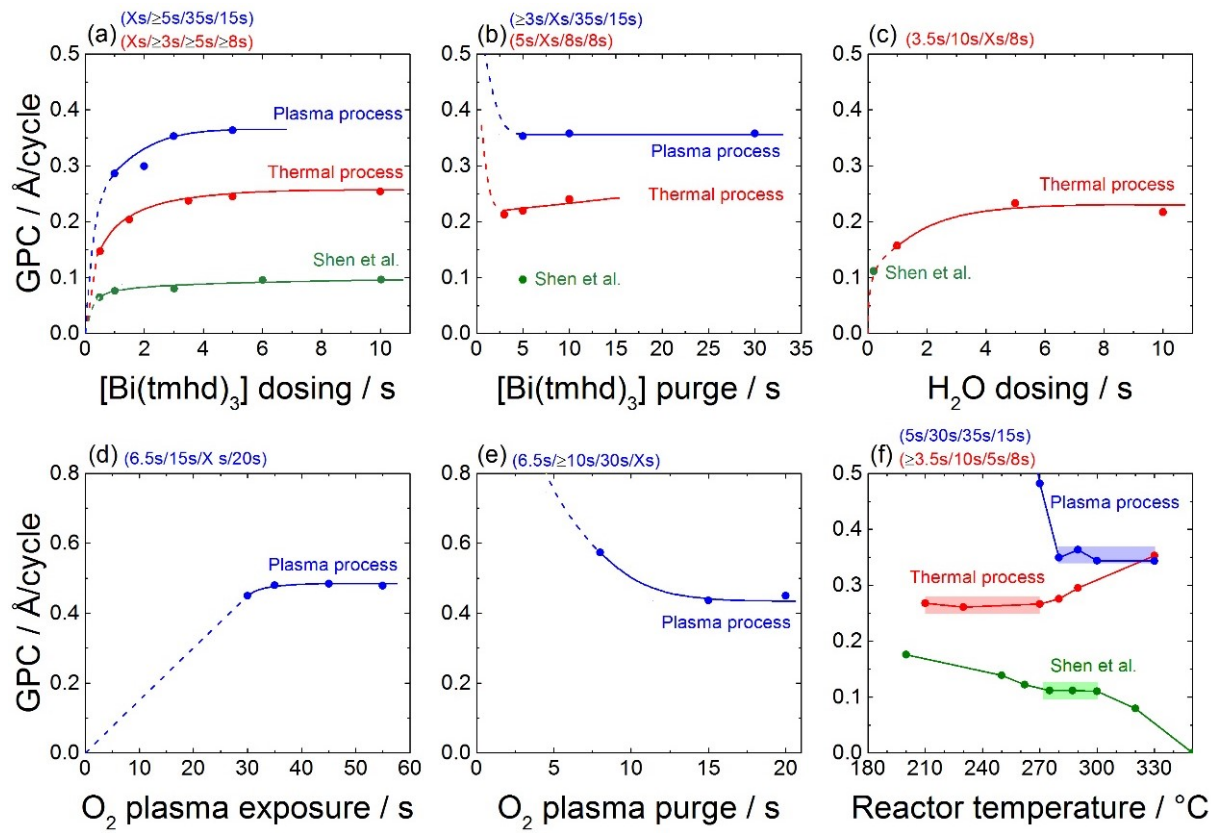


Figure 18: Growth per cycle (GPC) of bismuth oxide films as function of the ALD parameters of the plasma-enhanced process (blue), the thermal process (red), and as reported by Shen et al.¹²⁶ (green); (a) [Bi(tmhd)₃] exposure time (b) [Bi(tmhd)₃] purge time; (c) water exposure time; (d) oxygen plasma exposure time; (e) oxygen plasma purge time; (f) deposition temperature (temperature windows are indicated by the semitransparent rectangles). Full and dotted lines in (a)-(e) represent guides to the eye.

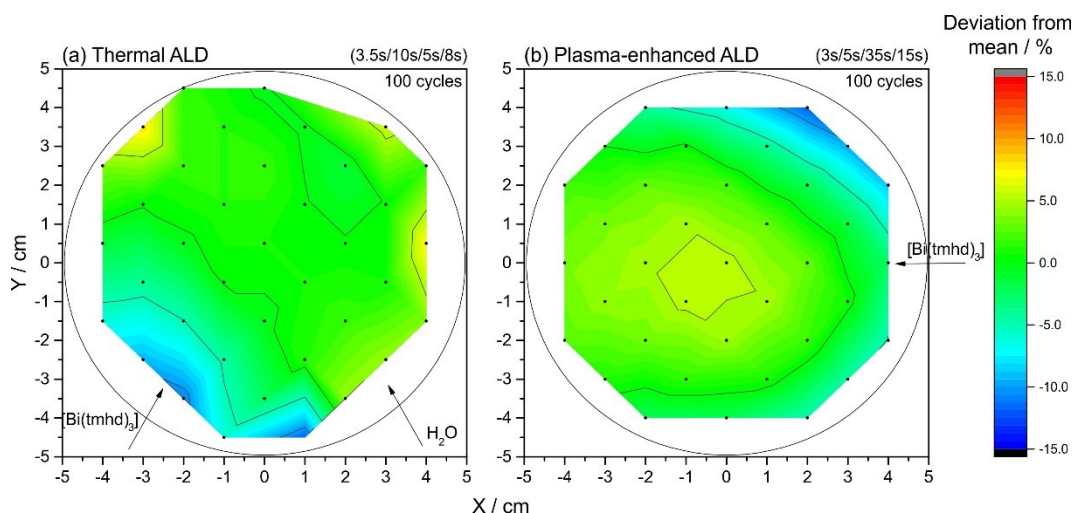


Figure 19: Thickness deviation from mean after 100 ALD cycles over a 4" wafer (a) thermal process, 96% uniformity; (b) plasma-enhanced process, 94% uniformity.

The growth rate is put in perspective by comparing it to GPCs reported by *Shen et al.*¹²⁶ They reported a thermal process using the same precursor and a similar setup (Picosun™ Sunale R-75). The saturation curves they obtained are depicted in green in Figure 18a-c & f. The needed $[\text{Bi}(\text{tmhd})_3]$ exposure time of 6 s is even longer than the 3.5 s identified in the present study. However, their GPC of 0.1 Å/cycle is much lower than the 0.24 Å/cycle reported in this thesis. This seems odd in the first place as most process parameters are alike (i.e. used precursors, process temperature, deposition equipment, and thickness evaluation method) but makes perfect sense when the water dosing time is considered. *Shen et al.* did not investigate the water dosing time but kept it constant at 0.2 s. Such short dosing times are often sufficient, especially when highly reactive precursors are used (e.g. Al_2O_3 from TMA), but our investigation suggests that a much longer water dose of 5 s is needed to achieve saturation. It is therefore very likely that the conditions used by *Shen et al.* do not lead to fully saturated growth in the second half-cycle, which would explain the lower GPC.

Furthermore, the GPC can be influenced by nucleation effects. *Shen et al.* deposited onto bare silicon wafers with a native oxide film and identify a nucleation delay of 40 cycles.¹²⁶ *Hatanpää et al.* published an alternative Bi_2O_3 ALD process from $[\text{Bi}(\text{OCMe}_2\text{Pr})_3]$ and water that also showed a nucleation delay.¹²⁷ The delay could be reduced by applying an Al_2O_3 adhesion layer.¹²⁷ Such a nucleation delay further decreases the apparent GPC. To avoid this an Al_2O_3 adhesion layer was grown prior to each Bi_2O_3 deposition in this thesis.

Figure 18f shows the dependence of the GPC on the substrate temperature (red curve). The temperature window with a constant GPC is visible between 210 – 270°C. On the lower end this temperature window is limited by the precursor bottle temperature of 190°C, which should be the coldest point of the setup to avoid condensation. An increase of the deposition rate is visible above 270°C which normally indicates decomposition of the precursor. Also a

gradual change in reaction mechanism may lead to higher GPCs as it will be discussed in more detail in section 3.4.1.

Interestingly, *Shen et al.* observe a different temperature window of 270 – 300°C. Below 270°C they observe an increase of the GPC which usually assigned to condensation of the precursor. Reasons for that could be a slightly higher pressure in the setup (6-15 hPa for *Shen et al.* vs. 6 hPa in this thesis) but also the rather long $[\text{Bi}(\text{tmhd})_3]$ dosing could facilitate condensation. Further discussions can be found in 3.2 when a plasma-enhanced ALD process is introduced.

3.2 Plasma-enhanced ALD of Bi₂O₃

A second ALD process using an O₂ plasma to oxidize [Bi(tmhd)₃] was investigated. Figure 18 shows the growth per cycle in dependence of the ALD parameters, with the data for the plasma-enhanced process shown in blue. Saturation is reached after 3 s [Bi(tmhd)₃] dosing, 5 s purge, 30 s plasma exposure and 15 s purge. The GPC is 0.35 Å/cycle with a uniformity of 94% over a 4 inch wafer, see Figure 19b. The growth rate in the plasma enhanced process is higher in the thermal process, which is regularly reported.^{66,77,128–130} This increased GPC is usually attributed to the superior reactivity of the plasma generating a higher density of reactive sites on the surface.^{81,87} Indeed exactly this behavior is confirmed and further discussed in section 3.4.

Figure 18f shows the temperature dependence of the growth rate, which is stable from 280-330°C. This is at higher temperatures than for the thermal process which is opposite to what is normally observed. The high reactivity of the plasma species usually extends the temperature window to lower substrate temperatures.^{66,77,128–130} The origin of this counterintuitive behavior is unclear. It may be possible that the plasma exposure decomposes the tmhd ligand into smaller fragments (e.g. CO) which bind more strongly to the sample surface. This could make a higher temperature necessary to form a Bi(tmhd)_x monolayer in the first half cycle. A sharp GPC increase below 280°C usually indicates multilayer absorption which is in disagreement with the thermal process results. The exact reason for this behavior could not be revealed. Additional investigations of the growth process, e.g. by IR, Raman spectroscopy or mass spectrometry, could give more detailed information e.g. on intermediate species and reaction products. This information could enable more thorough descriptions of the surface processes.

3.3 Film properties

After deposition the films deposited by T- and PE-ALD were investigated in terms of composition, morphology, crystallinity and their optical properties using XPS, TEM, AFM, XRD and SE.

3.3.1 Composition

The composition of the films was investigated by XPS. The samples prepared by thermal ALD are considered first with a survey spectrum shown in Figure 20. Most prominently various bismuth signals are visible (orange), with Bi 4f around 160 eV being the most prominent. The expected signals of oxygen (red) are accompanied by additional peaks which are assigned to carbon (black), aluminium (blue) and silicon (grey). The carbon mainly originates from air exposure while aluminium and silicon signals originate from the substrate.

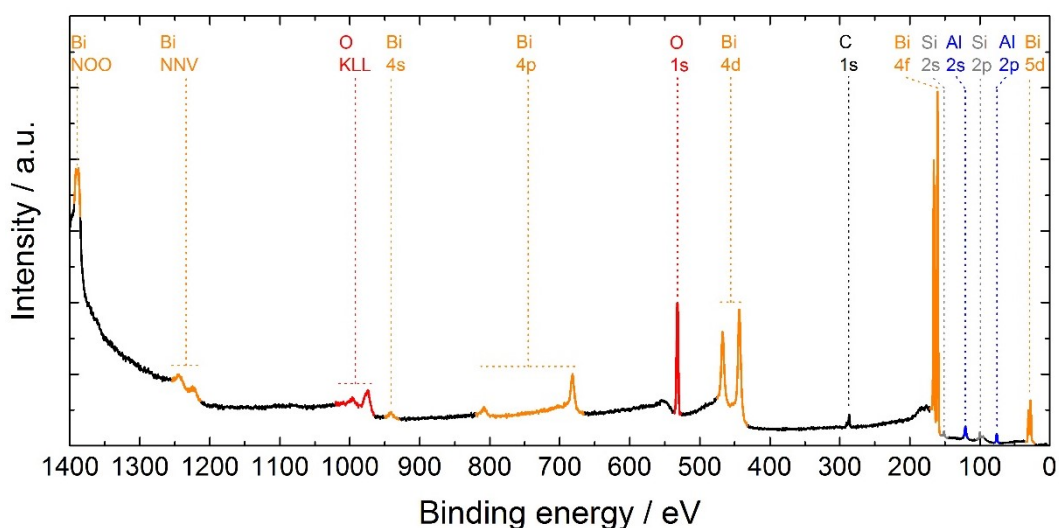


Figure 20: Survey XPS of Bi_2O_3 grown by thermal ALD. Indicated peaks belong to bismuth (orange), oxygen (red), carbon (black), aluminium (blue), and silicon (grey).

Even though XPS is a surface sensitive technique, contributions of the substrate are still visible. This is due to the minimal Bi_2O_3 film thickness of 2.4 nm. Below this is not only elemental silicon but also a native SiO_2 film and the Al_2O_3 adhesion layer, as depicted in Figure 21a. The surface sensitivity of XPS is caused by the strong interaction of the ejected electrons with matter. The inelastic mean free path may only be a few Å, depending on the energy of the electron. The exact distance further depends on the material but can be approximated with the universal curve, which is shown in Figure 21b.¹³¹ The approximated mean free path ranges from 3.0 nm for the O 1s core level to 3.6 nm for Al 2p (kinetic energy of ~957 eV and ~1412 eV, respectively, using 1486.6 eV Al K_α radiation). But electrons may travel further than this distance, therefore the information depth of XPS is usually assumed to be to three times the mean free path, 9.0 – 10.8 nm in the present case. As a consequence all layers from Figure 21a are visible in the XPS survey spectrum in Figure 20.

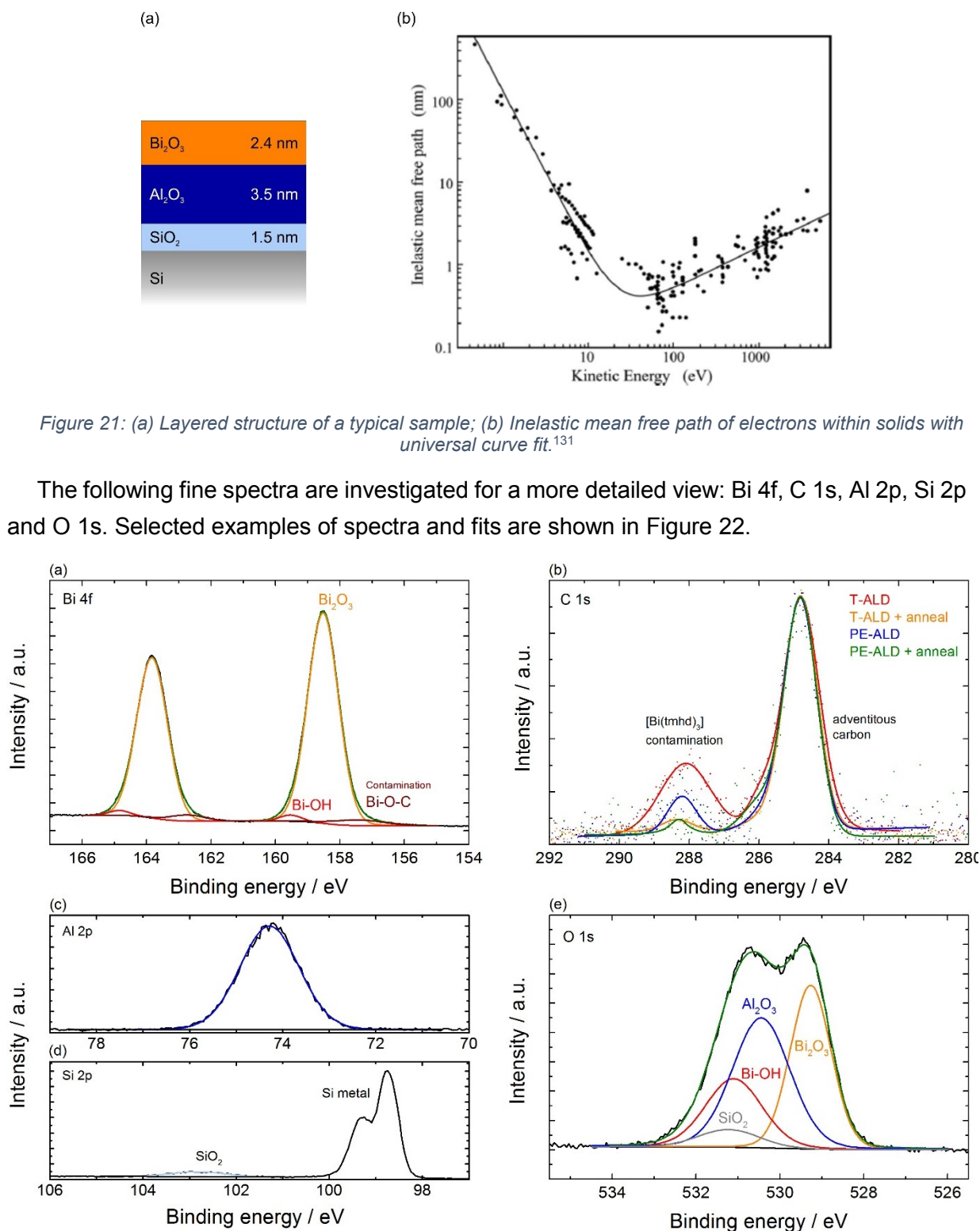


Figure 22: XPS fine spectra: (a) Bi 4f with peaks assigned to bulk Bi_2O_3 (orange), surface Bi-OH (red) and Bi-O-C contaminations (dark red), peak sum in green; (b) C 1s of a Bi_2O_3 sample grown by thermal ALD before (red) and after annealing (orange) and grown by plasma-enhanced ALD before (blue) and after annealing (green), raw data as dots and peak sum as full lines; (c) Al 2p with a single peak fit (blue) of a pure Al_2O_3 sample; (d) Si 2p with a single peak fit for SiO_2 (grey) of a bare silicon substrate; (e) O 1s with peaks assigned to bulk Bi_2O_3 (orange), surface Bi-OH (red), Al_2O_3 (blue), and SiO_2 (grey), peak sum in green.

The Bi 4f spectrum in Figure 22a exhibits a doublet with a spin-orbit splitting of 5.31 eV and an area ratio of 3:4 (these values were set as constraints while fitting). Three peaks are used

to model the data. The dominating feature at 158.5 eV (for $j = 7/2$, orange) originates from Bi^{3+} , confirming the intended Bi_2O_3 phase.^{109,132} At a slightly higher binding energy of 159.5 eV a small second feature (red) is assigned to bismuth atoms at the surface with a typical OH-termination. Peaks assigned to OH-terminated surface species in oxides are commonly found at slightly higher binding energies and a proof for this assignment will be presented later. A third peak is assigned to incorporation of remains of the thmd-ligand with a Bi-O-C type binding (dark red).

Figure 22b shows plots of the C 1s region of various samples. The low sensitivity to carbon causes an increased noise. Dotted data and full lines of the fit sum are therefore chosen for clear visualization. Two peaks model the C-C and C=C species of adventitious carbon, with the C-C position fixed to 284.8 eV as reference. A third peak at ca. 288.2 eV is assigned to contaminations from tmhd, similar to the Bi-O-C peak in the Bi 4f region. This assignment is further described in the appendix, see Figure S 1.

The Al 2p region is shown in Figure 22c. The data can be fitted with a single peak even though a doublet is expected. With a narrow spin-orbit-splitting of only 0.41 eV and a wide FWHM of 1.50 eV this is reasonable and common in literature as well.^{133,134} The spectrum shown in Figure 22c was recorded for a pure Al_2O_3 film grown on silicon (ca. 12 nm grown with the same process as the adhesion layer) for a low-noise representation. It was furthermore used for parameterization as it will be described below.

Figure 22d shows the Si 2p region of a bare silicon wafer to assign contributions from the silicon substrate. Two peaks are visible, a doublet at 99 eV originating from elemental Si and a smaller feature at 103 eV assigned to the native oxide. Similar to the aluminium interpretation a single peak is sufficient to fit the SiO_2 signal.

Finally Figure 22e shows the O 1s region. The raw data suggests an overlap of two peaks at about 529.4 eV and 530.8 eV. However, the other fine spectra suggest up to five different species are present: bulk Bi_2O_3 , surface Bi-OH, Al_2O_3 , SiO_2 , and a Bi-O-C contamination. A meaningful fit with so many species is not trivial but a few constraints can be applied to aid the fitting. The beforehand mentioned samples of pure Al_2O_3 and bare silicon are used for these constraints. The O 1s spectra of these reference samples only contain peaks associated to Al_2O_3 and SiO_2 , respectively. Therefore their O 1s peaks can be directly linked to the corresponding peaks in the Al 2p and Si 2p region, respectively, in terms of peak position and area ratio (i.e. the ratio between fitted Al 2p peak area and O 1s peak area for the Al_2O_3 contribution, vice versa for the SiO_2 contribution). From this the blue Al_2O_3 and the grey SiO_2 peak in Figure 22e are generated (parameterized peak position and area ratio). Then two peaks for bismuth oxide are added in red and orange. Their peak position and area were left as free fitting parameters. The fitted peak positions are 529.3 eV and 531.1 eV for bulk Bi_2O_3 and surface Bi-OH, respectively. Both values match reported values of 529.4 – 529.5 eV and 531.0 eV for bulk Bi_2O_3 and surface Bi-OH, respectively.^{132,135} With these four peaks a near-perfect fit is generated.

A contribution from Bi-O-C is omitted as the quality of the described fit does not require further optimization. Furthermore the information content of a possible Bi-O-C peak can be doubted. A possible position of a Bi-O-C peak could not be estimated. Also an area constraint could not be applied. The C 1s region gives clear indication for the amount of impurities in the film, which is the desired value, but a direct link to the Bi 4f region cannot be drawn.

From the fit of the O 1s spectrum, a bulk stoichiometry of $\text{Bi}_2\text{O}_{1.73}$ for the 2.4 nm film is calculated. Bulk refers to the stoichiometry calculated from peaks assigned to bulk Bi_2O_3 , orange in Figure 22a and e. The stoichiometry differs significantly from the theoretical value of Bi_2O_3 and various reasons may contribute to this:

1) The sensitivity factor of the different orbitals. These values are taken from a generally used database from Casa and are 3.1 for the O 1s orbital and 24.47 for the Bi 4f.¹¹¹ However, XPS measurements on a BiVO_4 single crystal prepared according to *Favaro et al.* suggest a Bi 4f sensitivity of 44.6. If this value is used for our data, a stoichiometry of $\text{Bi}_2\text{O}_{3.15}$ is calculated.¹¹²

2) Differences in the information depth of the different orbitals. These can introduce differences from the reported sensitivity values when the film thickness is below the information depth. This is indeed true in this study (e.g. 2.4 nm Bi_2O_3 film thickness and information depths around 10 nm).

3) Measurement to measurement variations. Each XPS measurement will give slightly different results. Reasons can be changes in the samples itself, e.g. by varying storage times, or batch-to-batch variations in the samples. Also the XPS setup itself changes over time in terms of alignment and X-ray electrode aging. However, the contribution of such variations is expected to be very low and does not explain significant deviations from the expected stoichiometry.

4) Errors in the derivation of the peak constraints. The described parametrization of the O 1s contributions from Al_2O_3 and SiO_2 is a model and not perfect. Despite the influence of the information depth also small charging effects could occur. With 12 nm Al_2O_3 on the reference sample small local charging cannot be fully excluded. Therefore little variations of the peak position of the Al_2O_3 contribution in the O 1s region could be possible. This could have an influence on the fit of the other species, considering the large peak area.

The described effects may alter the measured stoichiometry of the bismuth oxide thin film. 1) and 2) could lead to an underestimation of the oxygen content. For 3) and 4) it is not clear if they in- or decrease the apparent oxygen content. Even though clear quantifications are difficult, the effects are assumed to be small. It is therefore supposed that the film is indeed oxygen poor. Even the large deviation from the theoretical stoichiometry seems possible considering the extremely low thickness of 2.4 nm.

The extent of the carbon contamination is evaluated from the C 1s region in Figure 22c. The bulk carbon content calculates to 9.4 at.%. As the tmhd-ligand is the only carbon containing

component, the contamination is attributed to incomplete tmhd removal in the second half-cycle. Such an incomplete removal has been observed before when H₂O was used in combination with tmhd-containing precursors, leading to higher carbon contents.^{78,83,136} A post annealing of the film at 450°C in air was found to reduce the amount of carbon in the film (orange curve in Figure 22c) to 2.4 at. %.

Also the composition of PE-ALD films was investigated by XPS, as shown in Figure 23. Again, the dominant Bi 4f_{7/2} peak at 158.7 eV confirms the desired +3 oxidation state of bismuth. In the O 1s spectrum the contribution of the Al₂O₃ adhesion layer and the native SiO₂ is smaller due to the thicker Bi₂O₃ film (3.5 nm compared to 2.4 nm). This makes evaluation of the O 1s region slightly more accessible and the calculated stoichiometry more trustworthy. The calculated bulk stoichiometry is Bi₂O_{2.17} and thereby less oxygen poor than the T-ALD grown film.

The carbon content is 4.3 at. %, which is a significant improvement compared to the thermal process (blue vs. red lines in Figure 22b). This confirms that the O₂ plasma is a more potent oxidizer, as mentioned in section 2.1.1. Similar to the T-ALD film the samples were annealed in air. This led to a further reduction of the carbon content to 0.9 at. % (green plot in Figure 22b). This confirms the clear trend that annealing in air removes carbon impurities.

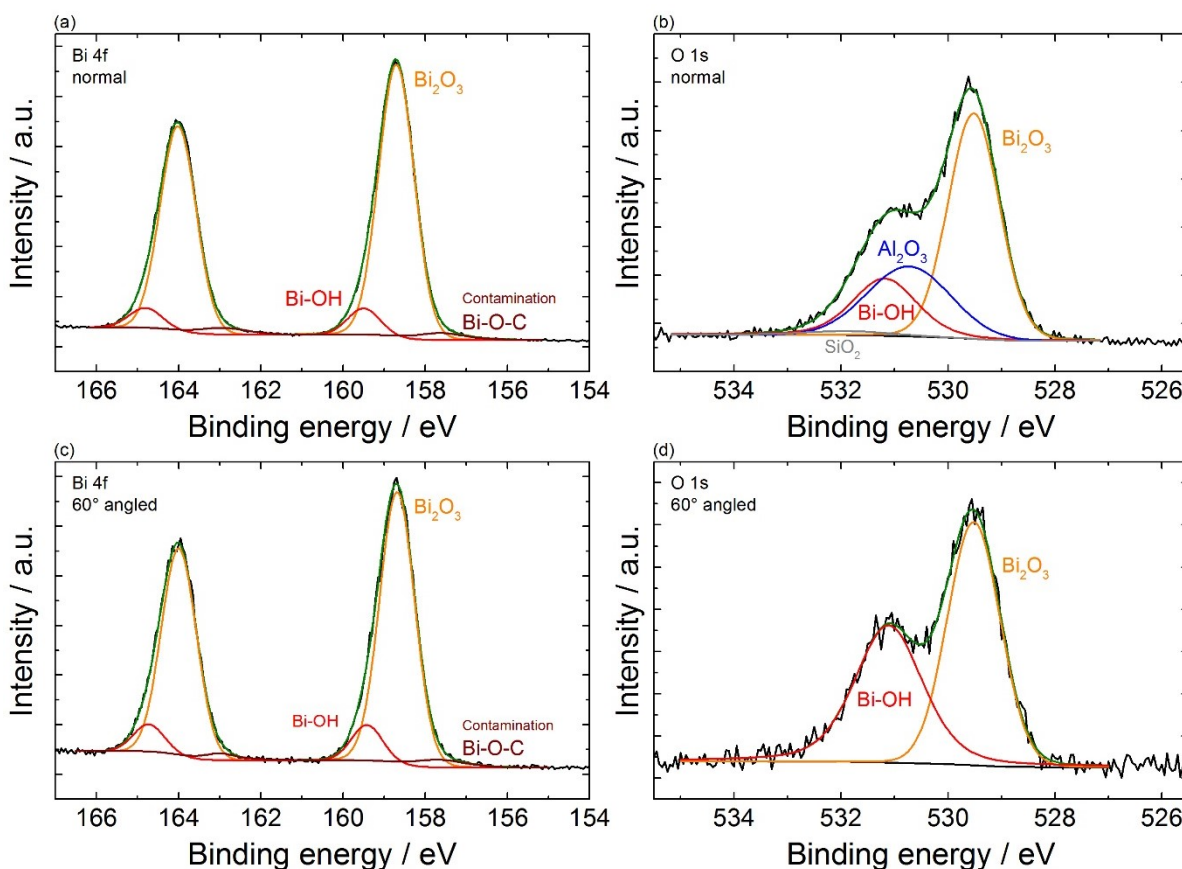


Figure 23: XPS fine spectra of PE-ALD films: (a) O 1s with peaks assigned to bulk Bi₂O₃ (orange), surface Bi-OH (red), Al₂O₃ (blue) and SiO₂ (grey), peak sum in green; (b) Bi 4f with peaks assigned to bulk Bi₂O₃ (orange), surface Bi-OH (red) and Bi-O-C contaminations (dark red), peak sum in green; (c) O 1s recorded in 60° angled configuration with peaks assigned to bulk Bi₂O₃ (orange) and surface Bi-OH (red), peak sum in green; (d) Bi 4f

recorded in 60° angled configuration with peaks assigned to bulk Bi₂O₃ (orange), surface Bi-OH (red), and Bi-O-C contaminations (dark red), peak sum in green.

Furthermore, measurements with a 60° angle between the surface normal and the detector were done. These measurements are more surface sensitive with only half the information depth. Thereby substrate contributions to the measurement are suppressed. The corresponding spectra are shown in Figure 23c and d.

The contributions of Al₂O₃ and SiO₂ completely vanish, see also Figure S 2. Still, the bulk stoichiometry is not affected (Bi₂O_{2.17} in normal vs. Bi₂O_{2.19} in angled configuration). The same is true for the carbon content (4.3 at.% in normal vs. 4.5 at.% in angled configuration), confirming that the described fitting of the O 1s region is fair.

In addition, the area of the peaks assigned to surface Bi-OH (red) increase, validating the previously made assignment to a surface species.

To the best of my knowledge only two other PE-ALD processes of bismuth oxide are reported and only one of them investigated a binary Bi₂O₃ process.^{122,137} In there a custom-built high-vacuum ALD reactor with a microwave cavity radical beam source and [Bi(tmhd)₃] are used. In this study oxygen-rich films with stoichiometries around Bi₂O_{3.6} were obtained.¹²² However, the carbon content of these films was above 22%, which is much too high for most electronic applications. Therefore the here presented study includes a significant improvement in film composition.

3.3.2 Morphology

TEM measurements were conducted on a subset of the ALD-grown samples: cross-sectional TEM images are shown in Figure 24. The layered structure is clearly visible in each picture with (from bottom to top) single crystalline silicon wafer, native SiO₂, ALD-Al₂O₃ adhesion layer, ALD-Bi₂O₃, and glue added during TEM sample preparation. Samples without post-deposition treatment show flat and homogeneous Bi₂O₃ films (overviews in a and b): no cracks or large pinholes are visible, illustrating the excellent coverage and growth control of both ALD processes. Annealing of the PE-ALD grown film does not affect the substrate coverage (c).

The thickness of the individual layers was determined at ten equidistant spots in the detailed images d-f. The values are compared to thicknesses determined by spectroscopic ellipsometry, as summarized in Table 2.

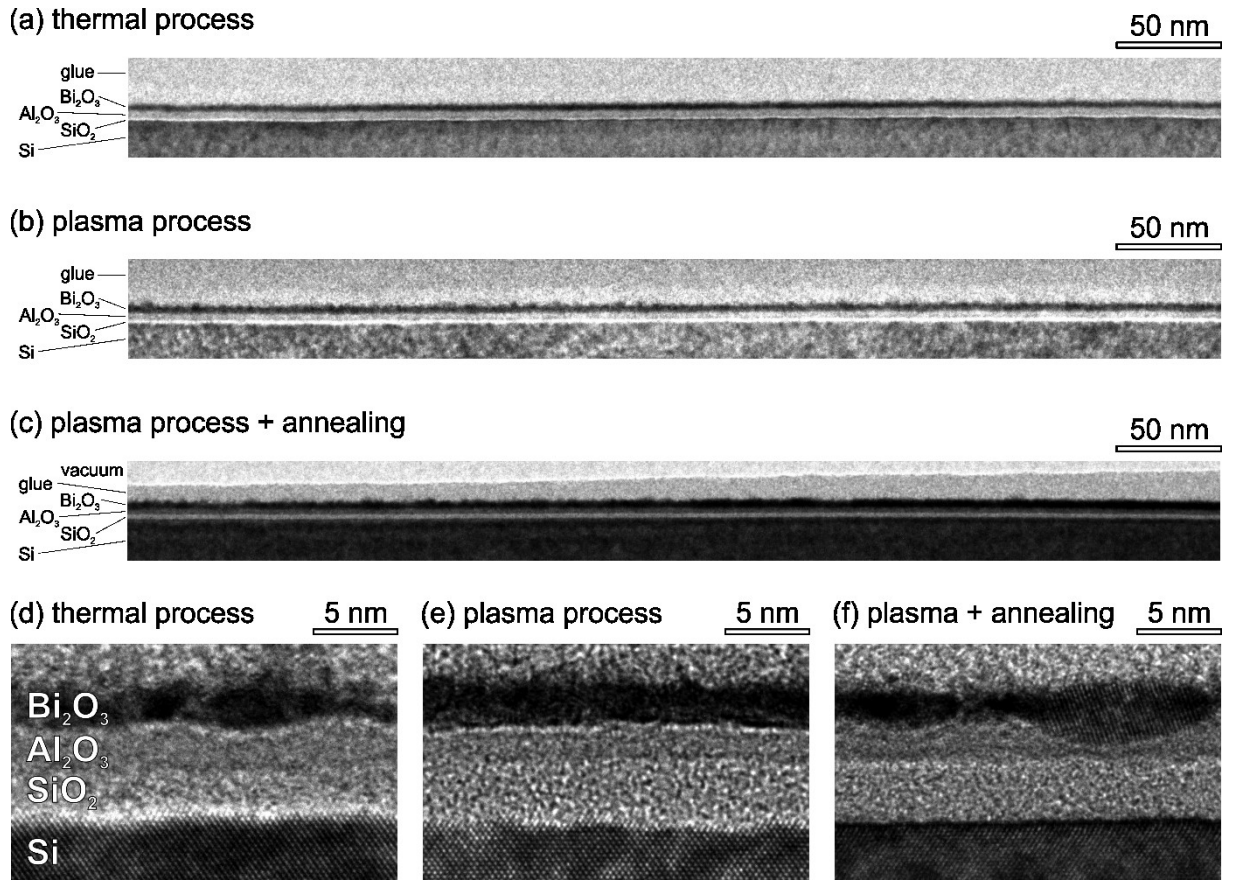


Figure 24: Cross sectional TEM images of bismuth oxide films. The samples exhibit a layered structure of the silicon substrate, its native oxide layer, the ALD grown alumina adhesion layer, the bismuth oxide film, and the glue applied during preparation (from bottom to top). (a-c): overviews, (d-f): detailed views of the T-ALD and PE-ALD sample, before and after annealing.

Table 2: Measured film thicknesses of SiO₂, Al₂O₃, and Bi₂O₃ by SE and TEM of the T-ALD, PE-ALD and PE-ALD sample after annealing. The error estimates correspond to the standard deviations, grey values after annealing could not be measured individually and are therefore assumed to be unaffected by the annealing.

Layer	Film thickness / nm					
	T-ALD		P-ALD		P-ALD + anneal	
	SE	TEM	SE	TEM	SE	TEM
SiO ₂	1.38	2.50 ± 0.23	1.52	3.67 ± 0.14	1.52	3.42 ± 0.32
Al ₂ O ₃	3.02	2.59 ± 0.29	3.67	2.06 ± 0.18	3.67	1.82 ± 0.29
Bi ₂ O ₃	3.03	2.55 ± 0.49	3.75	3.06 ± 0.26	4.10	3.12 ± 0.66

A comparison of the thicknesses of Bi₂O₃ and Al₂O₃ films shows that the values obtained from the TEM images are about 23% lower than the values estimated by spectroscopic ellipsometry. This is a known phenomenon as SE tends to slightly overestimate the thickness.^{138–140} SE measurements contain another uncertainty. Each film thickness and the corresponding optical constants were modeled in a separate measurement, i.e. in the following routine: SE measurement to model SiO₂ – ALD of Al₂O₃ – SE measurement to model Al₂O₃ – ALD of Bi₂O₃ – SE measurement to model Bi₂O₃ (– Annealing – SE measurement to model

Bi₂O₃, if applicable). For each SE measurements the already investigated films were assumed to be unaffected. This is a simplification but offers the most accurate SE estimations. The alternative would be to fit all thicknesses and optical constants from a single measurement. The many free fitting parameters in this approach do not results in meaningful results.

The TEM measured thicknesses of SiO₂ are about 80% and 140% larger for the T-ALD and the PE-ALD process, respectively. This odd observation has been made before and ascribed to the ALD process to deposit Al₂O₃ from TMA and water which induces a further oxidation of the underlying silicon substrate.¹⁴¹ As described SE can barely account for such changes, especially if extremely thin films are investigated. The present data suggests that the use of an oxygen plasma further enhances the silicon oxidation. Furthermore, the slight thickness increase of the PE-ALD film by annealing suggests a decreased density of the annealed Bi₂O₃.

In the TEM images some thickness deviations become visible. Annealing of the PE-ALD film seems to lead to some roughening of the surface, as visible in the left part of Figure 24c. The detailed view in f supports this observation. This surface roughness is put into numbers by the standard deviation of estimated thicknesses, as given in Table 2. The standard deviations of the PE-ALD film indeed increase upon annealing, from 0.26 to 0.66 nm. Without annealing, PE-ALD grows smoother films than T-ALD on microscopic scale with 0.26 nm standard deviation compared to 0.49 nm, respectively

AFM measurements were performed to extent the surface roughness investigation to an area in the micron scale. Measurements are shown in Figure 25, for the T-ALD and the PE-ALD before and after annealing, respectively. As expected the AFM images show overall smooth surfaces. The reduced contrast suggests that annealing of the T-ALD film leads to a further decrease in roughness, see Figure 25a and b. The opposite is true for the PE-ALD sample where a roughening is visible (c and d). These observations are confirmed by the calculation of the roughness RMS from the AFM images. The corresponding values are shown in Table 3. The roughness RMS of the T-ALD sample decreases from 1.1 nm (as deposited) to 0.72 nm (after annealing), whereas that of the PE-ALD films increases from 0.22 nm to 1.4 nm, confirming the observations from TEM. The roughening of the PE-ALD sample is caused by a large number of small triangular-shaped crystallites reaching out of the surface which suggest the partial crystallization of the PE-ALD film by annealing.

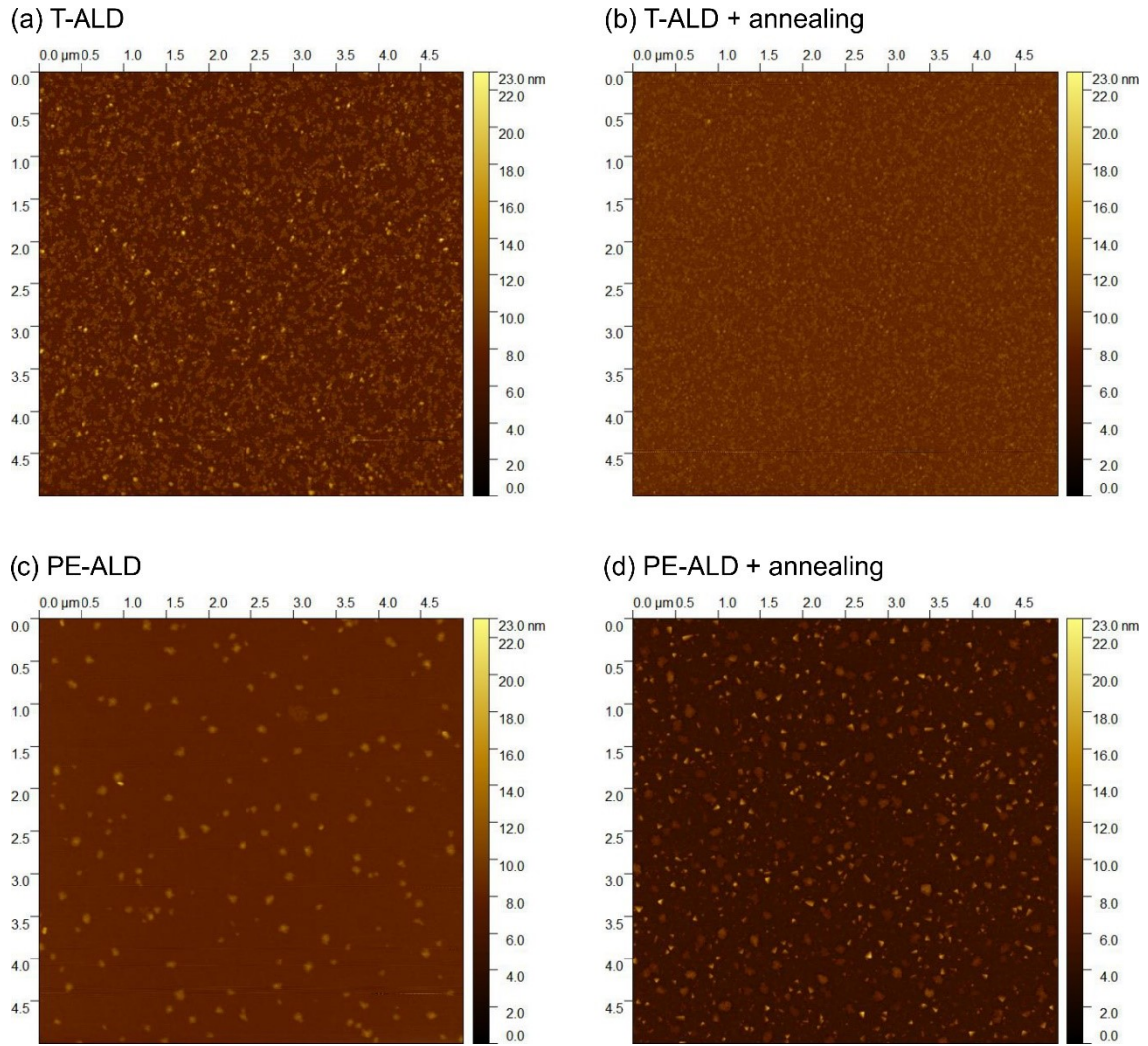


Figure 25: AFM images of the Bi_2O_3 samples: (a) Thermal ALD as deposited and (b) annealed; (c) plasma-enhanced ALD as deposited and (d) annealed.

Table 3: Calculated surface roughness as root mean square from AFM measurements of T-ALD and PE-ALD Bi_2O_3 sample, before and after annealing, respectively.

Sample	Roughness RMS / nm
T-ALD	1.1
T-ALD + annealing	0.72
PE-ALD	0.22
PE-ALD + annealing	1.4

3.3.3 Crystallinity

TEM gives information of the crystallinity as well. Figure 24d and e show no crystal lattice, indicating an amorphous phase. Annealing of the PE-ALD film leads to a partial crystallization as visible by the lattice fringes on the right side of Figure f. This is in agreement with the AFM observations.

XRD is utilized as another technique to investigate the crystallinity over a larger sample area (in the cm range rather than over $< 10 \mu\text{m}$ by TEM and AFM). The diffractograms are shown in Figure 26.

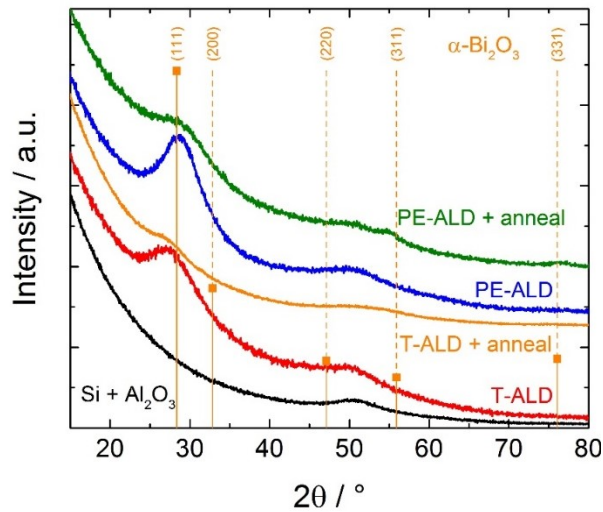


Figure 26: GIXRD patterns of a T-ALD Bi_2O_3 film before (red) and after annealing (orange) as well as a P-ALD film before (blue) and after annealing (green) compared to the Al_2O_3 covered Si substrate (black) and $\alpha\text{-Bi}_2\text{O}_3$ (orange, vertical drops).¹⁴²

All diffractograms show very broad and/or weak features which suggests predominantly amorphous films, as seen by TEM as well. The existing peaks can however be assigned to Bi_2O_3 with exception of the feature at 51° which is already visible in the diffractogram of the substrate (black curve). In both as deposited films the (111) reflection of $\alpha\text{-Bi}_2\text{O}_3$ is the most pronounced feature (red and blue curve). Annealing leads to a decrease in the (111) intensity, suggesting some sort of reorientation (orange and green curve). For the PE-ALD film a slight increase of the (311) and (331) reflections indicate a partial crystallization, as it was suggested by TEM and AFM results as well.

3.3.4 Optical properties

Spectroscopic ellipsometry was used to model the optical properties of the film. The dielectric function of bismuth oxide was modelled by a Tauc-Lorentz oscillator, which is commonly used for amorphous semiconductors.^{76,103,104} The modelled optical constants, i.e. refractive indices n and extinction coefficients k , are shown in Figure 27 as function of the photon energy. Measurements were conducted under three angles allowing simultaneous modelling of film thickness and optical constants.

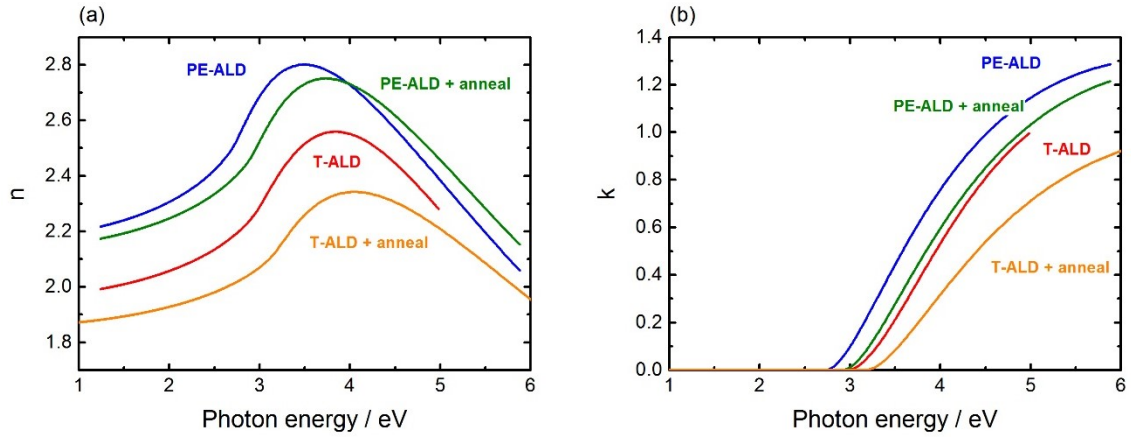


Figure 27: Modelled optical properties of Bi_2O_3 thin films: (a) refractive indices n and (b) extinction coefficients k for a T-ALD Bi_2O_3 film (red), a T-ALD film after annealing (orange), a PE-ALD film (blue), and a PE-ALD film after annealing (green).

The refractive index of the as-deposited bismuth oxide film grown by T-ALD (red curve) is 2.3 (at 3 eV). In the PE-ALD grown film this value is larger, 2.7 at 3 eV. Both values are typical for Bi_2O_3 grown by reactive sputtering or ALD (2.2 – 2.8 at 3 eV).^{123,143} As the refractive index is closely related to the film density, this suggests that the T-ALD grown Bi_2O_3 film have a lower density.¹⁴³ In both cases the refractive indices decrease upon annealing (green and orange curve). This observation is in agreement with the increased film thickness after annealing mentioned in 3.3.2.

From the extinction coefficients plotted in Figure 27b the optical bandgap can be estimated. In the Tauc-Lorentz model is a quadratic dependence of ε_2 (the imaginary part of the dielectric function) on the photon energy, resulting in an indirect bandgap. This is typical for amorphous bismuth oxide films and supports the suitability of the Tauc-Lorentz oscillator in the present case.^{106,144,145} The onset of the extinction coefficient marks the optical bandgap, which is 2.9 eV for the T-ALD film (red curve) and 2.7 eV for the PE-ALD film (blue curve). Annealing increases the bandgap of both samples by 0.2 eV, to 3.1 and 2.9 eV for the T-ALD and the PE-ALD, respectively (orange and green curve). A small increase in bandgap after annealing has been observed before and is often assigned to reorganization and improvement in crystallinity.^{146–149} All values are in the same range as previously reported values for Bi_2O_3 , between 2.7 and 3.0 eV.^{64,121,150} The reduction of both the refractive indices and the extinction coefficients by annealing suggests that a possible reorientation in the thin films leads to a decrease in film density as it was already suggested by the TEM image evaluation.

3.4 Real-time spectroscopic ellipsometry

3.4.1 Single-layer optical model

The growth of bismuth oxide was monitored *in situ* by real-time spectroscopic ellipsometry to get further insight into the ALD process. The growing film is modeled as a single layer using the Tauc-Lorentz oscillator similar to the *ex situ* data, i.e. as a bulk Bi₂O₃ layer. Describing the growing film as a single layer is common practice even though it simplifies the situation. The first half-cycle generates a surface layer with ligand termination while the second half-cycle leaves an OH-terminated surface. These surface layers can usually not be considered as their minimal thickness makes a distinction between them and the bulk layer ambiguous. Therefore the measured single layer thickness is an *apparent* thickness, especially after the first half-cycle. In fact it is a combination of the physical change in film thickness and the change in optical properties of the surface layer.⁷⁶

The development of this apparent thickness over the first 20 cycles of the T-ALD and a PE-ALD process is shown in Figure 28 with a zoom into the first cycle in Figure 29. It should be noted that the pulse and purge times are longer than used previously to maximize the thickness contrast in the ellipsometry data.

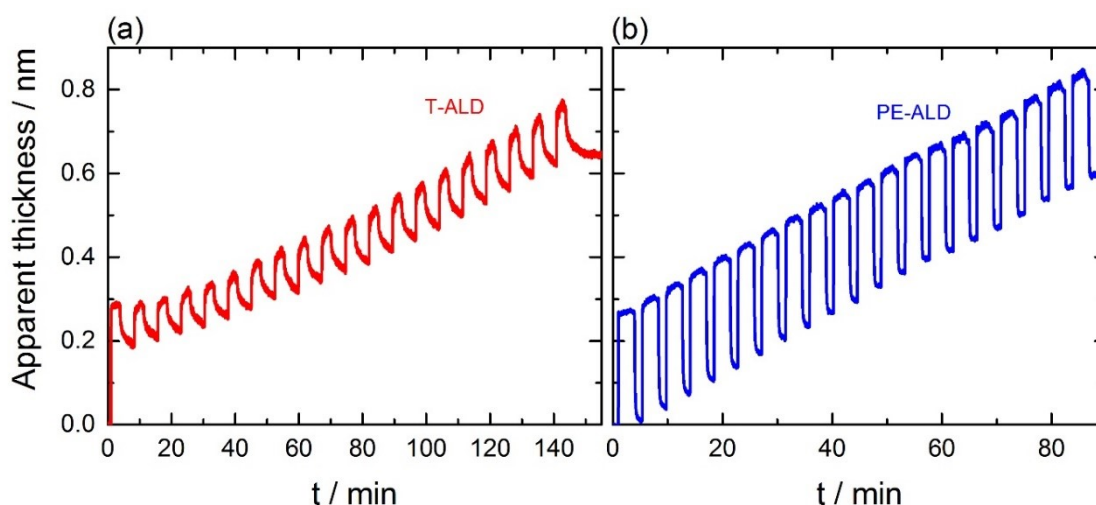
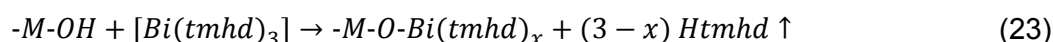


Figure 28: Development of the apparent thickness of Bi₂O₃ over 20 cycles of (a) thermal and (b) plasma-enhanced ALD.

The first [Bi(tmhd)₃] pulse induces a strong thickness increase of about 2.8 Å caused by chemisorption of the precursor molecule on the surface:



One or two of the tmhd ligands are released by the ligand exchange ($x = 1, 2$). After saturation and during the subsequent purge the apparent thickness stays constant, as expected for a typical ALD process.

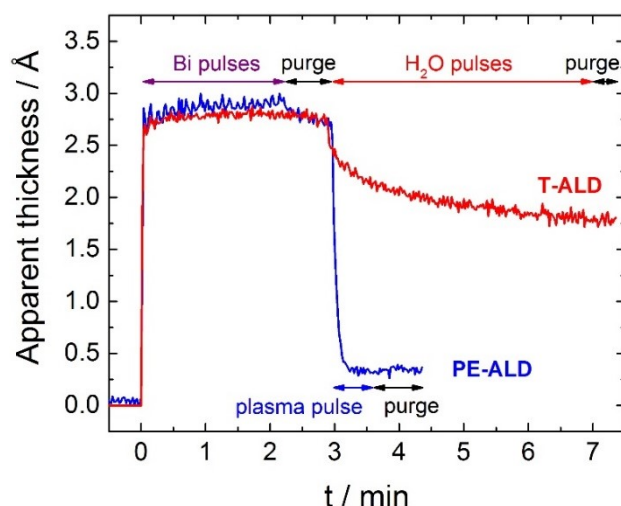
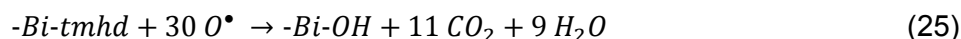


Figure 29: Zoom into the first cycle of Figure 28.

After three minutes the second half-cycle introduces the oxidant and the film thickness decreases. For the thermal process this is most likely due to a ligand exchange reaction where water removes the tmhd and results in OH-termination:



In contrast, the oxygen radicals of the plasma-enhanced process induce a combustion-like reaction forming H_2O and CO_2 .⁶⁶



An incomplete reaction could occur, forming smaller organic fragments during the plasma step.

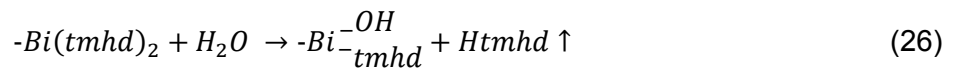
As the tmhd-ligands are much larger ($> 5 \text{ \AA}^{126}$) than a hydroxyl group the thickness decreases in the second half-cycle. Again, the thickness stays constant in the following purge step. Finally, after one full cycle a net increase is achieved, the growth per cycle.

For the PE-ALD process this GPC is constant from the first cycle, meaning that no nucleation delay or accelerated growth occurs. The T-ALD process exhibits an accelerated growth, stable GPC is achieved after around 10 cycles.

The first cycle is investigated in more detail to understand this difference in film growth (see Figure 29). The first half-cycle is the same for both processes, consisting of multiple 0.5 s $[Bi(tmhd)_3]$ pulses, short intermediate purges and a final 1 min purge. The second half-cycle however shows significant differences. The plasma exposure induces a rapid thickness decrease that saturates within ~ 15 s. With water exposure this thickness decrease is much slower. Even extensive dosing times (40 s in total with intermediate purges) only lead to about half the thickness decrease. This strongly suggests that not all tmhd-ligands are removed by water. Incorporation of tmhd (or fragments thereof) into the Bi_2O_3 film explains the higher carbon content and could be the reason for the lower optical density and increased roughness of T-ALD Bi_2O_3 films compared to the PE-ALD films.

An important consequence of the remaining tmhd ligands is that they reduce the number of generated OH-surface sites accessible during the next ALD cycle. Fewer precursor molecules can adsorb in the following half-cycle, leading to the reduced thickness increase during [Bi(tmhd)₃] dosing (visible in Figure 28). This also explains the lower GPC of the T-ALD process compared to PE-ALD, which was observed by *ex situ* measurements (see Figure 18). So indeed the assumption that the higher reactivity of the plasma induces a higher density of reactive surface sites seems to be true in the present process.

Since the generated surface after a full thermal ALD cycle is less reactive than the initial Al₂O₃ surface, accelerated growth is observed in the very first ALD cycle, see Figure 28a. The fact that the thickness decreases during water exposure is roughly half of the decrease during plasma exposure could hint towards a reaction like the following:



where two tmhd-ligands remain at the surface in the first half-cycle and water only removes one of these in the second half-cycle. This would mean that the $-Bi_{tmhd}^{OH}$ species is more stable than the initial $-Bi(tmhd)_2$ and more energy is needed to remove the remaining tmhd-ligand. In a thermal process this energy can only be provided by an elevated temperature. The increase of GPC in the T-ALD process above 270°C could hint towards such a change in reaction mechanism. Experiments at even higher temperatures (> 330°C) would be needed to investigate this behavior further. However, this was beyond the scope of this project.

3.4.2 Double-layer optical model

As discussed in the previous section, single-layer modelling of the growing film is only giving an apparent thickness development with unsatisfactory consideration of the varying surface species. Since such a surface layer can hardly be distinguished from the bulk a single layer model is usually the only possibility to following the film growth.

However, with a diameter of more than 10 Å the [Bi(tmhd)₃] molecule is larger than most ALD precursors.¹²⁶ Still, Figure 29 only shows a thickness increase of about 2.8 Å by the adsorption of [Bi(thmd)₃] onto the substrate. This seems like a rather low estimate when 1 – 2 tmhd ligands are removed. Considering these two factors, the thick expected surface layer and the low estimation thereof, the use of a single-layer model seems like an inappropriate simplification.

To validate this assumption of oversimplification the quality of the fit of the PE-process is investigated. For this the mean squared error (MSE) can be considered, which is shown in Figure 30a. Therein large, periodic fluctuations are visible which coincide with the half-cycles.

This shows that the single layer nicely represents the Bi_2O_3 film present in the second half-cycle but the not situation in the first half-cycle with $\text{Bi}(\text{tmhd})_x$ adsorbates.

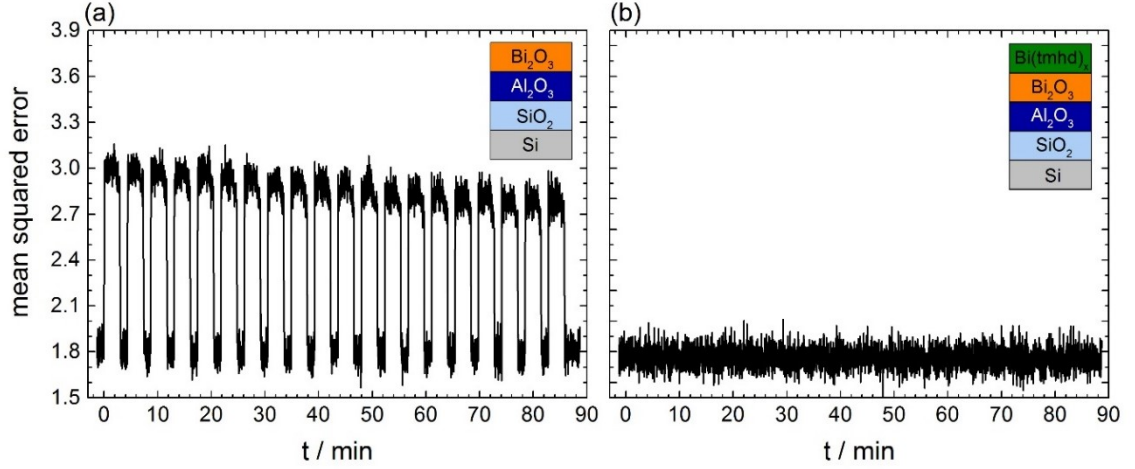


Figure 30: Mean squared error of the RTSE fit of Figure 28b: (a) with a single Bi_2O_3 layer; (b) with a bulk Bi_2O_3 and a surface $\text{Bi}(\text{tmhd})_x$ layer.

Therefore a more sophisticated double-layer optical model was developed. The earlier used Tauc-Lorentz oscillator is kept to represent the bulk Bi_2O_3 layer and an additional $\text{Bi}(\text{tmhd})_x$ layer is added on top, modelled by a transparent Cauchy oscillator. The resulting layer structure is sketched in the inset of Figure 30b. The optical constants of both layers were derived from the RTSE measurements as described in the appendix. The refractive indices found for the $\text{Bi}(\text{tmhd})_x$ surface layer are shown in Figure 31. To the best of my knowledge this is the first time the optical constants of an adsorbate layer were derived from real-time SE measurements.

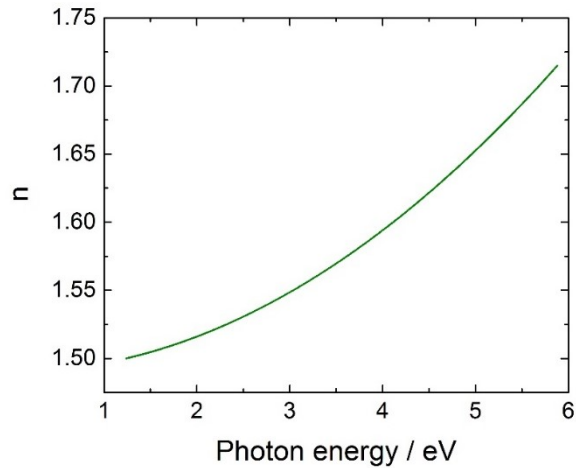


Figure 31: Refractive index n of the $\text{Bi}(\text{tmhd})_x$ surface layer.

With the identified optical constants the double-layer model was utilized to fit the RTSE data. The thicknesses of bulk Bi_2O_3 and surface $\text{Bi}(\text{tmhd})_x$ were the fitting parameters. This model indeed improves the fit, visible by the low and half-cycle-independent MSE values shown in Figure 30b. This suggests that the model is well-suited to resemble the film growth.

The resulting thickness development for the $\text{Bi}(\text{tmhd})_x$ surface layer and the bulk Bi_2O_3 is shown in Figure 32. The fit nicely shows the expected behavior during the ALD cycles: with dosing of $[\text{Bi}(\text{tmhd})_3]$ a $\text{Bi}(\text{tmhd})_x$ adsorbate layer forms which is fully removed during the subsequent plasma step. The thickness of the surface layer is approximately 4 Å which is significantly larger than the 2.8 Å from the single-layer model and a reasonable value for a 10 Å $[\text{Bi}(\text{tmhd})_3]$ molecule that has lost one or two of its tmhd ligands.

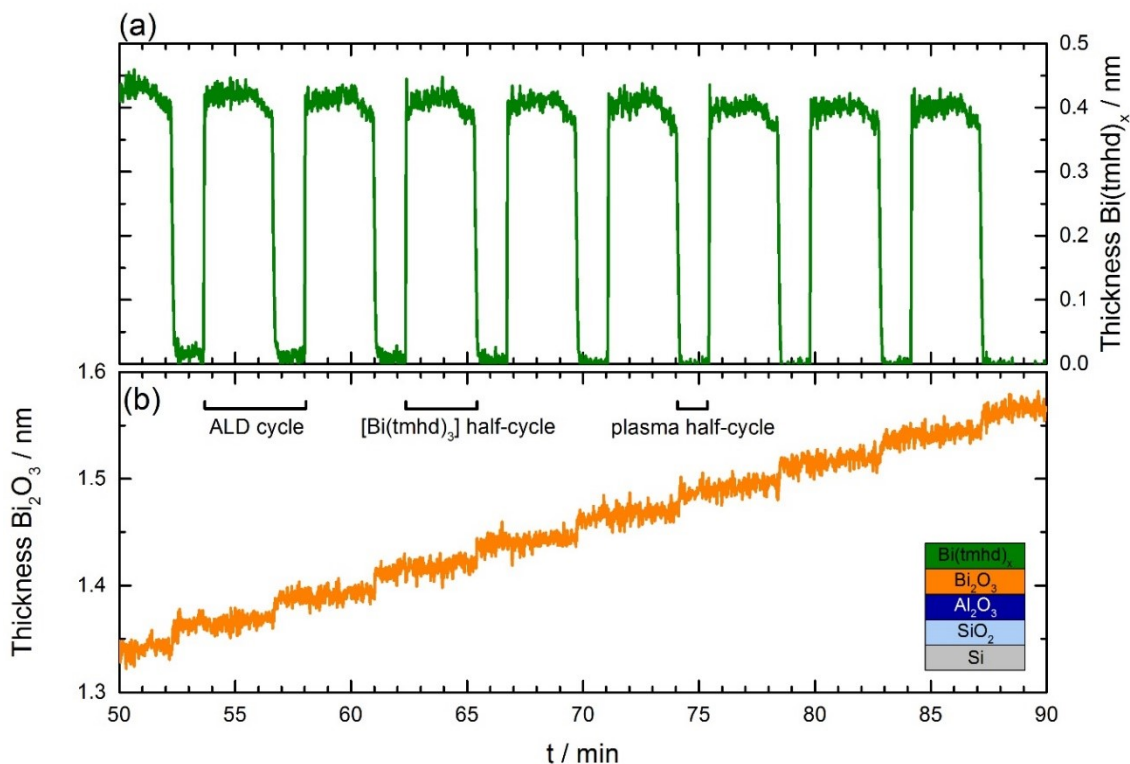


Figure 32: Thickness development of (a) the $\text{Bi}(\text{tmhd})_x$ surface layer and (b) the bulk Bi_2O_3 during PE-ALD, derived from the double-layer optical model.

The thickness of the Bi_2O_3 bulk increases in a stepwise manner with the plasma exposure. This means that the conversion into the desired bismuth oxide occurs in the second half-cycle when all ligands are removed and not upon $\text{Bi}(\text{tmhd})_x$ adsorption.

The introduction of the new double-layer model offers a versatile tool to follow ALD processes in more detail. It can easily be screened for full ligand removal in the second half-cycle (thickness of the surface layer decreases to zero) or possible side reactions can be tracked. For example CVD components would typically add a linear thickness increase of the bulk layer, resulting in non-horizontal step tops. The growth of the bulk film can directly be pinned to a step of the ALD cycle and thereby help to understand the reactions mechanism. Finally, the thickness and optical constants of the surface layer could act as a fingerprint of certain surface species, offering possibilities to track irregularities in the growth or changes in the mechanism. These insights can help to accelerate the development of novel ALD processes and give new insight into reaction mechanisms.

3.5 Conclusion, remarks and further steps

Two ALD processes from $[\text{Bi}(\text{tmhd})_3]$ were developed, a thermal process with a growth rate of 0.24 \AA/cycle and an oxygen plasma-enhanced process with a growth rate of 0.35 \AA/cycle . The temperature windows range from $210 - 270$ and from $280 - 330^\circ\text{C}$, respectively. The origin of the higher temperature window for the PE-ALD could not fully be resolved, further *in situ* characterization of intermediate species could give additional insights.

All films are identified as predominantly amorphous Bi_2O_3 . The use of the plasma significantly reduces the amount of carbon impurities (from tmhd) from 9.4 to 4.3 at.%. Annealing in air further reduces the amount of carbon to 2.4 and 0.9 at.% for the T-ALD and PE-ALD grown film, respectively. It further induces a partial crystallization of the PE-ALD film.

Real-time spectroscopic ellipsometry shows that H_2O is, contrary to the oxygen plasma, not reactive enough to fully remove the $\text{Bi}(\text{tmhd})_x$ surface termination in the second half-cycle. This explains the increased carbon content, the decreased GPC, and hints towards an alternative reaction mechanism due to the low temperature. Therefore, the oxygen plasma is the superior oxidant in the presented context.

The large tmhd ligands allow the introduction of a double-layer optical model and the estimation of the optical constants of the $\text{Bi}(\text{tmhd})_x$ surface layer. With the novel model it was shown that bulk Bi_2O_3 is formed during the plasma exposure and not during $[\text{Bi}(\text{tmhd})_3]$ chemisorption in the first half cycle. The double-layer optical model can easily be adapted for other ALD processes to give new insights into these processes, provided that the precursor molecules are large enough to give sufficient optical contrast. Large ligands and completed surface reactions facilitate the fit. After optical constants are determined the model can be used to quickly identify reaction issues as CVD components or to optimize reactant exposure times. Double-layer optical models can therefore accelerate the development or adaption of ALD processes.

Reproducibility was a main issue in all executed Bi_2O_3 depositions. In fact four different precursor batches have been used while all above presented data was generated from experiments with only two of these batches. The results using the other two batches are inconsistent for unknown reasons and were therefore discarded. Depositions of the two 'good' batches however were reproducible as e.g. shown by the PE-ALD process with the parameters 3.5s/3s/5s/8s at 290°C : in the first deposition to generate the saturation curve a growth rate of 0.353 \AA/cycle was measured (Figure 18). Later 'upscaling' to a 4 inch wafer (Figure 19b) gave a GPC of 0.347 \AA/cycle for the center of the wafer with an overall GPC of $0.331 \pm 0.015 \text{ \AA/cycle}$.

Reproducible ALD of binary Bi_2O_3 with e.g. BiPh_3 or $\text{Bi}(\text{N}(\text{Si}(\text{Me}_3)_2)_3)$ precursors has been reported as challenging, although difficulties with $[\text{Bi}(\text{tmhd})_3]$ are hardly mentioned in literature.^{124,127} Reproducibility issues are, in fact, not uncommon for powder precursors like

[Bi(tmhd)₃]. Batch-to-batch variations in powder size and purity level are, in general, more difficult to avoid than for liquid precursors. The latter are therefore more convenient. Variations in powder size can affect the evaporation behavior, which can lead to different saturation times. The presence of impurities can lead to clustering and/or adhesion to the precursor bottle. Indeed, about 20 wt% of residue was found in 'empty' [Bi(tmhd)₃] precursor bottles. The composition and origin of this residue could not be identified. In addition to batch-to-batch variations, varying storage times until usage and/or long storage at 190°C during usage could lead to decomposition of the precursor by aging. Therefore the use of [Bi(tmhd)₃] as an ALD precursor is not recommended.

ALD of Bi₂O₃ is just the first step towards extremely thin absorber films for photoelectrochemical cells. CuBi₂O₄ is a promising candidate material for these absorbers, as indicated earlier. It should be possible to grow this material by ALD when two binary processes of Bi₂O₃ and CuO are combined, e.g. in a supercycle approach. Several reports on ALD of copper containing materials exist, often to deposit elemental copper for e.g. microelectronic applications.^{151–154} Copper is easily reduced and therefore highly potent oxidizers as O₃ are regularly used to deposit copper oxides.^{155–157} Thermal ALD processes almost exclusively rely on [(ⁿBu₃P)₂Cu(acac)] as precursor but only at temperatures below 140°C. These are therefore not compatible in a supercycle with the Bi₂O₃ process.^{158–160} However, a promising study from *Törndahl et al.* describes the growth of Cu₃N from [Cu(hfac)₂] via a copper oxide species with H₂O and subsequent conversion into the nitride by NH₃.¹⁶¹ A temperature window from 210 – 303°C, a GPC of 0.35 Å/cycle and low contamination levels would enable a supercycle deposition of CuBi₂O₄.

Unfortunately, CuO depositions suffered from extremely low growth rates, reproducibility issues, vapor pressure inconsistencies and major contaminations of carbon and fluorine. Even though a possible etching by the reaction product Hhfac could be addresses as an obstacle, process control could not be achieved. Furthermore, the use of an oxygen plasma as alternative oxidizer did not lead to improvements. Therefore investigations of CuO ALD from [Cu(hfac)₂] were discontinued. Another possibility is growth in a stacking approach, as shown for CuWO₄.⁵⁴ Since ALD of Bi₂O₃ is already struggling with reproducibility over extended amounts of time this approach was not investigated for CuBi₂O₄.

To continue the development of extremely thin metal oxide absorbers for PEC devices two options arise: 1) a change of material and 2) a change in deposition technique. Both possibilities were investigated, ALD of Mn₂V₂O₇ in chapter 4 and PLD of CuBi₂O₄ in chapter 5.

4 ALD of $\text{Mn}_2\text{V}_2\text{O}_7$

As shown above ALD of ternary oxides is not trivial. When selecting a candidate photoelectrode material it is therefore essential to consider the availability of ALD processes additionally to the potential photoelectrochemical properties. Bismuth and copper containing materials can therefore not be recommended. From the experience of co-workers two materials are in focus due to their photoelectrochemical potentials, SnWO_4 and $\text{Mn}_2\text{V}_2\text{O}_7$.^{57,162}

While ALD processes exist for binary oxides of Sn, W, Mn and V, the implementation of a ternary SnWO_4 process seems very challenging. Problems are mainly non-overlapping temperature windows, the need for ozone as oxidizer for many WO_3 ALD processes (ozone is not yet available in our system), or incomplete process documentation.^{163–169} Furthermore tin in SnWO_4 has the oxidation state of +2 whereas all reported ALD processes for Sn result in the +4 oxidation state.^{57,167,169}

Growth of vanadium oxides and manganese oxides by ALD has been reported several times in literature.^{82,170–176} The most promising processes rely on VTIP and $[\text{Mn}(\text{CpEt})_2]$ as metal sources with H_2O as co-reactant.^{171,177–182} They further have overlapping temperature windows.

Manganese vanadates only play a minor role in solar fuel research so far. Most studies on manganese vanadates focus on magnetic properties and their application as lithium storage in batteries, similar to studies on the binary components MnO and V_2O_5 .^{180,183–186} However, recently it has been found that they are potential photoabsorbers as well.^{56,187} Especially a publication by Yan *et al.* introduces $\text{Mn}_2\text{V}_2\text{O}_7$ as a suitable wide band gap absorber with a near-direct band gap of 1.8 eV and suitable band positions for solar water splitting.⁵⁶ Possible difficulties of this material are an apparent mismatch in oxidation states (Mn(II) and V(V)), a phase transition near room temperature and limited thermodynamic stability under PEC conditions. However, these challenges seem addressable and therefore $\text{Mn}_2\text{V}_2\text{O}_7$ was selected as a candidate ternary metal oxide absorber for PEC applications to be made by ALD.

4.1 Film growth

4.1.1 Binary ALD of MnO_x and VO_x

The individual binary oxide ALD processes are investigated before attempting depositions of the ternary compound. As indicated above, the precursors VTIP and $[\text{Mn}(\text{CpEt})_2]$ are used as vanadium and manganese sources, respectively. Their structures are shown in Figure 33.

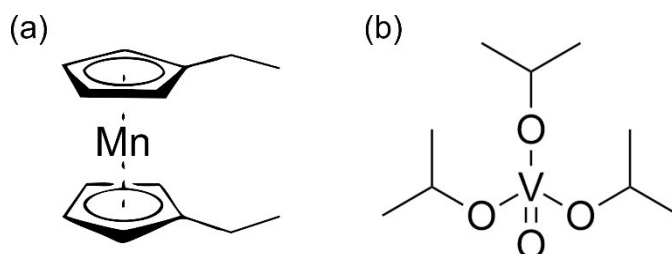


Figure 33: Chemical structure of (a) $[\text{Mn}(\text{CpEt})_2]$ or bis(ethylcyclopentadienyl)manganese(II) and (b) VTIP or vanadium(V)tri-isopropoxy oxide.

Saturation curves of the MnO_x process were recorded at 200°C substrate temperature and the results are shown in Figure 34. Saturation is achieved after 0.2 s $[\text{Mn}(\text{CpEt})_2]$ pulse with 10 s purge and 0.5 s H_2O pulse with 5 s purge. The uniformity, indicated by the error bars, was estimated from five distinct spots along the injection directions of the precursors. The error bars shorten with prolonged $[\text{Mn}(\text{CpEt})_2]$ pulse and both purge times. Therefore the pulse/purge sequence 0.5 s / 20 s / 0.5 s / 10 s (indicated by the green drop lines) was chosen for further experiments. The uniformity over a 4 inch wafer is 96.1% as shown in Figure 36a.

The 0.5 s exposure of H_2O indicates a higher reactivity of the precursor $[\text{Mn}(\text{CpEt})_2]$ compared to the $[\text{Bi}(\text{tmhd})_3]$ discussed in Chapter 3. This behavior was observed by *Burton et al.* as well and ascribed to the weak Mn-Cp bond.¹⁸⁰ They further observed an increased GPC compared to a $[\text{Mn}(\text{tmhd})_2]$ process due to the lower bulkiness of the CpEt ligand.¹⁸⁰ The GPC in the present experiments is 0.91 Å/cycle and thereby slightly below the 1.0 – 1.2 Å/cycle reported in literature.^{180–182} This is most likely due to the relatively high temperature of 200°C , which may decrease the number of available reactive surface sites (cf. Figure 6).¹⁸⁰ The slightly lower growth rate is consistent with the decline in GPC with increasing temperature that has been observed for this MnO_x ALD process.^{171,180} The employed temperature of 200°C is at the upper end of the temperature windows reported in literature. Depending on the study the lower temperature limit is between $100 - 150^\circ\text{C}$ and the higher one between $175 - 250^\circ\text{C}$.^{171,180,182} The temperature dependency was only roughly investigated in the present case and does not allow an estimation of the temperature window. We do, however, also observe a slight decrease in GPC with increasing temperature, see Figure S 4.

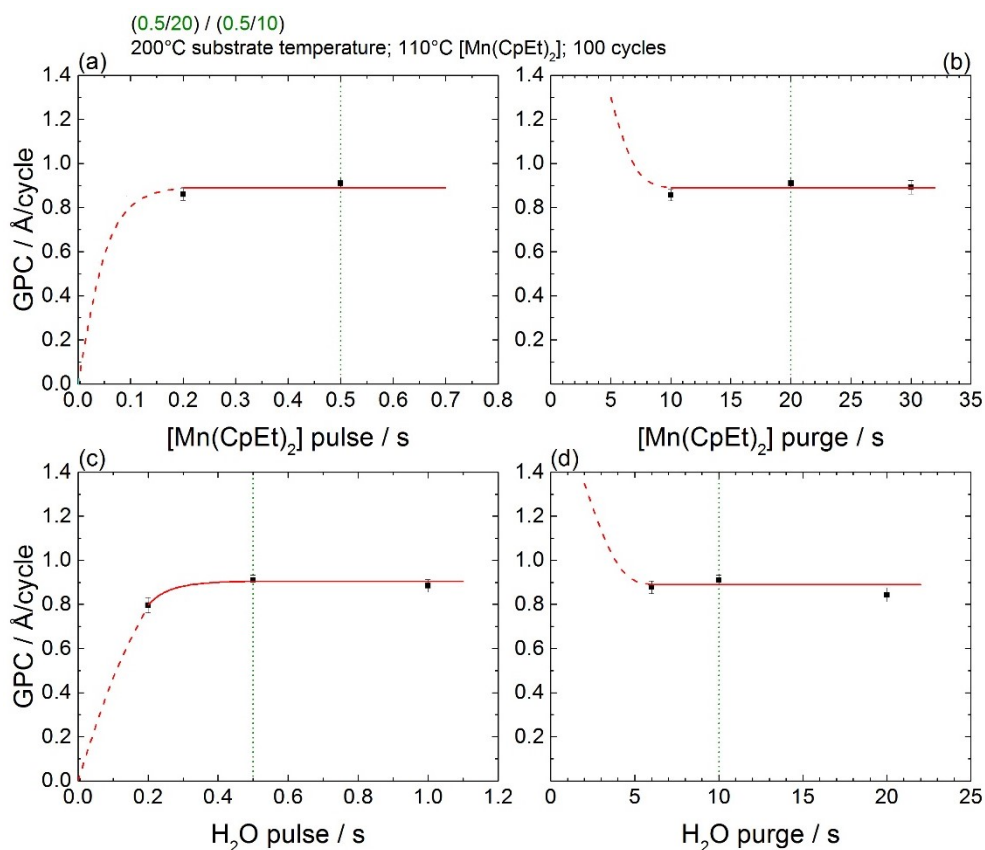


Figure 34: Growth per cycle of the MnO_x ALD process as a function of (a) the [Mn(CpEt)₂] pulse time; (b) the [Mn(CpEt)₂] purge time; (c) the H₂O pulse time and (d) the H₂O purge time; green vertical drop lines indicate saturative conditions used for future depositions; error bars indicate the spread of five spots distributed over 4 inch.

The VO_x ALD process was investigated using a study by *Musschoot et al.* as a guideline.¹⁷⁸ In there a wide temperature window from 50 – 200°C is reported with an increase of GPC with temperature. At the upper end the GPC was about 0.3 Å/cycle. Therefore the GPC of VO_x is expected to be much smaller than of MnO_x. As a consequence, VO_x ALD will be the more time demanding step in a stoichiometric deposition especially when the low molar density of vanadium in V₂O₅ compared to manganese in MnO is included (18 mmol/cm³ vs. 77 mmol/cm³). For this reason a shared deposition temperature of 200°C at the upper end of both ALD processes was chosen to accelerate VO_x deposition even if it involves a deceleration of the MnO_x process. The high temperature can furthermore accelerate reactions and reduce physisorption of the precursors, leading to reduced pulse and purge times.

The measured saturation curves are shown in Figure 35. Saturation, again with optimized uniformity, was achieved after 0.1 s VTIP pulse with 20 s purge and 2 s H₂O pulse with 10 s purge. Over a 4 inch wafer these conditions lead to a uniformity of 93.1%, as shown in Figure 36b. The relatively short H₂O purge times of 5 – 10 s also serve as an indication for the beforehand investigated thermal Bi₂O₃ ALD process. There 8 s of H₂O purge were used after a comparable extensive H₂O dose. The recorded saturation curves here suggest that 8 s purge can be enough.

The GPC is 0.25 Å/cycle and thereby in agreement with literature values between 0.2 – 0.3 Å/cycle.^{88,178} Interestingly depositions using VTIP with O₃ as oxidizer report a similar GPC of 0.27 Å/cycle suggesting that the reactivity of water is not rate limiting in this ALD process.^{87,174}

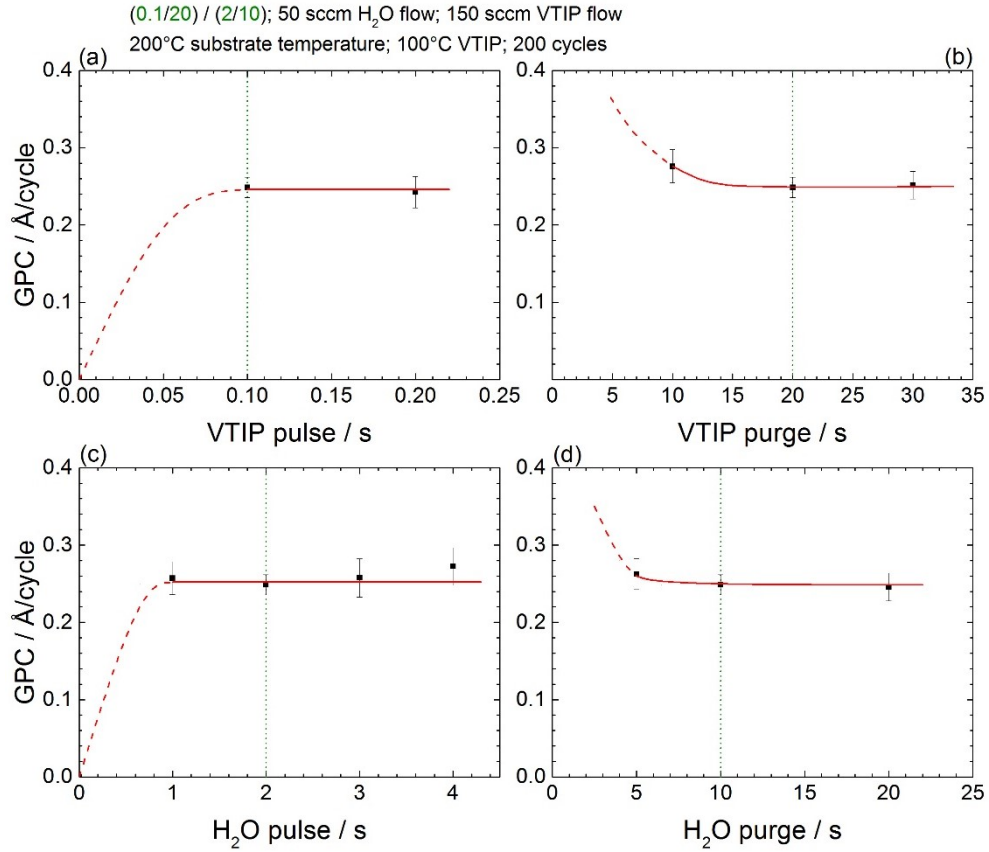


Figure 35: Growth per cycle of the VO_x ALD process as a function of (a) the VTIP pulse time; (b) the VTIP purge time; (c) the H₂O pulse time and (d) the H₂O purge time; green vertical drop lines indicate saturative conditions used for future depositions; error bars indicate the standard deviation of five spots distributed over 4 inch.

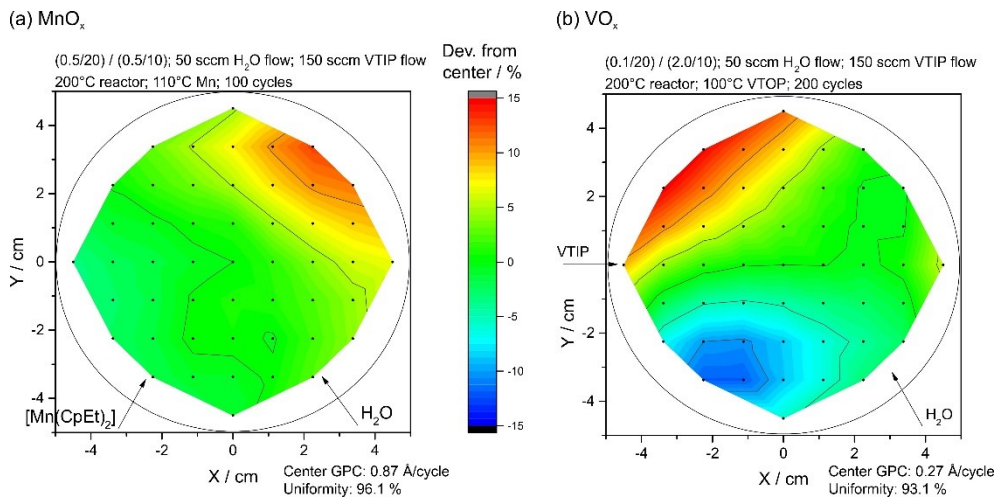


Figure 36: Thickness deviation from mean after 100 ALD cycles over a 4 inch wafer (a) MnO_x ALD, 96.1% uniformity; (b) VO_x ALD, 93.1% uniformity.

4.1.2 Ternary ALD of $\text{Mn}_x\text{V}_y\text{O}_z$

The identified conditions of the binary ALD processes were combined to supercycles without further optimization. The cycle ratio of MnO_x and VO_x ALD was calculated from their GPCs and assumed phase. The deposited films are expected to be MnO and V_2O_5 respectively which is a reasonable guess based on literature and XPS evaluations shown in 4.2.2.^{171,178,180–182} An 1:1 atomic ratio of Mn:V is expected for an ALD cycle ratio of 1:8 $\text{MnO}:\text{V}_2\text{O}_5$. This is due to the much higher atomic concentration of MnO compared to V_2O_5 and the larger GPC of the MnO ALD process. The large number of required V_2O_5 ALD cycles confirms the earlier assumption that V_2O_5 ALD will be the more time-demanding step of $\text{Mn}_2\text{V}_2\text{O}_7$ depositions. The high substrate temperature of 200°C , chosen to enhance the growth rate of V_2O_5 , is indeed beneficial in view of its slow growth.

Initial samples were grown on silicon for thin film analysis and annealing optimization. For these samples the optimization of the binary processes in terms of uniformity was not yet finished, which may cause stoichiometry fluctuations.

Another sample series, with optimized uniformity, was deposited on FTO substrates for photoelectrochemical measurements. These additionally include samples with cycle ratios of 1:7 and 1:9 to gain insight into the effect of altered stoichiometries. The film thickness of these PEC samples is about 23 nm and was chosen to limit deposition times to reasonable length.

4.2 Sample characterization

4.2.1 Crystallization into $\beta\text{-Mn}_2\text{V}_2\text{O}_7$

The crystallinity of the grown films was investigated by XRD. As-deposited films of MnO_x crystallize into cubic MnO which is in agreement with literature and indicates the desired Mn(II) oxidation state, see Figure S 5a.^{180,188} VO_x films appear amorphous after deposition, again in agreement with literature, see Figure S 5b.^{177–179}

The ternary films are predominantly amorphous without any post-deposition annealing. This is shown by the effective absence of reflections in the green line of the XRD diffractogram, shown in Figure 37. This indicates that the layer by layer growth of the ternary deposition largely inhibits the crystallization of MnO .

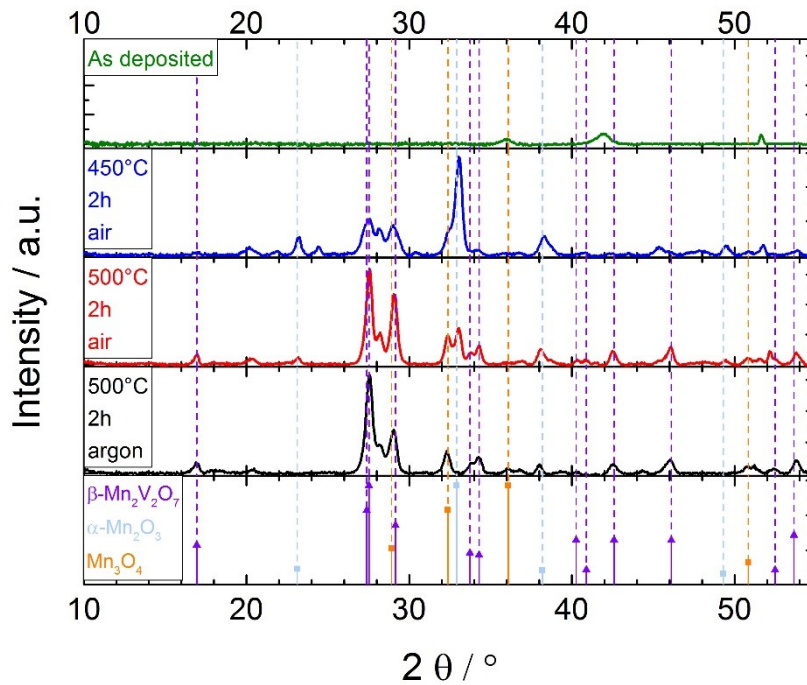


Figure 37: XRD patterns of $\text{Mn}_2\text{V}_2\text{O}_7$ on silicon substrates with varying post-deposition treatments and various reference signals.^{183,189,190}

An annealing step is needed to induce the crystallization into the desired $\beta\text{-Mn}_2\text{V}_2\text{O}_7$ phase. As shown in Figure 37, a mild annealing at 450°C for 2 hours in air (blue line) leads to a crystallization, partly into the desired phase (e.g. visible by the reflections at $\approx 28^\circ$) but other prominent signals are visible as well. The main impurity phase is identified as $\alpha\text{-Mn}_2\text{O}_3$ (e.g. 23° and 33° , light blue) but also some Mn_3O_4 appears to be present ($\approx 32^\circ$, orange).

Increasing the annealing temperature to 500°C (red line) improves the composition, visible by an increased $\beta\text{-Mn}_2\text{V}_2\text{O}_7$ (28°) and decreased $\alpha\text{-Mn}_2\text{O}_3$ reflection (23° and 33°). The Mn_3O_4 impurity seems more pronounced (32°).

While the desired $\beta\text{-Mn}_2\text{V}_2\text{O}_7$ phase contains manganese exclusively in the oxidation state +2, both impurity phases contain manganese(III). A non-oxidizing atmosphere may avoid

the +3 oxidation state. Indeed annealing in inert argon (black line) reduces the amount of impurities, the 23° and 33° α - Mn_2O_3 reflections are not visible and also the intensity of the 32° reflection of Mn_3O_4 is decreased.

Based on these results a two hour annealing in argon at 500°C was chosen as post-deposition anneal process. Even higher temperatures are avoided to exclude any possibility of impurity incorporation from FTO substrates while more reducing atmospheres (like hydrogen) could lead to undesired formations of $\text{Mn}(0)$ or vanadium with oxidation states below +5.^{191,192}

4.2.2 XPS evaluation of $\text{Mn}_2\text{V}_2\text{O}_7$

XPS is another way to investigate oxidation states in $\text{Mn}_2\text{V}_2\text{O}_7$. Both metals are known for their variety in oxidation states which range from 0 to +7 for manganese and from 0 to +5 for vanadium. The desired oxidation states are Mn(II) and V(V) . Furthermore, conclusions on the stoichiometry and carbon contaminations can be drawn when the O 1s and C 1s regions are taken into account. The fitting of each region is described first whereas the results are summarized at the end of this section.

Mn 2p region

Evaluating Mn 2p patterns is not trivial due to peak asymmetries, complex multiplet splitting, shake-up and plasmon loss structures, and uncertain, overlapping binding energies.^{193,194} Here a routine published by *Biesinger et al.* is employed.¹⁹³ Therein the entire Mn $2p_{3/2}$ region is fitted by one set of highly constrained peaks. Based on previous reports on manganese oxide ALD only the oxidation states +2, +3 and +4 are expected in the employed conditions.^{82,181} Example spectra and fits to the +2 and +3 oxidation state are shown in Figure 38, of the +4 oxidation state in Figure S 6.

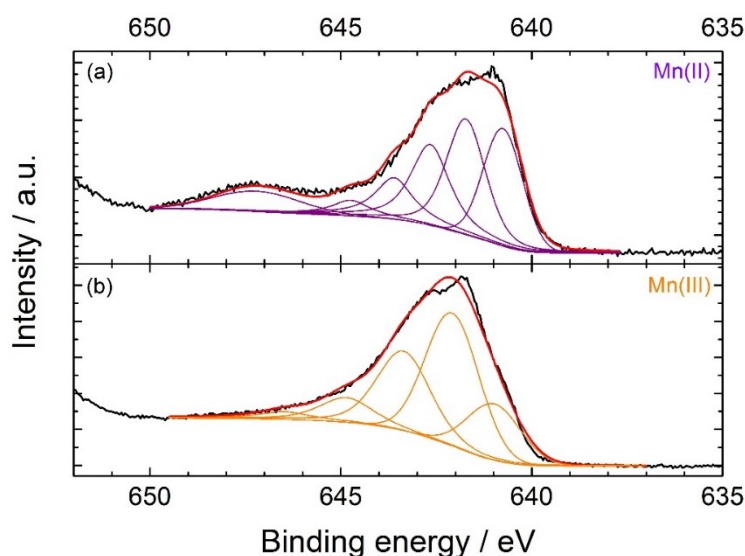


Figure 38: XPS measurements of the Mn $2p_{3/2}$ region fitted with different routines from *Biesinger et al.*¹⁹³, (a) Mn(II) fit in purple of an as-deposited $\text{Mn}_2\text{V}_2\text{O}_7$ film, (b) Mn(III) fit in orange of an $\text{Mn}_2\text{V}_2\text{O}_7$ film annealed in air, raw data in black, peak sum in red.

The top spectrum was recorded from a $\text{Mn}_2\text{V}_2\text{O}_7$ film without post-treatment. Although not perfect, the peak pattern that corresponds to the Mn(II) state (purple) gives a good fit. It consists of six features with a broad peak at about 647.5 eV as a characteristic feature, which originates from a shake-up process.¹⁹³

The bottom spectrum shows the XPS data for a $\text{Mn}_2\text{V}_2\text{O}_7$ sample annealed in air accompanied by a Mn(III) fit (orange). The fitting with five features with increased FWHMs does not exhibit a strong distinctive feature. As expected for a higher oxidation state the maximum intensity is located at a slightly higher binding energy.

The fitting routine for the Mn(IV) state was applied to all samples as well but in none of the cases this routine gave a reasonable fit. The features of the Mn(IV) fit are located at higher binding energies and therefore only give very weak overlaps with the measured data. An example of such a fit is shown in Figure S 6.

V 2p and O 1s region

The vanadium 2p and oxygen 1s region are in close proximity to each other. Therefore literature suggests a simultaneous fitting with a shared Shirley background for best results.^{194–196} Furthermore, literature relies on the main oxygen feature set to 530 eV as reference for the binding energy.^{194–196} From this the peak positions of the different vanadium oxidation states are well defined.^{194,196} Only the oxidation states +5 and +4 are expected in the grown films.¹⁷⁸ An example of the fit of both regions is shown in Figure 39.

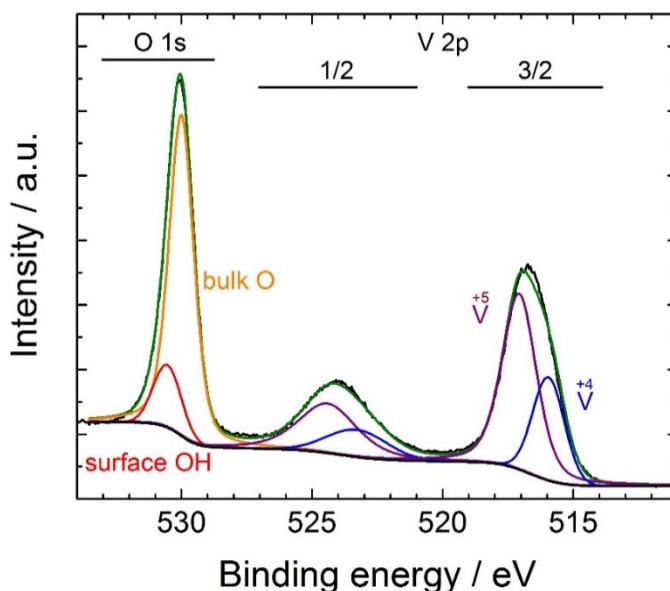


Figure 39: Typical XPS fine spectrum of the O 1s and V 2p region from an as-deposited vanadium oxide sample; raw data and shared Shirley background in black, bulk oxygen (set to 530 eV) in orange, surface hydroxyl groups in red, V(V) in purple, V(IV) in blue, peak sum in green.

Two peaks are needed for a sufficient fit of the O 1s region: a main feature assigned to bulk oxygen in the film (orange) and another feature originating from a hydroxyl surface layer (red) at slightly higher binding energies as it was already seen for the Bi_2O_3 . The vanadium 2p region is divided into 1/2 and 3/2 peaks with a fixed spin-orbit-splitting of 7.33 eV and an area ratio of

2:1.¹⁰⁹ The two features of V(V) (purple) and V(IV) (blue) can be clearly seen with a larger share of the +5 oxidation state. The 1/2 peaks exhibit an increased FWHM which has been observed before and ascribed to the Coster-Kronig effect, which is further described in literature.¹⁹⁴

C 1s region

The carbon 1s region was fitted similar to the routine of Bi₂O₃ samples in section 3.3.1. The use of adventitious carbon at 284.8 eV as reference binding energy is logically not valid for the O 1s and V 2p region, although differences are minimal. An example of the fit is shown in Figure 40. The feature at 288.5 eV is ascribed to remains of the precursor and is used to calculate the carbon content.

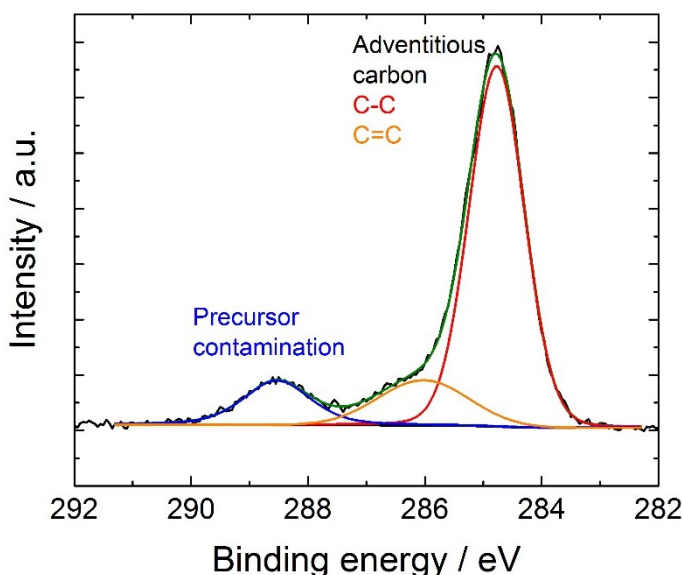


Figure 40: C 1s spectrum (black) with adventitious carbon features (red and orange) and precursor contamination feature (blue); peak sum in green.

Fitting results

The pure manganese oxide film without any post-deposition treatment exhibit manganese in the +2 oxidation state as the MSE of the corresponding fit is much lower than for the Mn(III) and Mn(IV) fit (1.9 vs. 35.5 and 104.4 respectively). This +2 is the desired oxidation state and in agreement with literature.^{171,180–182} Furthermore, a bulk stoichiometry of MnO_{1.10} (i.e. the stoichiometry calculated from the Mn 2p fit and the bulk O peak of the O 1s fit) supports the +2 oxidation state. The amount of carbon impurities is calculated to 2.44 at. %.

The pure vanadium oxide (without post-deposition treatment) contains V(IV) and V(V), as can be seen from the data in Figure 39. The ratio of the +5 : +4 oxidation state is 69% : 31% and therefore the V appears to be predominantly in the desired +5 state. The bulk stoichiometry is calculated to be V₂O_{3.89}, showing an oxygen deficiency. One reason could be that no distinctive surface vanadium state (e.g. V-OH) is resolved in the V 2p region which leads to an

apparent bulk oxygen deficiency. Almost no carbon was detected leading to an exceptional low carbon content of 0.24 at.%. This again shows that H₂O is a very suitable co-reactant in combination with VTIP.

The evaluation of the manganese vanadate films is not always conclusive. The different annealing processes lead to the following results. The calculated bulk stoichiometry is Mn₂V_{1.37}O_{3.93} without annealing (with the manganese count fixed to 2). Obviously the film is thereby oxygen deficient and it cannot be traced whether the MnO or the V₂O₅ part accounts for this. Also the amount of vanadium is below the theoretical value. A possible reason could be the initially suboptimal uniformity of the VO_x ALD process. However, the oxidation state ratio of vanadium is similar to the binary film (71% : 29% ratio of V(V) : V(IV)) and also the Mn 2p fitting suggest Mn(II) as dominant species (cf. Figure 38a). This means that the processes are in principle compatible. The carbon content is 8.74 at.% and thereby much higher than in the binary depositions. This indicates that some surface effect occurs that leads to insufficient oxidation or impurity incorporation.

XRD showed that annealing in air (500°C for 2 h) led to crystallization into Mn₂V₂O₇ with some impurities of Mn(III). This observation is confirmed by XPS. Although the Mn(II) gives a reasonable fit (MSE = 2.0), the Mn(III) fit resembles the data a little more accurate (MSE = 1.9). A direct comparison of both fits is given in Figure S 7. Especially the loss of the shake-up peak at 647.5 eV in the Mn(III) fit suggest that the majority of manganese is converted into Mn(III). The conversion into Mn(III) is more pronounced in the surface sensitive XPS measurement compared to the bulk sensitive XRD. This hints towards an enrichment of Mn(III) at the surface, which is reasonable as this surface is directly exposed to the oxidizing annealing atmosphere. Furthermore the annealing in air shifts the bulk stoichiometry to Mn₂V_{0.41}O_{4.48}, showing a significant loss of vanadium. Such a loss of vanadium by annealing in air has been observed before in BiVO₄ and may happen here as well.¹⁹⁷ The remaining vanadium consists to 93% of V(V) and only 7% V(IV). Whether the increase of V(V) fraction originates from oxidation or from preferential evaporation of V(IV) is uncertain. Furthermore the amount of carbon decreases to 1.42 at.%.

Annealing in an inert argon atmosphere leads to comparable results with 1.62 at.% carbon, a bulk stoichiometry of Mn₂V_{0.34}O_{4.21} and 87% : 13% V(V) : V(IV) ratio. But contrary to annealing in air the Mn(II) oxidation state is maintained by annealing in argon. Again in agreement with the XRD results. However, the metal oxidation states are in disagreement with the identified stoichiometry. The reason for this mismatch is unknown.

As mentioned above three sample batches with varying cycle ratios were produced on FTO substrates and subsequently annealed at 500°C for 2 h in argon. All samples were investigated by XPS leading to the following results:

Table 4: XPS evaluation of $\text{Mn}_2\text{V}_2\text{O}_7$ samples for photoelectrochemistry.

Cycle ratio Mn : V	1 : 7	1 : 8	1 : 9
As deposited			
Dominant Mn oxidation state	Mn(II)	Mn(II)	Mn(II)
V(V) : V(IV) ratio	89% : 11%	89% : 11%	89% : 11%
Bulk stoichiometry	$\text{Mn}_2\text{V}_{2.41}\text{O}_{7.38}$	$\text{Mn}_2\text{V}_{2.47}\text{O}_{7.64}$	$\text{Mn}_2\text{V}_{2.85}\text{O}_{8.91}$
Carbon content	9.26 at. %	9.39 at. %	6.56 at. %
After annealing			
Dominant Mn oxidation state	Mn(II)	Mn(II)	Mn(II)
V(V) : V(IV) ratio	94% : 6%	94% : 6%	94% : 6%
Bulk stoichiometry	$\text{Mn}_2\text{V}_{2.06}\text{O}_{7.12}$	$\text{Mn}_2\text{V}_{3.40}\text{O}_{10.06}$	$\text{Mn}_2\text{V}_{3.24}\text{O}_{9.66}$
Carbon content	5.52 at. %	3.44 at. %	3.48 at. %

All as deposited samples consist mainly of Mn(II) and V(V), indicating very reproducible depositions. Furthermore, they all have a slight excess of vanadium which increases with the vanadium oxide cycle ratio. The significant stoichiometry shift compared to the previously discussed samples may be explained by an improved uniformity of the ALD processes. The oxygen content increases with the increased vanadium content which is in agreement with the higher oxidation state of vanadium compared to manganese. The opposite is observed for the carbon content: an increase in vanadium content decreases the carbon content which is in agreement with the observations of the binary processes.

The annealing process does not have the same effect on all samples. Whereas the oxidation states of manganese and vanadium stay similar the stoichiometry develops in different ways. The 1:7 sample apparently loses some vanadium and oxygen, as well as small amounts of carbon. The final stoichiometry of $\text{Mn}_2\text{V}_{2.06}\text{O}_{7.12}$ is very close to the desired $\text{Mn}_2\text{V}_2\text{O}_7$. Contrary to that the other two samples seem to lose manganese and larger amounts of carbon. The low levels of carbon contamination are beneficial but the vanadium rich stoichiometries may be a disadvantage. Possible reasons for the different behaviors during the annealing step are unclear. Slight experiment to experiment variations, e.g. in argon flow rate during the annealing could introduce some variations. Furthermore microscopic sample damages, e.g. from physical contact, cannot be excluded. Also sample to sample variations of the thin films itself may occur, e.g. due to aging of the ALD precursors.

4.2.3 Further techniques

Mass-spectrometric analysis

To get some insight into the processes during annealing a $\text{Mn}_2\text{V}_2\text{O}_7$ powder sample was heated in an argon flow, mimicking the annealing conditions, while the gas phase was analyzed by mass spectrometry (MS). Contrary to an ALD thin film a powder sample supplies enough material to detect possible volatile compounds. So even though a powder may behave slightly different than a thin film it is a viable source of information.

A stepwise temperature profile was employed with the routine $500^\circ\text{C} - 700^\circ\text{C} - 600^\circ\text{C} - 800^\circ\text{C}$ with $10^\circ\text{C}/\text{min}$ heating rate and 2 h at each temperature, as shown in Figure 41. Volatile species are already detected at 500°C , the annealing temperature discussed earlier. These are Mn^+ (dark blue) and MnO^+ (blue), as well as to V^+ (dark red), VO^+ (red) and VO_2^+ (orange). All these signals nicely follow the temperature profile and show that more manganese species are evaporating compared to the vanadium species. Contrary to that, no MnO_2^+ could be detected at any temperature, indicating that manganese is predominantly in the +2 oxidation state in the used powder.

These findings partially explain the XPS results before and after annealing. Both metals can evaporate and thereby alter the stoichiometry of the film. However, sample to sample deviations in evaporation rate apparently occur.

The strong increase of ion currents at temperatures above 500°C clearly suggest that higher annealing temperatures should not be employed to avoid even stronger stoichiometry alterations.

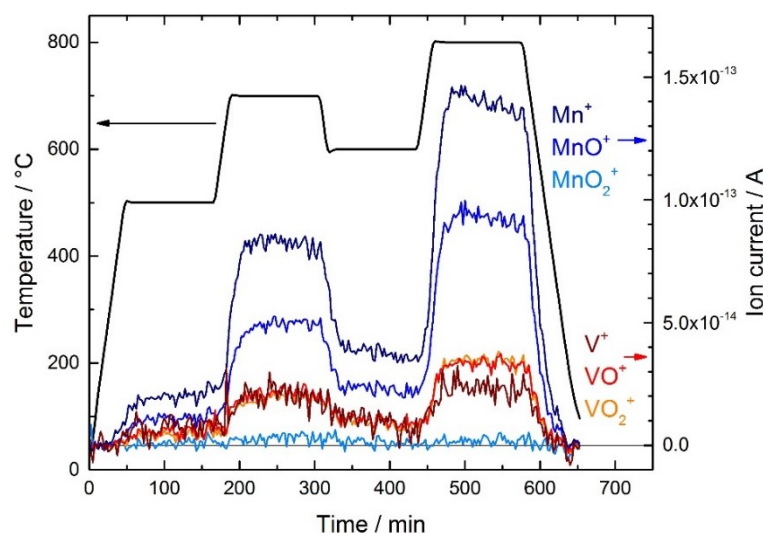


Figure 41: Mass spectrometry analysis of $\text{Mn}_2\text{V}_2\text{O}_7$ powder in argon. Temperature–time curve during the MS analysis (black) and ion currents for mass-to-charge ratios (m/q) of 51, 55, 67, 71, 83 and 87, assigned to V^+ (dark red), Mn^+ (dark blue), VO^+ (red), MnO^+ (blue), VO_2^+ (orange), and MnO_2^+ (light blue), respectively.

UV/Vis spectroscopy

The optical properties of the thin films were evaluated by UV/Vis measurements. All of the investigated samples were grown on FTO substrates absorbing in the UV-range as well. Therefore a background subtraction was employed as shown in Figure S 8b.

Figure 42a shows the absorption coefficient α of the 1:9 cycle ratio $\text{Mn}_2\text{V}_2\text{O}_7$ film in dependence of the wavelength. The difference in α of the 1:7 and 1:8 samples is negligible, as shown in Figure S 8a. The absorption starts to increase at wavelength below 670 nm, indicating the bandgap. Starting from 500 nm an increasing contribution of the FTO substrate is visible (compare also Figure S 8b), especially accounting for the sharp decrease below 350 nm. Tauc plots were generated to determine the bandgap more accurately as shown in the inset of Figure 42a and Figure S 8c. They reveal an indirect bandgap at 1.83 eV, corresponding to 677 nm, and a direct bandgap at 1.90 eV, which is consistent with literature.⁵⁶

The absorption coefficients are used to calculate the absorbed fraction of the incident AM 1.5 spectrum. This gives a theoretical upper photocurrent density j_{max} as shown in Figure 42b. Below bandgap absorptions do not originate from valence band – conduction band excitations and the generation of mobile charge carriers. They are usually assigned to excitations from/to defect states in the bandgap. However, they still account for absorption coefficients around $2.5 \times 10^5 \text{ cm}^{-1}$. Therefore, the absorption coefficients were reduced by this value in the theoretical absorption estimation in Figure 42b. The inset of the graph shows the integrated photon flux expressed in mA/cm^2 . This absorbed photon flux gives an upper limit for the photocurrent density, assuming that each absorbed photon generates one electron-hole pair which is extracted as a current without losses. Even the extremely thin films grown in this study (23 nm) show significant absorption resulting in a maximum photocurrent density of about 3 mA/cm^2 . This photocurrent can be significantly improved when the earlier discussed high-aspect ratio nanostructures are employed. For example a structure depth of 300 nm could in principle facilitate a photocurrent density of almost 14 mA/cm^2 . The overall upper limit of the photocurrent density is 18.8 mA/cm^2 when all photons above the bandgap are absorbed and contribute to the photocurrent.

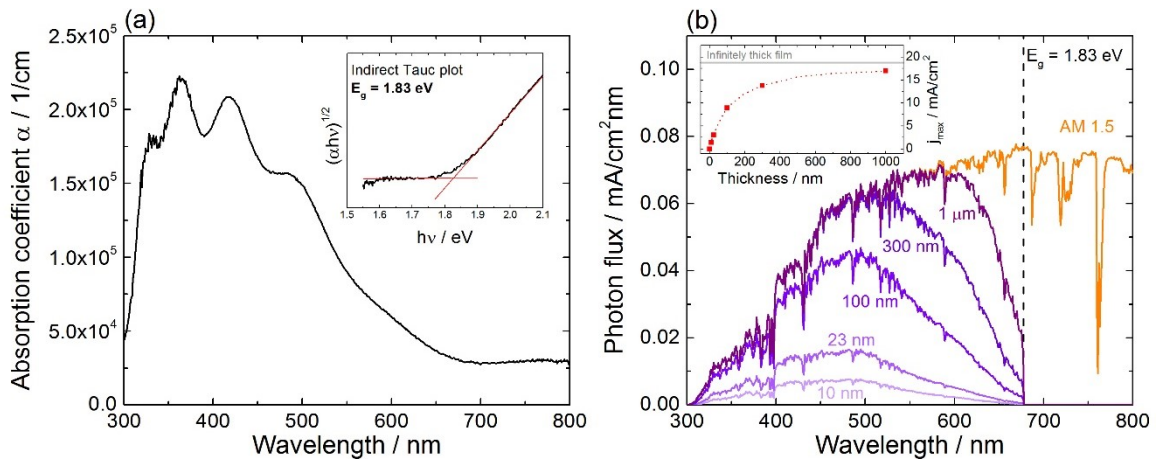


Figure 42: (a) Absorption coefficient α and indirect Tauc plot (inset) of $\text{Mn}_2\text{V}_2\text{O}_7$; (b) Estimated VB-CB absorption of the AM 1.5 spectrum by $\text{Mn}_2\text{V}_2\text{O}_7$ thin films and the maximal photocurrent density j_{max} (inset).

4.3 MnO_x sacrificial layer

Manganese oxides are known for their ability to change oxidation states easily.^{181,182,198} This may motivate catalyst applications but can introduce difficulties in Mn₂V₂O₇ thin films. As mentioned before this ternary oxide requires a manganese oxidation state of +2: XRD and XPS results have shown that even a partial oxidation into the +3 state can lead to phase segregation with significant amounts of Mn₂O₃.

The oxidation into the undesired +3 (or higher) state can also occur electrochemically when the Mn₂V₂O₇ thin film is immersed in the electrolyte as a (photo-)anode under OER conditions.^{181,182} This was investigated by cyclic voltammetry (CV) in the range of the OER in the dark. The results are shown in Figure 43.

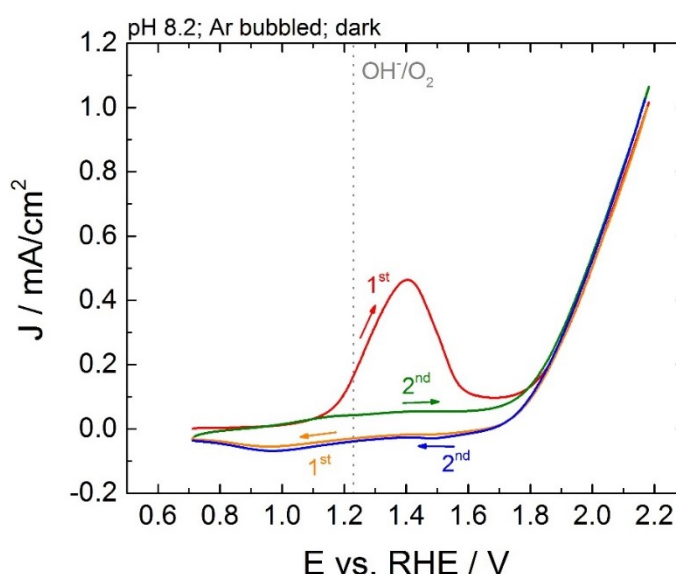


Figure 43: Cyclic voltammetry of Mn₂V₂O₇ on FTO in a borate buffered electrolyte at pH 8.2; the grey dashed line indicates the thermodynamic redox potential of the OER at 1.23 V vs. RHE.

One can clearly see the onset of the oxygen evolution at the right hand side at about 1.8 V vs. RHE. This corresponds to an overpotential η of about 0.6 V which is a typical value for manganese oxides.¹⁷¹ A prominent oxidation feature is located at 1.4 V vs. RHE before the OER starts. This large oxidation peak is only present in the first cycle, indicating an initial oxidation of the film. Similar features have been observed on pure manganese oxide films, although at slightly lower potentials of 1.0 – 1.1 V vs. RHE.¹⁷¹ Nevertheless this feature is assigned to oxidation of Mn(II) as the only oxidable species, apart from impurities. The shift towards higher potentials may be explained by an increased stability of Mn(II) in Mn₂V₂O₇ compared to MnO.

The transferred charge and thereby the amount of oxidized manganese can be calculated from the oxidation peak area, as described in the appendix. The peak in Figure 43 corresponds the oxidation of 3.87 nm of MnO or 12.24 nm of Mn₂V₂O₇. This means that more than 50% of the present manganese is oxidized in relation to the Mn₂V₂O₇ film thickness of ca. 23 nm. On one hand this validates the assignment as the oxidation of manganese (as no other oxidable

species are present in these amounts e.g. V(IV) or carbon impurities) but rises the issue of film stability. It seems unlikely that $\text{Mn}_2\text{V}_2\text{O}_7$ stays intact with only a minor fraction of Mn(II) remaining.

Interestingly XRD still shows the desired $\text{Mn}_2\text{V}_2\text{O}_7$ phase, see Figure S 9, although overall intensities are low and a contribution of material outside of the exposed area cannot be excluded. Also XPS measurements do not show an oxidation of manganese. The Mn(II) fit still gives the by far best fit, see Figure S 10. The apparent mismatch of film oxidation (in CV) and the inability to identify oxidized manganese in the film (by XPS) leads to the assumption that the oxidized species are not present in the film anymore. They rather dissolved in the electrolyte or have been reduced back to Mn(II) in the UHV chamber of the XPS setup. The first assumption of dissolution can be supported by XPS measurements of the Sn 3d region. Tin is the main component of the FTO substrate and should only be traceable by XPS if the $\text{Mn}_2\text{V}_2\text{O}_7$ top layer is very thin (< 10 nm). Indeed no tin signal is detected from a $\text{Mn}_2\text{V}_2\text{O}_7$ sample without any post-treatment, see Figure S 11. After annealing minor amounts of tin are seen as the film has lost some of its mass (see Mass-spectrometric analysis above) and maybe has undergone some roughening due to the crystallization. However, after electrochemistry the tin signal becomes significant, supporting the theory of electrochemical dissolution of $\text{Mn}_2\text{V}_2\text{O}_7$.

One approach to avoid such a desintegration of the film is the addition of a sacrificial layer of MnO, acting as protection and catalyst layer. This MnO is oxidized and partially dissolved, while the underlying $\text{Mn}_2\text{V}_2\text{O}_7$ should stay untouched. *Plate* examined the minimum thickness of ALD-grown MnO that is required to act as a stable OER catalyst and identified a thickness of 4 nm.¹⁷¹ This nicely lines up with the observed oxidized thickness of 3.87 nm in the present study. Therefore 4 nm MnO were deposited on top of the annealed $\text{Mn}_2\text{V}_2\text{O}_7$ film by ALD as sacrificial layer, using the binary MnO ALD process described in section 4.1.1. The electrode preparation is illustrated in Figure 44.

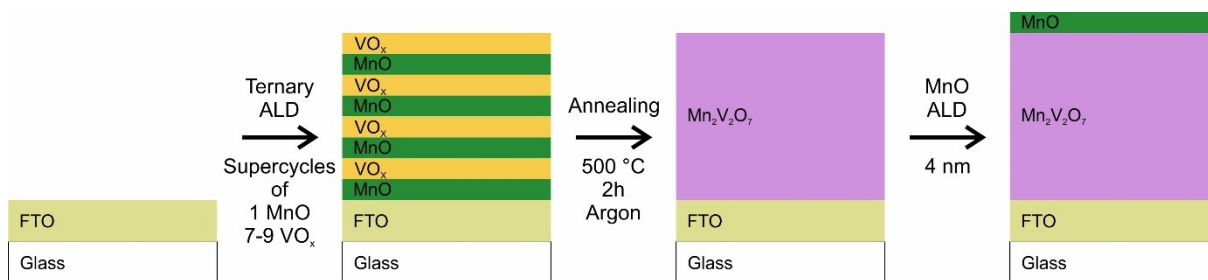


Figure 44: Schematic representation of the preparation of $\text{Mn}_2\text{V}_2\text{O}_7$ electrodes.

4.4 Photoelectrochemical film performance

The PEC performance of the samples was evaluated by chopped light measurements in three different electrolytes. The first electrolyte has near neutral pH adjusted with a borate buffer (similar to the conditions in 4.3 and used by *Plate*¹⁷¹) and sulfite as hole scavenger to avoid kinetic limitations of the OER. The second electrolyte consists of the same buffer but ferro-/ferricyanide as hole scavenger. Finally, the conditions of *Yan et al.* are used with pH 13 and ferro-/ferricyanide as hole scavenger.⁵⁶ All measurements were executed under front side illumination.

Figure 45 shows typical cyclic voltammetry (CV) and chronoamperometry (CA) plots of measurements in the first electrolyte. The CV shows an onset for light and dark current at about 0.9 V vs. RHE, which is a typical value.⁵⁵ Unfortunately the light current density is only marginally larger than the dark current density. This and the almost simultaneous onset of both indicates a rather weak photovoltage and -current.

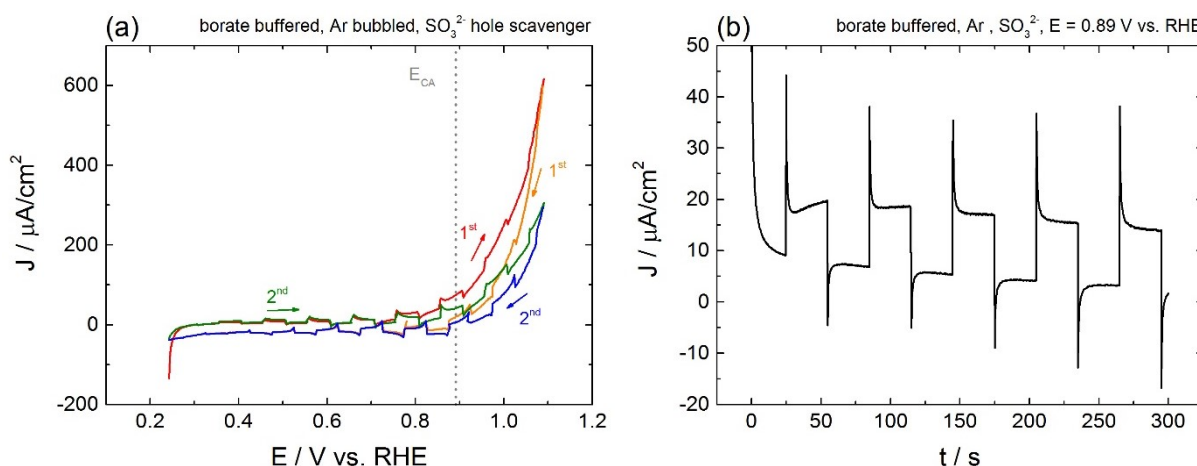


Figure 45: Chopped light photoelectrochemical measurements of $\text{Mn}_2\text{V}_2\text{O}_7$ in a borate buffer (pH 9.2) with sulfite hole scavenger: (a) Cyclic voltammetry; (b) Chronoamperometry at 0.89 V vs. RHE.

Indeed the current densities are so low that a possible contribution of the FTO substrate has to be considered. To exclude this substrate contribution the present measurement is compared to the photoresponse of an FTO substrate with only the MnO sacrificial layer in Figure S 12. It clearly shows that such a contribution does not exist and the photoresponse indeed originates from the $\text{Mn}_2\text{V}_2\text{O}_7$ ALD film.

A subsequent chronoamperometry measurement was executed at $E_{\text{CA}} = 0.89 \text{ V vs. RHE}$, the dark current onset, to quantify the photocurrent density. This measurement was done with a decreased chopping frequency as shown in Figure 45b. A clear photocurrent is visible but it is very small. The contribution of the dark current should therefore be considered. Hence the measured photocurrent densities will be expressed as $\Delta J = J_{\text{light}} - J_{\text{dark}}$.

There are significant spikes in current density when the shutter is opened and closed. Such transients usually indicate a limitation of the charge injection into the electrolyte i.e. the oxidation of SO_3^{2-} in this study.⁶⁰

Similar CA measurements were performed using the other two electrolytes and examples are shown in Figure S 13 and Figure S 14. The results of the measurements for the three different samples (1:7, 1:8 and 1:9 cycle ratio) are summarized in Figure 46.

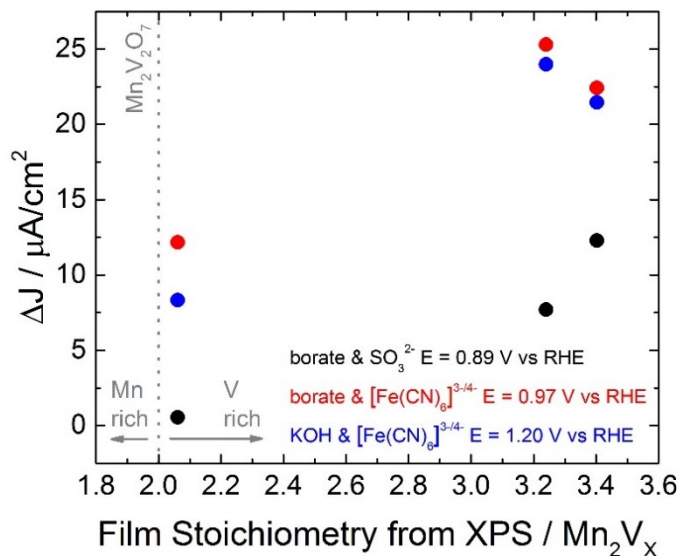


Figure 46: Measured photocurrent densities ΔJ in dependence of the manganese to vanadium ratio of the samples in the three different electrolytes: borate buffered (pH 9.2) and sulfite scavenger (black), borate buffered (pH 9.2) and $[\text{Fe}(\text{CN})_6]^{3-/4-}$ scavenger (red), and 0.1M KOH (pH 13) and $[\text{Fe}(\text{CN})_6]^{3-/4-}$ scavenger (blue).

All measured current densities are very low, the largest value barely exceeds $25 \mu\text{A}/\text{cm}^2$. The current densities employing sulfite as scavenger (black) are significantly lower than the ones using ferro-/ferricyanide. This and the transients mentioned above indicate that sulfite is not a suitable hole scavenger in the present case. Not all available charges carriers contribute to the sulfite oxidation and thereby to the measured photocurrent.

The pH on the other hand does not affect the photocurrent density significantly. The measured photocurrent densities barely differ between pH 9.2 (red) and 13 (blue). One reason to prefer the borate buffer could be the milder conditions possibly leading to an increased stability of the film.

Finally, the influence of the stoichiometry on the measured photocurrent density is considered. The two samples with an excess of vanadium show larger photocurrent densities. The difference in current density between those is rather low. Interestingly the sample with the almost ideal stoichiometry $\text{Mn}_2\text{V}_{2.06}\text{O}_{7.12}$ gives the lowest photocurrent density.

The reason for this counterintuitive behavior cannot be fully resolved. The higher carbon content (5.52 at.% compared to 3.44 and 3.48 at.%) could increase the number of defects in the film facilitating recombinations. Or the other way around an increase in vanadium and/or

oxygen content could reduce the amount of defects like oxygen vacancies, increasing the overall conductivity.

However, all measured current densities are extremely low compared to the absorbed photon flux of 3 mA/cm² leading to overall absorbed-photon-to-current efficiency (APCE) of less than 1%. The investigations of *Yan et al.* showed larger current densities of about 100 μ A/cm², even though they do not report a film thickness.⁵⁶ Publications on other ALD-grown photoabsorbers report photocurrent densities of 90 – 1200 μ A/cm² indicating that ALD is in principle suited to deposit photoabsorbers.^{54,88,89} Maybe this is not the case for Mn₂V₂O₇.

Moreover it is possible that Mn₂V₂O₇ is an intrinsically bad material for PEC applications. The absorbed photon flux could facilitate 3 mA/cm² and the scavenger inhibits kinetic limitations, but still very few charge carriers contribute to the photocurrent. Therefore major losses have to occur during the charge transport within Mn₂V₂O₇ i.e. the photogenerated carriers are unable to reach the Mn₂V₂O₇ interfaces. Time-resolved microwave conductivity (TRMC) is a suitable technique to investigate these charge carrier dynamics. Unfortunately this technique requires stronger microwave absorption than the ALD samples provide to achieve signals above the noise level. To still get a principle idea of the charge carrier dynamics TRMC measurements of PLD grown Mn₂V₂O₇ films were evaluated.¹⁶² These were deposited and investigated in a separate project. A more detailed look on TRMC measurements is given in 2.2.3 and 5.1.5.

The measurement in Figure 47 shows a very weak signal. Despite the poor signal to noise ratio, an exponential decay of the photoconductivity could be fitted to identify the peak photoconductivity $\sigma\mu_{\max} = 3.8 \cdot 10^{-6}$ cm²/Vs and the TRMC decay time $\tau = 111$ ns. Combined they account for a charge carrier diffusion length of 1.0 nm. This diffusion length is very low even on metal oxide scale with values in the range of 2 – 200 nm.⁵⁷ Such a short diffusion length, mainly caused by the exceptionally low peak photoconductivity, explains the low photocurrent densities. Only a small fraction of the excited charge carriers can reach the Mn₂V₂O₇ interfaces and thereby contribute to the photocurrent. Especially the low peak photoconductivity characterizes the PLD-Mn₂V₂O₇ as a poor photoabsorber as well. While charge carrier diffusion length in the range of 10 – 100 nm could be compensated by nanostructures it becomes increasingly difficult with extremely thin layers e.g. in terms of suitable nanostructures.

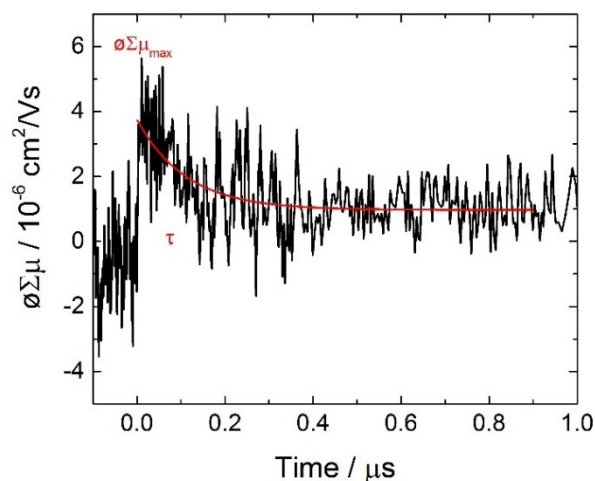


Figure 47: TRMC measurement on $\text{Mn}_2\text{V}_2\text{O}_7$ grown by PLD measured at 6.50×10^{14} photon/pulse $\cdot\text{cm}^2$ and 410 nm excitation irradiation.

When only 1.0 nm are considered the absorbed photons could facilitate a photocurrent density of about $150 \mu\text{A}/\text{cm}^2$. Factors further lowering this current density can be a weak charge separation, trapping of charge carriers at the $\text{Mn}_2\text{V}_2\text{O}_7$ -MnO or $\text{Mn}_2\text{V}_2\text{O}_7$ -FTO interface and tunneling of charge carriers throughout the thin film to recombine.

Furthermore the stability of the films still is an issue as Figure 48, a photograph of the investigated samples after the discussed PEC measurements, illustrates. The brighter cycles clearly show the area exposed to the electrolyte during the measurements with at least parts of the $\text{Mn}_2\text{V}_2\text{O}_7$ film dissolved. However, it cannot be distinguished which measurement contributed to the dissolution to which extent. The Pourbaix diagram in Figure S 15 suggests that especially the pH 13 electrolyte will dissolve the $\text{Mn}_2\text{V}_2\text{O}_7$ film.⁵⁶ Apparently even the specifically introduced MnO sacrificial layer does not adequately stabilize the $\text{Mn}_2\text{V}_2\text{O}_7$ thin film.



Figure 48: Photograph of $\text{Mn}_2\text{V}_2\text{O}_7$ samples after PEC measurements, from left to right: 9:1, 8:1, 7:1 cycle ratio.

4.5 Conclusion and outlook

Thermal binary ALD processes of MnO and VO_x were adapted starting from Mn(CpEt)₂ and VTIP, respectively. The individual binary materials could be deposited at a shared temperature of 200°C with the following precursor pulse/ purge/ H₂O pulse/ purge sequences: 0.5 s/ 20 s/ 0.5 s/ 10 s give a GPC of 0.91 Å/cycle of MnO with a uniformity of 96.1% over 4 inch; 0.1 s/ 20 s/ 2 s/ 10 s give 0.25 Å/cycle of VO_x with a uniformity of 93.1%.

These two binary processes are combined in a ternary supercycle ALD process to deposit Mn₂V₂O₇. By a change in cycle ratio the stoichiometry of the resulting film can be adjusted. Annealing for two hours at 500°C in argon leads to a crystallization into the desired β-Mn₂V₂O₇, although no phase purity is achieved. XPS measurements prove that the desired Mn(II) and V(V) state are the main species and that an almost-stoichiometric composition of Mn₂V_{2.06}O_{7.12} is achieved.

UV/Vis spectroscopy reveals an indirect bandgap of 1.83 eV which corresponds to a maximum photocurrent density of 18.8 mA/cm². The present ultra-thin films absorb enough light to theoretically generate a photocurrent density of up to 3 mA/cm².

Surface oxidation under OER conditions was observed. To avoid any influence on the Mn₂V₂O₇ absorber a sacrificial layer of 4 nm MnO is introduced to enhance the stability.

Despite all these promising initial results the measured photocurrent densities do not exceed 25.3 μA/cm², corresponding to an overall APCE of <1%. TRMC measurements on a different set of Mn₂V₂O₇ samples suggest that an exceptionally low photoconductivity of the material limits the photoactivity. Investigations on high-purity Mn₂V₂O₇ samples (e.g. a single crystal) could reveal if the weak PEC performance is an intrinsic property or if e.g. a possibly low defect tolerance of Mn₂V₂O₇ limits the performance of the present samples.

In summary, a novel ternary ALD process to deposit Mn₂V₂O₇ was established and the photoactivity of the resulting thin films has been proven. Aside from this minimal goal some options for further investigations are still open.

The temperature windows of both binary processes have barely been analyzed: A change in temperature could also affect the metal oxidation states and the amount of impurities additionally to influences on the GPCs. A deeper insight into the nucleation behavior of both processes, e.g. by real-time SE, could enable more accurate stoichiometry control of the ternary process. The use of a more potent oxidizer like O₃ in the VO_x ALD process could push to an even larger fraction of V(V) in the film. The annealing procedure could be further optimized e.g. by saturation of the atmosphere with vanadium and manganese to avoid material losses in the film. As another possible improvement, a different type of protection layer could be employed, such as TiO₂.¹⁹⁹

New samples deposited with optimized conditions could improve the PEC activity and also TRMC measurements would be possible from thicker ALD-grown films. However, the weak existing results do not justify further investigation of this Mn₂V₂O₇ as a photoabsorber.

5 PLD of CuBi₂O₄

CuBi₂O₄ is a p-type semiconductor which has attracted attention as promising photocathode material for the hydrogen evolution reaction.^{60,200,201} With a bandgap of 1.5 – 1.8 eV it is a very suitable top-absorber in a tandem architecture.^{60,202} The unusually positive photocurrent onset potential of +1 V vs RHE shows that a large internal photovoltage is generated.^{60,201}

Pulsed laser deposition (PLD) is a very suitable technique to grow high-quality thin films with precise thickness control.^{57,95,97} Depositions can be executed directly from high-purity solid targets via a stoichiometric material transfer onto the sample substrate.⁹⁵ Resulting thin films are dense and compact.⁹⁷ The material transfer can be tailored by adjustments of the laser fluence, the background gas and pressure and the substrate temperature.

The following chapter therefore investigates PLD of CuBi₂O₄. Especially the influence of the three mentioned deposition parameters on film properties and the PEC performance are evaluated. The results are compared to films grown by other techniques, such as spray-pyrolysis or drop-casting. One parameter which is beyond the scope of this investigation is the influence of a post-deposition annealing step, which has been explicitly investigated in a separate publication.¹¹⁴

5.1 Film growth & characterization

Three samples series were fabricated. In each series one of the deposition parameters was systematically varied giving a fluence series, a pressure series, and a temperature series.

A change in laser fluence affects the evaporation of the material from the target. Depositions at low fluences may suffer from non-stoichiometric material ablation due to differences in vapor pressure of the individual species.⁹² This effect can be detected by sample stoichiometry measurements e.g. by EDX. Too high fluences on the other hand may cause ablation of agglomerates rather than individual atoms and ions, leading to the formation of droplets on the substrate.¹⁰² This can lead to rougher films visible in SEM. Three fluences were used, 1.5, 2.0, and 2.5 J/cm².

The background gas and its pressure affect the material transfer between target and substrate. Collisions of the ablated species with atoms/molecules of the background gas change the trajectory of the species leading to an overall wider spread of the ablated material.⁹⁵ Heavier species, like bismuth, will be affected less than lighter species, as copper. The background pressure can therefore change the ratio of elements. Oxygen is used as background gas in this study. As a reactive gas it can further influence the oxidation states of the metals and the oxygen content of the film.^{100,203} Five different conditions were applied: no background gas, in the following referred to as vacuum (the remaining base pressure of the system is in the range of 10⁻⁷ mbar), 1·10⁻³, 5·10⁻³, 1·10⁻² and 5·10⁻² mbar oxygen.

The substrate temperature affects the adsorption of the material onto the substrate. Species with a higher vapor pressure may be resputtered at higher temperatures, shifting the stoichiometry.^{99,204} High temperatures furthermore increase the mobility of surface species and may influence the crystallinity of the film.¹⁰¹ Three different substrate temperatures were employed, room temperature (RT, 25°C), 150°C and 300°C.

All three series share one set of deposition conditions to ensure comparability. This reference sample was fabricated in vacuum, at room temperature, with a laser fluence of 2.0 J/cm². These conditions will be referred to as “standard” deposition conditions. All samples were annealed at 550°C for 2 h in air.

5.1.1 Film thickness

Two types of samples were fabricated depending on the substrate: A) on quartz. This is suited for measurements which do not require an electrical contact and benefit from very little overall influence of the substrate. This is especially needed for TRMC measurements, but also UV/Vis spectroscopy, XRD and thickness estimation by profilometry use these samples. B) on FTO. These samples are used when an electrical contact is needed for the measurement e.g. to prevent sample charging. This is especially the case for PEC, XPS and scanning electron microscopy (SEM) measurements.

Previous investigations have shown that TRMC measurements give good signals with a CuBi_2O_4 film thickness of around 100 nm.¹¹⁴ No further optimization is needed. The film thickness on FTO was optimized in terms of photocurrent density, as shown in Figure 49. The largest current density is achieved at a thickness of 75 nm. This CuBi_2O_4 thickness will be used as the target thickness for all following samples on FTO, even though a deviation of ± 25 nm only decreases the photocurrent density by about 2%. The actual thickness of the samples slightly differs from the targeted thickness, depending on the deposition conditions as shown in Figure S 16. Note that by convention, the current densities are negative for photocathodes. Nevertheless discussions will use the phrase increase to describe an increase in absolute current density even though the actual value is becoming more negative. Vice versa phrases like decrease are used.

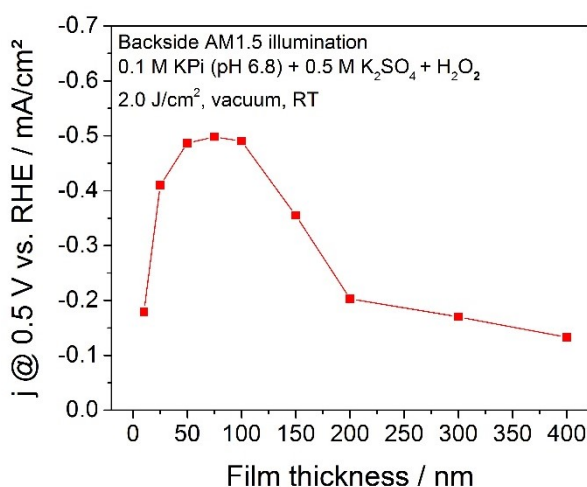


Figure 49: Photocurrent density at 0.5 V vs RHE in dependence of the CuBi_2O_4 film thickness.

5.1.2 Crystallinity and morphology

The crystallinity and morphology of the grown films were investigated by XRD, Raman spectroscopy and SEM.

Figure 50 shows XRD diffractograms of a sample grown with standard conditions compared to the desired CuBi_2O_4 phase. Without post-deposition treatment (blue) only a broad reflection around 28° is visible. This shows, that the film is predominantly amorphous although some crystallites are present.

After annealing (green and red) clear and sharp reflections are visible. These overlap with reflections of CuBi_2O_4 , shown in orange. Only one reflection is visible that cannot be assigned to CuBi_2O_4 . It is visible at ca. 52° in the red graph (highlighted by the *) and is assigned to the FTO substrate. A contribution from the quartz substrate is not visible, see Figure S 17c. The absence of additional reflections shows phase purity after annealing, independent from the substrate. CuBi_2O_4 films deposited with altered parameters show the same behavior, see Figure S 17.

The FWHM of the main feature at 28° is considered to get information on the crystallite size of the CuBi_2O_4 films. The FWHM is relatively constant over all measurements with 0.302 ± 0.018 , see Figure S 18. An increase in temperature or pressure leads to a slight decrease of the FWHM whereas a change in laser fluence shows no direct correlation. A more detailed analysis of the grain size using the Scherrer equation is non-trivial for grazing incidence measurements. It would require an in-depth investigation, e.g. on isometry of domains, orientation of crystallites and instrumental factors. It is therefore omitted.

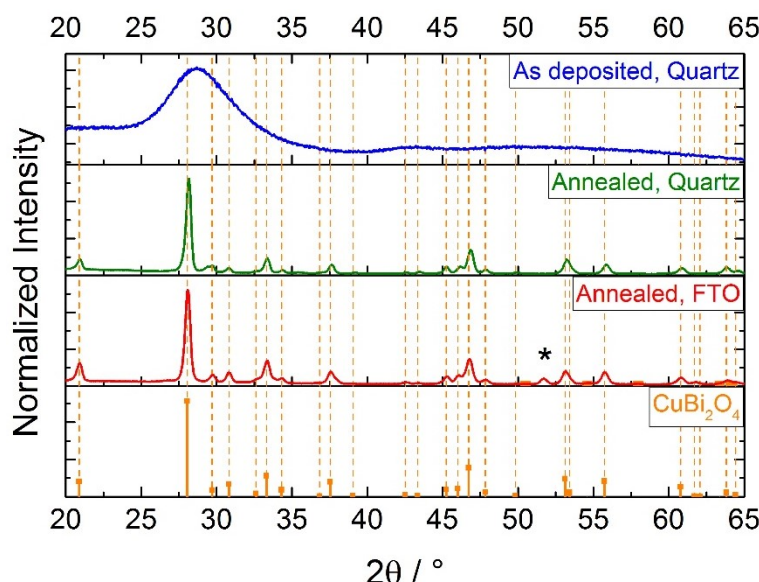


Figure 50: Grazing-incidence X-ray diffractograms of a CuBi_2O_4 thin film grown under standard conditions; blue: on quartz as deposited, green: on quartz after annealing, red: on FTO after annealing, orange: CuBi_2O_4 reference pattern.²⁰⁵

Raman measurements confirm the XRD observations, as shown in Figure 51. Independent from the deposition parameters all samples show four distinct bands around 130, 261, 406 and 589 cm^{-1} . All of them are in agreement with literature values for CuBi_2O_4 and are assigned as follows:^{206–209} Two peaks overlap around 130 cm^{-1} . One at 131 cm^{-1} is assigned to an A_{1g} mode originating from translational vibrations of CuO_4 planes along the z-axis. The second peak at 128 cm^{-1} originates from either another A_{1g} or a B_{2g} Bi atom vibration. The A_{1g} mode at 261 cm^{-1} originates from the rotation of two stacked CuO_4 squares in opposite direction. The band at 406 cm^{-1} is ascribed to the A_{1g} mode of the Bi-O stretching and the 589 cm^{-1} peak to an A_{1g} in-plane “breathing” of the CuO_4 squares. No other features are visible showing phase purity in agreement with the XRD observations.

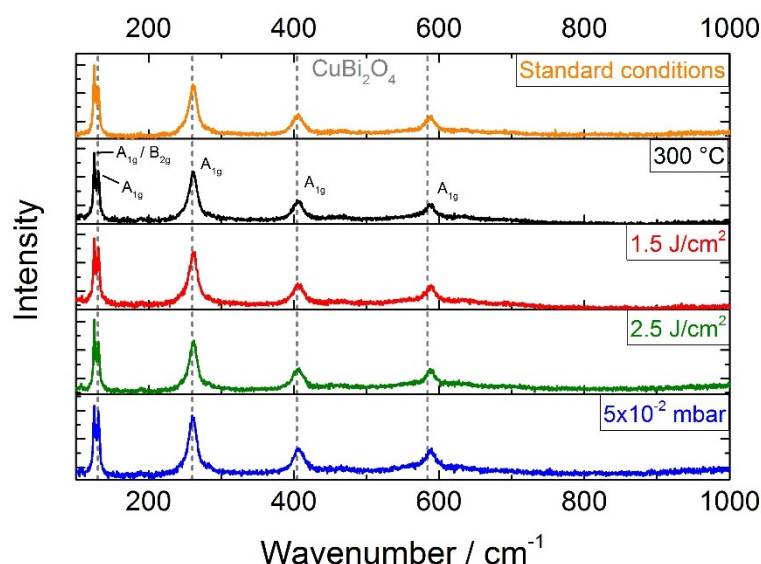


Figure 51: Raman spectra of annealed CuBi_2O_4 films grown with varying parameters after annealing compared to literature values of the most prominent vibrations (grey).²⁰⁶

The morphology of the samples was investigated by SEM investigations. Figure 52 shows examples of SEM images of the CuBi_2O_4 films. Images c and d show CuBi_2O_4 grown with standard parameters in top- and cross-sectional view, respectively. Images of all samples at various magnifications can be found in the appendix

SEM images Figure S 20 - 22.

The top view in c clearly shows a granular structure with particles sizes around 150 nm. The particles are irregular shaped with clear edges. Other shapes of agglomerated particles are especially visible in the bottom left part of the picture. In between the CuBi_2O_4 particles sharp features of the FTO surface are visible as well, e.g. at the bottom right. Figure S 26 shows a bare FTO substrate to compare.

The cross-section in d shows no sharp contrast between FTO and CuBi_2O_4 making strong statements questionable. However, the film appears widely closed and compact with a thickness of around 100 nm.

From top to bottom the laser fluence is increased (a, c & e). The coverage of the substrate is an issue in the 1.5 J/cm^2 image. Holes in the film are clearly visible and also individual sharp features of the FTO are exposed in multiple spots (cf. Figure S 26). This can be due to the slightly lower film thickness. Apart from that a comparable granular structure is visible with slightly larger particles and rounded edges.

An increase in laser fluence to 2.5 J/cm^2 (e) shows two developments. Individual grains are smaller but more densely packed. Furthermore agglomeration is increased. The proclaimed possible deposition of larger particles is only occasionally visible at lower magnification (see Figure S 20 and Figure S 24). In fact more distinct additional particles are visible under standard conditions (see Figure S 20). Overall the influence of the fluence on the morphology

seems small, a minor decrease in individual particle size and increase in packing density and size of agglomerates may be visible.

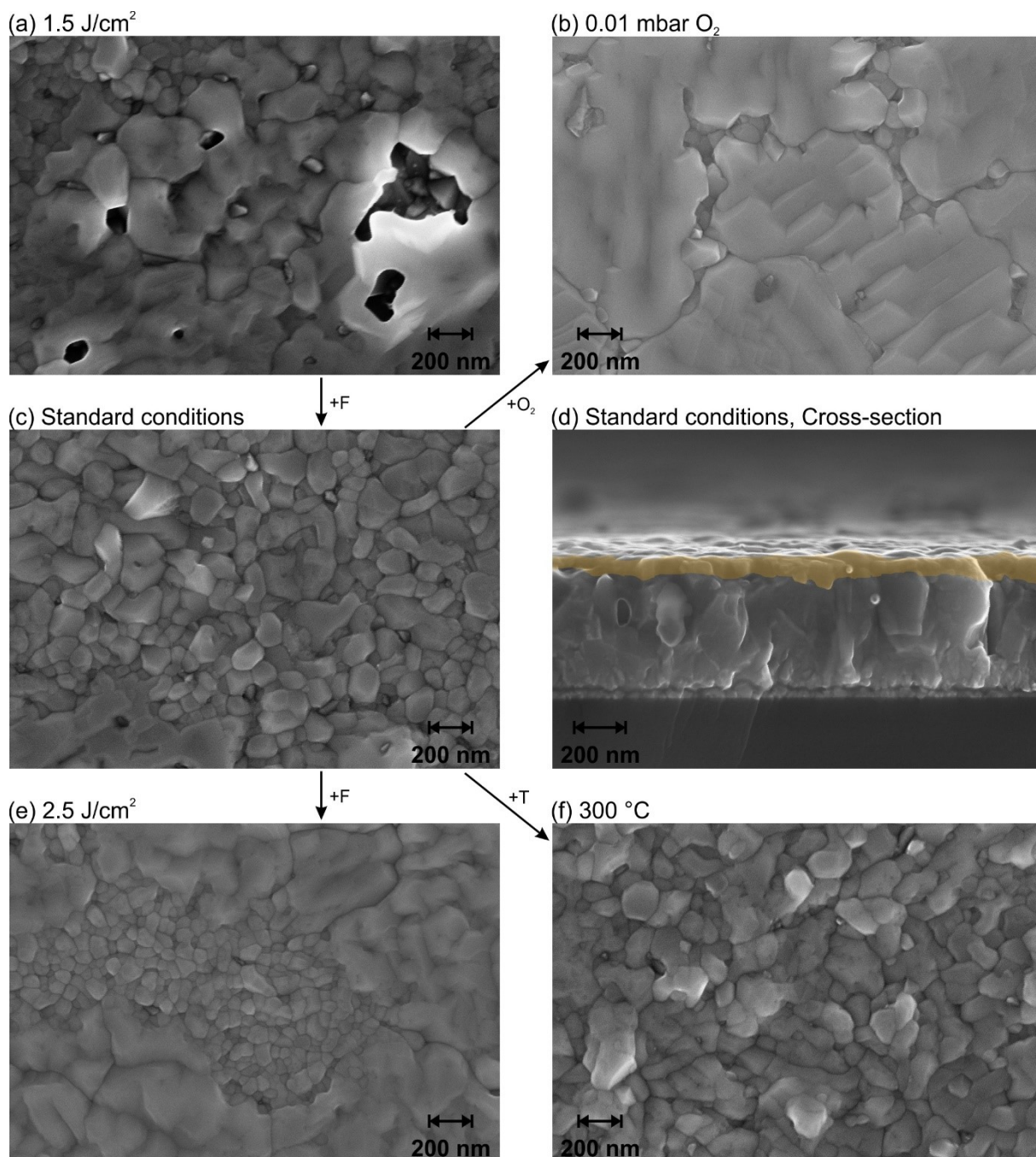


Figure 52: SEM images of CuBi_2O_4 films deposited with varying parameters after annealing; top views: (a) $F = 1.5 \text{ J/cm}^2$, (b) $p_{\text{O}_2} = 0.01 \text{ mbar}$, (c) standard conditions (vacuum, 2.0 J/cm^2 , RT), (e) $F = 2.5 \text{ J/cm}^2$, (f) $T = 300^\circ\text{C}$; (d) cross-sectional view, standard conditions, CuBi_2O_4 highlighted in orange.

A background pressure of oxygen is introduced by going from the standard conditions in c to the top right (b). A clear change in morphology is visible. Large and smooth domains are visible as dominant feature. A layered structure can be seen within them, indicating the previously observed crystallinity. Clear grain boundaries exist in between these domains which may be filled with individual smaller particles. These particles have the same morphology as seen under standard conditions. Already small amounts of oxygen introduce the described

large domains. A further increase in oxygen background pressure barely affects the morphology, as visible in Figure S 22. The formation of large domains is in agreement with the lower FWHM observed in the XRD measurements. The background pressure can alter the distribution of copper and bismuth, as mentioned in section 5.1, which may be beneficial for the agglomeration into larger domains. Furthermore the background pressure can increase the oxygen content of the film which may facilitate agglomeration as well.

When going to the bottom right (f) the substrate temperature is increased. The morphology is very little affected by this. The small grains are still visible. The edges appear less sharp and individual particles seem to be fused together into larger agglomerates. Such an agglomeration is expected as the increased substrate temperature increases the surface mobility during deposition.

5.1.3 Composition

The previous chapter on $\text{Mn}_2\text{V}_2\text{O}_7$ showed that the stoichiometry control of ternary oxides is essential. The ultra-thin films grown by ALD can accurately be investigated by XPS as the information depth is in the same range as the film thickness, around 10 nm. The situation is different with the PLD films. They are ca. 100 nm thick which means that XPS evaluation can only give information on $\approx 10\%$ of the film close to the surface. More bulk sensitive methods are therefore needed.

One of these techniques is energy-dispersive X-ray spectroscopy (EDX) within the SEM setup. It not only gives bulk stoichiometries but also the spatial distributions of individual elements. While EDX is fast and convenient it is also prone to various types of errors and inaccuracies.²¹⁰ Some errors can be addressed during the data evaluation e.g. different excitation efficiencies depending on the detected element and the X-ray source. For others such considerations are difficult, e.g. the particle size and surface texture of the sample affect different wavelengths to different degrees.²¹⁰ Furthermore, EDX does not allow distinction of oxidation states and the substrate will contribute significantly to the signal due to the information depth in the micron range.²¹⁰ The substrate in the present case is FTO therefore no quantitative evaluation of the oxygen is possible by EDX.

The accuracy of EDX can be improved by a calibration with a sample of known stoichiometry, which should be as close as possible to the samples stoichiometry.²¹⁰ Standard condition samples which were additionally evaluated by Rutherford backscattering spectrometry (RBS) fulfil this purpose. RBS is another bulk sensitive technique to accurately determine absolute stoichiometries which does not require a reference.^{211,212} An example measurement is shown in Figure S 19. The identified stoichiometry is $\text{CuBi}_{2.42}\text{O}_{4.12}$ and thereby bismuth rich whereas the oxygen fraction is very close to the desired value.

Additional information can be derived from the RBS investigation. RBS measures the absolute atom concentration in atoms per investigated sample area. From this value the density can be estimated if the thickness is known or vice versa. The sample grown on a flat

quartz substrate has a film thickness of 129.7 nm. Together with the RBS results the density is calculated to 6.91 g/cm^3 and thereby about 80% of the density of single-crystal CuBi_2O_4 (8.65 g/cm^3). This value is below the expectations as PLD should produce dense films.⁹⁷ Also a comparable study on PLD of CuBi_2O_4 reports a higher density of 8.49 g/cm^3 , although it relies on X-ray reflectivity to estimate the density.⁹⁷ It is therefore considered that the present density estimation is not fully accurate. Another hint in this direction is the measurement on the sample grown on FTO. The same evaluation gives a density is 9.31 g/cm^3 for this sample. Such a value above the theoretical density of the single crystal does not make physical sense and therefore illustrates the limits of RBS in terms of density and thickness estimation. One possible source of inaccuracy could be the influence of the rather rough FTO substrate compared to the flat quartz. However, the results still suggest that the density of the CuBi_2O_4 films at least 80% of the single-crystal density.

This mentioned stoichiometry of $\text{CuBi}_{2.42}\text{O}_{4.12}$ is used as calibration for the EDX measurements and the results are shown in Figure 53. Error bars in the Bi:Cu ratio are given if multiple EDX measurements were executed (e.g. at different magnifications).

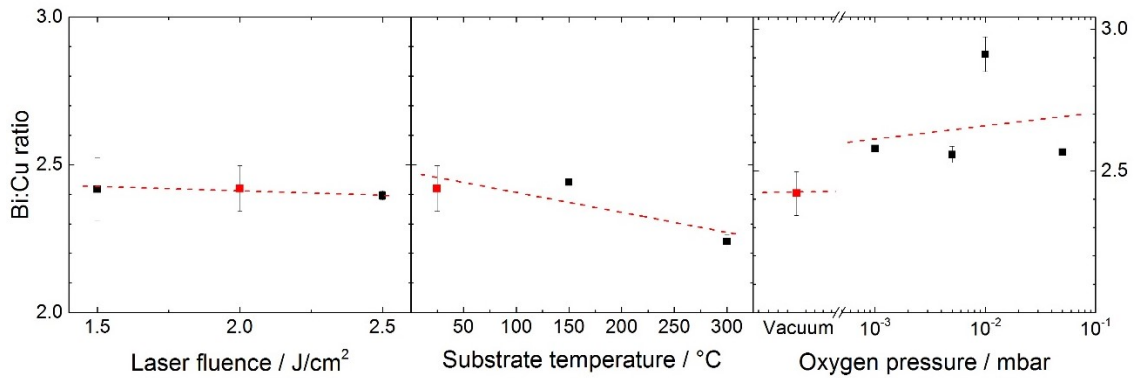


Figure 53: Bismuth:copper ratios estimated by EDX in dependence of the deposition parameters laser fluence, substrate temperature, and oxygen pressure. Standard conditions marked in red and dashed red lines show linear fits, error bars indicate the standard deviation if multiple measurements were executed.

It is clearly visible that all samples are bismuth rich i.e. the Bi:Cu ratio is above 2. The laser fluence does not affect the element ratio in the films, showing that the ratio of the target ablation is not affected by the fluence in the chosen regime.

An increase in substrate temperature to 150°C does not affect the Bi:Cu ratio whereas a further increase to 300°C decreases the amount of bismuth. Such a loss of bismuth was observed in BiVO_4 growth by PLD starting from 200°C .⁹⁵ The loss of bismuth is ascribed to re-evaporation or re-sputtering of the film by the impinging species from the plasma plume as an evaporation under thermodynamic equilibrium is unlikely.⁹⁵

The Bi:Cu ratio increases with the introduction of an oxygen background pressure. This is expected as the pressure causes collisions of the ablated species leading to a thermalization of the plasma plume.⁹⁵ The mean free path of a particle can give an idea of the number of collisions. It is calculated assuming spherical particles with a shared diameter. For oxygen

($d = 304 \text{ pm}$), this mean free path is around 1 km in 'vacuum' conditions and decreases to around 10 cm at 10^{-3} mbar and 0.1 cm at 10^{-1} mbar . The distance from the target to the substrate is 6 cm. Copper is much lighter than bismuth (atomic mass 63.5 vs. 209.0 u), therefore its trajectory will be deviated more by the collisions with oxygen, leading to a decreased mass transport onto the substrate surface. This behavior is further visible in the decline in deposition rate in Figure S 16. The sample grown at $1 \cdot 10^{-2} \text{ mbar O}_2$ produces an outlier in both, stoichiometry and film thickness. It cannot be excluded that an error occurred during sample preparation, even though no irregularities were observed.

The element distribution is evaluated by EDX mapping. Maps are collected in the EDX images section of the appendix (Figure S 23-25). The three elements Cu, Bi and O of the thin film are shown as well as Sn from the FTO substrate. Different features can clearly be assigned.

Distinct grains on the surface, especially visible in standard conditions, 150°C and 2.5 J/cm^2 samples, show an increased bismuth fraction. The lowered amount of oxygen in the same position could indicate bismuth in a lower oxidation state, e.g. metallic bismuth. The lowered amount of tin shows an increased thickness in the spot. Such additional bismuth grains may contribute to the increased bismuth content measured by RBS.

The previously described holes in the 1.5 J/cm^2 sample are clearly validated. The copper and bismuth intensities are decreased while a strong increase in the tin signal is visible. To some extent tin is also visible in the samples of the pressure series: it is more pronounced where holes in the film expose grains of FTO and along the domain boundaries. Interestingly the different microstructures of the domains do not alter the copper or bismuth distribution. This indicates that all domains exhibit the same stoichiometry but may differ in crystal orientation.

As a fourth technique XPS can give some additional insight. Its sensitivity is used to investigate oxidation states and potential contaminations even though it is not giving information on the whole film. Figure 54 shows a survey XPS spectrum where the majority of the peaks is assigned to the desired elements Cu, Bi and O (orange, blue and red, respectively). Apart from that adventitious carbon is visible at 284.4 eV (black, set as BE reference) as well as tin from the FTO substrate at 490 eV (green). Another peak may be visible at 825 eV (marked by the *) with the F KLL Auger signal as only reported species in this region.¹¹⁰ Fluorine is present as dopant in the FTO substrate and has the most prominent feature at 685 eV, overlapping with Bi $4p_{3/2}$. A clear assignment is therefore not possible and omitted from the spectrum. Aside from these no additional features are visible in the survey spectrum proving that no major contaminations exist.

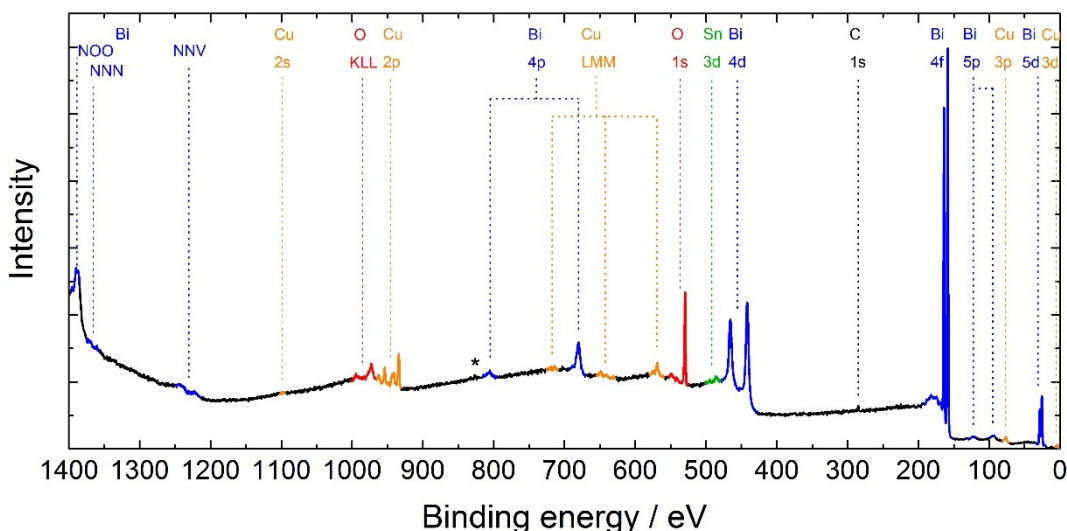


Figure 54: Survey XPS of CuBi_2O_4 grown PLD. Indicated peaks belong to copper (orange), bismuth (blue), oxygen (red), carbon (black), and tin (green).

The main species copper, bismuth and oxygen are investigated in more detail. The O 1s region (Figure S 27) shows the usual bulk O and surface OH peaks. The bismuth oxidation state is judged by the Bi $4f_{7/2}$ peak shown in Figure 55a and Figure S 28a. The peak is very close to the desired 158.5 eV of Bi(III) for all deposition conditions.^{109,132} A contribution of metallic bismuth, which would be expected at 156.6 eV, is not visible. The application of the oxygen background pressure does not affect the peak position. An increase in substrate temperature or a decrease in laser fluence slightly increases the binding energy, indicating higher average oxidation states. The reasons for this behavior cannot be fully resolved. It is possible that re-sputtering preferably ablates bismuth in lower oxidation states and that high fluences facilitate a partial reduction of bismuth during ablation.

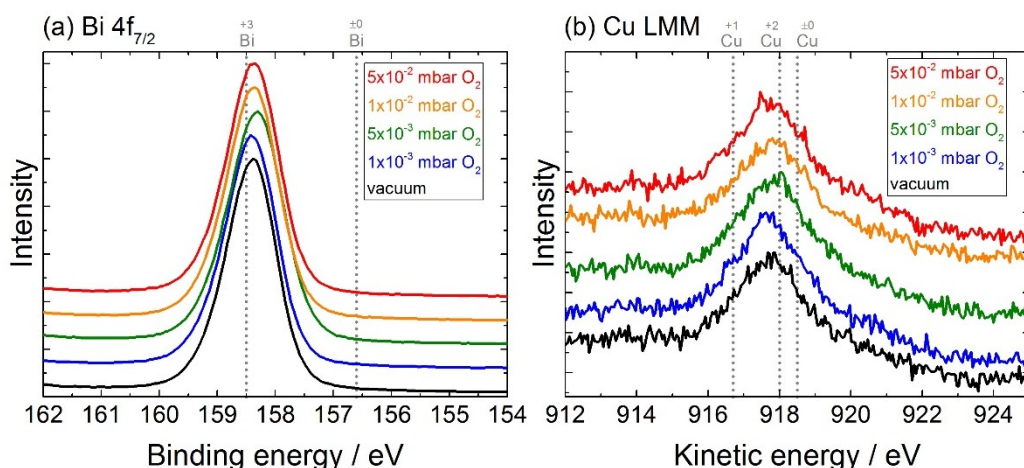


Figure 55: XPS fine spectra of (a) the Bi $4f_{7/2}$ feature and (b) a Cu LMM Auger feature from samples deposited under various background pressures; positions of important species indicated in grey.¹⁵⁹

The Cu LMM Auger region is used to evaluate the copper oxidation state. Figure 55b and Figure S 28b show this region on the kinetic energy scale. The Cu LMM region is frequently considered to distinguish copper oxidation states as this is not always easy in the Cu 2p region,

especially as signals of Bi 4s are present in the same region.^{155,159} All samples show the desired Cu(II) as dominant species independent from the deposition parameters. An additional contribution of Cu(I) may be visible at a reduced fluence of 1.5 J/cm².

In conclusion, PLD of CuBi₂O₄ with the employed conditions deposits slightly bismuth rich thin films. The excess of bismuth can be kept low by an increase of substrate temperature to 300°C and by the exclusion of a background pressure. Uncoated areas allow the detection of tin from the FTO substrate. Apart from this only adventitious carbon is detected as (surface) contamination. In combination with the desired dominant oxidation states Bi(III) and Cu(II) this section confirms the ability of PLD to grow high quality films.

5.1.4 Optical properties

The optical properties of CuBi₂O₄ were investigated by UVVis-spectroscopy. An example of the absorption coefficient over the wavelength is shown in Figure 56a. The absorption onset, indicating the bandgap, is located around 670 nm. Until ca. 450 nm the absorption is very modest with values below 20000 cm⁻¹. The development of the absorption coefficient with features around 490 and 600 nm is characteristic for high purity CuBi₂O₄ films and originates from the intrinsic electronic structure of the material.⁹⁸ The bandgap was determined in Tauc plots as shown in the inset. The indirect bandgap is located at 1.84 eV, the direct bandgap at an only slightly larger energy of 1.90 eV. These values are at the upper end of reported bandgaps between 1.5 - 1.9 eV and indicate high film quality with no to low amounts of additional CuO.^{53,97,98,213}

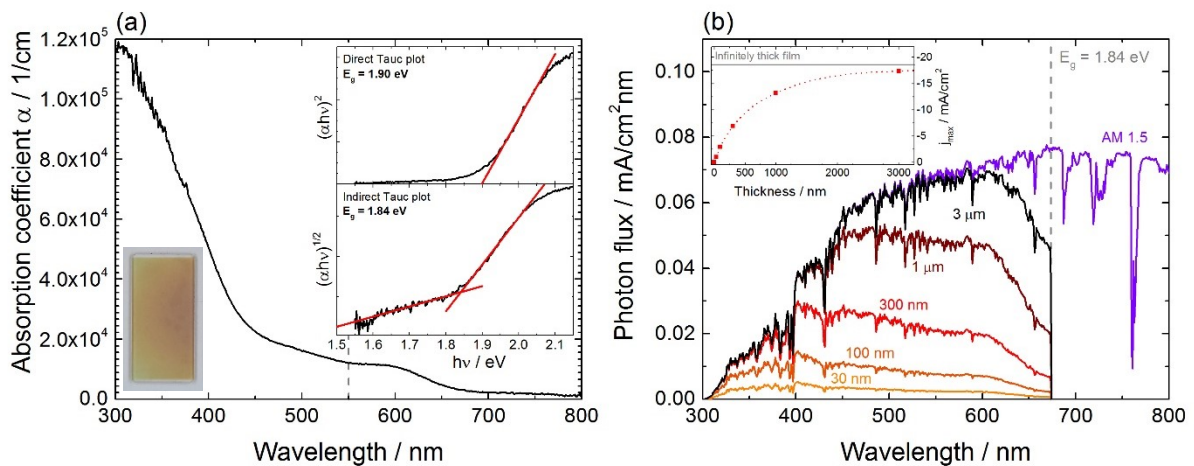


Figure 56: (a) Absorption coefficient α , photograph, direct and indirect Tauc plots (insets) of CuBi₂O₄; (b) Estimated above bandgap absorption of the AM 1.5 spectrum by CuBi₂O₄ thin films and corresponding maximal photocurrent density j_{max} (inset).

The amount of absorbed photons and thereby an upper limit of the photocurrent density j_{max} is calculated from the absorption coefficient and illustrated in Figure 56b and its inset. Again, below bandgap absorptions are excluded. The present films with thicknesses of 75 – 100 nm facilitate a photocurrent density of -2.3 to -2.9 mA/cm². These values seem rather low compared to the previously discussed Mn₂V₂O₇. While both materials have essentially the

same bandgap (1.84 eV for CuBi_2O_4 vs. 1.83 eV for $\text{Mn}_2\text{V}_2\text{O}_7$) and therefore the similar theoretical limit of -18.5 mA/cm^2 , $\text{Mn}_2\text{V}_2\text{O}_7$ absorbs photons more efficiently, expressed in larger absorption coefficients. To compare, a 100 nm $\text{Mn}_2\text{V}_2\text{O}_7$ film would already facilitate a current density $j_{\text{max}} = 11.3 \text{ mA/cm}^2$.

The influence of the deposition parameters on the bandgap and the extinction coefficients is investigated further as shown in Figure 57 and Figure 58. The effect on the bandgaps is minimal with indirect bandgaps ranging from 1.83 to 1.85 eV and direct bandgaps from 1.90 to 1.92 eV. These values are very close to a theoretical value from DFT calculations of 1.90 eV.²¹³ Literature almost exclusively reports on lower bandgaps down to 1.5 eV.^{53,60,97,98,213} The low bandgaps are usually ascribed to stoichiometry variations. These could include a) Cu vacancies which alter the band structure and lower the bandgap. These Cu vacancies further introduce empty states in the valence band, explaining the p-type behavior.^{52,213} b) segregation of CuO as a second optically active species with a lower bandgap (1.4 – 1.7 eV) altering the absorption profile.^{98,214} However, in the present case the film stoichiometry does not correlate with the measured bandgaps. Another reason for the minimal changes could be slightly differing degrees of crystallinity.

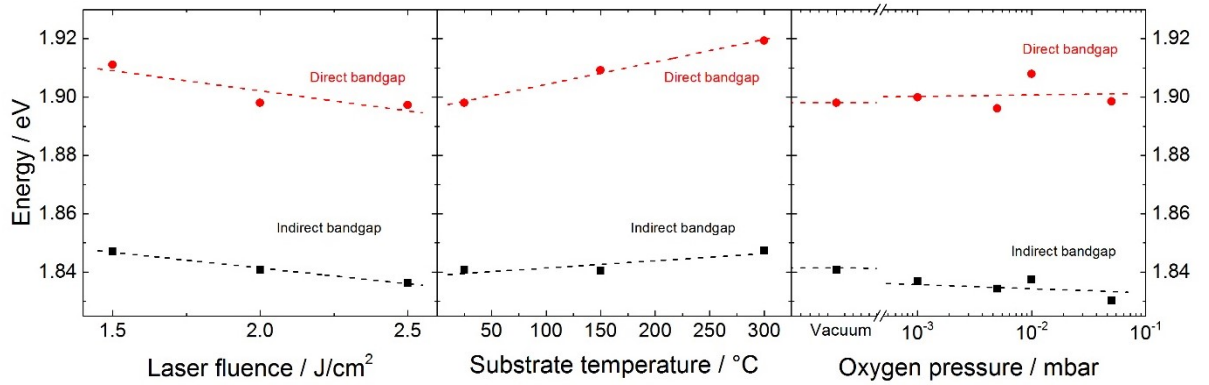


Figure 57: Direct (red) and indirect (black) bandgaps in dependence of the deposition parameters laser fluence, substrate temperature, and oxygen pressure. Dashed lines show linear fits.

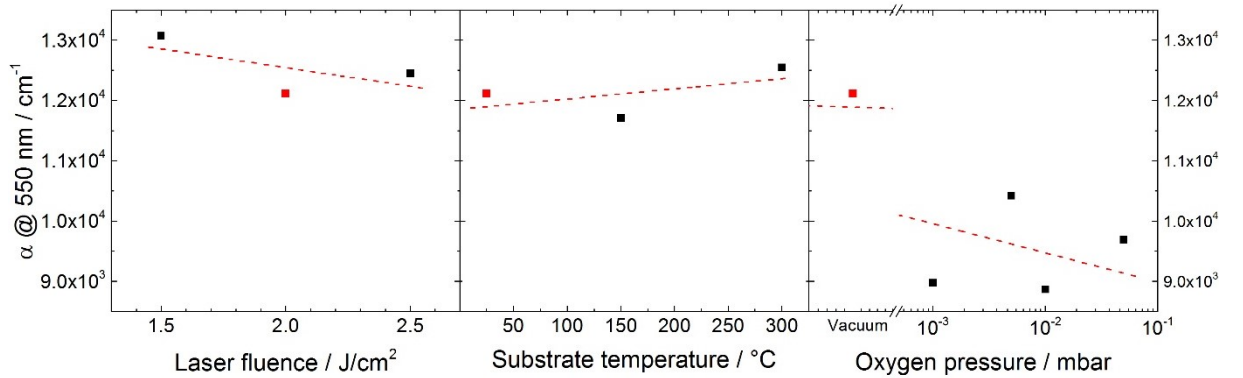


Figure 58: Absorption coefficient α at 550 nm in dependence of the deposition parameters laser fluence, substrate temperature, and oxygen pressure. Standard conditions marked in red and dashed red lines show linear fits.

The absorption coefficient is compared at 550 nm as it is a common value in literature.^{53,60,97} It is difficult to assign clear trends from the limited set of points for each parameter, especially in terms of laser fluence and substrate temperature. There values range from 11700 – 13100 cm⁻¹. In terms of oxygen background pressure it is at least clearly visible that a decline in absorption occurs if oxygen is present. A reason for that could be the suppression of oxygen vacancies in the material which could otherwise act as shallow or deep donors enabling additional absorption.³² A clear hint for this behavior gives the photograph in Figure 59. Contrary to all other shown data in this chapter it shows samples which have not been annealed yet. The vacuum sample (left, thickness 130 nm) has a deep brown color. The other four samples (thicknesses 115 – 130 nm) are brighter and more orange, similar to the annealed sample shown in Figure 56. Differences in sample thickness cannot explain the different colors. One can assume that the darker color is caused by oxygen vacancies in the film which are (partially) suppressed by the oxygen background pressure even though no direct evidence is provided.¹⁰⁰ A large fraction of these oxygen vacancies are filled during the annealing in air and the initially brown sample becomes orange as well. However, as the samples deposited with an oxygen background pressure have a lower initial amount of oxygen vacancies it is reasonable to assume that the same is true for the annealed samples, resulting in a reduced absorption coefficient (see also Figure S 29).



Figure 59: Photograph of CuBi₂O₄ grown on quartz at various oxygen background pressures: from left to right: vacuum, 1x10⁻³, 5x10⁻³, 1x10⁻², 5x10⁻² mbar O₂; all as deposited.

As mentioned above the absorption coefficients are rather low which means that film thicknesses around 1 μm are needed to facilitate current densities above 10 mA/cm². This inefficient light harvesting has been addressed as bottleneck of CuBi₂O₄ before.⁶⁰ It is therefore essential to compare the absorption coefficients from varying deposition techniques as one factor to evaluate their suitability. Unfortunately most studies do not publish easy to compare absorption coefficients but rather absorption profiles with arbitrary scales. Some available values are compared in Table 5.

Table 5: Absorption coefficients of CuBi₂O₄ from various studies.

Study	Deposition technique	α at 550 nm / cm ⁻¹
This study	PLD	8800 - 13100
Lee et al. ⁹⁷	PLD	15000
Berglund et al. ⁶⁰	Drop casting	41000 (calculated to 0% porosity)
Wang et al. ⁵³	Spray pyrolysis	35700

The lowest absorption coefficients are measured in this study. The study by *Lee et al.* is probably the best initial comparison as it is based on the same deposition technique. They report a slightly higher absorption coefficient of 15000 cm^{-1} . The presence of the characteristic absorption feature at 600 nm indicates similar high quality films, see Figure 60a. Furthermore they could accurately determine the density of their films to 8.49 g/cm^3 (98% of the theoretical value 8.65 g/cm^3) which could explain the increased absorption coefficient. The previously shown RBS measurements indicated a density down to 6.91 gm/cm^3 (80% of the theoretical value) in this study.

Berglund et al. report much larger absorption coefficients that cannot be explained by a consideration of the film density. Instead, two additional factors can play a role there. First, the deposited films show high porosity contrary to the widely flat films in this study. Such spongy structures allow multiple reflections and light trapping in the film, promoting absorption. Second, the absorption onset is at much lower energies around 1.5 eV (825 nm) with a gradual increase in absorption overlapping with the feature around 600 nm, see Figure 60b. Combined with the fact that no bandgap could be obtained from Tauc plots this leads to the assumption that some kind of impurity or defects are present in the film, increasing the overall absorption.

Wang et al. report similar high absorption coefficients for films deposited by spray pyrolysis. In this case the absorption shows a gradual increase where distinct features are barely visible, see Figure 60c. The onset is at even lower energies which could be due to a secondary CuO phase. CuO has a reported bandgap of 1.4 – 1.7 eV (885 – 730 nm).²¹⁴ A similar case was discussed by *Gottesman et al.* who ascribe the absorption behavior to a segregation of CuO, making comparisons difficult.⁹⁸

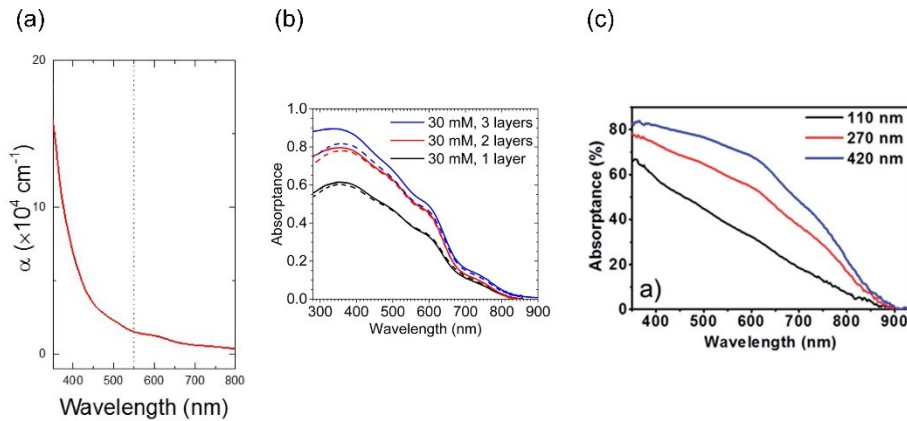


Figure 60: Reported absorption profiles of (a) *Lee et al.*⁹⁷, (b) *Berglund et al.*⁶⁰, and (c) *Wang et al.*⁵³.

5.1.5 Charge carrier dynamics

The charge carrier transport properties of the CuBi_2O_4 films were investigated by time-resolved microwave conductivity measurements (TRMC). An example measurement of the photoconductivity, expressed as $\sigma\mu$, over time after photoexcitation is shown in Figure 61a. A series of measurements with different excitation fluences was recorded for each sample. The individual peak photoconductivities $(\sigma\mu)_{\text{max}}$ directly after photoexcitation were extracted from these as descriptor of the charge carrier mobility and plotted in Figure 61b and Figure S 30 versus the photon fluence of the excitation pulse.

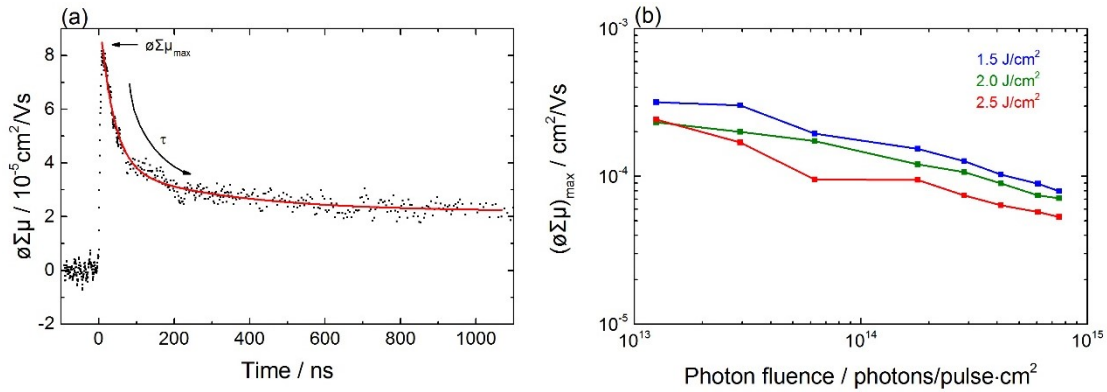


Figure 61: (a) TRMC measurement showing the photoconductivity over time after photoexcitation (black) and a decay fit (red); (b) peak photoconductivity over photon fluence of the excitation pulse for the fluence series.

It is clearly visible that the peak photoconductivity decreases with an increase in photon fluence. The same observation was made before for drop-casted CuBi_2O_4 films.⁶⁰ Such a decrease could be ascribed to non-geminate higher-order electron-hole recombination or electron-electron interactions.^{51,215,216} In principle $(\sigma\mu)_{\text{max}}$ can be extrapolated to AM1.5 illumination which corresponds to a photon fluence of $3.0 \cdot 10^9$ photons/pulse·cm².⁶⁰ However, two factors may interfere with the visible linear trend on log-log scale. First, higher-order recombination processes tend to be less pronounced at lower intensities.⁵¹ Therefore the peak photoconductivity could reach a plateau at lower photon fluences. Second, an initial filling of (immobile) trap states within the film or at the surface may reduce the mobility. This is especially visible when less charge carriers get photo-excited meaning that the measured peak photoconductivity could decline at lower photon fluences.²¹⁵ The absence of such a decline hints towards a low amount of trap states, although the range of employed photon fluences is small.^{61,215,217} The number of trap states is strongly connected to the film quality, e.g. to the stoichiometry and impurity levels as shown for BiVO_4 .⁵¹

Two peak photoconductivity values will be considered: 1) the extrapolated $(\sigma\mu)_{\text{max}}$ value at AM1.5 as an upper limit of the mobility and 2) the value of the same fit at $1.2 \cdot 10^{13}$ photons/pulse·cm². The latter value is used rather than the measured value at the same photon fluence as it reduces a possible influence of outliers.

The second characteristic value in TRMC is the lifetime of the mobile charge carriers which can in principle be deduced from the decay of the photoconductivity signal. However, the term

lifetime should be handled with care in the present context. Conventionally lifetime is considered as the average time needed until excited charge carriers recombine. Such a decrease in mobile charge carrier concentration leads to a decrease in photoconductivity visible as the exponential decay. In metal oxides it is furthermore possible that charge carriers are immobilized by polaron formation or trapping processes.^{61,218} It is not trivial to determine if the decay of the photoconductivity is caused by a decrease in mobility or by a decrease in charge carrier concentration. It has therefore been suggested to use the term TRMC decay time τ as a more suitable description.⁶¹

A double-exponential decay function has to be used to generate a reasonable fit of the experimental data in the present case, which is shown in Figure 61a as red line. The use of a double-exponential decay is common for CuBi_2O_4 and associated with two different time constants.^{52,60} This implies that different processes exist that reduce the photoconductivity.^{52,60} The lower value τ_1 will be limiting in terms of charge transport, therefore the second TRMC decay time τ_2 will not be discussed further. The TRMC decay time is, contrary to the photoconductivity, widely independent of the excitation pulse as shown in Figure S 31. The τ_1 deduced from the highest photon count will be used for further considerations as it offers the best quality of the fit.

Both values, the peak photoconductivity $(\sigma\mu)_{\text{max}}$ and the TRMC decay time τ_1 , can be combined to calculate the diffusion length L_D . Similar to the term lifetime the term diffusion length should be handled with care. The four discussed values and the influence of the deposition parameters are summarized in Figure 62.

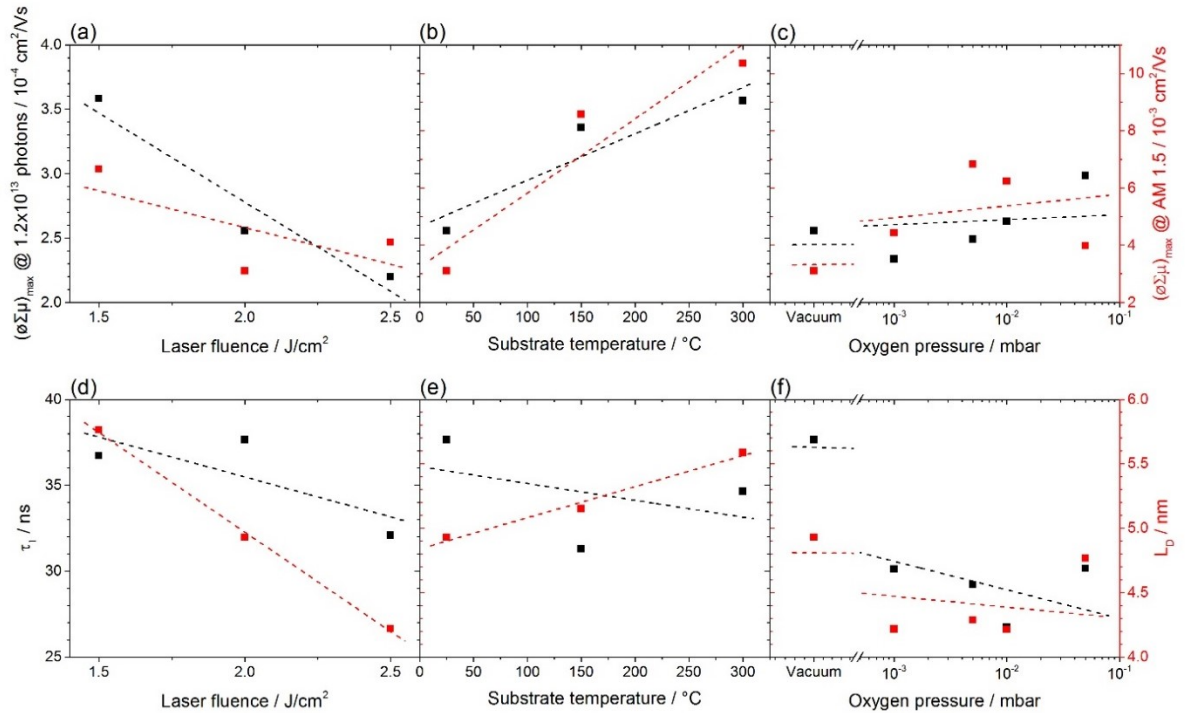


Figure 62: Peak mobilities, lifetimes, and diffusion length in dependence of the deposition parameters laser fluence, substrate temperature and oxygen pressure; dashed lines show linear fits.

Some clear trends can be seen for the peak photoconductivity at 1.2×10^{13} photons/pulse (black in a-c). The peak photoconductivity increases from ca. 2.5×10^{-4} cm²/Vs at standard conditions to ca. 3.5×10^{-4} cm²/Vs at 1.5 J/cm² or 300°C. The influence of the oxygen background pressure is less prominent. Apparently low amounts of oxygen slightly decrease the peak photoconductivity but larger amounts increase it again, although changes are rather subtle. The essentially same trends are visible when the extrapolated peak photoconductivities are considered (red in a-c) although the trends appear less prominent. It can be seen that the extrapolation increases the mobility by a factor of 10 - 20.

The trends are not as clear when the TRMC decay times are considered (black in d-f). The largest value is measured at standard growth conditions with 38 ns. A change in laser fluence in either direction slightly decreases the TRMC decay time, the same happens by an increase in deposition temperature. The introduction of oxygen into the system decreases the TRMC decay time to about 30 ns where a dependence on the amount of oxygen is barely visible.

The diffusion length combines both values (red in d-f). It shows an almost linear development with laser fluence and substrate temperature, benefiting from low fluences and high temperatures. The diffusion length thereby increases from about 5 nm to 5.6 – 5.8 nm. An oxygen background pressure decreases the diffusion length to about 4.3 nm. Judging from these observations a sample deposited with 1.5 J/cm² laser fluence and at 300°C substrate temperature is expected to show even better charge carrier dynamics.

An increase in peak photoconductivity and TRMC decay time is usually ascribed to an improved film quality in terms of surface and bulk defects, e.g. due to less impurities or grain boundaries.^{51,215} The number of grain boundaries is directly dependent on the grain and domain size of the CuBi₂O₄ film, represented by the FWHM in XRD measurements. The amount of impurities can be linked to the stoichiometry of the films, measured by EDX. And indeed this correlation is visible for the substrate temperature. An increase in temperature results in an increased peak photoconductivity and correlates to a decline in FWHM and a stoichiometry closer to the desired 1:2 ratio of Cu:Bi (cf. Figure S 18 and Figure 53). This indicates that indeed a decline in bulk defects and grain boundaries are responsible for the increased peak photoconductivity at higher substrate temperatures.

However, these correlations are not visible when the laser fluence is considered. Both, FWHM and Cu:Bi ratio, are barely affected by a change in laser fluence. This indicates that other factors are accountable. These factors could be surface defects or defects associated with oxygen as their occurrence cannot be quantified with the presented measurements.

The calculated diffusion length of about 5 nm is very small, even for a metal oxide.^{51,52,57,60} Two other studies investigated the charge carrier transport in CuBi₂O₄ using TRMC as well. Their results are summarized in Table 6.

Table 6: TRMC results of various studies.

Study	Deposition technique	$(\sigma \Sigma \mu)_{\max} / 10^{-4} \text{ cm}^2/\text{Vs}$	τ_1 / ns	L_D / nm
This study (largest values)	PLD	3.6	38	5.8
<i>Berglund et al.</i> ⁶⁰	Drop casting	11	32	10
<i>Wang et al.</i> ⁵²	Spray pyrolysis	46	22.7	16.3

Interestingly the values show opposing trends: while the peak photoconductivity in this study is much lower than in literature the TRMC decay time is slightly larger. In combination the present diffusion lengths are lower than in literature. This is counterintuitive as one would expect that both values, peak photoconductivity and TRMC decay time, would correlate as both are linked to material quality. As stated earlier PLD is able to grow high quality films where, compared to drop casting and spray pyrolysis, especially carbon contaminations should be avoided. From this perspective the low peak photoconductivities are unexpected.

However, a critical difference in data evaluation exists. The measured photoconductivity is proportional to the dielectric permittivity of the sample. In the case of the studies by *Berglund et al.* and *Wang et al.* this value is expected to be $\epsilon_r = 80$, the dielectric constant of CuBi_2O_4 .^{52,60,219} This assumption is however ambiguous as not the dielectric constant of the thin film alone is affecting the measurement but the ϵ_r of the whole sample, i.e. of the thin film and the quartz substrate. As the CuBi_2O_4 thin film (ca. 100 nm) is much thinner than the quartz substrate (1 mm) the influence of CuBi_2O_4 is negligible. It is therefore reasonable to assume the dielectric constant of quartz $\epsilon_r = 3.8$ for the whole sample, which has been done in this study. When (for comparison reasons only) the present data is adjusted for this difference in evaluation, the peak photoconductivity increases to a value of ca. $75.4 \times 10^{-4} \text{ cm}^2/\text{Vs}$ and the diffusion length increases to 26.4 nm. Thereby both, the peak photoconductivity and TRMC decay time, are larger for PLD grown samples, confirming an improved film quality compared to drop casting and spray pyrolysis.

5.2 Photoelectrochemical film performance

5.2.1 Linear sweep voltammetry

Photocurrent densities were measured by linear sweep voltammetry (LSV) in chopped light configuration. Measurements were conducted in a neutral, phosphate buffered electrolyte, with H_2O_2 as electron scavenger, and under backlight illumination, similar to various other studies.^{52,53,60,98,114} This ensures easy comparability of the results. An example of a measurement is shown in Figure 63 in black. Backside illumination generates larger photocurrent densities than frontside illumination (blue) as shown in a. Considering that more charge carriers are generated at the incident side of the sample (cf. Figure 4) and that electrons have to reach to CuBi_2O_4 – electrolyte interface this observation suggests that electron transport is more efficient than hole transport. This observation is in agreement with literature and is the reason why backside illumination is commonly used for CuBi_2O_4 .^{52,60,114}

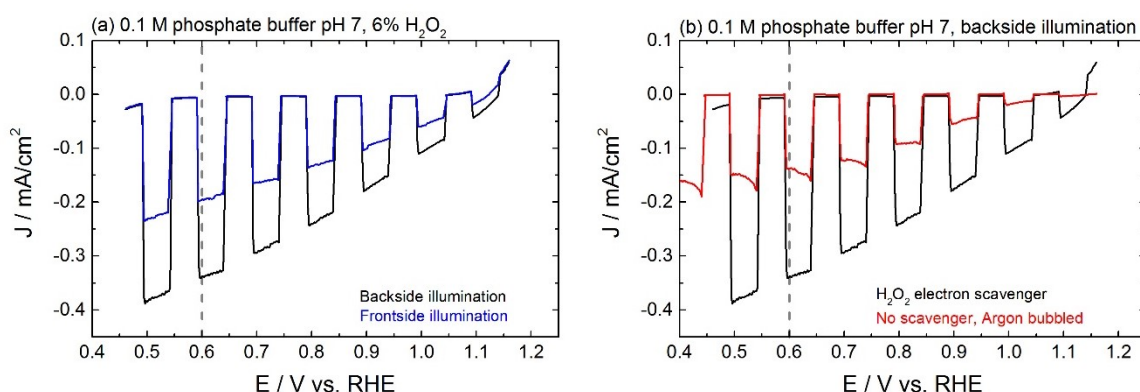


Figure 63: LSV measurements with chopped light: (a) Backside (black) vs. frontside (blue) illumination; (b) H_2O_2 as electron scavenger (black) vs. no scavenger (red); 0.6 V vs. RHE marked in grey.

An electron scavenger is used to avoid any kinetic limitations of the hydrogen evolution reaction (HER) as the (bulk) photoabsorber properties should be investigated and not the (surface) catalytic properties of CuBi_2O_4 . H_2O_2 has been found to be suited for this purpose as it successfully prevents any transient spikes in photocurrent densities (see Figure 63b compared to an electrolyte without scavenger), prevents photocorrosion and (as a polar liquid) does not show solubility issues.⁶⁰ However, it should be noted that H_2O_2 may induce current doubling.^{60,220}

The photocurrent density at 0.6 V vs RHE is used for comparison as it is commonly used in literature. It further avoids any dark current contribution, which is visible at more negative potentials (see Figure 63). This position is marked by the grey dashed line. The measured photocurrent densities are illustrated in Figure 64.

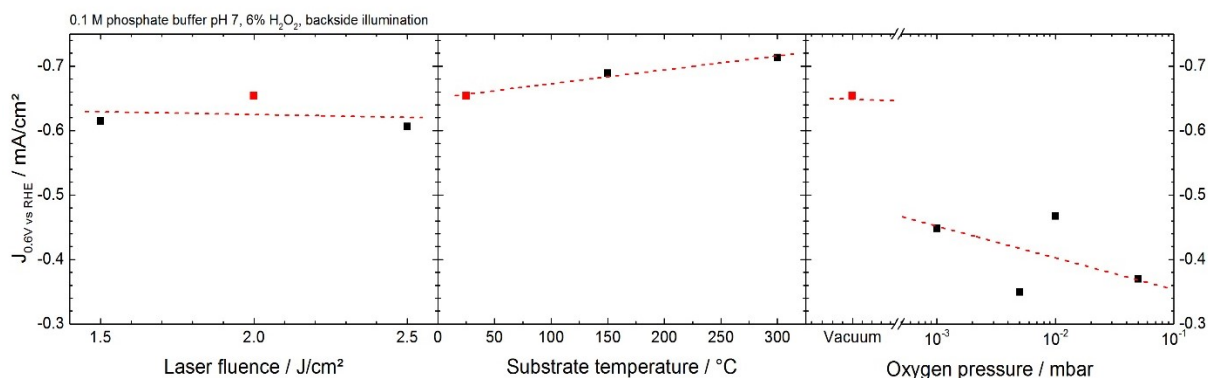


Figure 64: Photocurrent density at 0.6 V vs RHE in dependence of the deposition parameters laser fluence, substrate temperature, and oxygen pressure. Standard conditions marked in red and dashed red lines show linear fits.

The influence of the laser fluence is rather low without a certain trend. An increase in substrate temperature slightly increases the photocurrent density from -0.65 to -0.71 mA/cm². This increase is in agreement with the observed increase in charge carrier diffusion length. The introduction of a oxygen background pressure reduces the current density to values around -0.4 mA/cm², again in agreement with the TRMC results. These values are put in perspective by comparing them to literature values, which is done in Table 7. If multiple CuBi₂O₄ samples were investigated always the current density of the stoichiometric sample is given.

Table 7: Photocurrent densities of various studies, partially estimated from graphs.

Study	Deposition technique	J at 0.6 V vs RHE / mA/cm ²
This study	PLD (single target)	-0.35 – -0.71
Lamers et al. ¹¹⁴	PLD (single target)	-0.4
Lee et al. ⁹⁷	PLD (single target)	-0.6
Gottesman et al. ⁹⁸	PLD (alternating target)	-0.1
Wang et al. ⁵³	Spray pyrolysis	-2
Berglund et al. ⁶⁰	Drop casting	-0.9
Wang et al. ⁵²	Spray pyrolysis	-2

All reported values are in the same range as the values in this study. The comparison to PLD values shows, that the present approach of optimizing the deposition parameters is a successful addition to the annealing optimization by Lamers et al.¹¹⁴ It furthermore shows that the single target growth is superior in terms of photocurrent density and thereby that the stoichiometric target-to-substrate transfer of the ternary CuBi₂O₄ is successful.

Wet chemical deposited films give higher photocurrent densities. This is unexpected considering the TRMC results. The reason should therefore not be linked to the film quality. Obvious other factors are the film thickness and absorption coefficients of the wet chemical

deposited films. The absorption coefficients are much larger (cf. Table 5) and the films are thicker as well (between 270 and 410 nm)^{52,53,60} This means that a much larger fraction of incident photons is absorbed and more charge carriers are generated. However, considering the diffusion length the increased absorption should not affect the photocurrent density significantly. Additional charge carriers would not be able to reach the interfaces before recombining. The reason for the increased photocurrent densities is rather found in the sample morphology. These wet chemical deposited films exhibit a spongy or at least very rough surface compared to the flat PLD films.^{52,53,60} Such morphologies act as rudimentary nanostructures and shorten the distance charge carriers need to travel to reach an interface, similar to the situation in Figure 4c. This facilitates larger current densities even though the intrinsic material properties are inferior.

Another interesting factor is the phase purity of the CuBi_2O_4 films. A second crystalline phase of CuO is visible in samples grown by spray pyrolysis.^{52,53} CuO itself is a promising photocathode material which may generate additional current which cannot be distinguished from the CuBi_2O_4 contribution.²¹⁴ This makes comparisons difficult, similar to the UV/Vis results discussed earlier.

5.2.2 Incident photon-to-current and absorbed photon-to-current efficiency

The incident photon-to-current efficiency (IPCE, also external quantum efficiency EQE) and absorbed photon-to-current efficiency (APCE, also internal quantum efficiency IQE) are investigated to get a more detailed view on the photoelectrochemical performance. IPCE investigates the photocurrent in dependence of the wavelength of the incoming light as depicted in Figure 65a-c. As expected these graphs vaguely resemble the absorption coefficient from Figure 56a as a photocurrent can only be generated if photons are absorbed. A lower laser fluence and increased substrate temperatures lead to increased efficiencies at small wavelength where absorption is strong. The opposite behavior is visible if the oxygen background pressure is applied. The interpretation of these values is difficult as influences of absorption and charge separation efficiency are overlapping.

Therefore APCE is introduced which normalizes the IPCE values with the absorption of the individual sample at the corresponding wavelength. Thereby the ratio of extracted charge carriers to generated charge carriers is calculated and shown in Figure 65d-f. This calculation eliminates the influence of the absorption and therefore gives a better view on the intrinsic material properties. Naturally this evaluation gives no usable information if the absorption is low, i.e. around and below the bandgap for $\lambda > 600$ nm. For lower wavelength the APCE reaches values around 50 – 80% (standard deposition parameters) which indicates a good electrical quality of the films. The APCE increases to around 85% for a lowered laser fluence in the range of $\lambda < 400$ nm. An increase in substrate temperature gives similar rises with values of up to 90%, especially the 150°C sample. Again the introduction of oxygen reduces the APCE to values around 50% in the respective range. These values are in agreement with the TRMC

results and confirm the suitability of a reduced laser fluence and increased substrate temperatures. Another overall APCE value can be estimated when the measured photocurrent density from 5.2.1 is compared to the absorbed photon flux from 5.1.4. An overall APCE of ca. 25% is calculated from these values. This rather low value is explained by the large photon count at $\lambda > 500$ nm where the APCE is low.

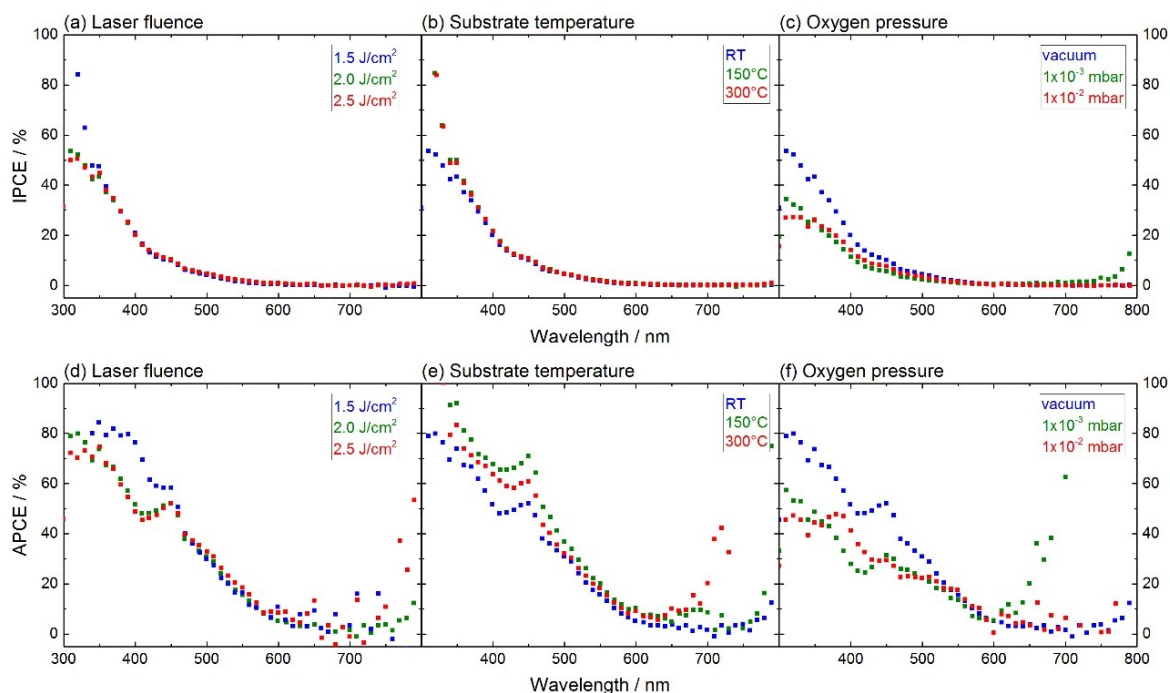


Figure 65: Incident photon-to-current efficiencies (a-c) and absorbed photon-to-current efficiencies (d-f) in dependence of the wavelength of the incident light for various deposition parameters.

Again these values are compared to literature values to put them in perspective. The IPCE and APCE values at 400 nm are selected to make the comparison comprehensible as shown in Table 8. Literature IPCE values range from 7 – 31% and the values from the present study are settled within these margins. This again shows that PLD is an at least a competitive technique in terms of photoelectrochemical film performance. Larger values again originate from increased film thicknesses, absorption coefficients and more complex morphologies as discussed above.

An influence of the first two is prohibited in the APCE. Literature values range from 22 – 43%, whereas the standard conditions PLD sample already shows 51.6%. It further increases to up to 76.4% with a lower laser fluence or higher deposition temperatures. These APCEs above literature values prove the superiority of PLD in terms of intrinsic photoelectrochemical performance compared to wet chemical techniques. Also other publications using PLD do not reach such large values.⁹⁷

Furthermore, the APCE shows the benefit of the lower fluence of 1.5 J/cm². This is also visible in the TRMC results but does not translate into the highest photocurrent densities due to a reduced film thickness and thereby reduced light absorption.

Table 8: Reported IPCE and APCE values from various publications, data estimated from graphs at 400 nm and 0.6 V vs RHE (if not stated otherwise).

Study	Deposition technique	IPCE _{400 nm} / %	APCE _{400 nm} / %
This study	PLD (single target)	11.4 – 21.8	28.0 – 76.4
<i>Lamers et al.</i> ¹¹⁴	PLD (single target)	15 _(0.8 V vs RHE)	37 _(0.8 V vs RHE)
<i>Lee et al.</i> ⁹⁷	PLD (single target)	7 _(0.4 V vs RHE)	35 _(0.4 V vs RHE)
<i>Gottesman et al.</i> ⁹⁸	PLD (alternating target)	14	22
<i>Wang et al.</i> ⁵³	Spray pyrolysis	31	43
<i>Berglund et al.</i> ⁶⁰	Drop casting	26	34
<i>Wang et al.</i> ⁵²	Spray pyrolysis	31	42

In summary, the APCE results are in agreement with the TRMC results showing the outstanding film quality that PLD can produce. A low laser fluence combined with an increased substrate temperature may give even larger efficiencies. Larger photocurrent densities should then be possible, especially when the initial thickness optimization is revisited.

5.3 Conclusion and outlook

CuBi₂O₄ was grown by PLD from a single target to assess the suitability of PLD to grow high quality complex metal oxides for solar fuel applications and to investigate the influence of the deposition parameters laser fluence, substrate temperature and oxygen background pressure.

All deposited films are phase pure by XRD and Raman spectroscopy. EDX and RBS measurements revealed slightly bismuth rich stoichiometries but increased substrate temperatures and no background pressure can keep the excess low. Occasional bismuth-rich grains may attribute for the excess. Apart from this, CuBi₂O₄ films are flat and show good coverage in SEM, only at low thicknesses (≈ 75 nm) incomplete substrate coverage becomes an issue. No contaminations could be traced by XPS beside the inevitable adventitious carbon at the surface.

The bandgap is around 1.85 eV independent from the deposition parameters. This is at the upper end of reported bandgaps between 1.5 - 1.9 eV, which indicates high film quality without additional CuO.^{53,97,98} Without any secondary phases the absorption is rather weak and decreases even further with the oxygen background pressure. This weak absorption has been addressed as a bottleneck before.⁶⁰

Unfavorable charge transport properties are often mentioned as another bottleneck on CuBi₂O₄.^{52,53} The TRMC measurements in this study validate this observation but low fluences and high substrate temperatures are beneficial. By that the charge carrier diffusion length can be roughly doubled compared to wet chemical depositions.^{52,60} This validates the excellent film quality of PLD grown CuBi₂O₄.

Photocurrent densities of up to -0.71 mA/cm² are competitive with literature values even though they do not represent new records. This view changes in IPCE and especially APCE considerations: APCE_{400nm} values of up to 76.4% are shown whereas literature values only reach 43%. These value prove a charge extraction which is unmatched in literature.

Building on these observations the PLD process could be further optimized by combining low fluences with high temperatures. A subsequent thickness optimization may improve photocurrents. Furthermore additional functional layers could be introduced, e.g. NiO as hole blocking layer at the FTO contact like *Song et. al.* employed.²⁰⁰ Also efforts could be pursued to avoid the H₂O₂ electron scavenger and to construct HER stable PEC cells as shown for Cu₂O photocathodes.^{49,50,221} Another way could be investigations on tandem devices or structured substrates even though the latter one is challenging for PLD.

Overall it can be concluded that PLD is an excellent tool for PEC research to deposit high quality thin films. The precise thickness control, the lack of contaminations and the flatness of the deposited films make it especially suited to investigate intrinsic properties of new potential materials like charge transport or optical properties.

6 Summary and outlook

Within this thesis the use of oxides as extremely thin absorbers for photoelectrochemical applications was investigated. Their limited charge carrier diffusion length make minimal absorber thicknesses inevitable to achieve efficient charge carrier extraction. A combination with nanostructures is furthermore beneficial to allow strong optical absorption with moderate absorption coefficients.

Three oxides, Bi_2O_3 , $\text{Mn}_2\text{V}_2\text{O}_7$ and CuBi_2O_4 , were deposited using two explicit thin film deposition techniques, ALD and PLD. The resulting thin films were subsequently investigated to evaluate key performance indicators for PEC applications and to benchmark the individual growth processes.

Chapter 3 investigated the growth of Bi_2O_3 from $[\text{Bi}(\text{tmhd})_3]$ in a thermal and a plasma-enhanced ALD process. The thermal process shows a growth rate of 0.24 \AA/cycle in the temperature window from $210 - 270^\circ\text{C}$. The resulting films exhibit significant carbon contaminations of $9.4 \text{ at.}\%$. The growth rate was increased to 0.35 \AA/cycle using an oxygen plasma in the temperature window from $280 - 330^\circ\text{C}$. The amount of carbon impurities decreases to $4.3 \text{ at.}\%$. While the shift of the temperature window could not be finally resolved the GPC increase and contamination level decrease were explained using real-time spectroscopic ellipsometry measurements: water is not able to fully remove the $\text{Bi}(\text{tmhd})_x$ surface layer but the oxygen plasma is. The RTSE investigations were extended by the introduction of a novel double-layer optical model. Thereby it is possible to follow the $\text{Bi}(\text{tmhd})_x$ surface layer in addition to the Bi_2O_3 bulk in the PE-ALD process. Furthermore it was observed that reproducibility of the depositions is a major issue, limiting the usability of the established processes.

Chapter 4 therefore expands the ALD topic to another material, the ternary oxide $\text{Mn}_2\text{V}_2\text{O}_7$. Thermal ALD processes to deposit the individual binary oxides MnO and VO_x were established at 200°C with growth rates of 0.91 \AA/cycle and 0.25 \AA/cycle , respectively. A supercycle was constructed from these values where slight adjustments of the cycle ratio allow changes in stoichiometry. Annealing in argon at 500°C induces a crystallization into the desired β -phase and an almost ideal stoichiometry of $\text{Mn}_2\text{V}_{2.06}\text{O}_{7.12}$ is achieved. An indirect bandgap of 1.83 eV was measured. Under OER conditions an oxidation of Mn(II) was observed. An additional sacrificial MnO top layer is introduced to avoid any influence on the integrity of the $\text{Mn}_2\text{V}_2\text{O}_7$ film. However, even with these promising material properties the measured photocurrent densities were minimal with an APCE below 1% . The reason for the weak PEC performance is likely an intrinsically low charge carrier mobility.

Further steps in ALD of Bi_2O_3 may include the identification of intermediate species, e.g. by IR spectroscopy. For $\text{Mn}_2\text{V}_2\text{O}_7$ this includes the influence of the deposition temperature and the investigation of nucleation effects. However, detailed further investigations are barely justified in both cases.

Instead the suitability of ALD to deposit extremely thin absorbers should be discussed. One fundamental benefit of ALD is the extraordinary process control in terms of films thickness, uniformity and conformality, making it very promising for nanostructured samples. However, the present investigations have shown that such a level of process control can be very challenging to achieve for certain multinary materials, even on flat samples. Process control will be even more challenging when the next step towards full coverage of nanostructures is tackled, especially if PE processes with their directional characteristics are employed. In that sense the effort to establish an ALD process can only be recommended if a promising oxide is identified and if the performance bottleneck is clearly assigned to a mismatch of absorption and charge carrier transport.

Another important consideration should be the impurity tolerance. The experiments have shown that carbon residues are an issue in ALD processes. Carbon contents of 1 – 5 at.% were observed after annealing in air. The stoichiometry in complex oxides adds another challenge. As shown the ALD processes are not 100% uniform and therefore slight alterations in the resulting stoichiometry will be present. Therefore the chosen material should be robust against such non-ideal compositions. Especially the charge carrier transport can be drastically hindered by defects caused by impurities as they can act as recombination centers.

The key to a successful use of ALD is therefore exceptional process control and low contamination levels. On a reaction mechanism level this means that the two surface reactions, chemisorption of the precursor and ligand removal, have to be complete while side reactions as multilayer absorption have to be avoided. Straightforward requirements are therefore high energy i.e. very reactive precursors and low energy i.e. stable reaction products, ideally with a mid-energy intermediate surface species. An example of such a process may be ALD of Al_2O_3 from the highly pyrophoric precursor TMA and water, which is often considered a model ALD process.^{67,75} The preference of stable products implies a prime use of ALD grown films in PEC application as protection layers. An example is TiO_2 .^{222,223}

Following the thought, stability can be fundamentally interpreted as the ability of a material to withstand electron loss or capture (stability against oxidation and reduction). Physically speaking this translates into a large ionization energy and a low electron affinity and hence: a large bandgap. The general trend that large bandgaps correlate with increased stability under PEC conditions has been reported in literature.¹¹ Concerning ALD this observation could be extended towards: Good process control points towards stable products, points towards large bandgaps. It certainly fits for Al_2O_3 with a bandgap of ca. 7 eV and the bandgap of TiO_2 with 3.2 eV is rather large as well.^{147,224} Although many other factors influence process control and bandgaps, ALD of promising low bandgap absorbers may be intrinsically difficult.

Chapter 5 followed a different pathway using PLD to grow CuBi_2O_4 . The influence of the deposition parameters laser fluence, substrate temperature and oxygen background pressure was investigated. The influence of the three parameters are rather subtle but general observations over all samples include: phase purity, shown by XRD and Raman spectroscopy;

slightly bismuth rich films without any further contamination, shown by EDX, RBS and XPS; an indirect bandgap around 1.85 eV, shown by UVVis; a roughly doubled charge carrier diffusion length compared to wet chemically deposited films, shown by TRMC; and almost doubled APCE values compared to literature values.

These observations prove that PLD is very suited to grow high quality thin films for PEC applications with comparatively low effort. The deposition parameters offer optimization potential, even though the influence of an optimized thermal post-deposition treatment may be larger.¹¹⁴

PLD therefore has a lot of potential for initial material evaluation within PEC research. With the precise thickness control and lack of impurities it is suited to investigate fundamental material properties on model like thin films. A possible extension of the present single-target approach to multi-target depositions offers the potential to alter the film stoichiometries or even to deposit high-quality material libraries to identify promising compositions. Further than that the applications of PLD are limited. An upscaling towards larger areas is not trivial and also the coverage of complex geometries is challenging with the strongly directional ablation and collection of the material.

On a broader scale two final aspects should be mentioned. The first one is the suitability of oxides as absorber materials in PEC devices. Three principle benefits of oxides were mentioned in the introductory part of this thesis. The first two are: (1) the ease of sample preparation and (2) the inherent stability of oxides. The present investigations have shown that these two factors can only be understood as general trends but not as absolute truths for all oxides. Especially the stability can be discussed. Not only can many oxides not withstand the harsh PEC conditions, in many cases such a stability may not be necessary.⁴⁹ In most cases the absorber material is accompanied by additional functional layers like protection layers or catalysts.^{43,45,62,221} In that way the absorber does not have to be an “all-in-one” stable photocatalyst but the different requirements may be met by multiple materials. The third benefit of oxides, (3) their extreme versatility, is however true and therefore offers the possibility that oxides fulfill critical functions in a final PEC device. Maybe even as absorber.

The second aspect is the contribution of PEC water splitting on a global energy scale. As shown in the introduction the solar-to-hydrogen efficiencies of PEC devices are rather low, below 10% using the presented metal oxide + bottom absorber approach. Other devices using expensive catalysts and III/V semiconductors reach efficiencies around 20%, on lab scale.⁴⁶ The combination of a photovoltaic cell with an electrolyzer is the direct architecture to compare to. Efficiencies around 30% can be achieved there.^{225,226} This superior efficiency already shows the challenge that PEC devices still have ahead. PEC devices are not available on commercial scale, contrary to PV systems and electrolyzers. Solar modules with an efficiency of up to 24% are currently available, the efficiency of electrolysis is 56 – 73%, depending on the technique.^{24,227} Therefore, STH efficiencies of around 17% are achievable using existing commercial solutions. The cost factor will be another challenge for PEC devices. Even if cheap

materials like some metal oxides are used it will be difficult to compete with existing silicon-based PV. Already today the main cost factor is not the solar module itself but the balance of system (BOS) costs, including wiring, installation systems etc. It seems unlikely that the BOS costs will decline for PEC devices with their need for electrolyte, hydrogen, and oxygen handling. Exactly these points were addressed by *Jacobsson*.²²⁹ The idealistic advantages of integrated PEC devices with lower losses and decreased overpotentials due to lower current densities are more than overcast by their practical cost. As a consequence, PEC devices will most likely not play a significant commercial role in the near future.

7 Appendix

7.1 Supporting data

7.1.1 ALD of Bi_2O_3

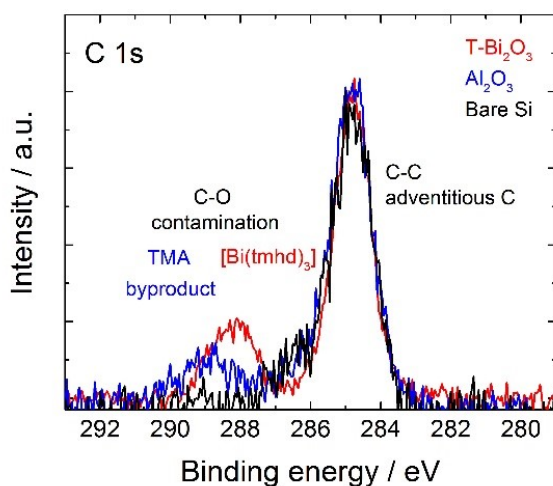


Figure S 1: C 1s spectra of a bare silicon wafer (black), a pure Al_2O_3 sample (blue), and a T-ALD Bi_2O_3 sample (red).

A bare silicon wafer only shows peaks assigned to adventitious carbon around 285 eV. A sample with only Al_2O_3 exhibits another peak at 289 eV which is therefore ascribed to contaminations from the Al_2O_3 ALD process. Measurements from Bi_2O_3 samples show a contamination peak at a different position of 288 eV which are therefore ascribed to contaminations from the $[\text{Bi}(\text{tmhd})_3]$ precursor.

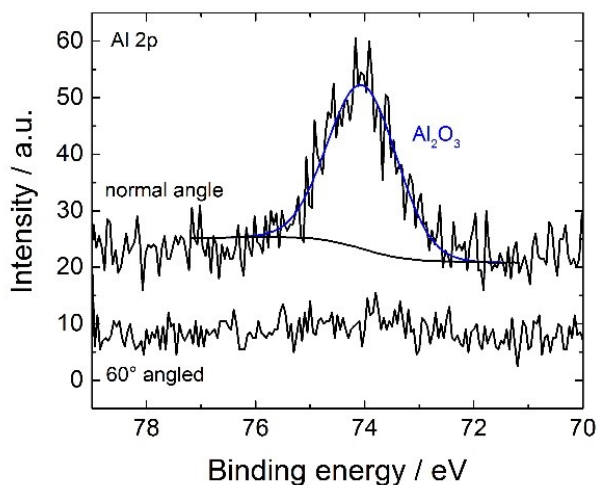


Figure S 2: Al 2p spectra of a PE-ALD Bi_2O_3 sample measured under normal angle (top) with a fit assigned to Al_2O_3 (blue) and the same sample measured under 60° (bottom).

Under normal angle a small amount of aluminium is detected for a PE-ALD sample of Bi₂O₃. This signal completely vanishes when measured under 60°.

Parameterization of the Bi(tmhd)_x surface layer

The refractive indices n of the chemisorbed surface layer of Bi(tmhd)_x were parameterized after the first [Bi(tmhd)₃] exposure, during the purge step, using a Cauchy model. Since no data is available on the refractive index of a single Bi(tmhd)_x layer, a certain dispersion model had to be assumed. Since there is no clear evidence of a resonant frequency (the presence of which would suggest a Lorentz oscillator model), the Cauchy model is the most appropriate choice. The Cauchy model describes the dispersion of n as¹⁰⁵:

$$n = n_0 + \frac{n_1}{\lambda^2} + \frac{n_2}{\lambda^4} \quad (27)$$

Although empirical in nature, it is an often used and powerful dispersion model for describing the index of refraction of dielectric (insulating) and semiconducting materials. It works best when there is little or no optical absorption in the region of interest, which is indeed the case for a monolayer of Bi(tmhd)_x. The Cauchy parameters n_0 , n_1 , and n_2 are fit parameters and have only limited physical meaning; specifically, n_0 represents the (usually constant) refractive index at long wavelengths, n_1 describes the curvature in the middle of the visible spectrum, and n_2 is used to describe the much stronger curvature towards the shorter wavelengths.¹⁰³ Values that were obtained for these parameters are $n_0 = 1.49$, $n_1 = 0.01$, $n_2 = 0.00$. The optical properties (n and k) of bulk Bi₂O₃ were determined after the last ALD cycle when the maximum Bi₂O₃ film thickness is achieved and no Bi(tmhd)_x surface layer is present. An example of the double layer fit is shown in Figure S 3.

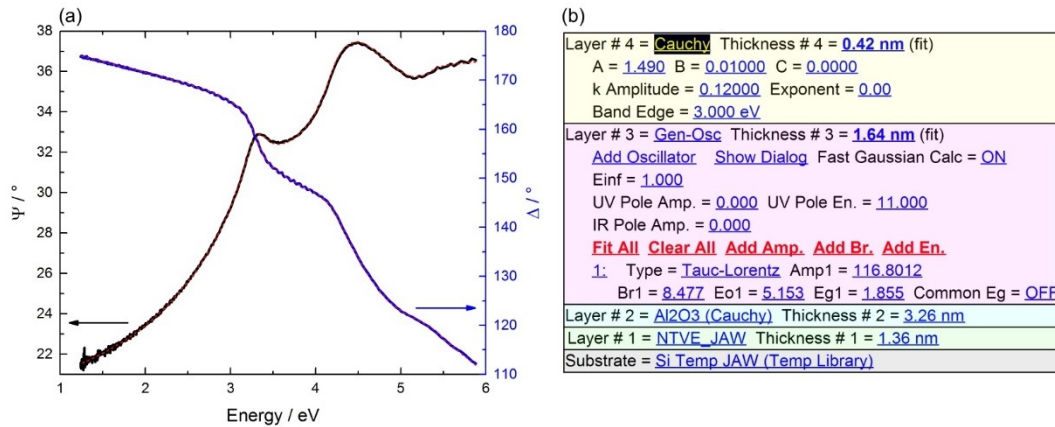


Figure S 3: Example of a fit of a RTSE spectrum: (a) measured Ψ (black) and Δ (blue) with fits (dashed red); (b) Double-layer optical model with fit parameters and variables.

7.1.2 ALD of $\text{Mn}_2\text{V}_2\text{O}_7$

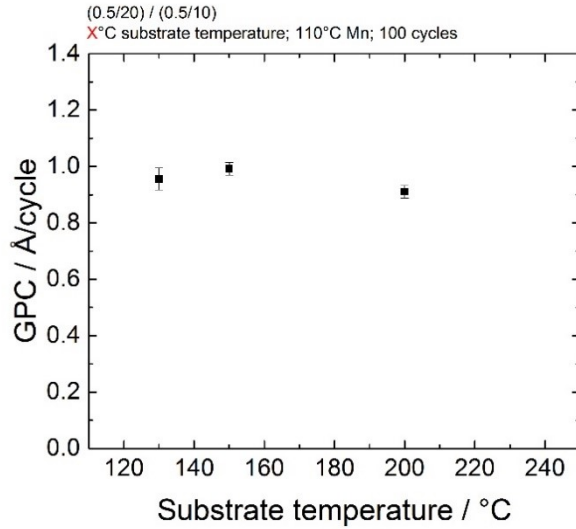


Figure S 4: Growth rate of the MnO_x ALD process as function of the substrate temperature.

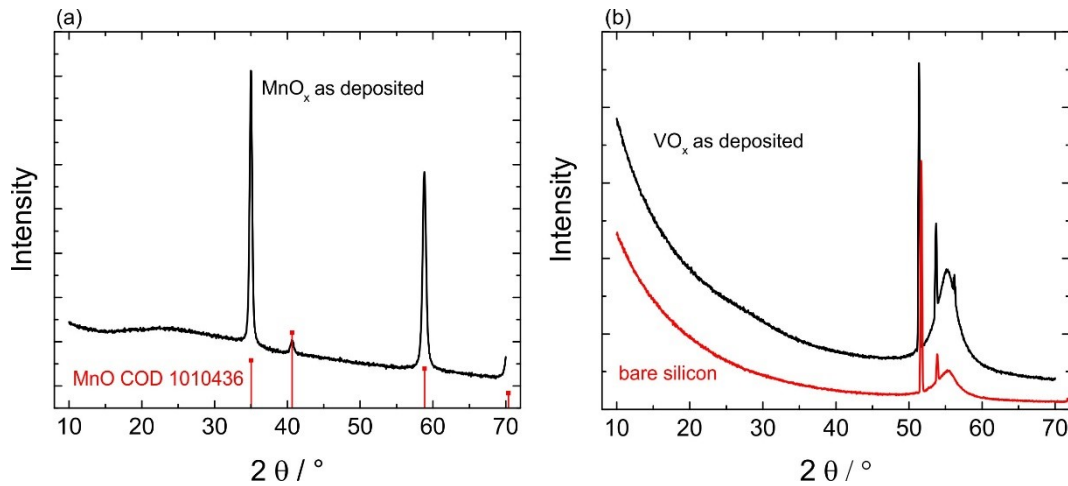


Figure S 5: Diffractograms of (a) MnO_x (black) on silicon and literature signals for MnO (red) and (b) VO_x (black) on silicon and a bare silicon substrate (red).¹⁸⁸ The reflections of silicon in (b) are only visible if the (square) sample is aligned with the direction of the X-rays. If the sample is rotated by 45° in the xy -plane these reflections vanish as visible in (a).

The reflections of the as deposited MnO_x film can be ascribed to cubic MnO proving at least partial crystallinity. Differences in intensities are usually due to a preferred orientation of the sample. As deposited VO_x shows the same signal as a bare silicon wafer, indicating an amorphous film. The reflections of the bare silicon wafer are only visible when the crystal lattice (and breaking edge of $\text{Si}(100)$ pieces) is perpendicular to the incoming X-rays. In other measurements the samples on silicon are usually rotated by 45° inhibiting this characteristic pattern.

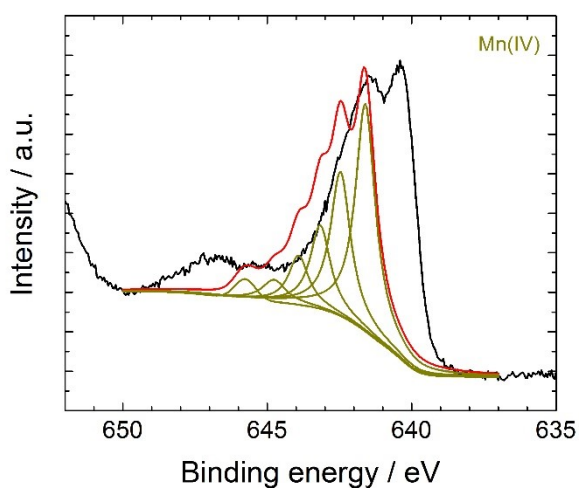


Figure S 6: Mn 2p region fitted with the Mn(IV) pattern suggested by Biesinger et al. (dark yellow), peak sum in red, raw data in black.¹⁹³

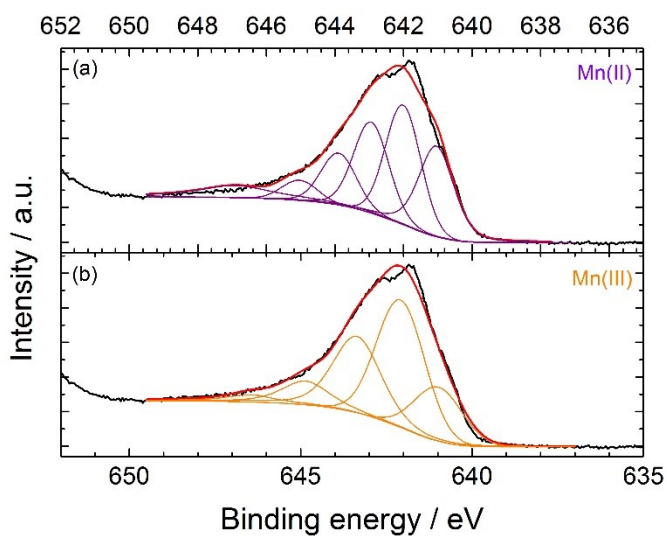


Figure S 7: Mn 2p region of an $\text{Mn}_2\text{V}_2\text{O}_7$ film annealed in air at 500°C, (a) with Mn(II) fit and (b) Mn(III) fit according to Biesinger et al.¹⁹³

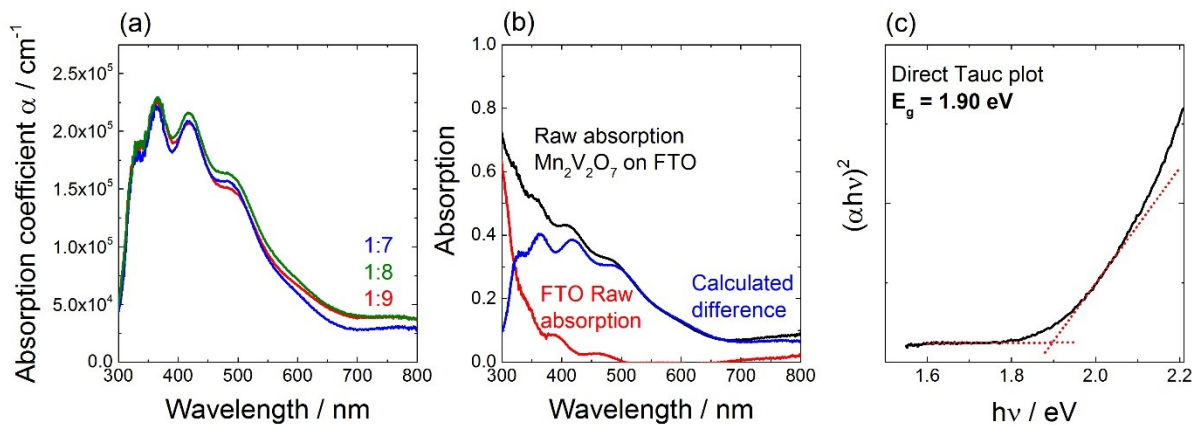


Figure S 8: (a) Absorption coefficient α vs. wavelength of the samples with 1:7 (blue), 1:8 (green), and 1:9 (red) cycle ratio; (b) Raw absorption of the 1:9 cycle ratio sample (black) vs. wavelength compared with the raw FTO raw absorption (red) and calculated difference (blue); (c) Direct Tauc plot $E_g = 1.90$ eV

absorption of a bare FTO substrate (red), and the difference of both measurements (blue) which builds the base for the UVVis considerations; (c) Indirect Tauc plot of the 1:9 cycle ratio sample with an estimated bandgap of 1.90 eV.

Calculation of the oxidized MnO film thickness

The showed CV was recorded at a scan rate of 25 mV/s, making it easily convertible into time vs. current density. Within this conversion the potential range of the first and the second cycle were integrated from 1.1 – 1.8 V vs. RHE, respectively. The difference of these integrations is the charge transferred during the oxidation (per area). It is calculated to:

$$q_{area} = 4.307 \frac{mC}{cm^2} \quad (28)$$

Combining the transferred charge with the Faraday constant F and the number of transferred electrons per manganese atom z gives the amount of oxidized manganese. z was set to 1.5 based on previous investigations.¹⁷¹

$$n_{area} = \frac{q_{area}}{z \cdot F} = 2.976 \cdot 10^{-8} \frac{mol}{cm^2} \quad (29)$$

Including the molar mass M = 70.94 g/mol of MnO gives the mass:

$$m_{area} = n_{area} \cdot M = 2.111 \cdot 10^{-6} \frac{g}{cm^2} \quad (30)$$

Finally the density $\rho = 5.45 \text{ g/cm}^3$ is needed to calculate the oxidized thickness of MnO.

$$d_{ox} = \frac{m_{area}}{\rho} = 3.874 \cdot 10^{-7} \text{ cm} = 3.874 \text{ nm} \quad (31)$$

To calculate the equivalent amount of MnO corresponding to the 23 nm $\text{Mn}_2\text{V}_2\text{O}_7$ the ALD growth rate and number of binary MnO ALD cycles is used

$$d_{MnO} = 0.91 \frac{\text{\AA}}{\text{cycle}} \cdot 80 \text{ cycles} = 7.28 \text{ nm} \quad (32)$$

Vice versa the corresponding thickness of oxidized $\text{Mn}_2\text{V}_2\text{O}_7$ is calculated by the simple relation

$$d_{ox, \text{Mn}_2\text{V}_2\text{O}_7} = \frac{23 \text{ nm} \cdot 3.874 \text{ nm}}{7.28 \text{ nm}} = 12.24 \text{ nm} \quad (33)$$

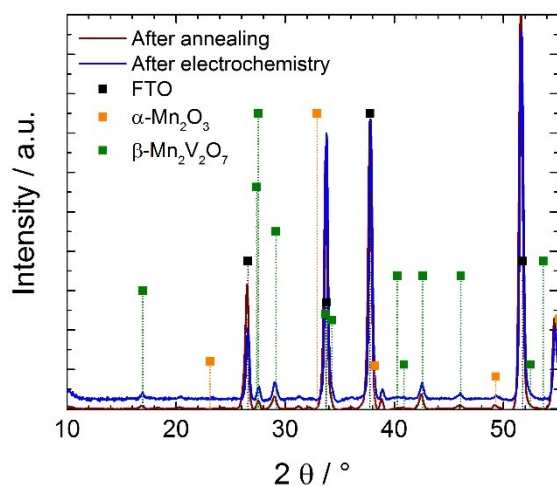


Figure S 9: Diffractograms of $\text{Mn}_2\text{V}_2\text{O}_7$ after annealing (red) and after electrochemistry (blue) compared to literature reflections of FTO (black), α - Mn_2O_3 (orange), and β - $\text{Mn}_2\text{V}_2\text{O}_7$ (green).^{183,190}

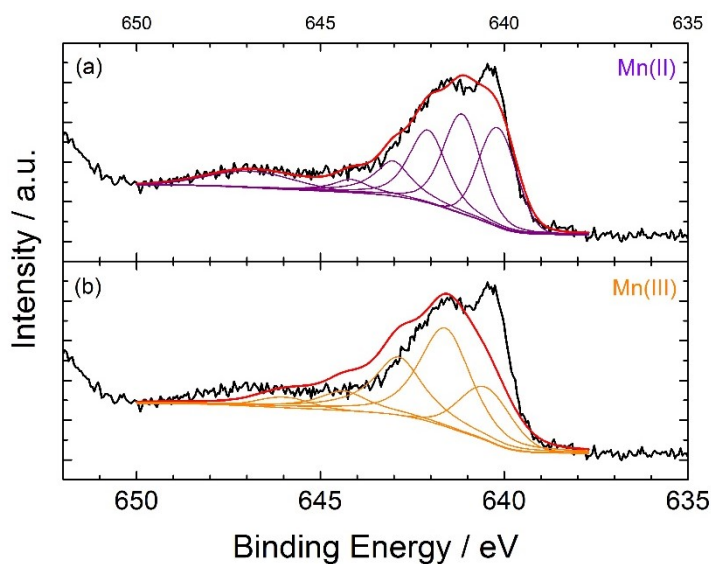


Figure S 10: XPS measurement of the Mn 2p 3/2 region of $\text{Mn}_2\text{V}_2\text{O}_7$ after electrochemistry fitted with different routines from Biesinger et al.¹⁹³, (a) Mn(II) fit in purple, (b) Mn(III) fit in orange, raw data in black, peak sum in red.

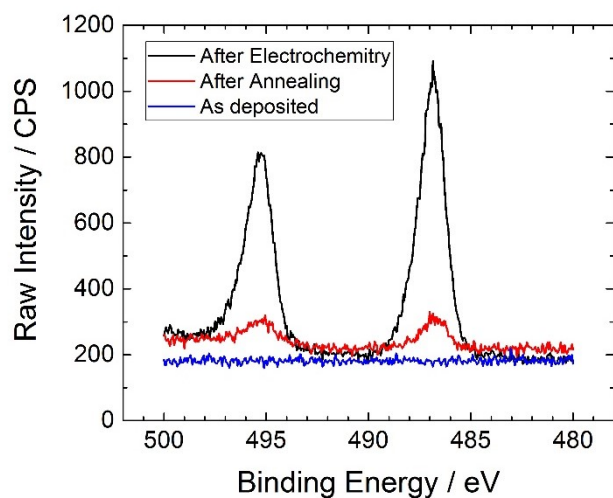


Figure S 11: Raw XPS spectra of the Sn 3d region of $\text{Mn}_2\text{V}_2\text{O}_7$ samples, red after annealing, black after electrochemistry.

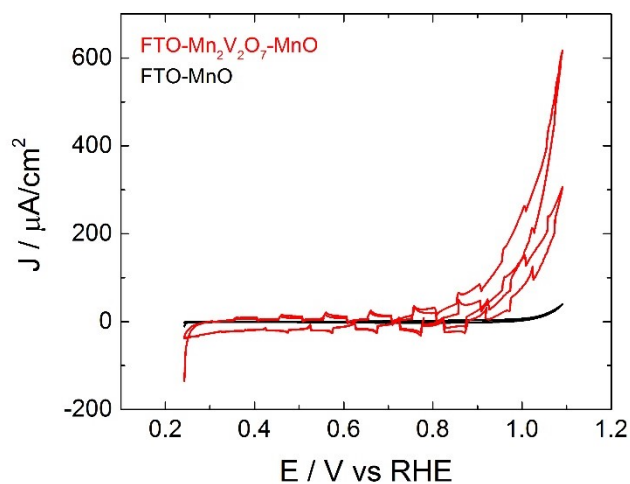


Figure S 12: CV scan of a $\text{Mn}_2\text{V}_2\text{O}_7$ sample (red) compared to an FTO substrate covered with the MnO sacrificial layer (black).

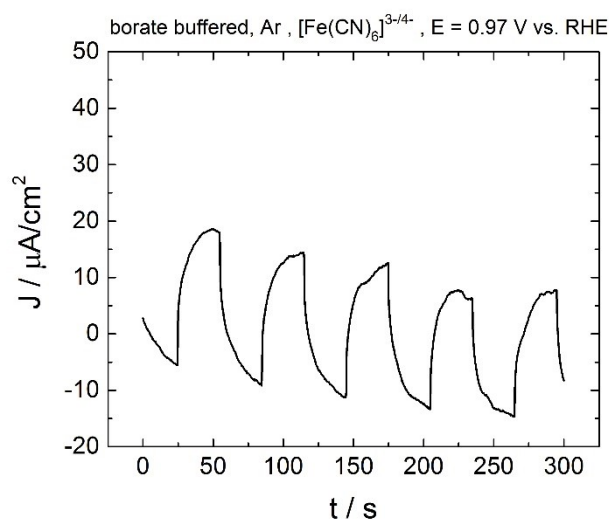


Figure S 13: CA measurement of $\text{Mn}_2\text{V}_2\text{O}_7$ in borate buffer with $[\text{Fe}(\text{CN})_6]^{3-/4-}$ scavenger.

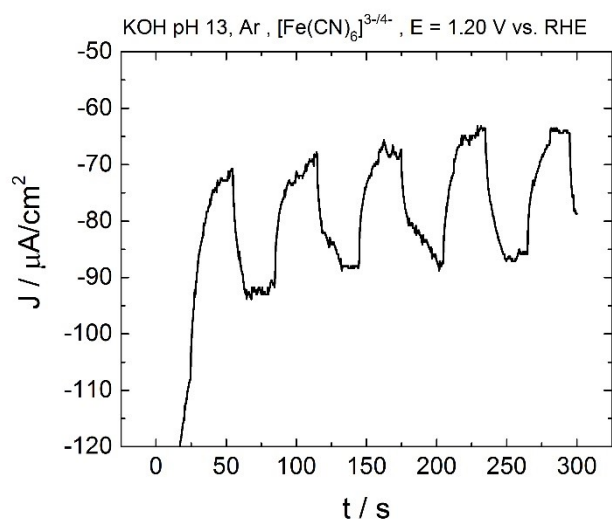


Figure S 14: CA measurement of $\text{Mn}_2\text{V}_2\text{O}_7$ in 0.1M KOH with $[\text{Fe}(\text{CN})_6]^{3-/4-}$ scavenger.

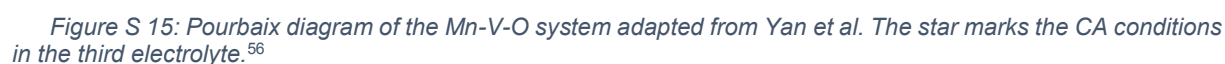


Figure 1 is a plot showing the dependence of film thickness (nm) on three parameters: Laser fluence (J/cm^2), Substrate temperature ($^{\circ}\text{C}$), and Oxygen pressure (mbar). The y-axis represents Film thickness / nm, ranging from 95 to 135. The x-axis is divided into three sections: Laser fluence / J/cm^2 (1.4 to 2.6), Substrate temperature / $^{\circ}\text{C}$ (50 to 300), and Oxygen pressure / mbar (Vacuum to 10^{-1}). The data points show that film thickness generally increases with laser fluence and substrate temperature, and decreases with increasing oxygen pressure.

Parameter	Value	Film thickness / nm
Laser fluence / J/cm^2	1.5	100
Laser fluence / J/cm^2	2.0	130
Laser fluence / J/cm^2	2.5	124
Substrate temperature / $^{\circ}\text{C}$	50	130
Substrate temperature / $^{\circ}\text{C}$	150	121
Substrate temperature / $^{\circ}\text{C}$	300	120
Oxygen pressure / mbar	Vacuum	130
Oxygen pressure / mbar	10^{-3}	123
Oxygen pressure / mbar	10^{-2}	119
Oxygen pressure / mbar	10^{-1}	115

(a) XRD patterns of CuBi_2O_4 at 300°C under different pressures. The y-axis is Normalized intensity and the x-axis is $2\theta / ^\circ$ (ranging from 20 to 65). The patterns are stacked vertically for pressures of 0 mbar (black), 1.5 J/cm^2 (red), 2.5 J/cm^2 (green), and $5 \times 10^{-2} \text{ mbar}$ (blue). The CuBi_2O_4 reference pattern is shown at the bottom in orange. The patterns show a clear shift and broadening of the peaks as the pressure increases, indicating a structural transition.

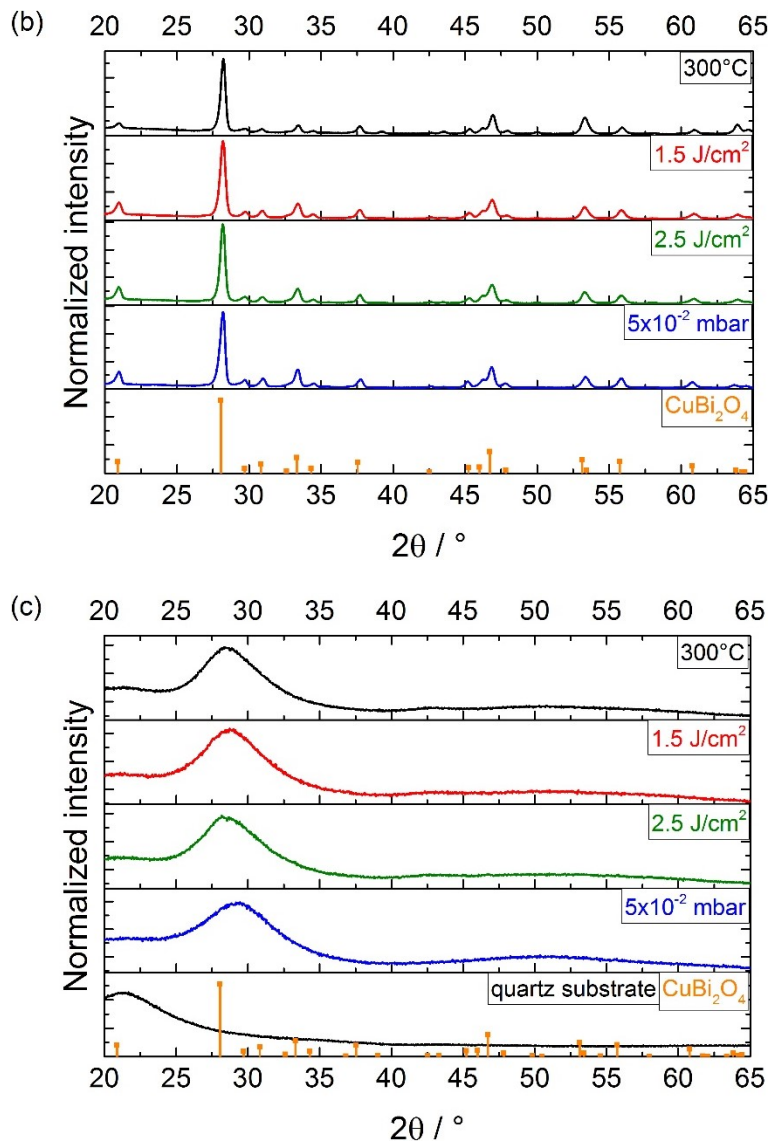


Figure S 17: GIXRD patterns of CuBi₂O₄ thin films grown with varying parameters, (a) on FTO after annealing; (b) on quartz after annealing; (c) on quartz as deposited, reference pattern in orange, quartz substrate in black.²⁰⁵

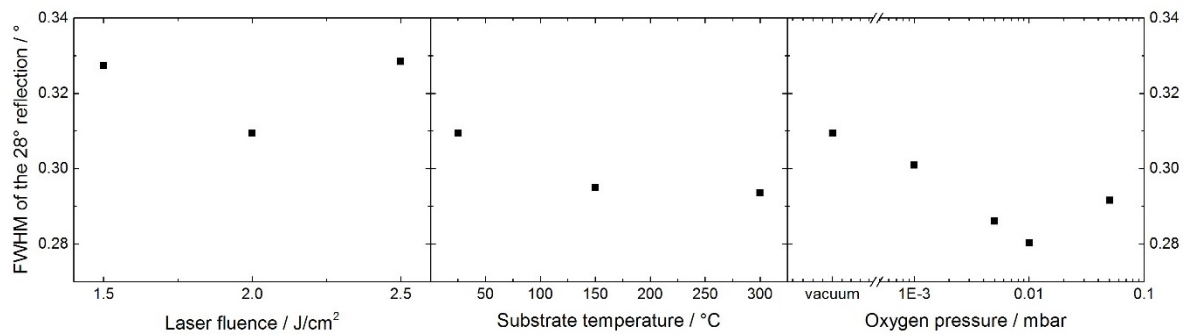


Figure S 18: Full width at half maximum of the 28° reflection in GIXRD measurements.

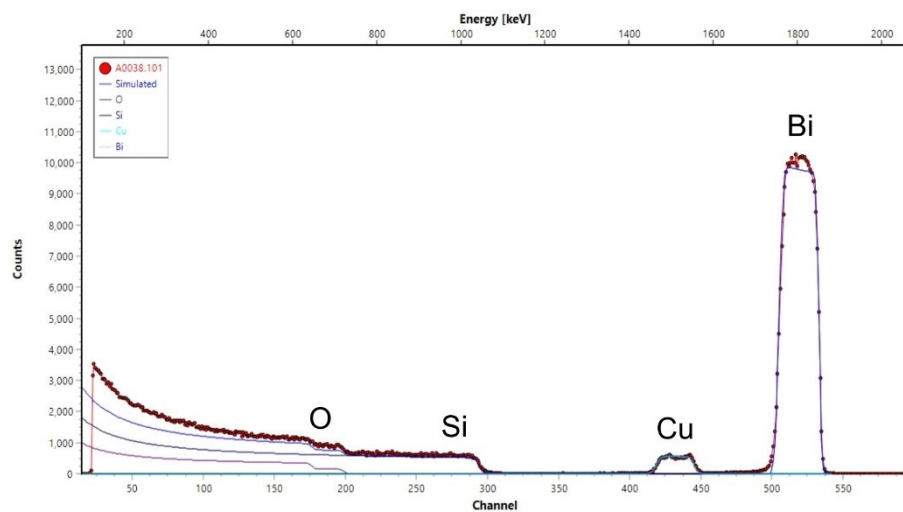


Figure S 19: RBS measurement of CuBi_2O_4 (standard deposition conditions) on quartz.

SEM images

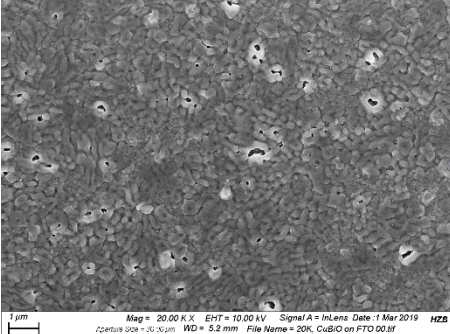
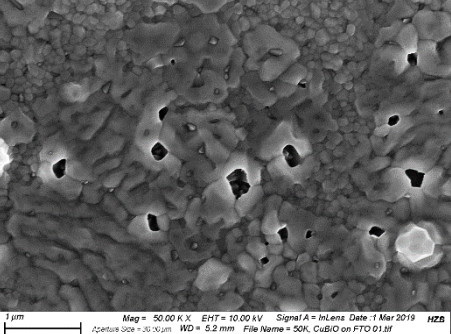
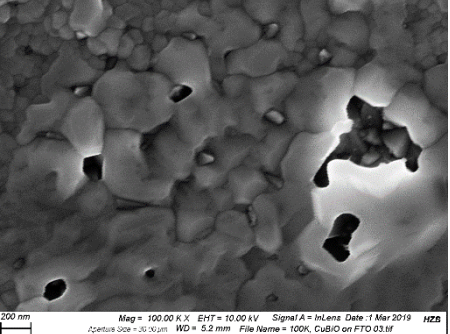
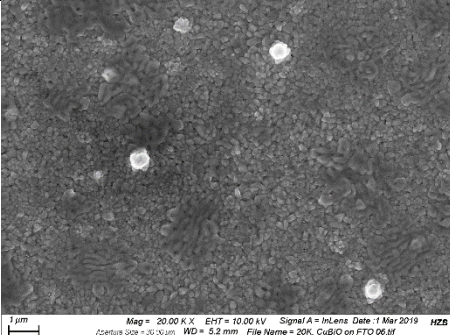
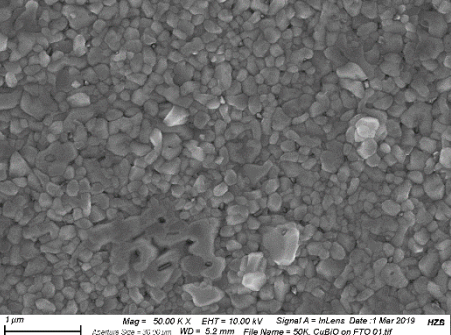
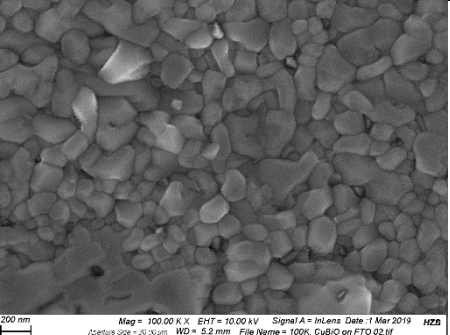
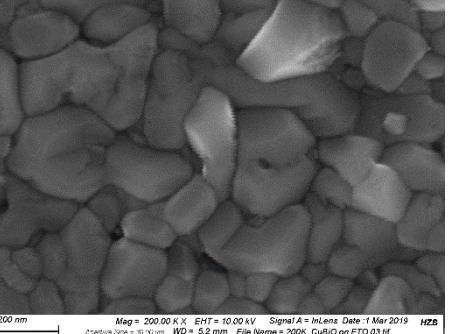
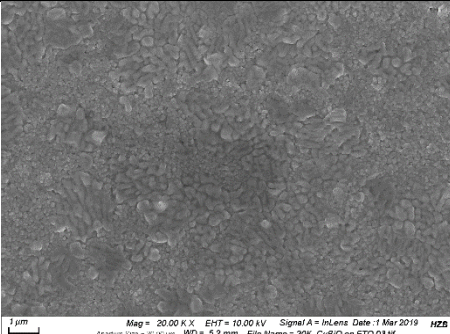
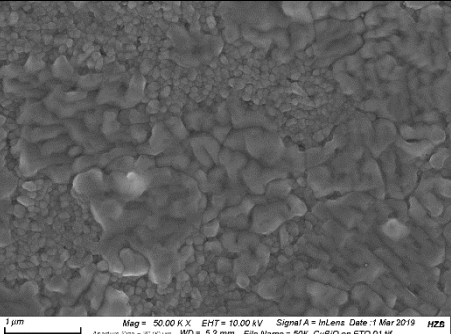
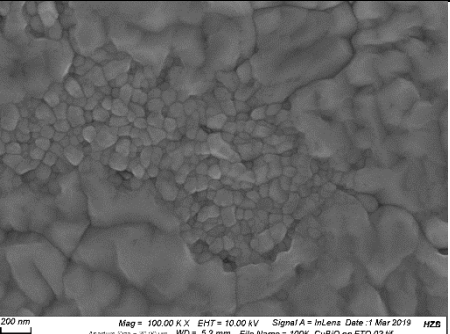
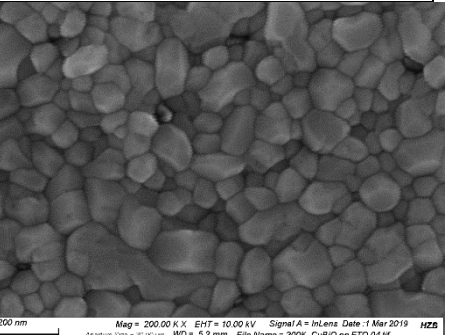
Fluence series	Magnification = 20k	50k	100k	200k
1.5 J/cm ²				
2.0 J/cm ² (Standard Conditions)				
F = 2.5 J/cm ²				

Figure S 20: SEM images part 1

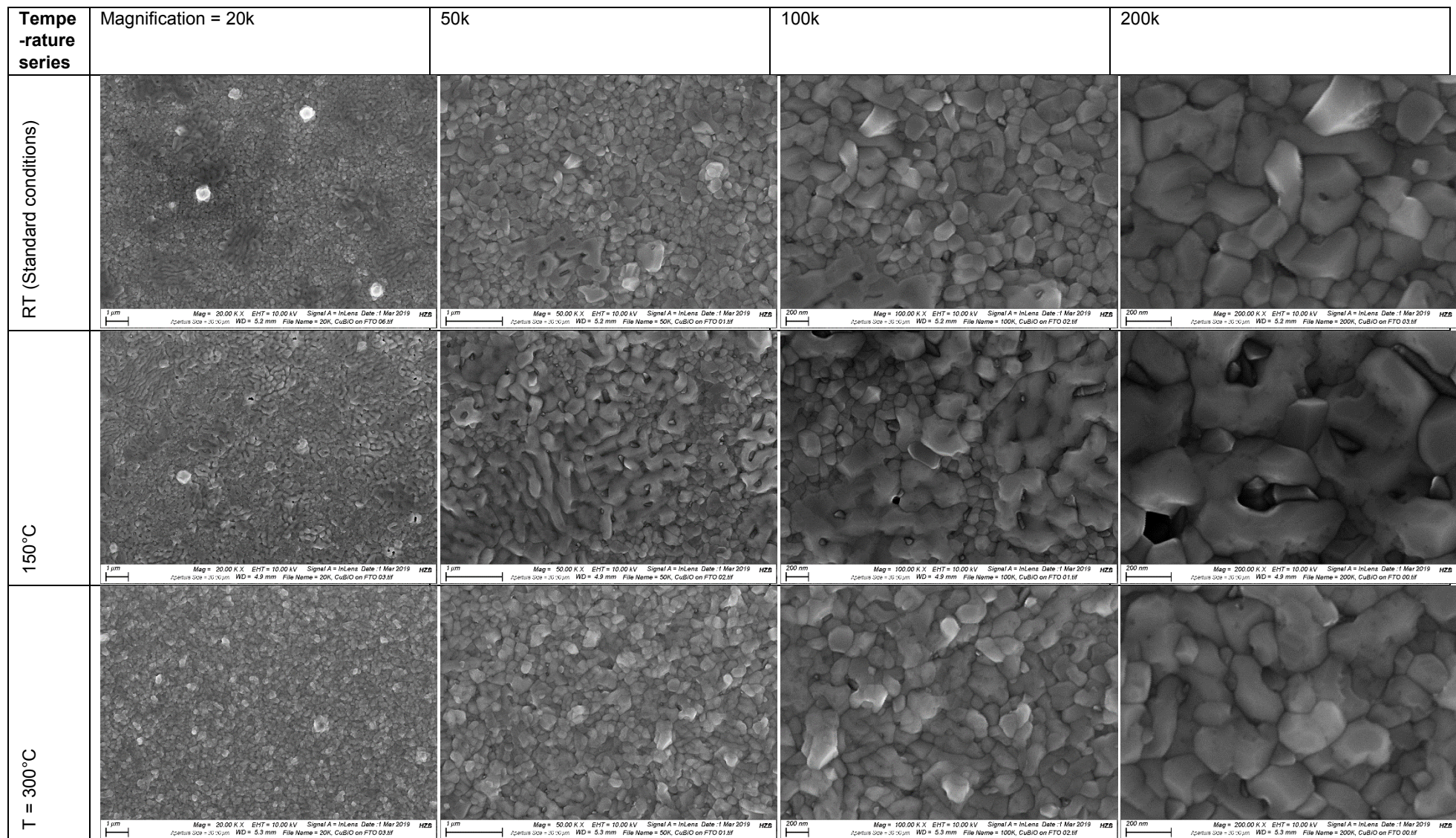


Figure S 21: SEM images part 2

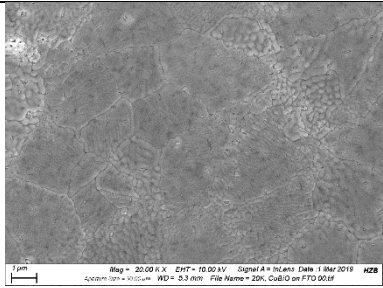
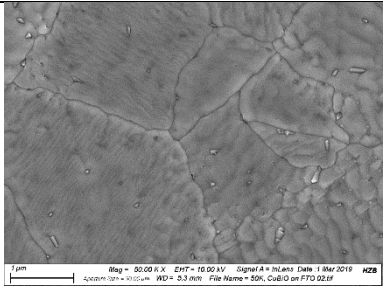
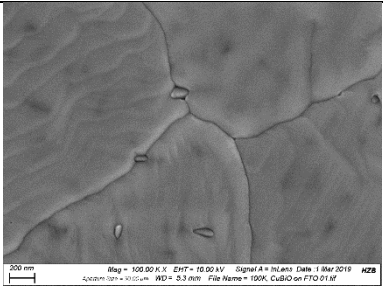
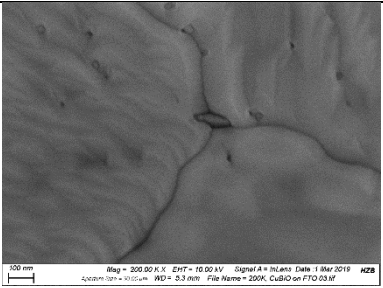
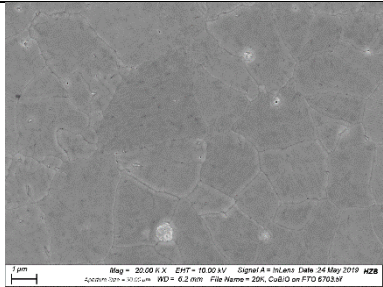
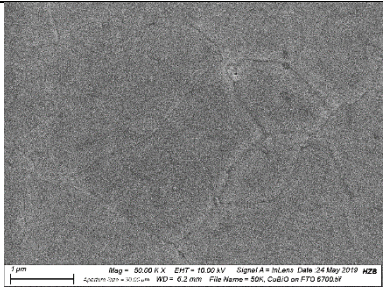
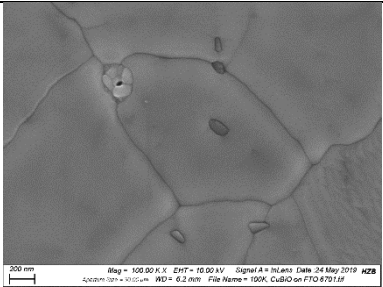
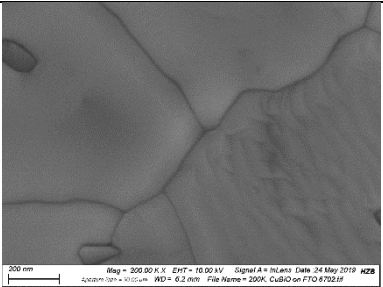
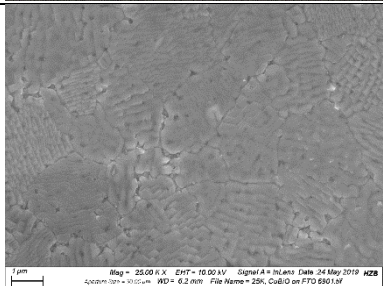
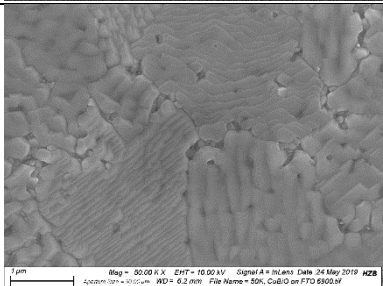
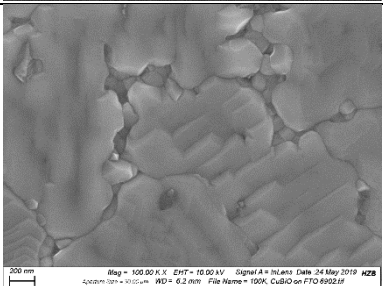
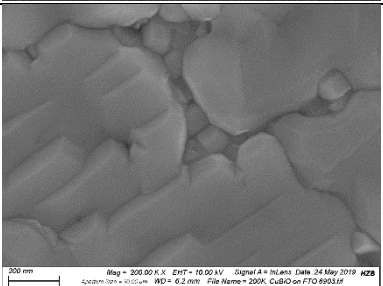
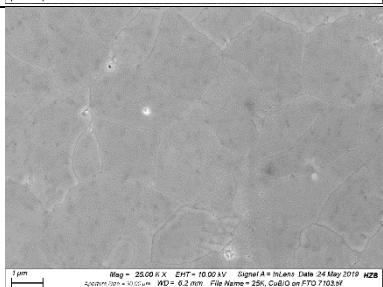
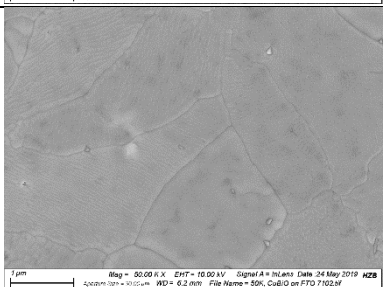
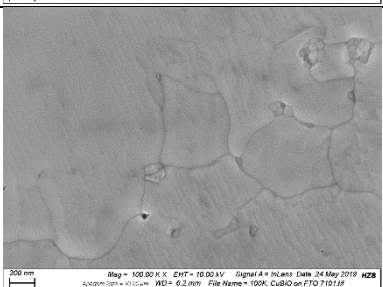
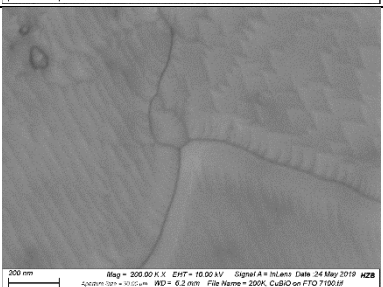
Pressure series	Magnification = 20k – 25k	50k	100k	200k
1E-3	 Mag = 20.00 K X EHT = 10.00 kV Signal A = InLens Date: 1 Mar 2019 #Z8 4200001017 = 1012.4µm WD = 5.3 mm File Name = 10K_CuBiO on FTO 021f	 Mag = 50.00 K X EHT = 10.00 kV Signal A = InLens Date: 1 Mar 2019 #Z8 4200001017 = 1012.4µm WD = 5.3 mm File Name = 10K_CuBiO on FTO 021f	 Mag = 100.00 K X EHT = 10.00 kV Signal A = InLens Date: 1 Mar 2019 #Z8 4200001017 = 1012.4µm WD = 5.3 mm File Name = 100K_CuBiO on FTO 021f	 Mag = 200.00 K X EHT = 10.00 kV Signal A = InLens Date: 1 Mar 2019 #Z8 4200001017 = 1012.4µm WD = 5.3 mm File Name = 200K_CuBiO on FTO 021f
5E-3	 Mag = 20.00 K X EHT = 10.00 kV Signal A = InLens Date: 24 May 2019 #Z8 4200001017 = 1012.4µm WD = 6.2 mm File Name = 25K_CuBiO on FTO 6703f	 Mag = 50.00 K X EHT = 10.00 kV Signal A = InLens Date: 24 May 2019 #Z8 4200001017 = 1012.4µm WD = 6.2 mm File Name = 50K_CuBiO on FTO 6703f	 Mag = 100.00 K X EHT = 10.00 kV Signal A = InLens Date: 24 May 2019 #Z8 4200001017 = 1012.4µm WD = 6.2 mm File Name = 100K_CuBiO on FTO 6703f	 Mag = 200.00 K X EHT = 10.00 kV Signal A = InLens Date: 24 May 2019 #Z8 4200001017 = 1012.4µm WD = 6.2 mm File Name = 200K_CuBiO on FTO 6703f
1E-2	 Mag = 20.00 K X EHT = 10.00 kV Signal A = InLens Date: 24 May 2019 #Z8 4200001017 = 1012.4µm WD = 6.2 mm File Name = 25K_CuBiO on FTO 7103f	 Mag = 50.00 K X EHT = 10.00 kV Signal A = InLens Date: 24 May 2019 #Z8 4200001017 = 1012.4µm WD = 6.2 mm File Name = 50K_CuBiO on FTO 7103f	 Mag = 100.00 K X EHT = 10.00 kV Signal A = InLens Date: 24 May 2019 #Z8 4200001017 = 1012.4µm WD = 6.2 mm File Name = 100K_CuBiO on FTO 7103f	 Mag = 200.00 K X EHT = 10.00 kV Signal A = InLens Date: 24 May 2019 #Z8 4200001017 = 1012.4µm WD = 6.2 mm File Name = 200K_CuBiO on FTO 7103f
p _{O2} = 5E-2	 Mag = 20.00 K X EHT = 10.00 kV Signal A = InLens Date: 24 May 2019 #Z8 4200001017 = 1012.4µm WD = 6.2 mm File Name = 25K_CuBiO on FTO 7103f	 Mag = 50.00 K X EHT = 10.00 kV Signal A = InLens Date: 24 May 2019 #Z8 4200001017 = 1012.4µm WD = 6.2 mm File Name = 50K_CuBiO on FTO 7103f	 Mag = 100.00 K X EHT = 10.00 kV Signal A = InLens Date: 24 May 2019 #Z8 4200001017 = 1012.4µm WD = 6.2 mm File Name = 100K_CuBiO on FTO 7103f	 Mag = 200.00 K X EHT = 10.00 kV Signal A = InLens Date: 24 May 2019 #Z8 4200001017 = 1012.4µm WD = 6.2 mm File Name = 200K_CuBiO on FTO 7103f

Figure S 22: SEM images part 3

EDX images

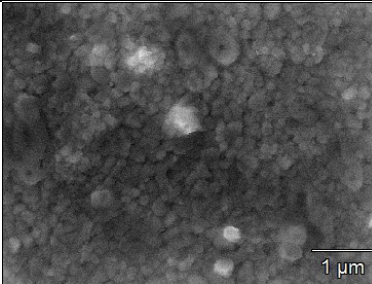
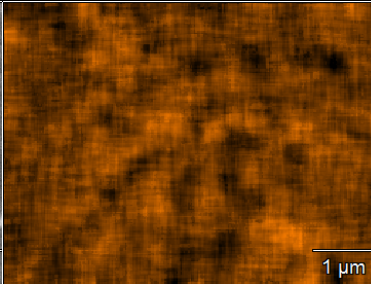
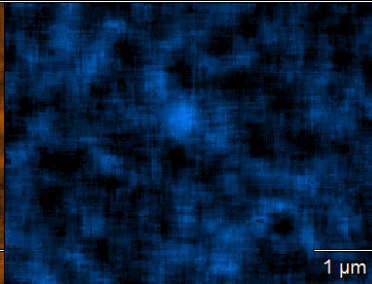
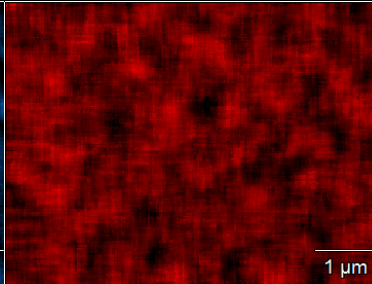
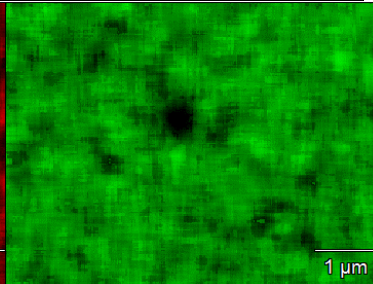

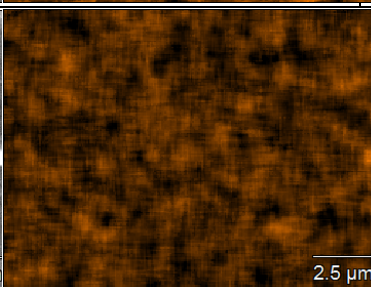
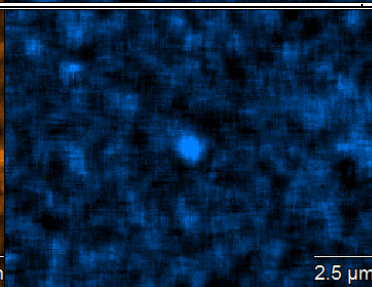
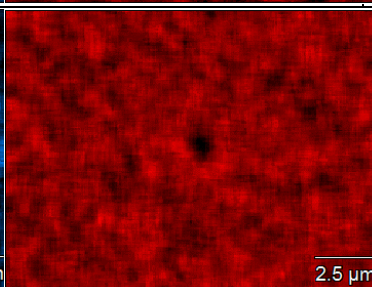
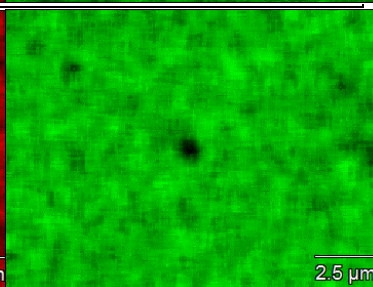
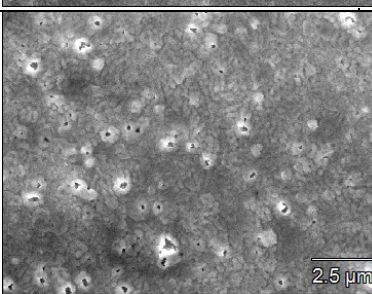
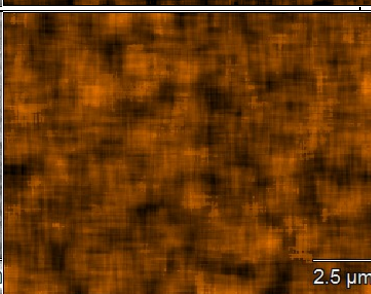
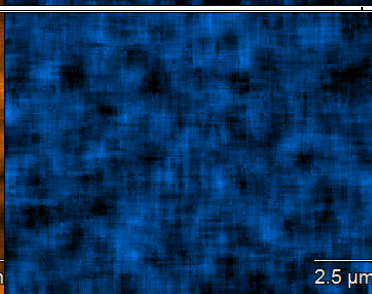
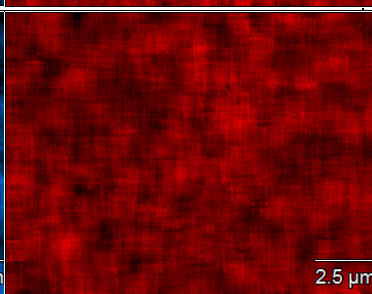
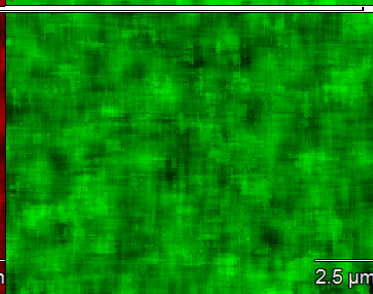
Con d	Image	Cu L	Bi M	O K	Sn L
Standard (2 J/cm ² , RT, vacuum)					
Standard (low magnification)					
1.5 J/cm ² (low magnification)					

Figure S 23: EDX images part 1

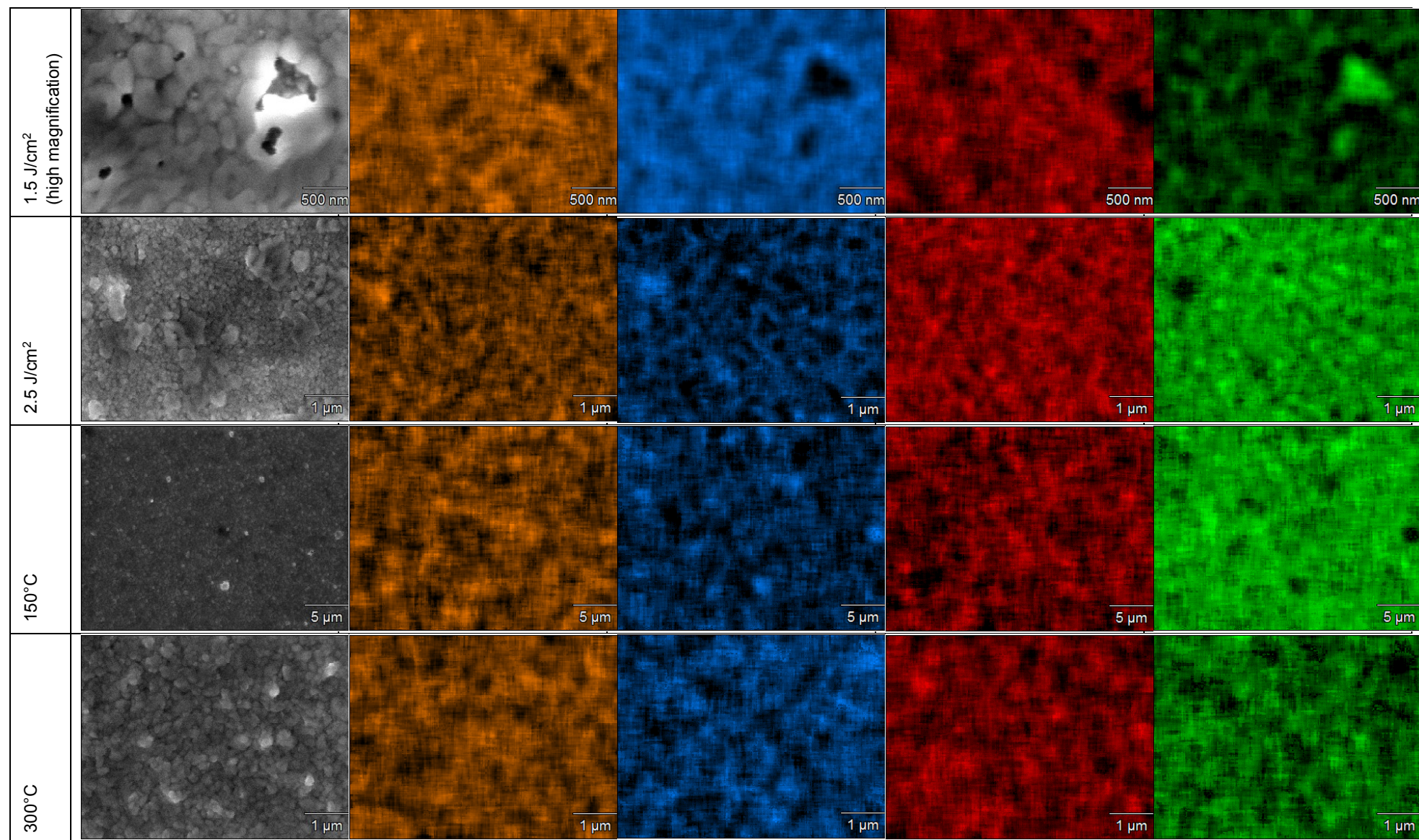


Figure S 24: EDX images part 2

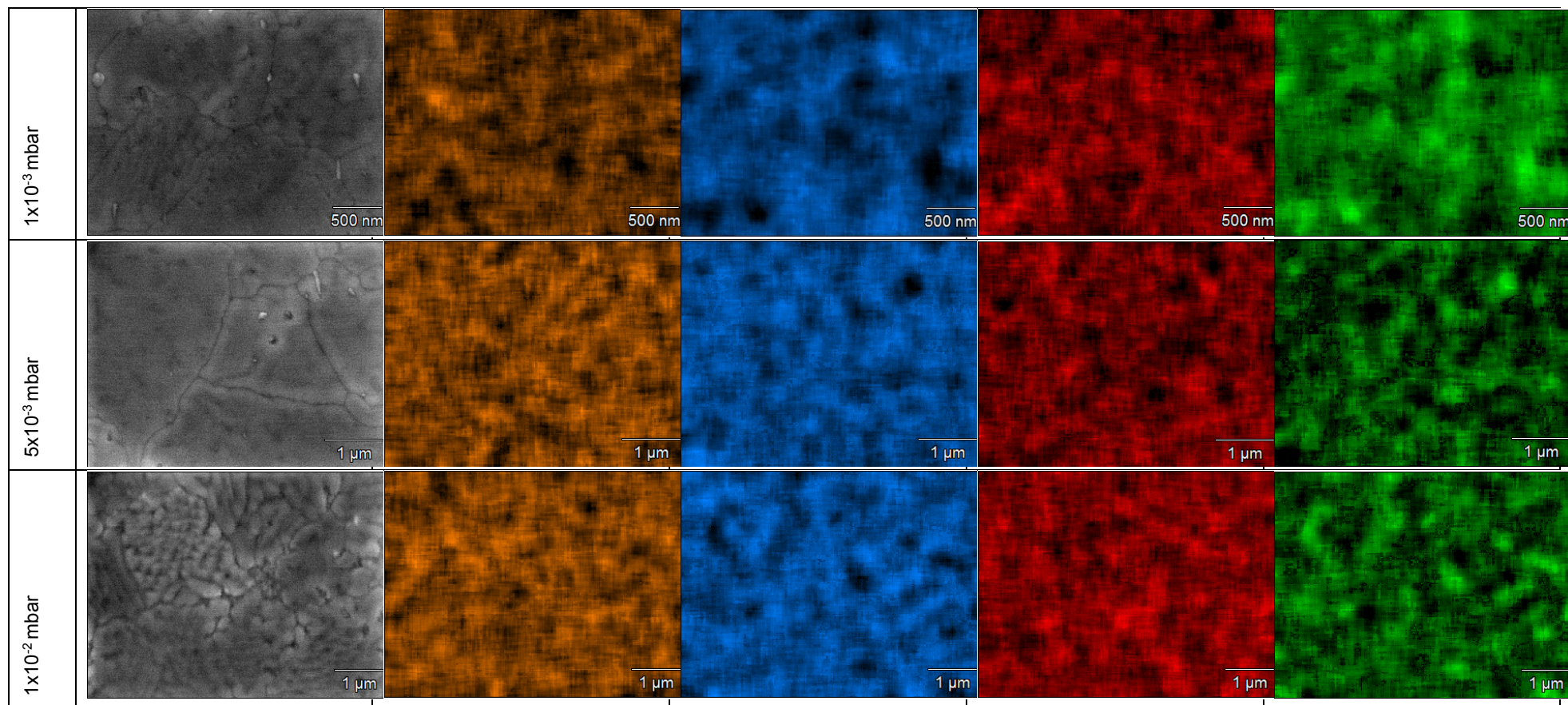


Figure S 25: EDX images part 3

Bare FTO

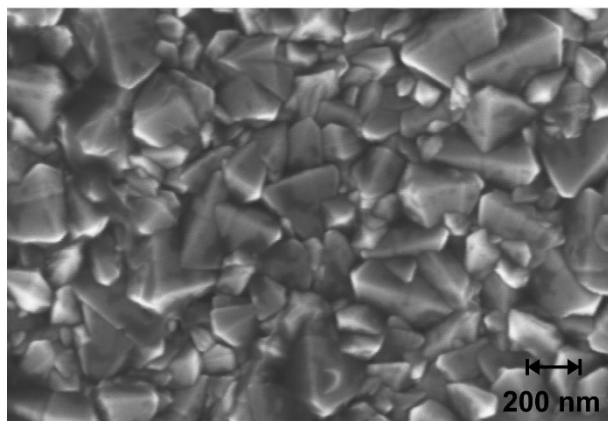


Figure S 26: SEM top view image of a bare FTO substrate.

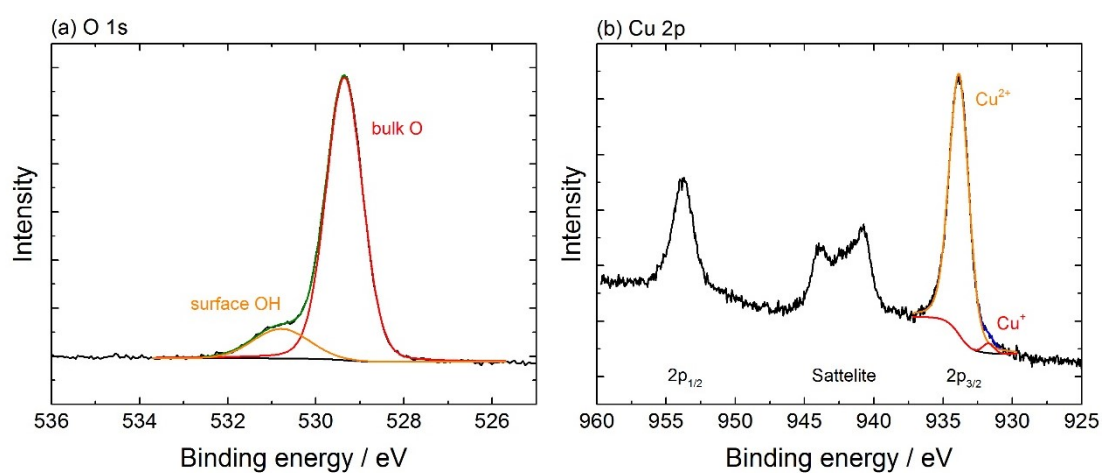


Figure S 27: Fine spectra of CuBi_2O_4 deposited with standard conditions (a) O 1s region, (b) Cu 2p region.

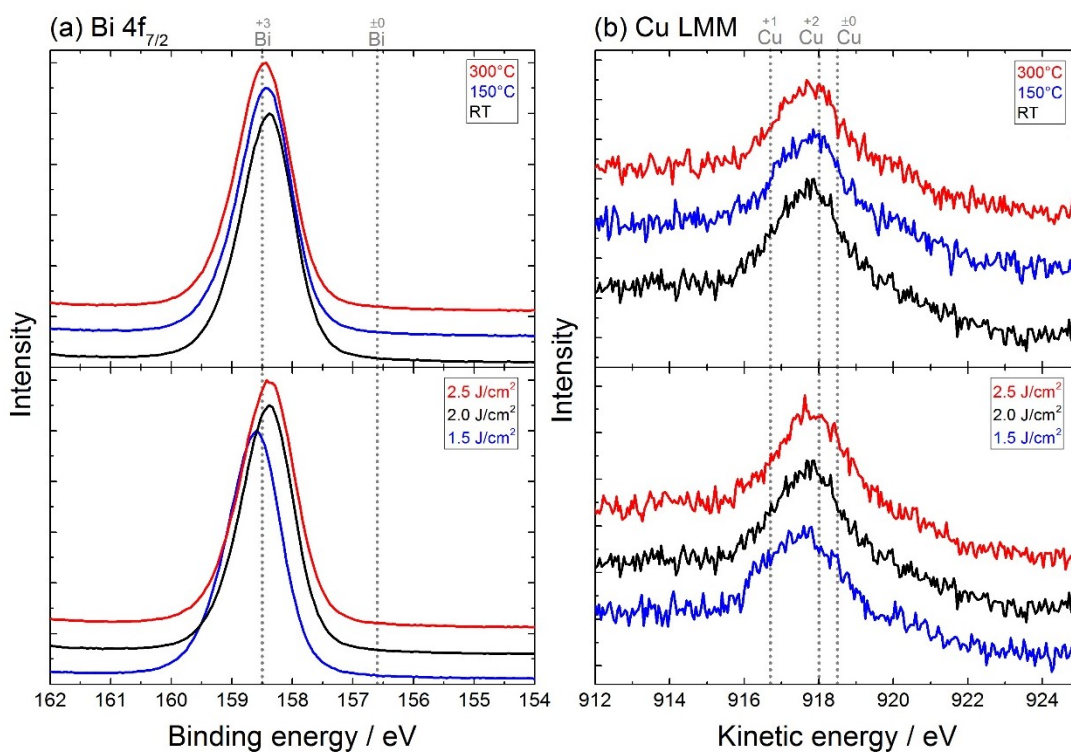


Figure S 28: XPS fine spectra of CuBi_2O_4 deposited under various conditions (a) Bi 4f region, (b) Cu LMM region.

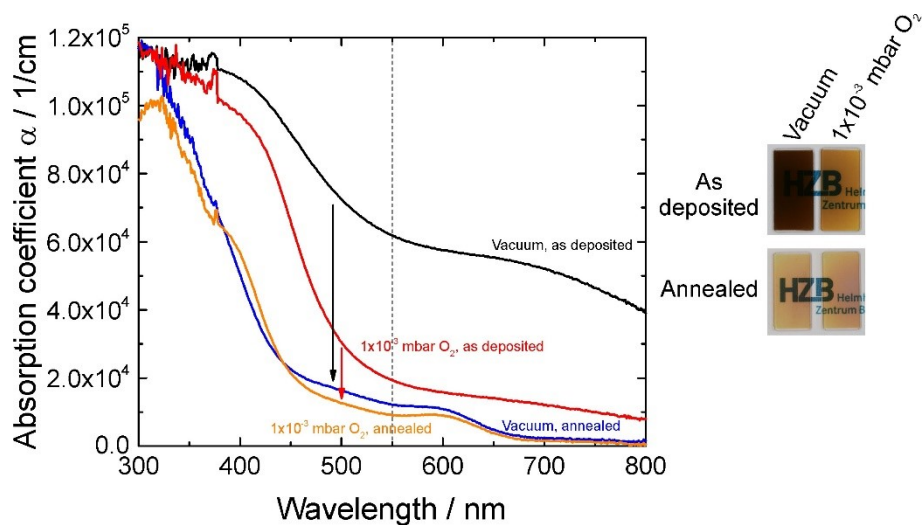


Figure S 29: Absorption coefficient and photographs of two samples before and after annealing in air.

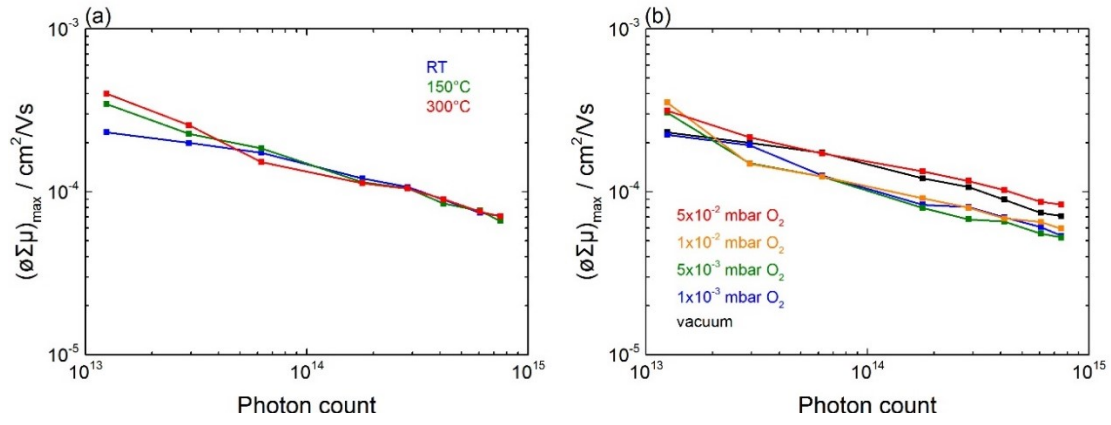


Figure S 30: Peak mobility in dependence of (a) the substrate temperature and (b) the oxygen background pressure vs. the photon count.

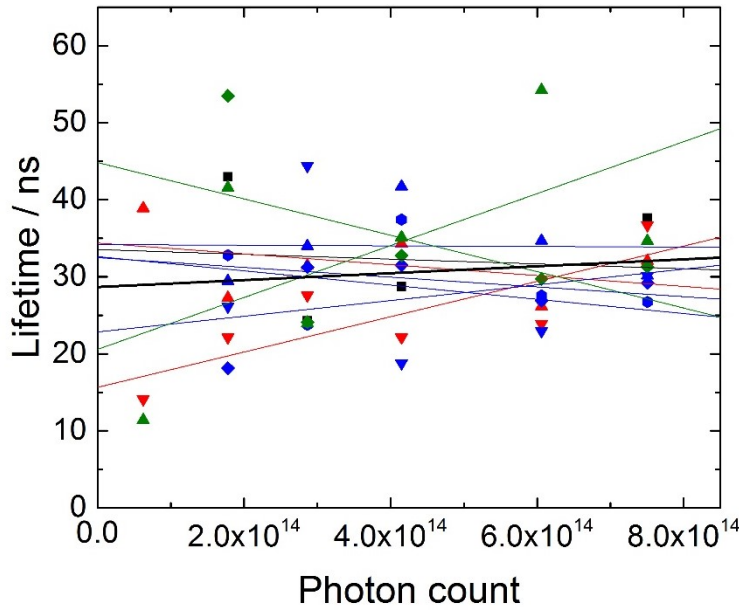


Figure S 31: Fitted lifetime τ_1 in dependence of the excitation photon count; black squares: standard conditions; red downward triangle: 1.5 J/cm², red upward triangle: 2.5 J/cm²; green diamond: 150°C, green upward triangle 300°C; blue downward triangle 10⁻³ mbar, blue diamond 5 × 10⁻³ mbar, blue hexagon 10⁻² mbar, blue upward triangle 5 × 10⁻² mbar; colored lines are respective linear fits, thick black line is the linear fit over all data points showing the negligible influence of the photon count.

7.2 List of abbreviations and used constants

Abbreviation	Definition
AFM	Atomic force microscopy
ALD	Atomic layer deposition
AM 1.5	Air mass 1.5
APCE	Absorbed photon to current efficiency
BOS	Balance of system
CA	Chronoamperometry
CCU	Carbon capture and storage
CE	Counter electrode
CR	Cycle ratio
CV	Cyclic voltammetry
CVD	Chemical vapor deposition
DFT	Density functional theory
DSSC	Dye synthesized solar cell
EDX	Energy-dispersive X-ray spectroscopy
ETA	Extremely thin absorber
FTO	Fluorine doped tin oxide
FWHM	Full width at half maximum
GIXRD	Grazing incidence X-ray diffraction
GPC	Growth per cycle
HER	Hydrogen evolution reaction
IPCE	Incident photon to current efficiency
IR	Infrared
LOHC	Liquid organic hydrogen carrier
LSV	Linear sweep voltammetry
MS	Mass spectrometry
MSE	Mean squared error
OER	Oxygen evolution reaction
PE	Plasma enhanced
PEC	Photoelectrochemistry
PLD	Pulsed laser deposition
PPA	Power purchase agreement

PtX	Power to X
PV	Photovoltaic
RBS	Rutherford Backscattering spectrometry
RHE	Reversible hydrogen electrode
RMS	Root mean square
RT	Room temperature
RTSE	Real time spectroscopic ellipsometry
SC	Semiconductor
SE	Spectroscopic ellipsometry
SEM	Scanning electron microscopy
STH	Solar to hydrogen
T-ALD	Thermal atomic layer deposition
TEM	Transmission electron microscopy
TMA	Trimethylaluminium
TRMC	Time resolved microwave conductivity
UV	Ultraviolet
Vis	Visible
VTIP	Vanadium(V)tri-isopropoxy oxide
WE	Working electrode
XPS	X-ray photoelectron spectroscopy
XRD	X-ray diffraction

Symbol	Name	Value	Unit
h	Planck constant	6.626×10^{-34}	Js
c	Speed of light	2.998×10^8	m/s
e	Elementary charge	1.602×10^{-19}	C
k_B	Boltzmann constant	1.380×10^{-23}	J/K
ϵ_0	Vacuum permittivity	8.854×10^{-12}	C ² /Jm

7.3 List of figures

Figure 1: (a) Average daily PV generation and load profile of a typical south Australian household for 2015; ²⁰ (b) Effect of latitude in the daily insolation throughout a year. ²¹	9
Figure 2: Energy diagrams of semiconductors; (a) intrinsic semiconductor including the definitions of the vacuum level E_{vac} , the energy of the conduction band minimum E_{CBM} , the Fermi level E_F the valence band maximum E_{VBM} , the ionization energy IE, the work function ϕ , the bandgap E_G , and the electron affinity EA; (b) an n-type semiconductor; (c) a p-type semiconductor.	12
Figure 3: Energy diagrams of (a) an n-type semiconductor and an electrolyte; (b) an n-type semiconductor and an electrolyte in electrical contact with equilibrated Fermi level and redox potential, also indicated the width of the space charge region W_{SC} and the potential drop $\Delta\phi_{SC}$; (c) the semiconductor-electrolyte junction under illumination (hv) with Fermi level splitting into quasi Fermi levels of the electrons $E_{F,n}$ and the holes $E_{F,p}$, and the photovoltage V_{ph}	12
Figure 4: (a) Charge carrier transport in a flat metal oxide absorber anode; (b) Absorption according to Lambert-Beer Law with a moderate extinction coefficient: (c) Charge carrier transport in an ETA on a nanostructured scaffold.	15
Figure 5: Surface reactions and saturation during an ALD cycle. ⁶⁷	19
Figure 6: Temperature window of an ALD process. ⁸²	21
Figure 7: Thickness control, uniformity and conformality in ALD. ⁶⁷	22
Figure 8: Perfectly conformal ALD-grown Al_2O_3 (light grey) on nanostructures (dark grey). ⁸⁴	23
Figure 9: Periodic table figure of the “Atomic limits” ALD database. ⁸⁵	25
Figure 10: Schematic steps of a binary and a supercycle ALD process. ⁶⁷	25
Figure 11: Thickness development during a supercycle ALD process; full line: ideal growth without nucleation effects, dashed line: with accelerated growth of B on A, dotted line: with nucleation delay of B on A. ^{67,72}	26
Figure 12: Photograph of the PLD setup during a deposition.	28
Figure 13: (a) Representation of the electric field part of p- and s-polarized light during reflection; (b) Interference at a thin film. ¹⁰³	29
Figure 14: Scheme of an SE measurement: incident linear polarized light ($\Delta=0^\circ$, $\Psi = 45^\circ$) and reflected elliptical polarized light with altered Δ and Ψ values.	30
Figure 15: Schematic microwave resonant cavity, the red sinusoidal waves represents the standing wave conditions with the sample at a maximum, photoexcitation by a monochromatic laser from the left and microwave probing from the right. ¹¹²	32
Figure 16: Schematic PEC cell with the sample as working electrode (WE), a platinum counter electrode (CE), a Ag/AgCl reference electrode (REF) and a quartz window for frontside illumination, illumination from the back is also possible through a hole (not visible) if the substrate is transparent. ¹¹³	35
Figure 17: Chemical structure of $[Bi(tmhd)_3]$ or Tris(2,2,6,6-tetramethyl-3,5-heptanedionato)bismuth(III).	42
Figure 18: Growth per cycle (GPC) of bismuth oxide films as function of the ALD parameters of the plasma-enhanced process (blue), the thermal process (red), and as reported by Shen et al. ¹²⁶ (green); (a) $[Bi(tmhd)_3]$ exposure time (b) $[Bi(tmhd)_3]$ purge time; (c) water exposure time; (d) oxygen plasma exposure time; (e) oxygen plasma purge time; (f) deposition temperature (temperature windows are indicated by the semitransparent rectangles). Full and dotted lines in (a)-(e) represent guides to the eye.	43
Figure 19: Thickness deviation from mean after 100 ALD cycles over a 4" wafer (a) thermal process, 96% uniformity; (b) plasma-enhanced process, 94% uniformity.	44
Figure 20: Survey XPS of Bi_2O_3 grown by thermal ALD. Indicated peaks belong to bismuth (orange), oxygen (red), carbon (black), aluminium (blue), and silicon (grey).	47

Figure 21: (a) Layered structure of a typical sample; (b) Inelastic mean free path of electrons within solids with universal curve fit. ¹³¹	48
Figure 22: XPS fine spectra: (a) Bi 4f with peaks assigned to bulk Bi ₂ O ₃ (orange), surface Bi-OH (red) and Bi-O-C contaminations (dark red), peak sum in green; (b) C 1s of a Bi ₂ O ₃ sample grown by thermal ALD before (red) and after annealing (orange) and grown by plasma enhanced ALD before (blue) and after annealing (green), raw data as dots and peak sum as full lines; (c) Al 2p with a single peak fit (blue) of a pure Al ₂ O ₃ sample; (d) Si 2p with a single peak fit for SiO ₂ (grey) of a bare silicon substrate; (e) O 1s with peaks assigned to bulk Bi ₂ O ₃ (orange), surface Bi-OH (red), Al ₂ O ₃ (blue), and SiO ₂ (grey), peak sum in green.	48
Figure 23: XPS fine spectra of PE-ALD films: (a) O 1s with peaks assigned to bulk Bi ₂ O ₃ (orange), surface Bi-OH (red), Al ₂ O ₃ (blue) and SiO ₂ (grey), peak sum in green; (b) Bi 4f with peaks assigned to bulk Bi ₂ O ₃ (orange), surface Bi-OH (red) and Bi-O-C contaminations (dark red), peak sum in green; (c) O 1s recorded in 60° angled configuration with peaks assigned to bulk Bi ₂ O ₃ (orange) and surface Bi-OH (red), peak sum in green; (d) Bi 4f recorded in 60° angled configuration with peaks assigned to bulk Bi ₂ O ₃ (orange), surface Bi-OH (red), and Bi-O-C contaminations (dark red), peak sum in green.	51
Figure 24: Cross sectional TEM images of bismuth oxide films. The samples exhibit a layered structure of the silicon substrate, its native oxide layer, the ALD grown alumina adhesion layer, the bismuth oxide film, and the glue applied during preparation (from bottom to top). (a-c): overviews, (d-f): detailed views of the T-ALD and PE-ALD sample, before and after annealing.	53
Figure 25: AFM images of the Bi ₂ O ₃ samples: (a) Thermal ALD as deposited and (b) annealed; (c) plasma-enhanced ALD as deposited and (d) annealed.	55
Figure 26: GIXRD patterns of a T-ALD Bi ₂ O ₃ film before (red) and after annealing (orange) as well as a P-ALD film before (blue) and after annealing (green) compared to the Al ₂ O ₃ covered Si substrate (black) and α-Bi ₂ O ₃ (orange, vertical drops). ¹⁴²	56
Figure 27: Modelled optical properties of Bi ₂ O ₃ thin films: (a) refractive indices n and (b) extinction coefficients k for a T-ALD Bi ₂ O ₃ film (red), a T-ALD film after annealing (orange), a PE-ALD film (blue), and a PE-ALD film after annealing (green).	57
Figure 28: Development of the apparent thickness of Bi ₂ O ₃ over 20 cycles of (a) thermal and (b) plasma-enhanced ALD.	58
Figure 29: Zoom into the first cycle of Figure 28.	59
Figure 30: Mean squared error of the RTSE fit of Figure 28b: (a) with a single Bi ₂ O ₃ layer; (b) with a bulk Bi ₂ O ₃ and a surface Bi(tmhd) _x layer.	61
Figure 31: Refractive index n of the Bi(tmhd) _x surface layer.	61
Figure 32: Thickness development of (a) the Bi(tmhd) _x surface layer and (b) the bulk Bi ₂ O ₃ during PE-ALD, derived from the double-layer optical model.	62
Figure 33: Chemical structure of (a) [Mn(CpEt) ₂] or bis(ethylcyclopentadienyl)manganese(II) and (b) VTIP or vanadium(V)tri-isopropoxy oxide.	66
Figure 34: Growth per cycle of the MnO _x ALD process as a function of (a) the [Mn(CpEt) ₂] pulse time; (b) the [Mn(CpEt) ₂] purge time; (c) the H ₂ O pulse time and (d) the H ₂ O purge time; green vertical drop lines indicate saturative conditions used for future depositions; error bars indicate the spread of five spots distributed over 4 inch.	67
Figure 35: Growth per cycle of the VO _x ALD process as a function of (a) the VTIP pulse time; (b) the VTIP purge time; (c) the H ₂ O pulse time and (d) the H ₂ O purge time; green vertical drop lines indicate saturative conditions used for future depositions; error bars indicate the standard deviation of five spots distributed over 4 inch.	68
Figure 36: Thickness deviation from mean after 100 ALD cycles over a 4 inch wafer (a) MnO _x ALD, 96.1% uniformity; (b) VO _x ALD, 93.1% uniformity.	68
Figure 37: XRD patterns of Mn ₂ V ₂ O ₇ on silicon substrates with varying post-deposition treatments and various reference signals. ^{183,189,190}	70

Figure 38: XPS measurements of the Mn 2p _{3/2} region fitted with different routines from Biesinger et al. ¹⁹³ , (a) Mn(II) fit in purple of an as-deposited Mn ₂ V ₂ O ₇ film, (b) Mn(III) fit in orange of an Mn ₂ V ₂ O ₇ film annealed in air, raw data in black, peak sum in red.	71
Figure 39: Typical XPS fine spectrum of the O 1s and V 2p region from an as-deposited vanadium oxide sample; raw data and shared Shirley background in black, bulk oxygen (set to 530 eV) in orange, surface hydroxyl groups in red, V(V) in purple, V(IV) in blue, peak sum in green.	72
Figure 40: C 1s spectrum (black) with adventitious carbon features (red and orange) and precursor contamination feature (blue); peak sum in green.	73
Figure 41: Mass spectrometry analysis of Mn ₂ V ₂ O ₇ powder in argon. Temperature–time curve during the MS analysis (black) and ion currents for mass-to-charge ratios (m/q) of 51, 55, 67, 71, 83 and 87, assigned to V ⁺ (dark red), Mn ⁺ (dark blue), VO ⁺ (red), MnO ⁺ (blue), VO ₂ ⁺ (orange), and MnO ₂ ⁺ (light blue), respectively.	76
Figure 42: (a) Absorption coefficient α and indirect Tauc plot (inset) of Mn ₂ V ₂ O ₇ ; (b) Estimated VB-CB absorption of the AM 1.5 spectrum by Mn ₂ V ₂ O ₇ thin films and the maximal photocurrent density j_{\max} (inset).	77
Figure 43: Cyclic voltammetry of Mn ₂ V ₂ O ₇ on FTO in a borate buffered electrolyte at pH 8.2; the grey dashed line indicates the thermodynamic redox potential of the OER at 1.23 V vs. RHE.	78
Figure 44: Schematic representation of the preparation of Mn ₂ V ₂ O ₇ electrodes.	79
Figure 45: Chopped light photoelectrochemical measurements of Mn ₂ V ₂ O ₇ in a borate buffer (pH 9.2) with sulfite hole scavenger: (a) Cyclic voltammetry; (b) Chronoamperometry at 0.89 V vs. RHE.	80
Figure 46: Measured photocurrent densities ΔJ in dependence of the manganese to vanadium ratio of the samples in the three different electrolytes: borate buffered (pH 9.2) and sulfite scavenger (black), borate buffered (pH 9.2) and [Fe(CN) ₆] ^{3-/4-} scavenger (red), and 0.1M KOH (pH 13) and [Fe(CN) ₆] ^{3-/4-} scavenger (blue).	81
Figure 47: TRMC measurement on Mn ₂ V ₂ O ₇ grown by PLD measured at 6.50x10 ¹⁴ photon/pulse·cm ² and 410 nm excitation irradiation.	83
Figure 48: Photograph of Mn ₂ V ₂ O ₇ samples after PEC measurements, from left to right: 9:1, 8:1, 7:1 cycle ratio.	83
Figure 49: Photocurrent density at 0.5 V vs RHE in dependence of the CuBi ₂ O ₄ film thickness.	87
Figure 50: Gracing-incidence X-ray diffractograms of a CuBi ₂ O ₄ thin film grown under standard conditions; red: on FTO after annealing, green: on quartz after annealing, blue: on quartz as deposited, orange: CuBi ₂ O ₄ reference pattern. ²⁰⁵	88
Figure 51: Raman spectra of annealed CuBi ₂ O ₄ films grown with varying parameters after annealing compared to literature values of the most prominent vibrations (grey). ²⁰⁶	89
Figure 52: SEM images of CuBi ₂ O ₄ films deposited with varying parameters after annealing; top views: (a) F = 1.5 J/cm ² , (b) pO ₂ = 0.01 mbar, (c) standard conditions (vacuum, 2.0 J/cm ² , RT), (e) F = 2.5 J/cm ² , (f) T = 300°C; (d) cross-sectional view, standard conditions, CuBi ₂ O ₄ highlighted in orange.	90
Figure 53: Bismuth:Copper ratios estimated by EDX in dependence of the deposition parameters laser fluence, substrate temperature, and oxygen pressure. Standard conditions marked in red and dashed red lines show linear fits, error bars indicate the standard deviation if multiple measurements were executed.	92
Figure 54: Survey XPS of CuBi ₂ O ₄ grown PLD. Indicated peaks belong to copper (orange), bismuth (blue), oxygen (red), carbon (black), and tin (green).	94
Figure 55: XPS fine spectra of (a) the Bi 4f _{7/2} feature and (b) a Cu LMM Auger feature from samples deposited under various background pressures; positions of important species indicated in grey. ¹⁵⁹	94
Figure 56: (a) Absorption coefficient α , photograph, direct and indirect Tauc plots (insets) of CuBi ₂ O ₄ ; (b) Estimated above bandgap absorption of the AM 1.5 spectrum by CuBi ₂ O ₄ thin films and corresponding maximal photocurrent density j_{\max} (inset).	95
Figure 57: Direct (red) and indirect (black) bandgaps in dependence of the deposition parameters laser fluence, substrate temperature, and oxygen pressure. Dashed lines show linear fits.	96

Figure 58: Absorption coefficient α at 550 nm in dependence of the deposition parameters laser fluence, substrate temperature, and oxygen pressure. Standard conditions marked in red and dashed red lines show linear fits.	96
Figure 59: Photograph of CuBi_2O_4 grown on quartz at various oxygen background pressures: from left to right: vacuum, 1×10^{-3} , 5×10^{-3} , 1×10^{-2} , 5×10^{-2} mbar O_2 ; all as deposited.	97
Figure 60: Reported absorption profiles of (a) Lee et al. ⁹⁶ , (b) Berglund et al. ⁶⁰ , and (c) Wang et al. ⁵³	98
Figure 61: (a) TRMC measurement showing the photoconductivity over time after photoexcitation (black) and a bi-exponential decay fit (red); (b) peak photoconductivity over photon fluence of the excitation pulse for samples of the fluence series.	99
Figure 62: Peak mobilities, lifetimes, and diffusion length in dependence of the deposition parameters laser fluence, substrate temperature and oxygen pressure; dashed lines show linear fits.	100
Figure 63: LSV measurements with chopped light: (a) Backside (black) vs. frontside (blue) illumination; (b) H_2O_2 as electron scavenger (black) vs. no scavenger (red); 0.6 V vs. RHE marked in grey.	103
Figure 64: Photocurrent density at 0.6 V vs RHE in dependence of the deposition parameters laser fluence, substrate temperature, and oxygen pressure. Standard conditions marked in red and dashed red lines show linear fits.	104
Figure 65: Incident photon-to-current efficiencies (a-c) and absorbed photon-to-current efficiencies (d-f) in dependence of the wavelength of the incident light for various deposition parameters.	106
Figure S 1: C 1s spectra of a bare silicon wafer (black), a pure Al_2O_3 sample (blue), and a T-ALD Bi_2O_3 sample (red).	113
Figure S 2: Al 2p spectra of a PE-ALD Bi_2O_3 sample measured under normal angle (top) with a fit assigned to Al_2O_3 (blue) and the same sample measured under 60° (bottom).	113
Figure S 3: Example of a fit of a RTSE spectrum: (a) measured Ψ (black) and Δ (blue) with fits (dashed red); (b) Double-layer optical model with fit parameters and variables.	114
Figure S 4: Growth rate of the MnO_x ALD process as function of the substrate temperature.	115
Figure S 5: Diffractograms of (a) MnO_x (black) on silicon and literature signals for MnO (red) and (b) VO_x (black) on silicon and a bare silicon substrate (red). ¹⁸⁸ The reflections of silicon in (b) are only visible if the (square) sample is aligned with the direction of the X-rays. If the sample is rotated by 45° in the xy-plane these reflections vanish as visible in (a).	115
Figure S 6: Mn 2p region fitted with the Mn(IV) pattern suggested by Biesinger et al. (dark yellow), peak sum in red, raw data in black. ¹⁹³	116
Figure S 7: Mn 2p region of an $\text{Mn}_2\text{V}_2\text{O}_7$ film annealed in air at 500°C , (a) with Mn(II) fit and (b) Mn(III) fit according to Biesinger et al. ¹⁹³	116
Figure S 8: (a) Absorption coefficient α vs. wavelength of the samples with 1:7 (blue), 1:8 (green), and 1:9 (red) cycle ratio; (b) Raw absorption of the 1:9 cycle ratio sample (black) vs. wavelength compared with the raw absorption of a bare FTO substrate (red), and the difference of both measurements (blue) which builds the base for the UVVis considerations; (c) Indirect Tauc plot of the 1:9 cycle ratio sample with an estimated bandgap of 1.90 eV.	116
Figure S 9: Diffractograms of $\text{Mn}_2\text{V}_2\text{O}_7$ after annealing (red) and after electrochemistry (blue) compared to literature reflections of FTO (black), $\alpha\text{-Mn}_2\text{O}_3$ (orange), and $\beta\text{-Mn}_2\text{V}_2\text{O}_7$ (green). ^{183,190}	118
Figure S 10: XPS measurement of the Mn 2p 3/2 region of $\text{Mn}_2\text{V}_2\text{O}_7$ after electrochemistry fitted with different routines from Biesinger et al. ¹⁹³ , (a) Mn(II) fit in purple, (b) Mn(III) fit in orange, raw data in black, peak sum in red.	118
Figure S 11: Raw XPS spectra of the Sn 3d region of $\text{Mn}_2\text{V}_2\text{O}_7$ samples, red after annealing, black after electrochemistry.	118

Figure S 12: CV scan of a $\text{Mn}_2\text{V}_2\text{O}_7$ sample (red) compared to an FTO substrate covered with the MnO sacrificial layer (black).	119
Figure S 13: CA measurement of $\text{Mn}_2\text{V}_2\text{O}_7$ in borate buffer with $[\text{Fe}(\text{CN})_6]^{3-/4-}$ scavenger.	119
Figure S 14: CA measurement of $\text{Mn}_2\text{V}_2\text{O}_7$ in 0.1M KOH with $[\text{Fe}(\text{CN})_6]^{3-/4-}$ scavenger.	119
Figure S 15: Pourbaix diagram of the Mn-V-O system adapted from Yan et al. The star marks the CA conditions in the third electrolyte. ⁵⁶	120
Figure S 16: Measured film thickness after PLD targeting 100 nm.	120
Figure S 17: GIXRD patterns of CuBi_2O_4 thin films grown with varying parameters, (a) on FTO after annealing; (b) on quartz after annealing; (c) on quartz as deposited, reference pattern in orange, quartz substrate in black. ²⁰⁵	121
Figure S 18: Full width at half maximum of the 28° reflection in GIXRD measurements.	121
Figure S 19: RBS measurement of CuBi_2O_4 (standard deposition conditions) on quartz.	122
Figure S 20: SEM images part 1	123
Figure S 21: SEM images part 2	124
Figure S 22: SEM images part 3	125
Figure S 23: EDX images part 1	126
Figure S 24: EDX images part 2	127
Figure S 25: EDX images part 3	128
Figure S 26: SEM top view image of a bare FTO substrate.	129
Figure S 27: Fine spectra of CuBi_2O_4 deposited with standard conditions (a) O 1s region, (b) Cu 2p region.	129
Figure S 28: XPS fine spectra of CuBi_2O_4 deposited under various conditions (a) Bi 4f region, (b) Cu LMM region.	130
Figure S 29: Absorption coefficient and photographs of two samples before and after annealing in air.	130
Figure S 30: Peak mobility in dependence of (a) the substrate temperature and (b) the oxygen background pressure vs. the photon count.	131
Figure S 31: Fitted lifetime τ_1 in dependence of the excitation photon count; black squares: standard conditions; red downward triangle: 1.5 J/cm^2 , red upward triangle: 2.5 J/cm^2 ; green diamond: 150°C , green upward triangle 300°C ; blue downward triangle 10^{-3} mbar , blue diamond $5 \times 10^{-3} \text{ mbar}$, blue hexagon 10^{-2} mbar , blue upward triangle $5 \times 10^{-2} \text{ mbar}$; colored lines are respective linear fits, thick black line is the linear fit over all data points showing the negligible influence of the photon count.	131

7.4 List of tables

Table 1: Overview on published nanostructured tandem PEC devices employing BiVO_4 .	16
Table 2: Measured film thicknesses of SiO_2 , Al_2O_3 , and Bi_2O_3 by SE and TEM of the T-ALD, PE-ALD and PE-ALD sample after annealing. The error estimates correspond to the standard deviations.	53
Table 3: Calculated surface roughness as root mean square from AFM measurements of T-ALD and PE-ALD Bi_2O_3 sample, before and after annealing, respectively.	55
Table 4: XPS evaluation of $\text{Mn}_2\text{V}_2\text{O}_7$ samples for photoelectrochemistry.	75
Table 5: Absorption coefficients of CuBi_2O_4 from various studies.	97
Table 6: TRMC results of various studies.	102
Table 7: Photocurrent densities of various studies, partially estimated from graphs.	104
Table 8: Reported IPCE and APCE values from various publications, data estimated from graphs at 400 nm and 0.6 V vs RHE (if not stated otherwise).	107

7.5 Acknowledgments

I want to thank Roel for supervising me and giving me the possibility to do my PhD in the solar fuels group at HZB. This thesis would not have been possible without your guidance, advice and patience over the years.

I further want to thank Julien for being the second evaluator of this thesis and Prof. Matthias Bickermann for being the chairman of my PhD committee. Both agreed to do me this favor without any hesitation.

A huge thanks goes to Aafke who helped me on any issue that came up without judgement but with incredible patience and always helpful input.

Furthermore I want to thank the other ALD and PLD people, Paul, Christian, Moritz, and Carsten, for their amazing support and entertainment at HZB. Thanks to all the other people of the solar fuels group and the other doctoral researchers at HZB for being a great scientific and social framework to do my PhD. Thanks for all the fruitful discussions and the help in all kinds of situations. I am especially thankful for Kristina for her initial work on ALD of Bi_2O_3 , Ulrike for the TEM measurements, Ibbi for the SEM and EDX evaluation, Marlene for the mass spectrometry measurements, Hanno for the AFM measurements and Erwin Zoethout from DIFFER for the RBS measurements.

Finally I want to thank my family and friends who always supported me along the way. The “I’m almost finished” is finally coming true.

7.6 References

- (1) United Nations FCCC. Paris Agreement. In *Conference of the Parties, Twenty-first session*; UN FCCC: Paris, 2015; p 32.
- (2) Powell, J. The Consensus on Anthropogenic Global Warming Matters. *Bull. Sci. Technol. Soc.* **2016**, 36 (3), 157–163, DOI: 10.1177/0270467617707079.
- (3) Powell, J. Scientists Reach 100% Consensus on Anthropogenic Global Warming. *Bull. Sci. Technol. Soc.* **2017**, 37 (4), 183–184, DOI: 10.1177/0270467619886266.
- (4) United Nations Environment Programme. Emissions Gap Report 2019. *Emiss. Gap Rep. 2019* **2019**, 82.
- (5) International Energy Agency. World Energy Outlook 2020. *World Energy Outlook 2020 - IEA* **2020**.
- (6) International Energy Agency. World Energy Outlook 2019 Executive Summary. *World Energy Outlook 2019 - IEA* **2019**, 11.
- (7) International Energy Agency. IEA Data and statistics <https://www.iea.org/data-and-statistics/data-tables>.
- (8) Perez, M.; Perez, R. Update 2015--A Fundamental Look at Supply Side Energy Reserves for the Planet. *Nat. Gas* 2 (9), 215.
- (9) Perez, R.; Perez, M. A Fundamental Look at Energy Reserves for the Planet. *IEA SHC Sol. Updat.* **2009**, 50 (2).
- (10) Moriarty, P.; Honnery, D. What Is the Global Potential for Renewable Energy? *Renew. Sustain. Energy Rev.* **2012**, 16 (1), 244–252, DOI: <https://doi.org/10.1016/j.rser.2011.07.151>.
- (11) *Photoelectrochemical Hydrogen Production*; van de Krol, R., Grätzel, M., Eds.; Electronic Materials: Science & Technology; Springer US: Boston, MA, 2012; Vol. 102, DOI: 10.1007/978-1-4614-1380-6.
- (12) Lu, X.; McElroy, M. B.; Kiviluoma, J. Global Potential for Wind-Generated Electricity. *Proc. Natl. Acad. Sci.* **2009**, 106 (27), 10933 LP – 10938, DOI: 10.1073/pnas.0904101106.
- (13) Korfiati, A.; Gkonos, C.; Veronesi, F.; Gaki, A.; Grassi, S.; Schenkel, R.; Volkwein, S.; Raubal, M.; Hurni, L. Estimation of the Global Solar Energy Potential and Photovoltaic Cost. *Int. J. Sustain. Energy Plan. Manag.* **2016**, 09, 17–30, DOI: [dx.doi.org/10.5278/ijsepm.2016.9.3](https://doi.org/10.5278/ijsepm.2016.9.3).
- (14) International Renewable Energy Agency. *Renewable Power Generation Costs in 2019*; Abu Dhabi, 2020.
- (15) UN HABITAT. The Strategic Plan 2020-23, 2019.
- (16) Bergner, J.; Siegel, B.; Quaschnig, V. Das Berliner Solarpotenzial. **2018**, 65.
- (17) Eggers, J.-B.; Behnisch, M.; Eisenlohr, J.; Poglitsch, H.; Phung, W.-F.; Muenzinger, M.; Ferrara, C.; Kuhn, T. PV-Ausbauerfordernisse versus Gebäudepotenzial: Ergebnis Einer Gebäudescharfen Analyse Für Ganz Deutschland; 2020.
- (18) Umweltbundesamt. Energieverbrauch nach Energieträgern und Sektoren <https://www.umweltbundesamt.de/daten/energie/energieverbrauch-nach-energetraegern-sektoren>.
- (19) Frankfurter Allgemeine Zeitung. Der Traum vom Wüstenstrom ist gescheitert <https://www.faz.net/aktuell/wirtschaft/wirtschaftspolitik/wuestenstrom-projekt-desertec-ist-gescheitert-13207437.html>.
- (20) Sharma, V.; Haque, M. H.; Aziz, S. M. PV Generation and Load Profile Data of Net Zero Energy Homes in South Australia. *Data Br.* **2019**, 25, 104235, DOI: 10.1016/j.dib.2019.104235.
- (21) MIT Energy Initiative. *The Future of Solar Energy*; Massachusetts Institute of Technology: Cambridge, 2015.
- (22) Fan, X.; Liu, B.; Liu, J.; Ding, J.; Han, X.; Deng, Y.; Lv, X.; Xie, Y.; Chen, B.; Hu, W.; et al. Battery Technologies for Grid-Level Large-Scale Electrical Energy Storage. *Trans. Tianjin Univ.* **2020**, 26 (2), 92–103, DOI: 10.1007/s12209-019-00231-w.
- (23) International Renewable Energy Agency. *Hydrogen: A Renewable Energy Perspective*; Abu Dhabi, 2019.
- (24) Tuller, H. L. *Solar to Fuels Conversion Technologies*; Cambridge, 2015.
- (25) Ministerial Council on Renewable Energy, H. and R. I. *Basic Hydrogen Strategy*; Tokio, 2017.

- (26) COAG Energy Council. *Australia's National Hydrogen Strategy*; Commonwealth of Australia, 2019.
- (27) Bundesministerium für Wirtschaft und Energie (BMWi). Die Nationale Wasserstoffstrategie. *Energiewende* **2020**, 29.
- (28) International Renewable Energy Agency. *Global Renewables Outlook: Energy Transformation 2050*, 2020th ed.; IRENA, Ed.; Abu Dhabi, 2020.
- (29) Gardiner, M. *Energy Requirements for Hydrogen Gas Compression and Liquefaction as Related to Vehicle Storage Needs*; 2009; Vol. 25.
- (30) Herron, J. A.; Kim, J.; Upadhye, A. A.; Huber, G. W.; Maravelias, C. T. A General Framework for the Assessment of Solar Fuel Technologies. *Energy Environ. Sci.* **2015**, 8 (1), 126–157, DOI: 10.1039/C4EE01958J.
- (31) Smets, A. H. M.; Jäger, K.; Isabella, O.; Swaaij, R. A. van; Zeman, M. *Solar Energy: The Physics and Engineering of Photovoltaic Conversion, Technologies and Systems*; UIT Cambridge, 2016.
- (32) *Photoelectrochemical Solar Fuel Production*; Giménez, S., Bisquert, J., Eds.; Springer International Publishing: Cham, 2016, DOI: 10.1007/978-3-319-29641-8.
- (33) Prévot, M. S.; Sivula, K. Photoelectrochemical Tandem Cells for Solar Water Splitting. *J. Phys. Chem. C* **2013**, 117 (35), 17879–17893, DOI: 10.1021/jp405291g.
- (34) Abdi, F. F.; Han, L.; Smets, A. H. M.; Zeman, M.; Dam, B.; van de Krol, R. Efficient Solar Water Splitting by Enhanced Charge Separation in a Bismuth Vanadate-Silicon Tandem Photoelectrode. *Nat. Commun.* **2013**, 4 (1), 2195, DOI: 10.1038/ncomms3195.
- (35) Bornoz, P.; Abdi, F. F.; Tilley, S. D.; Dam, B.; van de Krol, R.; Graetzel, M.; Sivula, K. A Bismuth Vanadate–Cuprous Oxide Tandem Cell for Overall Solar Water Splitting. *J. Phys. Chem. C* **2014**, 118 (30), 16959–16966, DOI: 10.1021/jp500441h.
- (36) Luo, J.; Im, J.-H.; Mayer, M. T.; Schreiber, M.; Nazeeruddin, M. K.; Park, N.-G.; Tilley, S. D.; Fan, H. J.; Grätzel, M. Water Photolysis at 12.3% Efficiency via Perovskite Photovoltaics and Earth-Abundant Catalysts. *Science* **2014**, 345 (6204), 1593–1596, DOI: 10.1126/science.1258307.
- (37) Ager, J. W.; Shaner, M. R.; Walczak, K. A.; Sharp, I. D.; Ardo, S. Experimental Demonstrations of Spontaneous, Solar-Driven Photoelectrochemical Water Splitting. *Energy Environ. Sci.* **2015**, 8 (10), 2811–2824, DOI: 10.1039/C5EE00457H.
- (38) Seitz, L. C.; Chen, Z.; Forman, A. J.; Pinaud, B. A.; Benck, J. D.; Jaramillo, T. F. Modeling Practical Performance Limits of Photoelectrochemical Water Splitting Based on the Current State of Materials Research. *ChemSusChem* **2014**, 7 (5), 1372–1385, DOI: 10.1002/cssc.201301030.
- (39) Hu, S.; Xiang, C.; Haussener, S.; Berger, A. D.; Lewis, N. S. An Analysis of the Optimal Band Gaps of Light Absorbers in Integrated Tandem Photoelectrochemical Water-Splitting Systems. *Energy Environ. Sci.* **2013**, 6 (10), 2984, DOI: 10.1039/c3ee40453f.
- (40) Brillet, J.; Cornuz, M.; Formal, F. Le; Yum, J.-H.; Grätzel, M.; Sivula, K. Examining Architectures of Photoanode–Photovoltaic Tandem Cells for Solar Water Splitting. *J. Mater. Res.* **2010**, 25 (1), 17–24, DOI: 10.1557/JMR.2010.0009.
- (41) Brillet, J.; Yum, J.-H.; Cornuz, M.; Hisatomi, T.; Solarska, R.; Augustynski, J.; Graetzel, M.; Sivula, K. Highly Efficient Water Splitting by a Dual-Absorber Tandem Cell. *Nat. Photonics* **2012**, 6 (12), 824–828, DOI: 10.1038/nphoton.2012.265.
- (42) Gurudayal; Sabba, D.; Kumar, M. H.; Wong, L. H.; Barber, J.; Grätzel, M.; Mathews, N. Perovskite–Hematite Tandem Cells for Efficient Overall Solar Driven Water Splitting. *Nano Lett.* **2015**, 15 (6), 3833–3839, DOI: 10.1021/acs.nanolett.5b00616.
- (43) Shi, X.; Zhang, K.; Shin, K.; Ma, M.; Kwon, J.; Choi, I. T.; Kim, J. K.; Kim, H. K.; Wang, D. H.; Park, J. H. Unassisted Photoelectrochemical Water Splitting beyond 5.7% Solar-to-Hydrogen Conversion Efficiency by a Wireless Monolithic Photoanode/Dye-Sensitized Solar Cell Tandem Device. *Nano Energy* **2015**, 13, 182–191, DOI: 10.1016/j.nanoen.2015.02.018.
- (44) Li, F.; Fan, K.; Xu, B.; Gabrielsson, E.; Daniel, Q.; Li, L.; Sun, L. Organic Dye-Sensitized Tandem Photoelectrochemical Cell for Light Driven Total Water Splitting. *J. Am. Chem. Soc.* **2015**, 137 (28), 9153–9159, DOI: 10.1021/jacs.5b04856.
- (45) Kim, J. H.; Jo, Y.; Kim, J. H.; Jang, J. W.; Kang, H. J.; Lee, Y. H.; Kim, D. S.; Jun, Y.; Lee, J. S. Wireless Solar Water Splitting Device with Robust Cobalt-Catalyzed, Dual-Doped BiVO₄ Photoanode and Perovskite Solar Cell in Tandem: A Dual Absorber Artificial Leaf. *ACS Nano* **2015**, 9 (12), 11820–11829, DOI: 10.1021/acs.nano.5b03859.
- (46) Cheng, W.-H.; Richter, M. H.; May, M. M.; Ohlmann, J.; Lackner, D.; Dimroth, F.; Hannappel, T.;

- Atwater, H. A.; Lewerenz, H.-J. Monolithic Photoelectrochemical Device for Direct Water Splitting with 19% Efficiency. *ACS Energy Lett.* **2018**, *3* (8), 1795–1800, DOI: 10.1021/acsenenergylett.8b00920.
- (47) Abdi, F. F.; Berglund, S. P. Recent Developments in Complex Metal Oxide Photoelectrodes. *J. Phys. D. Appl. Phys.* **2017**, *50* (19), 193002, DOI: 10.1088/1361-6463/aa6738.
 - (48) Tilley, S. D.; Cornuz, M.; Sivula, K.; Grätzel, M. Light-Induced Water Splitting with Hematite: Improved Nanostructure and Iridium Oxide Catalysis. *Angew. Chemie Int. Ed.* **2010**, *49* (36), 6405–6408, DOI: 10.1002/anie.201003110.
 - (49) Paracchino, A.; Mathews, N.; Hisatomi, T.; Stefik, M.; Tilley, S. D.; Grätzel, M. Ultrathin Films on Copper(I) Oxide Water Splitting Photocathodes: A Study on Performance and Stability. *Energy Environ. Sci.* **2012**, *5* (9), 8673–8681, DOI: 10.1039/C2EE22063F.
 - (50) Paracchino, A.; Laporte, V.; Sivula, K.; Grätzel, M.; Thimsen, E. Highly Active Oxide Photocathode for Photoelectrochemical Water Reduction. *Nat. Mater.* **2011**, *10* (6), 456–461, DOI: 10.1038/nmat3017.
 - (51) Abdi, F. F.; Savenije, T. J.; May, M. M.; Dam, B.; van de Krol, R. The Origin of Slow Carrier Transport in BiVO₄ Thin Film Photoanodes: A Time-Resolved Microwave Conductivity Study. *J. Phys. Chem. Lett.* **2013**, *4* (16), 2752–2757, DOI: 10.1021/jz4013257.
 - (52) Wang, F.; Septina, W.; Chemseddine, A.; Abdi, F. F.; Friedrich, D.; Bogdanoff, P.; van de Krol, R.; Tilley, S. D.; Berglund, S. P. Gradient Self-Doped CuBi₂O₄ with Highly Improved Charge Separation Efficiency. *J. Am. Chem. Soc.* **2017**, *139* (42), 15094–15103, DOI: 10.1021/jacs.7b07847.
 - (53) Wang, F.; Chemseddine, A.; Abdi, F. F.; van de Krol, R.; Berglund, S. P. Spray Pyrolysis of CuBi₂O₄ Photocathodes: Improved Solution Chemistry for Highly Homogeneous Thin Films. *J. Mater. Chem. A* **2017**, *5* (25), 12838–12847, DOI: 10.1039/C7TA03009F.
 - (54) Gao, Y.; Zandi, O.; Hamann, T. W. Atomic Layer Stack Deposition-Annealing Synthesis of CuWO₄. *J. Mater. Chem. A* **2016**, *4* (8), 2826–2830, DOI: 10.1039/C5TA06899A.
 - (55) Newhouse, P. F.; Reyes-Lillo, S. E.; Li, G.; Zhou, L.; Shinde, A.; Guevarra, D.; Suram, S. K.; Soedarmadji, E.; Richter, M. H.; Qu, X.; et al. Discovery and Characterization of a Pourbaix-Stable, 1.8 eV Direct Gap Bismuth Manganate Photoanode. *Chem. Mater.* **2017**, *29* (23), 10027–10036, DOI: 10.1021/acs.chemmater.7b03591.
 - (56) Yan, Q.; Li, G.; Newhouse, P. F.; Yu, J.; Persson, K. A.; Gregoire, J. M.; Neaton, J. B. Mn₂V₂O₇: An Earth Abundant Light Absorber for Solar Water Splitting. *Adv. Energy Mater.* **2015**, *5* (8), 1401840, DOI: 10.1002/aenm.201401840.
 - (57) Kölbach, M.; Pereira, I. J.; Harbauer, K.; Plate, P.; Höflich, K.; Berglund, S. P.; Friedrich, D.; van de Krol, R.; Abdi, F. F. Revealing the Performance-Limiting Factors in α -SnWO₄ Photoanodes for Solar Water Splitting. *Chem. Mater.* **2018**, *30* (22), 8322–8331, DOI: 10.1021/acs.chemmater.8b03883.
 - (58) Gurudayal; Bassi, P. S.; Sritharan, T.; Wong, L. H. Recent Progress in Iron Oxide Based Photoanodes for Solar Water Splitting. *J. Phys. D. Appl. Phys.* **2018**, *51* (47), 473002, DOI: 10.1088/1361-6463/aae138.
 - (59) Wang, P.; Yang, H.; Wang, D.; Chen, A.; Dai, W.-L.; Zhao, X.; Yang, J.; Wang, X. Activation of Kagome Lattice-Structured Cu₃V₂O₇(OH)₂·2H₂O Volborthite via Hydrothermal Crystallization for Boosting Visible Light-Driven Water Oxidation. *Phys. Chem. Chem. Phys.* **2018**, *20* (38), 24561–24569, DOI: 10.1039/C8CP03530J.
 - (60) Berglund, S. P.; Abdi, F. F.; Bogdanoff, P.; Chemseddine, A.; Friedrich, D.; Van De Krol, R. Comprehensive Evaluation of CuBi₂O₄ as a Photocathode Material for Photoelectrochemical Water Splitting. *Chem. Mater.* **2016**, *28* (12), 4231–4242, DOI: 10.1021/acs.chemmater.6b00830.
 - (61) Kölbach, M.; Hempel, H.; Harbauer, K.; Schleuning, M.; Petsiuk, A.; Höflich, K.; Deinhart, V.; Friedrich, D.; Eichberger, R.; Abdi, F. F.; et al. Grain Boundaries Limit the Charge Carrier Transport in Pulsed Laser Deposited α -SnWO₄ Thin Film Photoabsorbers. *ACS Appl. Energy Mater.* **2020**, *3* (5), 4320–4330, DOI: 10.1021/acsaem.0c00028.
 - (62) Pihosh, Y.; Turkevych, I.; Mawatari, K.; Uemura, J.; Kazoe, Y.; Kosar, S.; Makita, K.; Sugaya, T.; Matsui, T.; Fujita, D.; et al. Photocatalytic Generation of Hydrogen by Core-Shell WO₃/BiVO₄ Nanorods with Ultimate Water Splitting Efficiency. *Sci. Rep.* **2015**, *5* (1), 11141, DOI: 10.1038/srep11141.

- (63) Chakthranont, P.; Hellstern, T. R.; McEnaney, J. M.; Jaramillo, T. F. Design and Fabrication of a Precious Metal-Free Tandem Core–Shell P+n Si/W-Doped BiVO₄ Photoanode for Unassisted Water Splitting. *Adv. Energy Mater.* **2017**, 7 (22), 1–8, DOI: 10.1002/aenm.201701515.
- (64) Weng, B.; Xu, F.; Xu, J. Core–Shell Photoanode Developed by Atomic Layer Deposition of Bi₂O₃ on Si Nanowires for Enhanced Photoelectrochemical Water Splitting. *Nanotechnology* **2014**, 25 (45), 455402, DOI: 10.1088/0957-4484/25/45/455402.
- (65) Qiu, Y.; Liu, W.; Chen, W.; Chen, W.; Zhou, G.; Hsu, P.-C.; Zhang, R.; Liang, Z.; Fan, S.; Zhang, Y.; et al. Efficient Solar-Driven Water Splitting by Nanocone BiVO₄-Perovskite Tandem Cells. *Sci. Adv.* **2016**, 2 (6), e1501764, DOI: 10.1126/sciadv.1501764.
- (66) Profijt, H. B.; Potts, S. E.; van de Sanden, M. C. M.; Kessels, W. M. M. Plasma-Assisted Atomic Layer Deposition: Basics, Opportunities, and Challenges. *J. Vac. Sci. Technol. A Vacuum, Surfaces, Film.* **2011**, 29 (5), 050801, DOI: 10.1116/1.3609974.
- (67) Knoop, H. C. M.; Potts, S. E.; Bol, A. A.; Kessels, W. M. M. Atomic Layer Deposition. In *Handbook of Crystal Growth*; Elsevier, 2015; pp 1101–1134, DOI: 10.1016/B978-0-444-63304-0.00027-5.
- (68) Haukka, S.; Suntola, T. Advanced Materials Processing by Adsorption Control. *Interface Sci.* **1997**, 5, 119–128, DOI: 10.1023/A:1008601024870.
- (69) Leskelä, M.; Ritala, M. Atomic Layer Deposition(ALD): From Precursors to Thin Film Structures. *Thin Solid Films* **2002**, 409 (1), 138–146, DOI: 10.1016/S0040-6090(02)00117-7.
- (70) Leskelä, M.; Ritala, M. Atomic Layer Deposition Chemistry: Recent Developments and Future Challenges. *Angew. Chemie Int. Ed.* **2003**, 42 (45), 5548–5554, DOI: 10.1002/anie.200301652.
- (71) Wu, Y.; Döhler, D.; Barr, M.; Oks, E.; Wolf, M.; Santinacci, L.; Bachmann, J. Atomic Layer Deposition from Dissolved Precursors. *Nano Lett.* **2015**, 15 (10), 6379–6385, DOI: 10.1021/acs.nanolett.5b01424.
- (72) Mackus, A. J. M.; Schneider, J. R.; MacIsaac, C.; Baker, J. G.; Bent, S. F. Synthesis of Doped, Ternary, and Quaternary Materials by Atomic Layer Deposition: A Review. *Chem. Mater.* **2019**, 31 (4), 1142–1183, DOI: 10.1021/acs.chemmater.8b02878.
- (73) Puurunen, R. L. Growth Per Cycle in Atomic Layer Deposition: A Theoretical Model. *Chem. Vap. Depos.* **2003**, 9 (5), 249–257, DOI: 10.1002/cvde.200306265.
- (74) Cappus, D.; Xu, C.; Ehrlich, D.; Dillmann, B.; Ventrice, C. A.; Al Shamery, K.; Kuhlbeck, H.; Freund, H.-J. Hydroxyl Groups on Oxide Surfaces: NiO(100), NiO(111) and Cr₂O₃(111). *Chem. Phys.* **1993**, 177 (2), 533–546, DOI: 10.1016/0301-0104(93)80031-4.
- (75) Puurunen, R. L. Surface Chemistry of Atomic Layer Deposition: A Case Study for the Trimethylaluminum/Water Process. *J. Appl. Phys.* **2005**, 97 (12), 121301, DOI: 10.1063/1.1940727.
- (76) Langereis, E.; Heil, S. B. S.; Knoop, H. C. M.; Keuning, W.; van de Sanden, M. C. M.; Kessels, W. M. M. In Situ Spectroscopic Ellipsometry as a Versatile Tool for Studying Atomic Layer Deposition. *J. Phys. D. Appl. Phys.* **2009**, 42 (7), 073001, DOI: 10.1088/0022-3727/42/7/073001.
- (77) Kim, W.-H.; Maeng, W. J.; Moon, K.-J.; Myoung, J.-M.; Kim, H. Growth Characteristics and Electrical Properties of La₂O₃ Gate Oxides Grown by Thermal and Plasma-Enhanced Atomic Layer Deposition. *Thin Solid Films* **2010**, 519 (1), 362–366, DOI: 10.1016/j.tsf.2010.07.108.
- (78) Hatanpää, T.; Ihanus, J.; Kansikas, J.; Mutikainen, I.; Ritala, M.; Leskelä, M. Properties of [Mg₂(Thd)₄] as a Precursor for Atomic Layer Deposition of MgO Thin Films and Crystal Structures of [Mg₂(Thd)₄] and [Mg(Thd)₂(EtOH)₂]. *Chem. Mater.* **1999**, 11 (7), 1846–1852, DOI: 10.1021/cm991008e.
- (79) Ylilampi, M. Monolayer Thickness in Atomic Layer Deposition. *Thin Solid Films* **1996**, 279 (1–2), 124–130, DOI: 10.1016/0040-6090(95)08159-3.
- (80) Cremers, V.; Puurunen, R. L.; Dendooven, J. Conformality in Atomic Layer Deposition: Current Status Overview of Analysis and Modelling. *Appl. Phys. Rev.* **2019**, 6 (2), 021302, DOI: 10.1063/1.5060967.
- (81) *Atomic Layer Deposition of Nanostructured Materials*; Pinna, N., Knez, M., Eds.; Wiley-VCH Verlag GmbH & Co. KGaA: Weinheim, Germany, 2011, DOI: 10.1002/9783527639915.
- (82) Mattelaer, F.; Vereecken, P. M.; Dendooven, J.; Detavernier, C. Deposition of MnO Anode and MnO₂ Cathode Thin Films by Plasma Enhanced Atomic Layer Deposition Using the Mn(Thd)₃ Precursor. *Chem. Mater.* **2015**, 27 (10), 3628–3635, DOI: 10.1021/acs.chemmater.5b00255.
- (83) de Rouffignac, P.; Park, J.-S.; Gordon, R. G. Atomic Layer Deposition of Y₂O₃ Thin Films from

- Yttrium Tris(N,N'-Diisopropylacetamidinate) and Water. *Chem. Mater.* **2005**, *17* (19), 4808–4814, DOI: 10.1021/cm050624+.
- (84) Ritala, M.; Leskelä, M.; Dekker, J.-P.; Mutsaers, C.; Soininen, P. J.; Skarp, J. Perfectly Conformal TiN and Al₂O₃ Films Deposited by Atomic Layer Deposition. *Chem. Vap. Depos.* **1999**, *5* (1), 7–9, DOI: 10.1002/(SICI)1521-3862(199901)5:1<7::AID-CVDE7>3.0.CO;2-J.
 - (85) Database of ALD processes <https://www.atomiclimits.com/alddatabase/> (accessed May 3, 2019), DOI: 10.6100/alddatabase.
 - (86) Elam, J. W.; George, S. M. Growth of ZnO/Al₂O₃ Alloy Films Using Atomic Layer Deposition Techniques. *Chem. Mater.* **2003**, *15* (4), 1020–1028, DOI: 10.1021/cm020607+.
 - (87) Chen, X.; Pomerantseva, E.; Banerjee, P.; Gregorczyk, K.; Ghodssi, R.; Rubloff, G. Ozone-Based Atomic Layer Deposition of Crystalline V₂O₅ Films for High Performance Electrochemical Energy Storage. *Chem. Mater.* **2012**, *24* (7), 1255–1261, DOI: 10.1021/cm202901z.
 - (88) Stefik, M. Atomic Layer Deposition of Bismuth Vanadates for Solar Energy Materials. *ChemSusChem* **2016**, *9* (13), 1727–1735, DOI: 10.1002/cssc.201600457.
 - (89) Lamm, B.; Sarkar, A.; Stefik, M. Surface Functionalized Atomic Layer Deposition of Bismuth Vanadate for Single-Phase Scheelite. *J. Mater. Chem. A* **2017**, *5* (13), 6060–6069, DOI: 10.1039/C6TA09485F.
 - (90) Smith, H. M.; Turner, A. F. Vacuum Deposited Thin Films Using a Ruby Laser. *Appl. Opt.* **1965**, *4* (1), 147–148, DOI: 10.1364/AO.4.000147.
 - (91) Dijkkamp, D.; Venkatesan, T.; Wu, X. D.; Shaheen, S. A.; Jisrawi, N.; Min-Lee, Y. H.; McLean, W. L.; Croft, M. Preparation of Y-Ba-Cu Oxide Superconductor Thin Films Using Pulsed Laser Evaporation from High T_c Bulk Material. *Appl. Phys. Lett.* **1987**, *51* (8), 619–621, DOI: 10.1063/1.98366.
 - (92) Schou, J. Physical Aspects of the Pulsed Laser Deposition Technique: The Stoichiometric Transfer of Material from Target to Film. *Appl. Surf. Sci.* **2009**, *255* (10), 5191–5198, DOI: <https://doi.org/10.1016/j.apsusc.2008.10.101>.
 - (93) Andor. A Simple Overview of Pulsed Laser Deposition <https://andor.oxinst.com/learning/view/article/pulsed-laser-deposition>.
 - (94) Fähler, S.; Krebs, H.-U. Calculations and Experiments of Material Removal and Kinetic Energy during Pulsed Laser Ablation of Metals. *Appl. Surf. Sci.* **1996**, *96–98*, 61–65, DOI: [https://doi.org/10.1016/0169-4332\(95\)00466-1](https://doi.org/10.1016/0169-4332(95)00466-1).
 - (95) Kölbach, M.; Harbauer, K.; Ellmer, K.; van de Krol, R. Elucidating the Pulsed Laser Deposition Process of BiVO₄ Photoelectrodes for Solar Water Splitting. *J. Phys. Chem. C* **2020**, *124* (8), 4438–4447, DOI: 10.1021/acs.jpcc.9b11265.
 - (96) Kölbach, M. Pulsed Laser Deposition of Efficient Ternary Metal Oxide Photoelectrodes, TU Berlin, Helmholtz-Zentrum Berlin, 2019.
 - (97) Lee, J.; Yoon, H.; Kim, S.; Seo, S.; Song, J.; Choi, B.-U.; Choi, S. Y.; Park, H.; Ryu, S.; Oh, J.; et al. Long-Term Stabilized High-Density CuBi₂O₄/NiO Heterostructure Thin Film Photocathode Grown by Pulsed Laser Deposition. *Chem. Commun.* **2019**, *55* (83), 12447–12450, DOI: 10.1039/C9CC06092H.
 - (98) Gottesman, R.; Song, A.; Levine, I.; Krause, M.; Islam, A. T. M. N.; Abou-Ras, D.; Dittrich, T.; van de Krol, R.; Chemseddine, A. Pure CuBi₂O₄ Photoelectrodes with Increased Stability by Rapid Thermal Processing of Bi₂O₃/CuO Grown by Pulsed Laser Deposition. *Adv. Funct. Mater.* **2020**, *1910832*, DOI: 10.1002/adfm.201910832.
 - (99) Arnold, C. B.; Aziz, M. J. Stoichiometry Issues in Pulsed-Laser Deposition of Alloys Grown from Multicomponent Targets. *Appl. Phys. A Mater. Sci. Process.* **1999**, *69* (7), S23–S27, DOI: 10.1007/s003390051349.
 - (100) Gomez-San Roman, R.; Casero, R. P.; Maréchal, C.; Enard, J. P.; Perrière, J. ¹⁸O Isotopic Tracer Studies of the Laser Ablation of Bi₂Sr₂Ca₁Cu₂O₈. *J. Appl. Phys.* **1996**, *80* (3), 1787–1793, DOI: 10.1063/1.362989.
 - (101) Soltan, S. *Interaction of Superconductivity and Ferromagnetism in YBCO-LCMO Heterostructures*; Cuvillier, 2005.
 - (102) Riet, E. van de; Nillesen, C. J. C. M.; Dieleman, J. Reduction of Droplet Emission and Target Roughening in Laser Ablation and Deposition of Metals. *J. Appl. Phys.* **1993**, *74* (3), 2008–2012, DOI: 10.1063/1.354763.

- (103) Tompkins, H. G.; Irene, E. A. *Handbook of Ellipsometry*; William Andrew Pub., 2005.
- (104) Fujiwara, H. Spectroscopic Ellipsometry. In *Spectroscopic Ellipsometry*; John Wiley & Sons, Ltd: Chichester, UK, 2007; pp i–xviii, DOI: 10.1002/9780470060193.fmatter.
- (105) *Spectroscopic Ellipsometry and Reflectometry: A User's Guide*; Tompkins, H., McGahan, W., Eds.; Wiley, 1999.
- (106) Jellison, G. E.; Modine, F. A. Parameterization of the Optical Functions of Amorphous Materials in the Interband Region. *Appl. Phys. Lett.* **1996**, *69* (3), 371–373, DOI: 10.1063/1.118064.
- (107) Hüfner, S. *Photoelectron Spectroscopy*; Springer: Berlin, Heidelberg, 2003, DOI: <https://doi.org/10.1007/978-3-662-09280-4>.
- (108) Ratner, B. D.; Castner, D. G. Electron Spectroscopy for Chemical Analysis. *Surface Analysis – The Principal Techniques*. April 3, 2009, pp 47–112, DOI: doi:10.1002/9780470721582.ch3.
- (109) Moulder, J. F.; Stickle, W. F.; Sobol, P. E.; Bomben, K. D. *Handbook of X-Ray Photoelectron Spectroscopy*; 1995.
- (110) NIST XPS Database srdata.nist.gov/xps (accessed Apr 1, 2020), DOI: 10.18434/T4T88K.
- (111) SPECS. Quantification in XPS Using SpecsLab and CasaXPS; 2009; pp 1–57.
- (112) Favaro, M.; Uecker, R.; Nappini, S.; Piš, I.; Magnano, E.; Bluhm, H.; van de Krol, R.; Starr, D. E. Chemical, Structural, and Electronic Characterization of the (010) Surface of Single Crystalline Bismuth Vanadate. *J. Phys. Chem. C* **2019**, *123* (13), 8347–8359, DOI: 10.1021/acs.jpcc.8b09016.
- (113) Savenije, T. J.; Ferguson, A. J.; Kopidakis, N.; Rumbles, G. Revealing the Dynamics of Charge Carriers in Polymer:Fullerene Blends Using Photoinduced Time-Resolved Microwave Conductivity. *J. Phys. Chem. C* **2013**, *117* (46), 24085–24103, DOI: 10.1021/jp406706u.
- (114) Lamers, M.; Sahre, M.; Müller, M. J.; Abou-Ras, D.; van de Krol, R.; Abdi, F. F. Influence of Post-Deposition Annealing on the Photoelectrochemical Performance of CuBi₂O₄ Thin Films. *APL Mater.* **2020**, *8* (6), 61101, DOI: 10.1063/5.0003005.
- (115) Müller, M. J.; Komander, K.; Höhn, C.; van de Krol, R.; Bronneberg, A. C. Growth of Bi₂O₃ Films by Thermal- and Plasma-Enhanced Atomic Layer Deposition Monitored with Real-Time Spectroscopic Ellipsometry for Photocatalytic Water Splitting. *ACS Appl. Nano Mater.* **2019**, *2* (10), 6277–6286, DOI: 10.1021/acsanm.9b01261.
- (116) Amano, F.; Nogami, K.; Abe, R.; Ohtani, B. Preparation and Characterization of Bismuth Tungstate Polycrystalline Flake-Ball Particles for Photocatalytic Reactions. *J. Phys. Chem. C* **2008**, *112* (25), 9320–9326, DOI: 10.1021/jp801861r.
- (117) Moniz, S. J. A.; Quesada-Cabrera, R.; Blackman, C. S.; Tang, J.; Southern, P.; Weaver, P. M.; Carmalt, C. J. A Simple, Low-Cost CVD Route to Thin Films of BiFeO₃ for Efficient Water Photo-Oxidation. *J. Mater. Chem. A* **2014**, *2* (9), 2922, DOI: 10.1039/c3ta14824f.
- (118) Li, Y.; Liu, J.; Huang, X. Synthesis and Visible-Light Photocatalytic Property of Bi₂WO₆ Hierarchical Octahedron-Like Structures. *Nanoscale Res. Lett.* **2008**, *3* (10), 365–371, DOI: 10.1007/s11671-008-9168-7.
- (119) Lamm, B.; Zhou, L.; Rao, P.; Stefik, M. Atomic Layer Deposition of Space-Efficient SnO₂ Underlayers for BiVO₄ Host–Guest Architectures for Photoassisted Water Splitting. *ChemSusChem* **2019**, *12* (9), 1770–1770, DOI: 10.1002/cssc.201901063.
- (120) Schuisky, M.; Kukli, K.; Ritala, M.; Härsta, A.; Leskelä, M. Atomic Layer CVD in the Bi–Ti–O System. *Chem. Vap. Depos.* **2000**, *6* (3), 139–145, DOI: 10.1002/(SICI)1521-3862(200006)6:3<139::AID-CVDE139>3.0.CO;2-T.
- (121) Liu, H. F.; Antwi, K. K. A.; Wang, Y. D.; Ong, L. T.; Chua, S. J.; Chi, D. Z. Atomic Layer Deposition of Crystalline Bi₂O₃ Thin Films and Their Conversion into Bi₂S₃ by Thermal Vapor Sulfurization. *RSC Adv.* **2014**, *4* (102), 58724–58731, DOI: 10.1039/C4RA09896J.
- (122) Pham, C. D.; Chang, J.; Zurbuchen, M. A.; Chang, J. P. Synthesis and Characterization of BiFeO₃ Thin Films for Multiferroic Applications by Radical Enhanced Atomic Layer Deposition. *Chem. Mater.* **2015**, *27* (21), 7282–7288, DOI: 10.1021/acs.chemmater.5b02162.
- (123) Austin, D. Z.; Allman, D.; Price, D.; Hose, S.; Saly, M.; Conley, J. F. Atomic Layer Deposition of Bismuth Oxide Using Bi(OCMe₂iPr)₃ and H₂O. *J. Vac. Sci. Technol. A Vacuum, Surfaces, Film.* **2014**, *32* (1), 01A113, DOI: 10.1116/1.4840835.
- (124) Vehkamäki, M.; Hatanpää, T.; Ritala, M.; Leskelä, M. Bismuth Precursors for Atomic Layer Deposition of Bismuth-Containing Oxide Films. *J. Mater. Chem.* **2004**, *14* (21), 3191–3197, DOI:

- 10.1039/B405891G.
- (125) Bronneberg, A. On the Origin and Formation of Defect States in ALD-Grown 'Leaky' TiO₂. **2021**, to be submitted.
 - (126) Shen, Y. D.; Li, Y. W.; Li, W. M.; Zhang, J. Z.; Hu, Z. G.; Chu, J. H. Growth of Bi₂O₃ Ultrathin Films by Atomic Layer Deposition. *J. Phys. Chem. C* **2012**, *116* (5), 3449–3456, DOI: 10.1021/jp205180p.
 - (127) Hatanpää, T.; Vehkamäki, M.; Ritala, M.; Leskelä, M. Study of Bismuth Alkoxides as Possible Precursors for ALD. *Dalt. Trans.* **2010**, *39* (13), 3219, DOI: 10.1039/b918175j.
 - (128) Xie, Q.; Musschoot, J.; Deduytsche, D.; Van Meirhaeghe, R. L.; Detavernier, C.; Van den Berghe, S.; Jiang, Y.-L.; Ru, G.-P.; Li, B.-Z.; Qu, X.-P. Growth Kinetics and Crystallization Behavior of TiO₂ Films Prepared by Plasma Enhanced Atomic Layer Deposition. *J. Electrochem. Soc.* **2008**, *155* (9), H688, DOI: 10.1149/1.2955724.
 - (129) Maeng, W. J.; Kim, H. Thermal and Plasma-Enhanced ALD of Ta and Ti Oxide Thin Films from Alkylamide Precursors. *Electrochem. Solid-State Lett.* **2006**, *9* (6), G191, DOI: 10.1149/1.2186427.
 - (130) van Hemmen, J. L.; Heil, S. B. S.; Klootwijk, J. H.; Roozeboom, F.; Hodson, C. J.; van de Sanden, M. C. M.; Kessels, W. M. M. Plasma and Thermal ALD of Al₂O₃ in a Commercial 200 Mm ALD Reactor. *J. Electrochem. Soc.* **2007**, *154* (7), G165, DOI: 10.1149/1.2737629.
 - (131) Seah, M. P.; Dench, W. A. Quantitative Electron Spectroscopy of Surfaces: A Standard Data Base for Electron Inelastic Mean Free Paths in Solids. *Surf. Interface Anal.* **1979**, *1* (1), 2–11, DOI: 10.1002/sia.740010103.
 - (132) Uchida, K.; Ayame, A. Dynamic XPS Measurements on Bismuth Molybdate Surfaces. *Surf. Sci.* **1996**, *357–358*, 170–175, DOI: 10.1016/0039-6028(96)00083-0.
 - (133) Berg, C.; Raaen, S.; Borg, A.; Andersen, J. N.; Lundgren, E.; Nyholm, R. Observation of a Low-Binding-Energy Peak in the 2 p Core-Level Photoemission from Oxidized Al(111). *Phys. Rev. B* **1993**, *47* (19), 13063–13066, DOI: 10.1103/PhysRevB.47.13063.
 - (134) Iatsunskyi, I.; Kempirski, M.; Jancelewicz, M.; Załęski, K.; Jurga, S.; Smyntyna, V. Structural and XPS Characterization of ALD Al₂O₃ Coated Porous Silicon. *Vacuum* **2015**, *113*, 52–58, DOI: 10.1016/j.vacuum.2014.12.015.
 - (135) Barreca, D.; Morazzoni, F.; Rizzi, G. A.; Scotti, R.; Tondello, E. Molecular Oxygen Interaction with Bi₂O₃: A Spectroscopic and Spectromagnetic Investigation. *Phys. Chem. Chem. Phys.* **2001**, *3* (9), 1743–1749, DOI: 10.1039/B009482J.
 - (136) McDaniel, M. D.; Ngo, T. Q.; Hu, S.; Posadas, A.; Demkov, A. A.; Ekerdt, J. G. Atomic Layer Deposition of Perovskite Oxides and Their Epitaxial Integration with Si, Ge, and Other Semiconductors. *Appl. Phys. Rev.* **2015**, *2* (4), 041301, DOI: 10.1063/1.4934574.
 - (137) Shin, W. C.; Ryu, S. O.; You, I. K.; Yoon, S. M.; Cho, S. M.; Lee, N. Y.; Kim, K. D.; Yu, B. G.; Lee, W. J.; Choi, K. J.; et al. Low Voltage Switching Characteristics of 60 Nm Thick SrBi[Sub 2]Ta[Sub 2]O[Sub 9] Thin Films Deposited by Plasma-Enhanced ALD. *Electrochem. Solid-State Lett.* **2004**, *7* (5), F31, DOI: 10.1149/1.1667017.
 - (138) Ehrstein, J. Thickness Evaluation for 2nm SiO₂ Films, a Comparison of Ellipsometric, Capacitance-Voltage and HRTEM Measurements. In *AIP Conference Proceedings*; AIP, 2003; Vol. 683, pp 331–336, DOI: 10.1063/1.1622491.
 - (139) Kohli, S.; Rithner, C. D.; Dorhout, P. K.; Dummer, A. M.; Menoni, C. S. Comparison of Nanometer-Thick Films by x-Ray Reflectivity and Spectroscopic Ellipsometry. *Rev. Sci. Instrum.* **2005**, *76* (2), 023906, DOI: 10.1063/1.1848660.
 - (140) Jellison, G. E.; Chisholm, M. F.; Gorbalkin, S. M. Optical Functions of Chemical Vapor Deposited Thin-film Silicon Determined by Spectroscopic Ellipsometry. *Appl. Phys. Lett.* **1993**, *62* (25), 3348–3350, DOI: 10.1063/1.109067.
 - (141) Zhang, L.; Jiang, H. C.; Liu, C.; Dong, J. W.; Chow, P. Annealing of Al₂O₃ Thin Films Prepared by Atomic Layer Deposition. *J. Phys. D. Appl. Phys.* **2007**, *40* (12), 3707–3713, DOI: 10.1088/0022-3727/40/12/025.
 - (142) Zav'yalova, A. A.; Imamov, R. M. Special Features of the Crystal Structure of Bismuth Oxides. *J. Struct. Chem.* **1973**, *13* (5), 811–814, DOI: 10.1007/BF00738892.
 - (143) Fan, H. T.; Teng, X. M.; Pan, S. S.; Ye, C.; Li, G. H.; Zhang, L. D. Optical Properties of δ-Bi₂O₃ Thin Films Grown by Reactive Sputtering. *Appl. Phys. Lett.* **2005**, *87* (23), 231916, DOI: 10.1063/1.2136351.

- (144) Leontie, L.; Caraman, M.; Visinoiu, A.; Rusu, G. I. On the Optical Properties of Bismuth Oxide Thin Films Prepared by Pulsed Laser Deposition. *Thin Solid Films* **2005**, *473* (2), 230–235, DOI: 10.1016/j.tsf.2004.07.061.
- (145) Leontie, L.; Caraman, M.; Alexe, M.; Harnagea, C. Structural and Optical Characteristics of Bismuth Oxide Thin Films. *Surf. Sci.* **2002**, *507–510*, 480–485, DOI: 10.1016/S0039-6028(02)01289-X.
- (146) Ma, S.; Liang, H.; Wang, X.; Zhou, J.; Li, L.; Sun, C. Q. Controlling the Band Gap of ZnO by Programmable Annealing. *J. Phys. Chem. C* **2011**, *115* (42), 20487–20490, DOI: 10.1021/jp207237d.
- (147) Madhusudan Reddy, K.; Manorama, S. V.; Ramachandra Reddy, A. Bandgap Studies on Anatase Titanium Dioxide Nanoparticles. *Mater. Chem. Phys.* **2003**, *78* (1), 239–245, DOI: 10.1016/S0254-0584(02)00343-7.
- (148) Wang, J.; Wang, Z.; Huang, B.; Ma, Y.; Liu, Y.; Qin, X.; Zhang, X.; Dai, Y. Oxygen Vacancy Induced Band-Gap Narrowing and Enhanced Visible Light Photocatalytic Activity of ZnO. *ACS Appl. Mater. Interfaces* **2012**, *4* (8), 4024–4030, DOI: 10.1021/am300835p.
- (149) Han, H.; Mayer, J. W.; Alford, T. L. Band Gap Shift in the Indium-Tin-Oxide Films on Polyethylene Naphthalate after Thermal Annealing in Air. *J. Appl. Phys.* **2006**, *100* (8), 083715, DOI: 10.1063/1.2357647.
- (150) Ho, C.-H.; Chan, C.-H.; Huang, Y.-S.; Tien, L.-C.; Chao, L.-C. The Study of Optical Band Edge Property of Bismuth Oxide Nanowires α -Bi₂O₃. *Opt. Express* **2013**, *21* (10), 11965, DOI: 10.1364/OE.21.011965.
- (151) Gordon, P. G.; Kurek, A.; Barry, S. T. Trends in Copper Precursor Development for CVD and ALD Applications. *ECS J. Solid State Sci. Technol.* **2015**, *4* (1), N3188–N3197, DOI: 10.1149/2.0261501jss.
- (152) Kalutarage, L. C.; Clendenning, S. B.; Winter, C. H. Low-Temperature Atomic Layer Deposition of Copper Films Using Borane Dimethylamine as the Reducing Co-Reagent. *Chem. Mater.* **2014**, *26* (12), 3731–3738, DOI: 10.1021/cm501109r.
- (153) Törndahl, T.; Ottosson, M.; Carlsson, J.-O. Growth of Copper Metal by Atomic Layer Deposition Using Copper(I) Chloride, Water and Hydrogen as Precursors. *Thin Solid Films* **2004**, *458* (1–2), 129–136, DOI: 10.1016/j.tsf.2003.12.063.
- (154) Reijnen, L.; Meester, B.; Goossens, A.; Schoonman, J. Atomic Layer Deposition of Cu_xS for Solar Energy Conversion. *Chem. Vap. Depos.* **2003**, *9* (1), 15–20, DOI: 10.1002/cvde.200290001.
- (155) Iivonen, T.; Hämäläinen, J.; Marchand, B.; Mizohata, K.; Mattinen, M.; Popov, G.; Kim, J.; Fischer, R. A.; Leskelä, M. Low-Temperature Atomic Layer Deposition of Copper(II) Oxide Thin Films. *J. Vac. Sci. Technol. A Vacuum, Surfaces, Film.* **2016**, *34* (1), 01A109, DOI: 10.1116/1.4933089.
- (156) Maeng, W.; Lee, S.-H.; Kwon, J.-D.; Park, J.; Park, J.-S. Atomic Layer Deposited P-Type Copper Oxide Thin Films and the Associated Thin Film Transistor Properties. *Ceram. Int.* **2016**, *42* (4), 5517–5522, DOI: 10.1016/j.ceramint.2015.12.109.
- (157) Alnes, M. E.; Monakhov, E.; Fjellvåg, H.; Nilsen, O. Atomic Layer Deposition of Copper Oxide Using Copper(II) Acetylacetonate and Ozone. *Chem. Vap. Depos.* **2012**, *18* (4–6), 173–178, DOI: 10.1002/cvde.201106959.
- (158) Fronk, M.; Müller, S.; Waechtler, T.; Schulz, S. E.; Mothes, R.; Lang, H.; Zahn, D. R. T.; Salvan, G. Magneto-Optical Kerr-Effect Studies on Copper Oxide Thin Films Produced by Atomic Layer Deposition on SiO₂. *Thin Solid Films* **2012**, *520* (14), 4741–4744, DOI: 10.1016/j.tsf.2011.10.204.
- (159) Waechtler, T.; Oswald, S.; Roth, N.; Jakob, A.; Lang, H.; Ecke, R.; Schulz, S. E.; Gessner, T.; Moskvina, A.; Schulze, S.; et al. Copper Oxide Films Grown by Atomic Layer Deposition from Bis(Tri-*n*-Butylphosphane)Copper(I)Acetylacetonate on Ta, TaN, Ru, and Si O₂. *J. Electrochem. Soc.* **2009**, *156* (6), 1–10, DOI: 10.1149/1.3110842.
- (160) Melzer, M.; Waechtler, T.; Müller, S.; Fiedler, H.; Hermann, S.; Rodriguez, R. D.; Villabona, A.; Sendzik, A.; Mothes, R.; Schulz, S. E.; et al. Copper Oxide Atomic Layer Deposition on Thermally Pretreated Multi-Walled Carbon Nanotubes for Interconnect Applications. *Microelectron. Eng.* **2013**, *107*, 223–228, DOI: 10.1016/j.mee.2012.10.026.
- (161) Törndahl, T.; Ottosson, M.; Carlsson, J. O. Growth of Copper(I) Nitride by ALD Using Copper(II)

- Hexafluoroacetylacetonate, Water, and Ammonia as Precursors. *J. Electrochem. Soc.* **2006**, *153* (3), 146–151, DOI: 10.1149/1.2160427.
- (162) Gottesman, R.; Van De Krol, R. Mn₂V₂O₇ as Possible Photoabsorber by PLD, 2018, oral communication.
- (163) Malm, J.; Sajavaara, T.; Karppinen, M. Atomic Layer Deposition of WO₃ Thin Films Using W(CO)₆ and O₃ Precursors. *Chem. Vap. Depos.* **2012**, *18* (7–9), 245–248, DOI: 10.1002/cvde.201206986.
- (164) Mamun, M. A.; Zhang, K.; Baumgart, H.; Elmustafa, A. A. Nanomechanical Properties of Tungsten Trioxide (WO₃) Grown by Atomic Layer Deposition. *ECS Trans.* **2014**, *64* (9), 211–217, DOI: 10.1149/06409.0211ecst.
- (165) Nandi, D. K.; Sarkar, S. K. Atomic Layer Deposition of Tungsten Oxide for Solar Cell Application. *Energy Procedia* **2014**, *54*, 782–788, DOI: 10.1016/j.egypro.2014.07.321.
- (166) Strobel, A.; Schnabel, H.-D.; Reinhold, U.; Rauer, S.; Neidhardt, A. Room Temperature Plasma Enhanced Atomic Layer Deposition for TiO₂ and WO₃ Films. *J. Vac. Sci. Technol. A Vacuum, Surfaces, Film.* **2016**, *34* (1), 01A118, DOI: 10.1116/1.4935356.
- (167) Popovich, A. A.; Maximov, M. Y.; Nazarov, D. V.; Novikov, P. A.; Silin, A. O.; Shamsurin, A. I. Low-Temperature Deposition of Tin(IV) Oxide Films for Thin-Film Power Sources. *Russ. J. Appl. Chem.* **2016**, *89* (5), 805–808, DOI: 10.1134/S1070427216050190.
- (168) Liu, R.; Lin, Y.; Chou, L. Y.; Sheehan, S. W.; He, W.; Zhang, F.; Hou, H. J. M.; Wang, D. Water Splitting by Tungsten Oxide Prepared by Atomic Layer Deposition and Decorated with an Oxygen-Evolving Catalyst. *Angew. Chemie - Int. Ed.* **2011**, *50* (2), 499–502, DOI: 10.1002/anie.201004801.
- (169) Zhang, H.; Ren, W.; Cheng, C. Three-Dimensional SnO₂@TiO₂ Double-Shell Nanotubes on Carbon Cloth as a Flexible Anode for Lithium-Ion Batteries. *Nanotechnology* **2015**, *26* (27), 274002, DOI: 10.1088/0957-4484/26/27/274002.
- (170) Mattelaer, F.; Bosserez, T.; Rongé, J.; Martens, J. A.; Dendooven, J.; Detavernier, C. Manganese Oxide Films with Controlled Oxidation State for Water Splitting Devices through a Combination of Atomic Layer Deposition and Post-Deposition Annealing. *RSC Adv.* **2016**, *6* (100), 98337–98343, DOI: 10.1039/c6ra19188f.
- (171) Plate, P. Model-System Studies on Manganese Oxide-Based Water Oxidation Catalysts Made with Atomic Layer Deposition, TU Berlin, Helmholtz-Zentrum Berlin, 2019.
- (172) Blanquart, T.; Niinistö, J.; Gavagnin, M.; Longo, V.; Heikkilä, M.; Puukilainen, E.; Pallem, V. R.; Dussarrat, C.; Ritala, M.; Leskelä, M. Atomic Layer Deposition and Characterization of Vanadium Oxide Thin Films. *RSC Adv.* **2013**, *3* (4), 1179–1185, DOI: 10.1039/C2RA22820C.
- (173) Willinger, M.-G.; Neri, G.; Rauwel, E.; Bonavita, A.; Micali, G.; Pinna, N. Vanadium Oxide Sensing Layer Grown on Carbon Nanotubes by a New Atomic Layer Deposition Process. *Nano Lett.* **2008**, *8* (12), 4201–4204, DOI: 10.1021/nl801785b.
- (174) Santos, L.; Światowska, J.; Lair, V.; Zanna, S.; Seyeux, A.; Melendez-Ceballos, A.; Tran-Van, P.; Cassir, M.; Marcus, P. Mechanisms of Enhanced Lithium Intercalation into Thin Film V₂O₅ in Ionic Liquids Investigated by X-Ray Photoelectron Spectroscopy and Time-of-Flight Secondary Ion Mass Spectrometry. *J. Power Sources* **2017**, *364*, 61–71, DOI: 10.1016/j.jpowsour.2017.08.003.
- (175) Weimer, M. S.; Kim, I. S.; Guo, P.; Schaller, R. D.; Martinson, A. B. F.; Hock, A. S. Oxidation State Discrimination in the Atomic Layer Deposition of Vanadium Oxides. *Chem. Mater.* **2017**, *29* (15), 6238–6244, DOI: 10.1021/acs.chemmater.7b01130.
- (176) Wang, X.; Guo, Z.; Gao, Y.; Wang, J. Atomic Layer Deposition of Vanadium Oxide Thin Films from Tetrakis(Dimethylamino)Vanadium Precursor. *J. Mater. Res.* **2017**, *32* (1), 37–44, DOI: 10.1557/jmr.2016.303.
- (177) Badot, J. C. Atomic Layer Epitaxy of Vanadium Oxide Thin Films and Electrochemical Behavior in Presence of Lithium Ions. *Electrochem. Solid-State Lett.* **1999**, *3* (10), 485, DOI: 10.1149/1.1391187.
- (178) Musschoot, J.; Deduytsche, D.; Poelman, H.; Haemers, J.; Van Meirhaeghe, R. L.; Van den Berghe, S.; Detavernier, C. Comparison of Thermal and Plasma-Enhanced ALD/CVD of Vanadium Pentoxide. *J. Electrochem. Soc.* **2009**, *156* (7), P122, DOI: 10.1149/1.3133169.
- (179) Boukhalfa, S.; Evanoff, K.; Yushin, G. Atomic Layer Deposition of Vanadium Oxide on Carbon Nanotubes for High-Power Supercapacitor Electrodes. *Energy Environ. Sci.* **2012**, *5* (5), 6872,

DOI: 10.1039/c2ee21110f.

- (180) Burton, B. B.; Fabreguette, F. H.; George, S. M. Atomic Layer Deposition of MnO Using Bis(Ethylcyclopentadienyl)Manganese and H₂O. *Thin Solid Films* **2009**, *517* (19), 5658–5665, DOI: 10.1016/j.tsf.2009.02.050.
- (181) Pickrahn, K. L.; Gorlin, Y.; Seitz, L. C.; Garg, A.; Nordlund, D.; Jaramillo, T. F.; Bent, S. F. Applications of ALD MnO to Electrochemical Water Splitting. *Phys. Chem. Chem. Phys.* **2015**, *17* (21), 14003–14011, DOI: 10.1039/C5CP00843C.
- (182) Strandwitz, N. C.; Comstock, D. J.; Grimm, R. L.; Nichols-Niellander, A. C.; Elam, J.; Lewis, N. S. Photoelectrochemical Behavior of N-Type Si(100) Electrodes Coated with Thin Films of Manganese Oxide Grown by Atomic Layer Deposition. *J. Phys. Chem. C* **2013**, *117* (10), 4931–4936, DOI: 10.1021/jp311207x.
- (183) Liao, J.-H.; Leroux, F.; Piffard, Y.; Guyomard, D.; Payen, C. Synthesis, Structures, Magnetic Properties, and Phase Transition of Manganese(II) Divanadate: Mn₂V₂O₇. *J. Solid State Chem.* **1996**, *121* (1), 214–224, DOI: 10.1006/jssc.1996.0030.
- (184) Sambandam, B.; Soundharajan, V.; Song, J.; Kim, S.; Jo, J.; Duong, P. T.; Kim, S.; Mathew, V.; Kim, J. Investigation of Li-Ion Storage Properties of Earth Abundant B-Mn₂V₂O₇ prepared Using Facile Green Strategy. *J. Power Sources* **2017**, *350*, 80–86, DOI: 10.1016/j.jpowsour.2017.03.054.
- (185) Sannigrahi, J.; Giri, S.; Majumdar, S. Magnetic and Dielectric Properties of Mn₂V₂O₇. *Solid State Commun.* **2016**, *228*, 10–15, DOI: 10.1016/j.ssc.2015.11.020.
- (186) Mattelaer, F.; Geryl, K.; Rempelberg, G.; Dobbelaere, T.; Dendooven, J.; Detavernier, C. Atomic Layer Deposition of Vanadium Oxides for Thin-Film Lithium-Ion Battery Applications. *RSC Adv.* **2016**, *6* (115), 114658–114665, DOI: 10.1039/C6RA25742A.
- (187) Zoellner, B.; Gordon, E.; Maggard, P. A. A Small Bandgap Semiconductor, p-Type Mn₂V₂O₆, Active for Photocatalytic Hydrogen and Oxygen Production. *Dalt. Trans.* **2017**, *46* (32), 10657–10664, DOI: 10.1039/c7dt00780a.
- (188) Ruhemann, F. Temperaturabhängigkeit Der Gitterkonstanten von Manganoxyd. *Phys. Ber* **1935**, *16*, 2337.
- (189) Jarosch, D. Crystal Structure Refinement and Reflectance Measurements of Hausmannite, Mn₃O₄. *Mineral. Petrol.* **1987**, *37* (1), 15–23, DOI: 10.1007/BF01163155.
- (190) Norrestam, R.; Ingri, N.; Östlund, E.; Bloom, G.; Hagen, G. Alpha-Manganese(III) Oxide --- a C-Type Sesquioxide of Orthorhombic Symmetry. *Acta Chem. Scand.* **1967**, *21*, 2871–2884.
- (191) Shinde, P. S.; Annamalai, A.; Kim, J. H.; Choi, S. H.; Lee, J. S.; Jang, J. S. Exploiting the Dynamic Sn Diffusion from Deformation of FTO to Boost the Photocurrent Performance of Hematite Photoanodes. *Sol. Energy Mater. Sol. Cells* **2015**, *141*, 71–79, DOI: 10.1016/j.solmat.2015.05.020.
- (192) Bedoya-Lora, F. E.; Hankin, A.; Holmes-Gentle, I.; Regoutz, A.; Nania, M.; Payne, D. J.; Cabral, J. T.; Kelsall, G. H. Effects of Low Temperature Annealing on the Photo-Electrochemical Performance of Tin-Doped Hematite Photo-Anodes. *Electrochim. Acta* **2017**, *251*, 1–11, DOI: 10.1016/j.electacta.2017.08.090.
- (193) Biesinger, M. C.; Payne, B. P.; Grosvenor, A. P.; Lau, L. W. M.; Gerson, A. R.; Smart, R. S. C. Resolving Surface Chemical States in XPS Analysis of First Row Transition Metals, Oxides and Hydroxides: Cr, Mn, Fe, Co and Ni. *Appl. Surf. Sci.* **2011**, *257* (7), 2717–2730, DOI: 10.1016/j.apsusc.2010.10.051.
- (194) Biesinger, M. C.; Lau, L. W. M.; Gerson, A. R.; Smart, R. S. C. Resolving Surface Chemical States in XPS Analysis of First Row Transition Metals, Oxides and Hydroxides: Sc, Ti, V, Cu and Zn. *Appl. Surf. Sci.* **2010**, *257* (3), 887–898, DOI: 10.1016/j.apsusc.2010.07.086.
- (195) Ureña-Begara, F.; Crunteanu, A.; Raskin, J. P. Raman and XPS Characterization of Vanadium Oxide Thin Films with Temperature. *Appl. Surf. Sci.* **2017**, *403*, 717–727, DOI: 10.1016/j.apsusc.2017.01.160.
- (196) Silversmit, G.; Depla, D.; Poelman, H.; Marin, G. B.; De Gryse, R. Determination of the V_{2p} XPS Binding Energies for Different Vanadium Oxidation States (V⁵⁺ to V⁰⁺). *J. Electron Spectros. Relat. Phenomena* **2004**, *135* (2–3), 167–175, DOI: 10.1016/j.elspec.2004.03.004.
- (197) Lamers, M.; Fiechter, S.; Friedrich, D.; Abdi, F. F.; van de Krol, R. Formation and Suppression of Defects during Heat Treatment of BiVO₄ Photoanodes for Solar Water Splitting. *J. Mater. Chem. A* **2018**, *6* (38), 18694–18700, DOI: 10.1039/C8TA06269B.

- (198) Stoerzinger, K. A.; Risch, M.; Han, B.; Shao-Horn, Y. Recent Insights into Manganese Oxides in Catalyzing Oxygen Reduction Kinetics. *ACS Catal.* **2015**, *5* (10), 6021–6031, DOI: 10.1021/acscatal.5b01444.
- (199) Lokhande, C. D.; Park, B.-O.; Park, H.-S.; Jung, K.-D.; Joo, O.-S. Electrodeposition of TiO₂ and RuO₂ Thin Films for Morphology-Dependent Applications. *Ultramicroscopy* **2005**, *105* (1–4), 267–274, DOI: 10.1016/j.ultramic.2005.06.048.
- (200) Song, A.; Plate, P.; Chemseddine, A.; Wang, F.; Abdi, F. F.; Wollgarten, M.; van de Krol, R.; Berglund, S. P. Cu:NiO as a Hole-Selective Back Contact to Improve the Photoelectrochemical Performance of CuBi₂O₄ Thin Film Photocathodes. *J. Mater. Chem. A* **2019**, *7* (15), 9183–9194, DOI: 10.1039/C9TA01489F.
- (201) Kang, D.; Hill, J. C.; Park, Y.; Choi, K.-S. Photoelectrochemical Properties and Photostabilities of High Surface Area CuBi₂O₄ and Ag-Doped CuBi₂O₄ Photocathodes. *Chem. Mater.* **2016**, *28* (12), 4331–4340, DOI: 10.1021/acs.chemmater.6b01294.
- (202) Arai, T.; Konishi, Y.; Iwasaki, Y.; Sugihara, H.; Sayama, K. High-Throughput Screening Using Porous Photoelectrode for the Development of Visible-Light-Responsive Semiconductors. *J. Comb. Chem.* **2007**, *9* (4), 574–581, DOI: 10.1021/cc0700142.
- (203) Davila, Y.; Petitmangin, A.; Hebert, C.; Perrière, J.; Seiler, W. Oxygen Deficiency in Oxide Films Grown by PLD. *Appl. Surf. Sci.* **2011**, *257* (12), 5354–5357, DOI: <https://doi.org/10.1016/j.apsusc.2010.10.075>.
- (204) Hau, S. K.; Wong, K. H.; Chan, P. W.; Choy, C. L. Intrinsic Resputtering in Pulsed-laser Deposition of Lead-zirconate-titanate Thin Films. *Appl. Phys. Lett.* **1995**, *66* (2), 245–247, DOI: 10.1063/1.113560.
- (205) Garcia-Munoz, J. L.; Rodriguez-Carvajal, J.; Sapina, F.; Sanchis, M. J.; Ibanez, R.; Beltran-Porter, D. Crystal and Magnetic Structures of Bi₂CuO₄. *J. Phys. Condens. Matter* **1990**, *2* (9), 2205–2214, DOI: 10.1088/0953-8984/2/9/010.
- (206) Popović, Z. V.; Kliche, G.; Cardona, M.; Liu, R. Vibrational Properties of Bi₂CuO₄. *Phys. Rev. B* **1990**, *41* (6), 3824–3828, DOI: 10.1103/PhysRevB.41.3824.
- (207) Yuvaraj, S.; Karthikeyan, K.; Kalpana, D.; Lee, Y. S.; Selvan, R. K. Surfactant-Free Hydrothermal Synthesis of Hierarchically Structured Spherical CuBi₂O₄ as Negative Electrodes for Li-Ion Hybrid Capacitors. *J. Colloid Interface Sci.* **2016**, *469*, 47–56, DOI: 10.1016/j.jcis.2016.01.060.
- (208) Popovic, Z. V.; Kliche, G.; Konstantinovic, M. J.; Revcolevschi, A. Polarized Far-Infrared and Raman Spectra of Bi₂CuO₄ single Crystals. *J. Phys. Condens. Matter* **1992**, *4* (49), 10085–10092, DOI: 10.1088/0953-8984/4/49/036.
- (209) Zhang, F. X.; Saxena, S. K. Raman Studies of Bi₂CuO₄ at High Pressures. *Appl. Phys. Lett.* **2006**, *88* (14), 141926, DOI: 10.1063/1.2189450.
- (210) Bertin, E. P. *Principles and Practice of X-Ray Spectrometric Analysis*; Springer US: Boston, MA, 1975, DOI: 10.1007/978-1-4613-4416-2.
- (211) Jose Chirayil, C.; Abraham, J.; Kumar Mishra, R.; George, S. C.; Thomas, S. Instrumental Techniques for the Characterization of Nanoparticles. In *Thermal and Rheological Measurement Techniques for Nanomaterials Characterization*; Thomas, S., Thomas, R., Zachariah, A. K., Mishra, R. K. B. T.-T. and R. M. T. for N. C., Eds.; Elsevier, 2017; pp 1–36, DOI: 10.1016/B978-0-323-46139-9.00001-3.
- (212) Karl, H.; Grosshans, I.; Wenzel, A.; Stritzker, B.; Claessen, R.; Strocov, V. N.; Cirlin, G. E.; Egorov, V. A.; Polyakov, N. K.; Samsonenko, Y. B.; et al. Stoichiometry and Absolute Atomic Concentration Profiles Obtained by Combined Rutherford Backscattering Spectroscopy and Secondary-Ion Mass Spectroscopy: InAs Nanocrystals in Si. *Nanotechnology* **2002**, *13* (5), 631–634, DOI: 10.1088/0957-4484/13/5/318.
- (213) Sharma, G.; Zhao, Z.; Sarker, P.; Nail, B. A.; Wang, J.; Huda, M. N.; Osterloh, F. E. Electronic Structure, Photovoltage, and Photocatalytic Hydrogen Evolution with p-CuBi₂O₄ Nanocrystals. *J. Mater. Chem. A* **2016**, *4* (8), 2936–2942, DOI: 10.1039/C5TA07040F.
- (214) Septina, W.; Prabhakar, R. R.; Wick, R.; Moehl, T.; Tilley, S. D. Stabilized Solar Hydrogen Production with CuO/CdS Heterojunction Thin Film Photocathodes. *Chem. Mater.* **2017**, *29* (4), 1735–1743, DOI: 10.1021/acs.chemmater.6b05248.
- (215) Kroeze, J. E.; Savenije, T. J.; Warman, J. M. Electrodeless Determination of the Trap Density, Decay Kinetics, and Charge Separation Efficiency of Dye-Sensitized Nanocrystalline TiO₂. *J. Am. Chem. Soc.* **2004**, *126* (24), 7608–7618, DOI: 10.1021/ja039303u.

- (216) Kroeze, J. E.; Savenije, T. J.; Vermeulen, M. J. W.; Warman, J. M. Contactless Determination of the Photoconductivity Action Spectrum, Exciton Diffusion Length, and Charge Separation Efficiency in Polythiophene-Sensitized TiO₂ Bilayers. *J. Phys. Chem. B* **2003**, *107* (31), 7696–7705, DOI: 10.1021/jp0217738.
- (217) Jang, J.-W.; Friedrich, D.; Müller, S.; Lamers, M.; Hempel, H.; Lardhi, S.; Cao, Z.; Harb, M.; Cavallo, L.; Heller, R.; et al. Enhancing Charge Carrier Lifetime in Metal Oxide Photoelectrodes through Mild Hydrogen Treatment. *Adv. Energy Mater.* **2017**, *7* (22), 1701536, DOI: <https://doi.org/10.1002/aenm.201701536>.
- (218) Ziwrtsch, M.; Müller, S.; Hempel, H.; Unold, T.; Abdi, F. F.; van de Krol, R.; Friedrich, D.; Eichberger, R. Direct Time-Resolved Observation of Carrier Trapping and Polaron Conductivity in BiVO₄. *ACS Energy Lett.* **2016**, *1* (5), 888–894, DOI: 10.1021/acsenerylett.6b00423.
- (219) Klyndyuk, A. I.; Petrov, G. S.; Bashkirov, L. A.; Akimov, A. I.; Poluyan, A. F. Thermal Stability and Phase Transformations in CuBi₂O₄. *Russ. J. Inorg. Chem.* **1999**, *44* (1), 1–4.
- (220) Minks, B. P.; Vanmaekelbergh, D.; Kelly, J. J. Current-Doubling, Chemical Etching and the Mechanism of Two-Electron Reduction Reactions at GaAs: Part 2. A Unified Model. *J. Electroanal. Chem. Interfacial Electrochem.* **1989**, *273* (1), 133–145, DOI: [https://doi.org/10.1016/0022-0728\(89\)87008-1](https://doi.org/10.1016/0022-0728(89)87008-1).
- (221) Luo, J.; Steier, L.; Son, M.-K.; Schreier, M.; Mayer, M. T.; Grätzel, M. Cu₂O Nanowire Photocathodes for Efficient and Durable Solar Water Splitting. *Nano Lett.* **2016**, *16* (3), 1848–1857, DOI: 10.1021/acs.nanolett.5b04929.
- (222) Hu, S.; Shaner, M. R.; Beardslee, J. A.; Lichterman, M.; Brunschwig, B. S.; Lewis, N. S. Amorphous TiO₂ Coatings Stabilize Si, GaAs, and GaP Photoanodes for Efficient Water Oxidation. *Science* **2014**, *344* (6187), 1005–1009, DOI: 10.1126/science.1251428.
- (223) Bronneberg, A. C.; Höhn, C.; van de Krol, R. Probing the Interfacial Chemistry of Ultrathin ALD-Grown TiO₂ Films: An In-Line XPS Study. *J. Phys. Chem. C* **2017**, *121* (10), 5531–5538, DOI: 10.1021/acs.jpcc.6b09468.
- (224) Filatova, E. O.; Konashuk, A. S. Interpretation of the Changing the Band Gap of Al₂O₃ Depending on Its Crystalline Form: Connection with Different Local Symmetries. *J. Phys. Chem. C* **2015**, *119* (35), 20755–20761, DOI: 10.1021/acs.jpcc.5b06843.
- (225) Jia, J.; Seitz, L. C.; Benck, J. D.; Huo, Y.; Chen, Y.; Ng, J. W. D.; Bilir, T.; Harris, J. S.; Jaramillo, T. F. Solar Water Splitting by Photovoltaic-Electrolysis with a Solar-to-Hydrogen Efficiency over 30%. *Nat. Commun.* **2016**, *7* (1), 13237, DOI: 10.1038/ncomms13237.
- (226) Nakamura, A.; Ota, Y.; Koike, K.; Hidaka, Y.; Nishioka, K.; Sugiyama, M.; Fujii, K. A 24.4% Solar to Hydrogen Energy Conversion Efficiency by Combining Concentrator Photovoltaic Modules and Electrochemical Cells. *Appl. Phys. Express* **2015**, *8* (10), 107101, DOI: 10.7567/APEX.8.107101.
- (227) Wegatech. Photovoltaik Wirkungsgrad - das leisten moderne Photovoltaik-anlagen <https://www.wegatech.de/ratgeber/photovoltaik/grundlagen/wirkungsgrad/> (accessed Dec 10, 2020).
- (228) Fraunhofer ISE. *Photovoltaics Report*; Freiburg, 2020.
- (229) Jacobsson, T. J. Photoelectrochemical Water Splitting: An Idea Heading towards Obsolescence? *Energy Environ. Sci.* **2018**, *11* (8), 1977–1979, DOI: 10.1039/C8EE00772A.

Eidesstattliche Erklärung

Ich erkläre, dass ich die vorliegende, unter der Betreuung von Prof. Dr. Roel van de Krol angefertigte Dissertation selbständig verfasst habe. Andere als die angegebenen Hilfsmittel wurden von mir nicht benutzt. Alle angeführten Zitate wurden kenntlich gemacht.

Berlin den 31.03.2021

Matthias Müller